Numerical Modelling of Advanced Materials Subjected to High-Energy Particle Beam Impacts

Marcus Portelli

Department of Mechanical Engineering
Faculty of Engineering
University of Malta

A dissertation submitted to the University of Malta for the Degree of Doctor of Philosophy

March 2021

Funding

This project has received funding from the European Union's Horizon 2020 Research and Innovation programme under grant agreement no. 730871.

L-Università ta' Malta

Declaration of Authenticity

Student's I.D.:	176094M
Student's Name & Surname:	Marcus Portelli
Course:	Doctor of Philosophy in Mechanical Engineering
Title of Dissertation:	Numerical Modelling of Advanced Materials Subjected to High-Energy Particle Beam Impacts

I hereby declare that I am the legitimate author of this thesis and that it is my original work.

No portion of this work has been submitted in support of an application for another degree or qualification of this or any other university or institution of higher education.

_____ _____

Signature of Student Name of Student

_____

Date

Copyright Notice

Signed _____ Date _____

Għal Luana, u għall-għażiż nannu Joe.

Abstract

The High-Luminosity Large Hadron Collider (HL-LHC) upgrade for the LHC brings with it an increase in beam energy, necessitating improvements in all systems. The development of novel, high-performing materials is crucial in assuring targets are achieved. This is especially true in the context of collimators and other beam intercepting devices, which are required to cope with elevated intensities, while delivering a lower contribution to machine impedance. For this reason, experimental campaigns such as those conducted in the HiRadMat facility at the European Organisation for Nuclear Research (CERN) are essential for testing of materials under intense particle beam impact. Thermal and structural measurements allow for the validation of mathematical models describing the material behaviour, which are implemented in numerical models simulating the experimental scenario. Once validated, such models can be applied to simulate more complex, full-scale scenarios.

In this Ph.D. study, a number of materials of interest in the field of particle accelerators and other thermomechanical applications are studied. Research on available literature highlights the need for accurate mathematical models describing the behaviour of materials under the extreme conditions imposed by quasi-instantaneous particle beam impacts. With this in mind, models for Silicon Carbide (SiC), Titanium Zirconium Molybdenum (TZM) alloy, and Copper Diamond (CuCD) metal-matrix composite are proposed and applied in finite element analyses modelling beam impacts from the HRMT36 experiment. The large amount of data collected in the experiment is used to benchmark computed numerical results. The material models put forward can be applied in analyses modelling impacts on collimator jaws and other absorbers and targets commissioned in CERN's accelerator complex. The models are found to be able to successfully simulate various impact scenarios from the HRMT36 experiment, as well as phenomena of interest such as boundary condition effects and wave propagation in failure scenarios. Further study is conducted on the behaviour of CuCD on a mesoscopic level, for which a numerical model is built to simulate wave-particle interaction for particle-reinforced composites subjected to intense impacts. Additionally, a tabular equation of state for the material is formulated from constituent material data. The work presented also identifies a number of key areas of interest for future study of the materials considered, namely related to material testing at elevated temperatures and high strain-rates, which would allow for the full description of the material behaviour for the application in question.

Acknowledgements

Firstly, I would like to express my gratitude and appreciation to my supervisors at the University of Malta, Pierluigi Mollicone and Nicholas Sammut, for their help and support throughout the course of this Ph.D. program, and for introducing me to this collaborative effort in my MSc.

I am extremely grateful for having had the opportunity to work together with many wonderful and talented people involved in this project, and am especially appreciative of the guidance provided by Michele Pasquali, Federico Carra and Alessandro Bertarelli. Special thanks also goes to Jorge Guardia Valenzuela and Óscar Sacristán de Frutos, who were of great assistance. I would also like to thank all industrial and academic stakeholders forming part of the ARIES network, for their contributions and feedback on presented results.

A warm thank you goes to my University of Malta colleagues from Room 217 for their company: Marija, Donald, Robert, Daniel, Brian, Jessica, Federica, the other Daniel, and all others. Additionally, thanks goes to the staff at the Faculty of Engineering: all the secretaries, lecturers who gave me the opportunity to guide undergraduate students in lab sessions, Roberto Bonello, and Kevin Farrugia.

I would like to thank my friends and family for their constant interest and support, despite the abstract nature of my work. Finally, I am very much thankful to my fiancée Luana for her constant loving support, encouragement and patience.

Table of Contents

List of Figures

List of Tables

List of Acronyms

AD	Antiproton Decelerator
APDL	Ansys Parametric Design Language
BCC	Body-Centred Cubic
BID	Beam Intercepting Devices
BLT	Beam Lifetime
CCC	CERN Control Centre
CCD	Charge-Coupled Device
CERN	European Organisation for Nuclear Research Conseil européen pour la recherche nucléaire
CFC	Carbon Fibre Composite
CTE	Coefficient of Thermal Expansion
CuCD	Copper Diamond metal-matrix composite
CuCrZr	Copper Chromium Zirconium alloy
CuNi	Copper Nickel alloy
CVD	Chemical Vapour Deposition
DBTT	Ductile-to-Brittle Transition Temperature
DS	Dispersion Suppressor
DSC	Differential Scanning Calorimeter
EOS	Equation of State
FCC	Future Circular Collider
FEA	Finite Element Analysis
FEM	Finite Element Method
HCP	Hexagonal Cubic Packing
HIP	Hot Isostatic Pressing
HIPIMS	High-power impulse magnetron sputtering
HL-LHC	High Luminosity Large Hadron Collider
HRMT	HiRadMat (High-Radiation to Materials)
IET	Impulse Excitation Technique
IR	Interaction Region
JC	Johnson-Cook

LDV	Laser Doppler Vibrometer
LFA	Laser Flash Apparatus
LHC	Large Hadron Collider
MMC	Metal-Matrix Composite
MoGr	Molybdenum Graphite graphite-matrix composite
PRMMC	Particulate-Reinforced Metal-Matrix Composite
PS	Proton Synchrotron
RF	Radio Frequency
RFI	RF Impedance Index
RMS	Root Mean Square
RVE	Representative Volume Element
SC	Superconducting
SEM	Scanning Electron Microscope
SiC	Silicon Carbide ceramic
SPS	Super Proton Synchrotron
SS	Stainless Steel alloy
TaW	Tantalum Tungsten alloy
TCC	Thermal Contact Conductance
TCLA	Long Absorber
TCP	Primary Collimator
TCSG	Secondary Collimator
TCT	Tertiary Collimator
TiN	Titanium Nitride ceramic
TRI	Thermomechanical Robustness Index
TSI	Thermal Stability Index
TZM	Titanium Zirconium Molybdenum alloy
ZA	Zerilli-Armstrong

Nomenclature

$\dot{\varepsilon}_0$	$m \cdot m^{-1}$	Effective plastic strain rate in quasistatic test
$\dot{\varepsilon}_{pl}$	$m \cdot m^{-1}$	Plastic strain rate
t_L	μs	Fundamental period of longitudinal vibrations
t_d	s	Thermal diffusion time
ε_{pl}	$m \cdot m^{-1}$	Equivalent plastic strain
A, B, n	*MPa, MPa, -*	Quasistatic limit and work hardening parameters for JC model
c / c_0	$m \cdot s^{-1}$	Speed of sound in an elastic medium
C	-	Sensitivity to strain rate (JC model)
$C_{i=1,2,3,4,5}$	MPa / K^{-1}	ZA material parameters
c_p	$J \cdot K^{-1} \cdot kg^{-1}$	Specific heat capacity at a constant pressure
c_v	$J \cdot K^{-1} \cdot kg^{-1}$	Specific heat capacity at a constant volume
E	GPa / $J \cdot kg^{-1}$	Young's modulus / Specific internal energy
f	Hz	Frequency
H	J	Helmholtz free energy
K[1]	GPa	Bulk modulus
k	$W \cdot m^{-1} \cdot K^{-1}$	Thermal conductivity
L	m	Length of cylindrical rod
m	kg / -	Mass / thermal softening coefficient
P	Pa	Pressure
p	-	Proton
r	m	Radial coordinate

[1] The bulk modulus is sometimes denoted by B in literature (B^T for the isothermal bulk modulus, B^S for the isentropic bulk modulus). In this case, the compressibility is denoted by $K = 1/B$.

R	m	Radius of cylindrical rod
t	s	Time
T	$°C$	Temperature
t_d	s	Thermal diffusion time
T_m	$°C$	Melting temperature
T_r	$°C$	Reference temperature
u	$m \cdot s^{-1}$	Wave velocity
U_{max}	$J \cdot kg^{-1}$	Maximum deposited specific energy
U_p	$m \cdot s^{-1}$	Particle velocity
U_s	$m \cdot s^{-1}$	Shock front velocity
v	m^3	Specific volume
V	$m^3 \cdot kg^{-1}$	Volume
x / y / z	m	Displacement in X, Y and Z coordinates
Y_0	MPa	Yield Strength
α	K^{-1}	Linear thermal expansion coefficient / mass coefficient
α_v	K^{-1}	Volumetric coefficient of thermal expansion
β	-	Stiffness coefficient
γ	-	Grüneisen parameter
δ	-	Logarithmic decrement
Δt	s	Time step
Δx	m	Mesh interval length
ε	$m \cdot m^{-1}$	Strain
η	mm	Eccentricity of energy distribution w.r.t. axis of interest
κ	$m^2 \cdot s^{-1}$	Thermal diffusivity
Λ	m	Wavelength
ν	-	Poisson's ratio
ρ	$kg \cdot m^{-3}$	Density

σ	*Pa*	Stress
σ_{ref}	*Pa*	Reference axial stress
τ	*μs*	Thermal pulse duration / energy deposition time / beam lifetime
Φ or σ	*mm*	Transverse beam size (one standard deviation)
ζ	-	Rayleigh damping ratio

List of Publications

The following peer-reviewed submissions and/or publications are a result of the work conducted throughout the course of the project presented in this thesis.

M. Portelli, A. Bertarelli, F. Carra, M. Pasquali, P. Mollicone, N. Sammut, *"Numerical and experimental benchmarking of dynamic responses of SiC and TZM in the MultiMat experiment",* published in *Journal of Mechanics of Materials*, 2019 (DOI: 10.1016/j.mechmat.2019.103169).

M. Portelli, A. Bertarelli, F. Carra, M. Pasquali, P. Mollicone, N. Sammut, Óscar Sacristán de Frutos, Jorge Guardia Valenzuela, Erich Neubauer, Michael Kitzmantel, David Grech, *"Thermomechanical Characterisation of Copper Diamond and Benchmarking with the MultiMat experiment"*, published in *Shock and Vibration*, 2021 (DOI: 10.1155/2021/8879400).

M. Portelli, A. Bertarelli, F. Carra, P. Mollicone, N. Sammut, *"Modelling of wave-particle interactions in Copper Diamond"*, submitted to *Physical Review Accelerators and Beams*, 2021.

F. Carra, A. Bertarelli, E. Berthomé, C. Fichera, T. Furness, M. Guinchard, L. K. Mettler, **M. Portelli**, S. Redaelli, O. Sacristan de Frutos , *"The MultiMat experiment at CERN HiRadMat facility: Advanced testing of novel materials and instrumentation for HL-LHC collimators"*, published in *Journal of Physics: Conference Series IPAC17*, 2017 (DOI: 10.1088/1742-6596/874/1/012001).

A. Bertarelli, C. Accettura, E. Berthomé, L. Bianchi, P. Bolz, F. Carra, C. Fichera, M. I. Frankl, T. Furness, G. Gobbi, P. Grosclaude, J. Guardia Valenzuela, M. Guinchard, A. Lechner, P. Mollicone, M. Pasquali, **M. Portelli**, S. Redaelli, E. Rigutto, O. Sacristan de Frutos, P. Simon, "*Dynamic Testing and Characterization of Advanced Materials in a New Experiment at CERN HiRadMat Facility*", published in *Journal of Physics: Conference Series IPAC18*, 2018 (DOI: 10.1088/1742-6596/1067/8/082021).

M. Pasquali, A. Bertarelli. C. Accettura, E. Berthomé, L. Bianchi, P. Bolz, F. Carra, C. Fichera, M. I. Frankl, T. Furness, G. Gobbi, P. Grosclaude, J. Guardia Valenzuela, M. Guinchard, M. D. Jedrychowsky, F. J. Harden, A. Lechner, P. Mollicone, P. D. Pastuszak, **M. Portelli**, S. Redaelli, E. Rigutto, O. Sacristan de Frutos, P. Simon, *"Dynamic response of*

advanced materials impacted by particle beams: The MultiMat experiment", published in *Journal of Dynamic Behaviour of Materials*, 2019 (DOI: 10.1007/s40870-019-00210-1).

C. Accettura, A. Baris, M. Beghi, A. Bertarelli, P. Bolz, F. Carra, P. Pastuszak, A. Perez, **M. Portelli**, A. Prosvetov, V. Raffuzzi, S. Redaelli, P. Simon, M. Tomut, A. Waets*, "Calcium ions irradiation test on materials for HL-LHC collimators: experiment description and outcome"*, submitted to *Physical Review Accelerators and Beams*, 2020.

Chapter 1:
Introduction

1.1 General Introduction

The European Organisation for Nuclear Research, CERN, operates the largest particle physics laboratory in the world, with its main aim being that of studying the elementary particles, the basic constituents of matter. The fundamental laws of nature are studied by colliding subatomic particles together at close to the speed of light. The instruments used are particle accelerators and detectors: the former boost beams of electrons, protons or ionised particles to high energies before colliding; whilst the latter are used to observe and record the results of these collisions [1]. High-energy particle beams are brought to collision against another beam or a fixed target, causing the formation of a vast array of subatomic particles. The state of this matter can be compared to that of the universe in its very first moments.

CERN was established in 1954 with the original idea to study atomic nuclei, and was soon applied to study high-energy physics. A number of accelerators and a decelerator are currently operated in chain, either delivering the beam to a more powerful accelerator operating at a higher beam energy, or to an experiment. Various discoveries in the field of particle physics have been made at the facility, the most recent and notable being the discovery of the Higgs Boson in the Large Hadron Collider in 2012, which confirmed the prediction of its existence by François Englert and Peter Higgs, leading to them being awarded the Nobel Prize in Physics [2], [3]. The strong engineering background required to build and maintain the accelerator complex has led to a number of other discoveries, including the development of the world wide web and the first web browser by Tim Berners-Lee in 1989, as a means to share information within CERN [4], [5].

Currently active machines at CERN include Linac 2 and Linac 3, the Proton Synchrotron (PS), the Super Proton Synchrotron (SPS), and the Large Hadron Collider (LHC) – the latter being the world's largest circular accelerator, housed in a 27-km-long underground tunnel. Two 450 GeV beams of 3.2×10^{14} protons are brought into the LHC from the SPS, after being accelerated in the injection chain, shown in Figure 1. The LHC mainly provides proton to proton collisions with a centre-of-mass of 14 TeV, with a stored energy of 360 MJ per beam [6], [7]. The upcoming high luminosity upgrade for the LHC (HL-LHC) brings an increase in beam intensity, requiring an improvement in the performance of all systems, including the collimation system, which also needs to guarantee a reduction in machine

impedance[2] in order to minimise beam instability risks. As shown in Figure 2, the LHC is currently in its second long shutdown (LS2), following which the third physics run will span a period of 3 years. The HL-LHC installation period is scheduled between 2025 and 2027, following which the machine will run for an undefined period until an integrated luminosity[3] of 3000-4000 fb^{-1} is achieved.

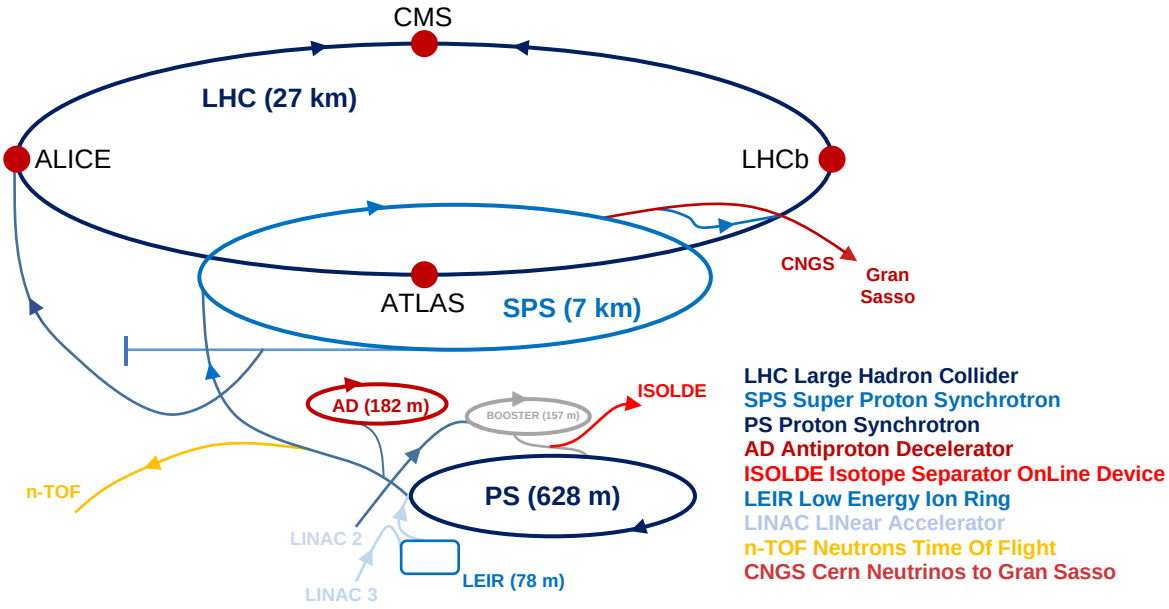

Figure 1 – CERN accelerator complex, including the accelerator chain from Linac2 to the LHC [1].

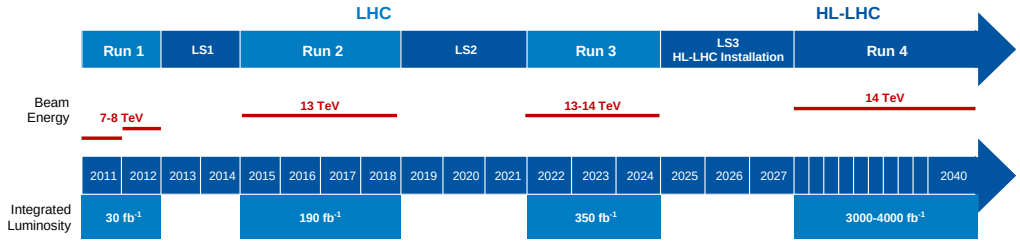

Figure 2 – Timeline for the LHC's Run 1/2/3, Long Shutdown 1/2/3, and Run 4 following the HL-LHC upgrade [1].

[2] In particle physics, machine impedance is a quantity which characterises the self-interaction of charged particle beams. The impedance is dependent on factors such as the quality of the ultra-high vacuum, the collimators' electrical resistivity, and other elements the beam encounters in the accelerator ring.

[3] The luminosity is the ratio of the number of detected events (in a certain time period) to the interaction cross-section of a particle accelerator (measured in $cm^{-2}s^{-1}$). The value is dependent on beam parameters such as particle flow rate and beam width. The integrated luminosity is the integral of the luminosity with respect to time. Along with the luminosity, it is used to characterise the performance of particle accelerators. Collider experiments look to maximise this value, since this means that more data is available to analyse.

The LHC beams collide at four interaction region, each housing one of the four particle detectors, namely ALICE, ATLAS, CMS and LHCb. The detectors are made of layers of subdetectors, such as tracking devices and calorimeters, designed to look for a specific type of particle or property. The locations of the different experiments along the LHC tunnel are shown in Figure 3, along with an image of the ATLAS detector, one of the two experiments involved in the detection of the Higgs boson [8]. An image of the LHC tunnel is also shown, with a view of the two proton beams [9]. The LHC beams travel in opposite directions in an ultra-high vacuum, guided along the accelerator ring by superconducting (SC) electromagnets, which require cooling by liquid helium to a temperature of -271.3°C to operate in a superconducting state.

Due to the high energy in the LHC beams, a multi-stage collimation system is required at all stages of machine operation. The collimation system is made out of blocks of material along the tunnel, surrounding the beams. The main function of this system is beam cleaning, i.e., the interception of beam halo particles which escape the correct beam trajectory during normal operation. The system protects sensitive equipment, such as the SC magnets, in both normal scenarios and in the case of accidental impacts. Interactions between high-energy particle beams and solids result in an energy deposition on the body, inducing a temperature increase. In nominal conditions, a continuous energy deposition rate is provoked by beam losses, which can last from a few seconds up to hours. In abnormal depositions, energy can be rapidly dumped on a structure in the order of nanoseconds, in turn leading to a dynamic response. A schematic diagram displaying the current multi-stage collimation system is shown in Figure 4 [10].

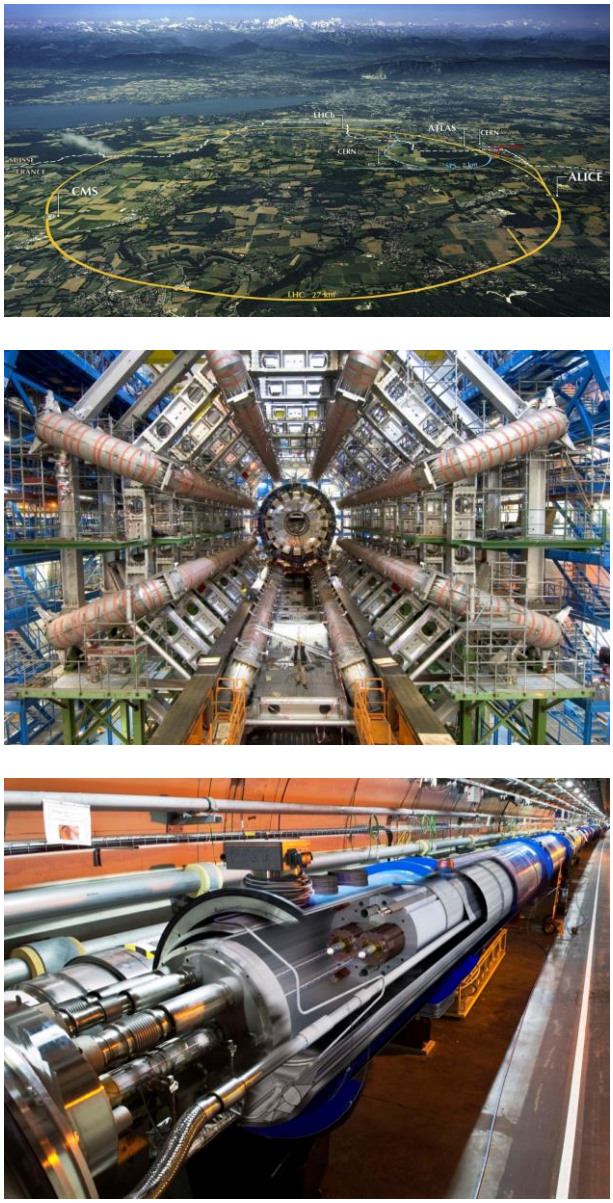

Figure 3 – Location of particle detectors along the LHC (top), the ATLAS detector in the LHC (middle) [8], and the LHC tunnel (bottom) [9].

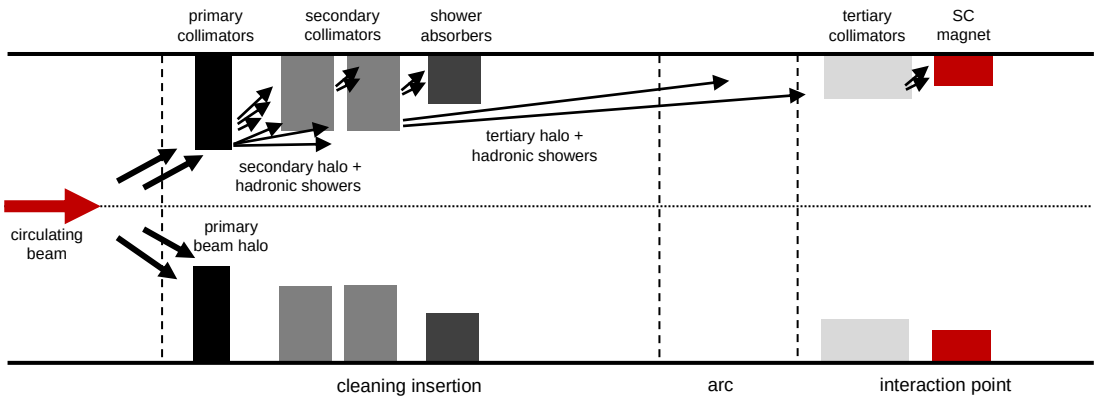

Figure 4 – Schematic displaying concept of current multi-stage collimation system.

1.2 Motivation and Objectives

As mentioned, the operation of the LHC is strongly dependent on its collimation system. This is especially true for the HL-LHC upgrade as well as the Future Circular Collider (FCC), where the machine's reliability and luminosity targets require the handling of high-intensity circulating beams. Such high intensities result in a need to study the thermal and mechanical response of structures subject to fast internal heating as a result of impacts by high-energy particle beams. The collimator jaws are the closest elements to the proton beam and are therefore constantly at risk of impact in normal operations and in the case of accidental impacts, which can result in a dynamic thermomechanical response in the impacted structure. Beam intercepting devices utilise materials which need to be able to withstand such conditions. Such materials are tested in CERN's HiRadMat facility, in experiments such as the HRMT36 campaign, which was conducted to assess the dynamic response of current and future materials used in beam intercepting devices commissioned in CERN's accelerator complex.

Within the described context, this thesis delves into the data collected throughout this experimental campaign, presents numerical simulations performed to benchmark and extend material constitutive models with experimental results, and additionally presents newly formulated models. The materials used in the collimation system are subjected to extreme conditions, at times making it impossible to perform experimental tests on full-scale models. For this reason, smaller-scale experiments such as HRMT36 are essential, allowing the development of reliable and accurate computational models which can be applied in large-scale analyses to simulate and estimate the material behaviour during accidental impacts. In this study, a numerical finite element approach is implemented in transient, thermomechanical analyses to model quasi-instantaneous particle beam impacts, considering scenarios tested in the HRMT36 experiment. The material behaviour is modelled in the elasto-plastic domain and the material models implemented are benchmarked with experimental measurements. This thesis presents a number of case studies modelling the behaviour of a variety of materials under beam impact, and delves into specific aspects such as boundary condition effects and the influence of the mesoscale structure in metal-matrix composites.

The main objectives of this project are:

- The collection of characteristic thermal and structural data on materials of interest in the field of beam intercepting devices, with the intention of building numerical models accurately describing the materials' behaviour. Specifically, this study focuses on three materials tested in the HRMT36 experiment, namely Silicon Carbide (SiC), Titanium Zirconium Molybdenum alloy (TZM), and Copper Diamond metal-matrix composite (CuCD). Limited literature is currently available on these materials, particularly in the context of beam intercepting devices;
- The application of the formulated material models in thermomechanical finite element analyses simulating dynamic effects experienced by material specimens tested under beam impact in the HRMT36 experiment;
- The benchmarking of numerical models with experimental measurements from HRMT36, allowing for fine-tuning and additional commissioning of material testing to improve the currently available material models for future applications;
- The development of a deeper understanding of a variety of phenomena observed in the experimental campaign, including boundary condition effects and failure scenarios observed in measurements for SiC and TZM, and wave attenuation in the case of CuCD.

Hence, a study on the dynamic response of a number of specimens tested in the HRMT36 experiment is presented, from which conclusions on the proposed material models can be achieved. The work shown in this thesis will help to achieve a better understanding of the dynamic thermomechanical behaviour of the different materials considered, thus giving valuable insights on the thermal and mechanical constraints imposed on components making use of such materials. Additionally, the research completed serves as an important steppingstone for avenues of interest in the study of strain-rate dependent failure and the mesoscale behaviour of materials subjected to dynamic impacts.

1.3 Structure of Thesis

The thesis is divided in six main chapters. Following this introductory chapter describing the project within the context of CERN's accelerator complex and the HL-LHC timeline, Chapter 2 provides an extensive literature review, presenting an overview of the fundamental concepts on which the work carried out in this project is based on. The core

concepts of dynamic phenomena, including elastic, plastic and shock waves, as well as strength and failure models used to describe and simulate such conditions, are discussed. The importance of beam intercepting devices in the LHC and future accelerators is reviewed, along with the role of the HiRadMat facility and experiments such as HRMT36. The three materials studied extensively in this thesis are presented and discussed. Additionally, the main methods adopted for the analytical and numerical modelling of the propagation of stress waves in slender rods are introduced.

Chapter 3 presents the study of two materials of interest tested in the HRMT36 experiment, namely Titanium Zirconium Molybdenum and Silicon Carbide. The models adopted for the two materials are discussed, along with the experimental scenarios considered and the numerical methodology implemented. The benchmarking of the numerical model with experimental results is presented and debated. This is followed by targeted modelling of boundary condition effects on the dynamic bending response, the modelling of internal damping effects, as well as the analysis and simulation of failure experienced by SiC and TZM specimens. Additionally, results related to the post-irradiation campaign conducted in the months following the experiment are shown and reviewed in the context of the obtained results.

Chapter 4 starts off with the thermomechanical characterisation campaign carried out on the CuCD RHP3434 grade. The results presented in this chapter include measurements of thermal and structural properties such as density, specific heat capacity, diffusivity, coefficient of thermal expansion, as well as the elastic and plastic behaviour of the material. Additional temperature sensitivity testing is also shown, and the degradational effect of temperature cycling on the thermal diffusivity of the material is discussed. This is followed by the application of the formulated elastoplastic material model in finite element thermomechanical analyses, the results of which are benchmarked with measurements from the HRMT36 experiment.

In Chapter 5, the mesoscale structure of the CuCD metal matrix is studied numerically by the modelling of the material's internal structure in mechanical and thermomechanical analyses. The performance of homogenised models is compared with one considering the mesoscale nature of the material, and the main benefits and drawbacks of the two approaches are discussed in detail. Finally, the calculation of the Mie–Grüneisen equation of state for Copper Diamond is proposed, considering the Shock-Hugoniot data for the

two constituent materials available in literature. The final chapter gives a summary of the main achievements and contributions of the study to the development of the research field, along with concluding remarks and a number of suggestions for future work.

Chapter 2:
Literature Review

2.1 Dynamic Phenomena and Wave Propagation in Solids

Dynamic processes which occur when a body is exposed to rapidly changing loads can differ significantly from the phenomena that occur under slow loads (i.e., static or quasistatic). A good example of this can be seen in the behaviour of a sandbag, which is sometimes used in military situations to protect soldiers from oncoming bullets. The soft, free-flowing sand in the bag is highly effective in stopping high velocity impacts, but can easily be penetrated by a knife. On the other hand, a solid wood door is hard to penetrate with a knife, but can easily be pierced by a bullet [11].

There are fundamental differences between static and dynamic phenomena. In static or quasistatic deformation, there is a condition of static equilibrium at any time i.e., the summation of forces acting on the body is zero or close to zero. In contrast, when deformation is imparted on a part of the body at a high enough rate, the impacted part becomes stressed while the other portion does not experience the stress imparted on the body immediately. The stress and its associated deformation (or strain) travels in the body in the form of a wave, at specified velocities that can be calculated with good approximation. Therefore, while quasistatic deformation can be considered as a series of equilibrium states which can be treated by well-known mechanics of materials equations (such as the summation of forces and moments being equal to zero, constitutive relationships, etc.), dynamic deformation involves wave propagation [11].

Applications involving high strain-rate and dynamic deformation can be divided into two categories: industrial and military. Industrial applications involve the production of something, while military applications are usually intended to destroy or protect. Some examples of the former include explosive metalworking, developed in the 1960s. For instance, shock consolidation uses the energy imparted by shock waves to bond fine metal powders. As the shock wave travels through the powder, it deposits extremely high energies in the particles, resulting in partial melting and bonding. Another application is that of explosive welding, which involves the detonation of an explosive on top of a metal plate, propelling it against a bottom plate with a high velocity. A high peak pressure is induced at the impact surface, resulting in a metallurgical bond allowing for the joining of materials having very different melting points (which therefore could not be welded conventionally). Aluminium and titanium, for example, can be welded with steel with this technology. On the other hand, military applications involving impact, dynamic deformation and explosive detonation are numerous, with one example being the destruction of structures with the

use of high-velocity projectiles. Figure 5 illustrates some of the scientific disciplines contributing to the study of dynamic processes in materials, as well as additional applications such as crashworthiness testing for accidental impacts of vehicles and damage to structures as a result of earthquakes [11].

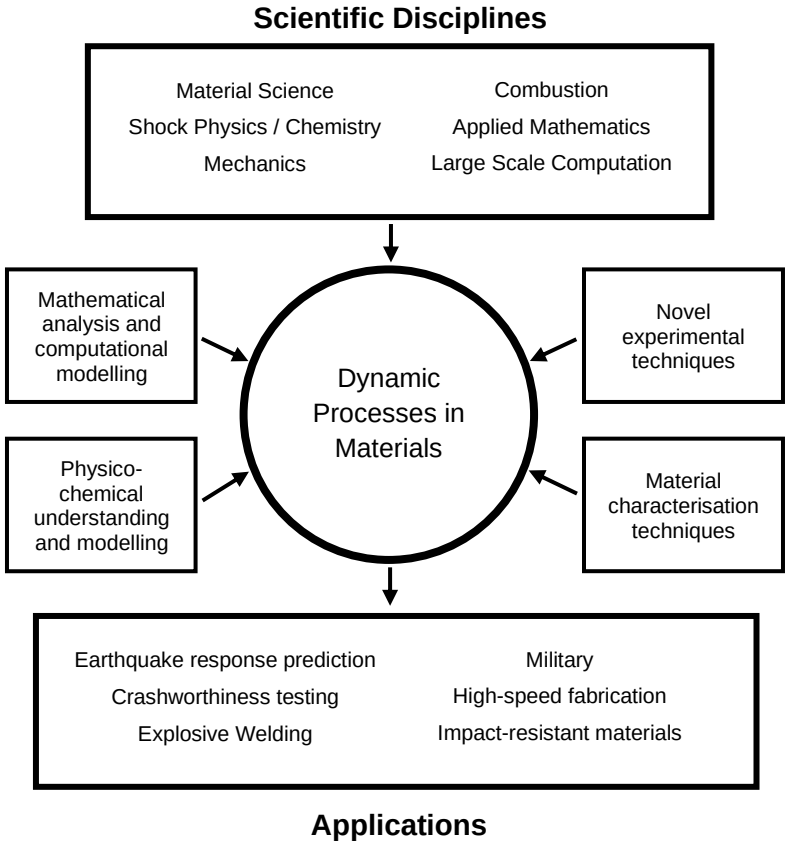

Figure 5 – Contributing disciplines and principal applications of dynamic processes [12].

2.1.1 Elastic Waves

The process of applying an external force to a body is intrinsically a dynamic process. However, when the rate of change of the applied force is low, the process can be considered as a sequence of states in static equilibrium. Nevertheless, internal stresses are not transmitted instantaneously from the point of application to different parts of the body, but rather transmitted at a specific velocity, that is, the speed of sound. Through a simple calculation considering individual atoms that make up a solid, one can estimate the speed of an elastic pulse in a solid to a good degree of accuracy. Considering a case where a force is applied from the left-hand side to a group of atoms making up a solid, the transmission has a time lag related to the average period of the natural vibration of the atoms, which is generally in the order of 10^{-13} s. The atoms in the middle will transmit the pushing force to

those on the right. To calculate the velocity of this disturbance, one needs to know the separation between neighbouring atoms. In the case of a solid metal such as iron, this distance is approximately 3×10^{-10} m. The velocity can thus be calculated by dividing this value by the time period, resulting in a velocity of 3000 m/s, which is close to the velocity of propagation of an elastic wave in iron at 3500 m/s [13].

The velocity of propagation of an elastic wave travelling in a cylindrical bar can be easily derived by considering a striker bar impacting a long cylindrical rod at a velocity *V*, as shown in Figure 6.

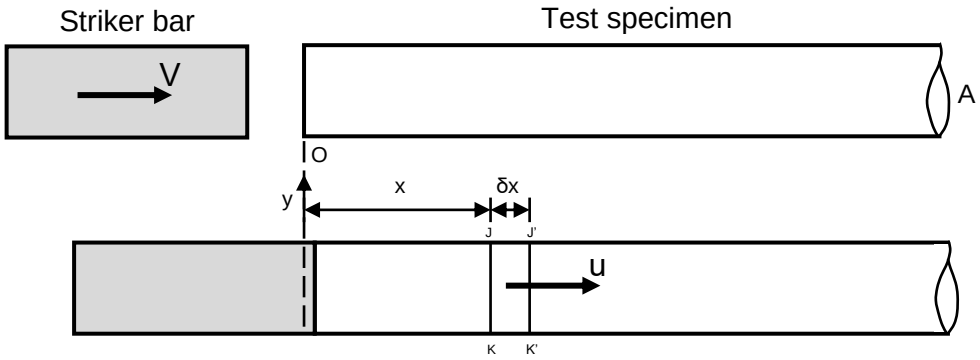

Figure 6 – Propagation of an elastic wave in a long cylindrical bar, before and after impact of a striker bar [13].

The impact results in a compressive stress wave travelling from the end of the bar, which reaches a length *x* at a time *t*. Assuming uniaxial stress along the length of the rod, we can consider the stress state between two sections of the rod JK and J'K', which are at a distance *x* and $x + \delta x$ from the impact position. Newton's second law, $F = ma$, can be applied between JK and J'K' to obtain:

$$-\left[A\sigma - A\left(\sigma + \frac{\partial \sigma}{\partial x}\delta x\right)\right] = A\rho\delta x\frac{\partial^2 u}{\partial t^2} \tag{1}$$

$$\frac{\partial \sigma}{\partial x} = \rho\frac{\partial^2 u}{\partial t^2} \tag{2}$$

Where *A* is the cross-sectional area, and σ is the stress (therefore $A\sigma$ is the force). For an elastic deformation, Hooke's law can be applied:

$$\frac{\sigma}{\varepsilon} = E \tag{3}$$

Note that the strain ε is defined as $\frac{\partial u}{\partial x}$, therefore:

$$\frac{\partial}{\partial x}\left[E\frac{\partial u}{\partial x}\right] = \rho\frac{\partial^2 u}{\partial t^2} \tag{4}$$

$$\frac{E}{\rho}\frac{\partial^2 u}{\partial x^2} = \frac{\partial^2 u}{\partial t^2} \tag{5}$$

The latter is the differential equation describing the motion of a wave, for which the velocity is given by:

$$C_0 = \sqrt{\frac{E}{\rho}} \tag{6}$$

The characteristic velocity at which disturbances travel through an elastic material can thus be seen to be a function of the material's elastic constants, i.e., its stiffness (the strain response of the material to an applied stress) and its density. For calculations related to plastic waves, work hardening needs to be additionally incorporated, while the compressibility needs to be considered in the case of shock waves.

Various kinds of elastic waves can propagate through solids, defined by the motion of particles (discrete portions of the solid) in the material in relation to the direction of propagation of the wave [12], [13]. Some common types include:

- *Longitudinal waves*, also called *dilatational* or *primary waves*. These involve particle motion in the same direction as the wave propagation. In this case only longitudinal waves are generated as no rotation is involved in the impact. An example of

longitudinal wave generation is in the case of a striker impacting a rod in a split-Hopkinson bar experiment[4];

- *Shear waves*, also called *transverse* or *secondary waves*, involve particle motion in a direction orthogonal to the direction of propagation. An example of transverse waves is in the case of a rod suddenly submitted to torsion;
- *Rayleigh waves*, also called *surface waves*, similar to gravitational waves in a liquid, are generated in the presence of a bounding surface, with a maximum amplitude at the surface which decays exponentially with depth;
- *Flexural waves*, also called bending oscillations.

When a wave travelling through a material encounters a medium with a different sonic impedance, the interaction results in effects such as reflection and refraction. The sonic impedance can be defined as the product of the material's density and its elastic wave velocity. Considering a uniaxial condition (i.e., the angle of incidence is zero and therefore the wave direction is normal to the boundary between the two materials), a longitudinal wave refracts (i.e., transmits) and reflects at a boundary. The amplitude of transmitted and reflected waves can be computed from the densities and speed of sound of the two media by considering conservation of momentum. For a wave travelling from a material A to a material B:

$$\frac{\sigma_T}{\sigma_I} = \frac{2\rho_B C_B}{\rho_B C_B + \rho_A C_A} \tag{7}$$

$$\frac{\sigma_R}{\sigma_I} = \frac{\rho_B C_B - \rho_A C_A}{\rho_B C_B + \rho_A C_A} \tag{8}$$

Where σ_I, σ_T, and σ_R are respectively the incident, transmitted and reflected stress pulses. When the impedance of material B is greater than that of A, a pulse of the same sign as the incident pulse is reflected back (i.e., for a compressive wave, another compressive wave is

[4] The Hopkinson pressure bar is used to measure stress pulse propagation in metal bars. A specimen is placed between the ends of two straight bars (the incident bar and the transmitted bar). A stress wave is created at the end of the specimen bar, which propagates through the bar towards the specimen. Upon reaching the specimen, the incident wave splits into a transmitted wave travelling through the transmitted rod, causing plastic deformation in the specimen. The reflected wave travels back down the incident bar. Strain gauges are used to measure the strains cause by the wave propagation.

reflected). When the impedance of *B* is less than that of *A*, a pulse with the opposite sign is reflected. Two limiting conditions can then be defined, the first being when a wave meets a free surface. Here the stiffness can be considered to be zero, thus $\rho_B C_B = 0$:

$$\frac{\sigma_T}{\sigma_I} = 0 \qquad \frac{\sigma_R}{\sigma_I} = -1$$

The second condition is when the wave meets a rigid boundary (infinite stiffness, thus $\rho_B C_B = \infty$):

$$\frac{\sigma_T}{\sigma_I} \approx 2 \qquad \frac{\sigma_R}{\sigma_I} \approx 1$$

This shows that when a compressive wave meets a free surface, it is reflected back as a tensile wave (i.e., stress sign is changed), while the particle velocity is preserved. Conversely, when a compressive wave meets a rigid boundary, the stress sign does not change while the particle velocity is reversed in direction [14].

With regard to elastic wave propagation in slender rods, wave dispersion must also be considered [15]. The topic of wave dispersion in cylindrical rods has been studied for a long time, with Pochhammer [16] providing the first calculations of elastic wave velocities. Similar to the work presented by Graff [17] later on, Pochhammer describes the phase velocity of a wave travelling in a longitudinal bar by the expression:

$$\bar{c} = \frac{c_p}{c_0} = 1 - \nu^2\pi^2\left(\frac{R}{\Lambda}\right)^2 \tag{9}$$

where ν is the Poisson's ratio, c_p is the phase velocity, c_0 is the ideal velocity, Λ is the wavelength, and R is the radius. Similarly, Rayleigh [18] also estimated the velocity of longitudinal waves in slender bars and described the phase velocity with a similar expression:

$$\frac{c_p}{c_0} = 1 - 3\nu^2\pi^2\left(\frac{R}{\Lambda}\right)^2 \tag{10}$$

As can be seen, wave dispersion is a function of the material's Poisson's ratio and the cylindrical dimensions of the rod in relation to the wavelength. Carra [19] discusses that

high-frequency disturbances in longitudinal waves are related two distinct phenomena. These are dispersion of the longitudinal wave due to boundary condition effects, and cylindrical waves propagating from the centre of the rod. The first phenomenon is related to longitudinal wave dispersion due to interaction with the external surface of the rod. Since the wave's velocity is frequency-dependent, higher frequencies caused by boundary effects at the free lateral surface travel slower. On the other hand, radial inertia leads to waves travelling outwards towards the external surface of the rod, at which point they are reflected back. The radial vibrations produced by such waves leads to an axial component associated with the material's Poisson's ratio. Radial displacements are small, and therefore the Poisson's ratio's effect on the propagating longitudinal wave is not substantial. The propagation of waves in a cylinder is depicted in Figure 7. Release waves generate at the free surface and trail the main wave due to their lower velocities. This variability in particle velocity can be observed in strain and stress measurements at the rod's surface [12]. Figure 8 shows the prediction of the stress pulse produced by such phenomena in an impacted cylinder, as computed by Skalak [20], showing high-frequency oscillations superimposing the rectangular pulse predicted by elementary theory.

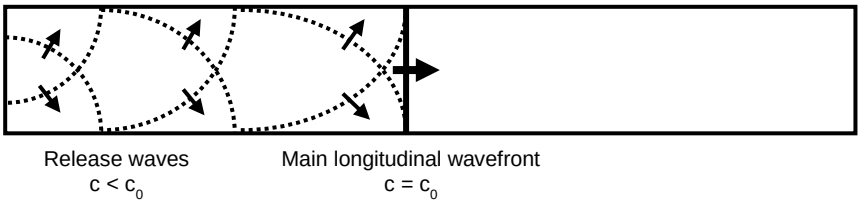

Figure 7 – Dispersive boundary effects due to longitudinal wave propagation in a cylindrical elastic bar.

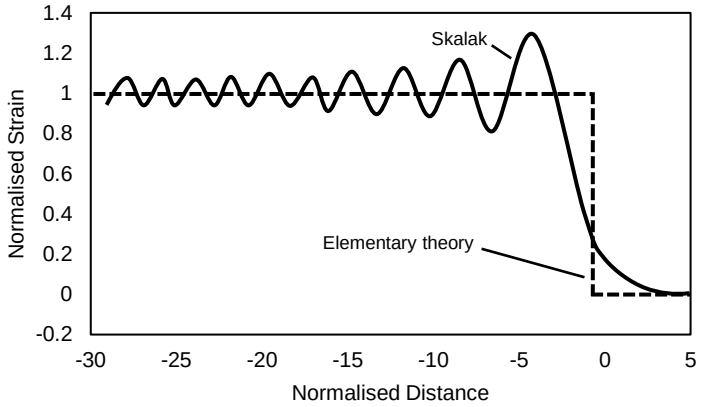

Figure 8 – Comparison of idealised (dotted) and calculated (solid) stress pulse shape [20].

2.1.2 Plastic Waves

When the transmitted pulse exceeds the elastic limit, the propagating wave is made up of elastic and plastic components. In the plastic regime, the material can experience strain and

strain-rate dependent hardening and temperature-induced softening. A bilinear stress-strain curve is the simplest representation of a strength model with plasticity, with the first slope (the Young's modulus) defining the elastic regime, and the second slope (the tangent modulus) defining the plastic regime. It is interesting to note that when plasticity is induced, the wave propagates at lower speeds due to uniaxial stress and the resultant concavity of the stress-strain function (i.e., lower stiffness when compared to a state of elasticity). This results in dispersion at the wave front, and consequently the plastic wave travels at speeds slower than the elastic component [21].

2.1.3 Shock Waves and Equations of State

At energies resulting in the stress wave amplitude far exceeding the dynamic flow strength, shock waves can develop. Uniaxial strain conditions result in a convex stress-strain function, with an increase in slope with strain. This leads to the steepening of the wave front, generating a pressure, temperature and density discontinuity, resulting in what is called a shock front. The propagating shock wave travels at a higher velocity than the elastic wave. This case occurs when there is a build-up of hydrostatic stress of much higher amplitude than the material strength, resulting in the material behaving as a fluid (i.e., with a negligible shear modulus) [22].

Material behaviour can be described as a stress tensor made up of two components: the hydrostatic (or dilatational) stress, that acts to change the material volume only, and the deviatoric stress, that acts only to change the shape. In crystalline metals, the process leading to plastic deformation is slip, where the shape of the material changes through the action of shear stresses. With this in mind, the yield of such materials is independent of the hydrostatic stress component. This differs from the behaviour of amorphous metals, where the yield stress has been experimentally found to have a slight dependence on the hydrostatic component of the stress tensor [23].

The hydrostatic response in a hydrocode is governed by equations of state (EOS) which express the relation between thermodynamic variables, namely pressure P, internal energy E, entropy S, density ϱ and temperature T. Equations of state give the constitutive relationship between these variables, thus describing the state of matter. When implemented in numerical hydrocodes, these EOS can be analytical (i.e., governed by an equation) or tabular (i.e., a list of values). The ideal gas law is an example of a linear analytical EOS, while an example of a polynomial EOS is the Mie-Grüneisen EOS [24]. Tabular EOS,

such as those provided by the SESAME database [25], can be utilised to evaluate material behaviour over different phases.

2.1.4 Strength models and plastic deformation at high strain rates

The variables dictating the material behaviour in the elastic and plastic regimes are expressed by a strength model, which gives the deviatoric behaviour of the material. The simplest of models express the stress-strain behaviour of the material. An example of this is Hooke's law, which is the linear stress-strain relationship of a material in elastic conditions. More complex models can include the plastic and viscoplastic behaviour of materials, and additional variables such as strain rate and temperature. Strength models are divided in three classifications. Empirical models are obtained via interpolation of experimental data with no physical basis, an example being the Johnson-Cook strength model [26]. Additionally, models can be semi-empirical, such as the Zerilli-Armstrong strength model [27], and physical-based, such as the Mechanical Threshold Stress model [28]. These material models can usually be implemented in standard finite element analysis (FEA) codes.

The Johnson-Cook strength model is one of the most adopted when strain-rate is an important component in the analysis, and is particularly suitable for metals and other ductile materials. For this model, the flow stress is described by:

$$\sigma_y = \left(A + B{\varepsilon_{pl}}^n\right)\left(1 + C\ln\frac{\dot{\varepsilon}_{pl}}{\dot{\varepsilon}_0}\right)\left[1 - \left(\frac{T - T_r}{T_m - T_r}\right)^m\right] \tag{11}$$

Where A is the quasistatic elastic limit, B and n are work hardening parameters (namely the influence slope and shape of flow stress in the plastic domain. n is in the range between 0, for a perfectly plastic model, and 1, for a piecewise linear model), ε_{pl} is the equivalent plastic strain, C is the sensitivity to strain rate, $\dot{\varepsilon}_{pl}$ is the plastic strain rate, and $\dot{\varepsilon}_0$ is the effective plastic strain rate of a quasistatic test used to determine yield and hardening parameters (A, B, and n) originally set to 1. T is the actual temperature, T_m is the melting temperature (at which the material loses its shear strength), T_r is the reference temperature (used when determining parameters A, B, and n), and m is a thermal softening coefficient which determines the concavity of the temperature function (when $m < 1$ the function is convex, when $m > 1$ the function is concave, when $m = 1$ the temperature influence is linear) [26]. The parameters are generally obtained through a combination of tests such as

the Split-Hopkinson bar experiment, Taylor tests, and tensile or compressive quasistatic tests.

The Zerilli-Armstrong strength model is suitable for materials with a body centred cubic crystalline structure, and takes into account the coupling between temperature and strain-rate by expressing the flow stress as a function of plastic strain, strain-rate, and absolute temperature:

$$\sigma_y = C_1 + C_2 e^{(-C_3 + C_4 \ln \dot{\varepsilon})T} + C_5 \varepsilon^n \tag{12}$$

Where C_1, C_2, C_3, C_4, and C_5 are material parameters obtained experimentally [27].

2.1.5 Failure models

Strength models express the material behaviour without any stress or strain limits. This is instead addressed by a failure model, which has the role of describing the fracture phenomena resulting in the material's failure. Once a maximum level of stress or strain is reached, the material breaks and the flow stress goes to zero (i.e., the material is no longer able to bear shear loads). This is similar to how a change in phase (such as melting) is handled by numerical codes, with the difference being that failure is irreversible.

Factors that typically influence dynamic failure include the material's thermomechanical properties and microstructure, the applied loads and the conditions they induce in the material (such as stress, strain-rate and temperature increase), as well as the ambient conditions. Depending on the failure model, materials can be classified as brittle or ductile. The former is exemplified by ceramics, characterised by limited plastic deformation before failure and single crack propagation leading to fracture. Most metals are ductile and thus exhibit large plastic deformations. Nucleation and growth of voids within such materials typically leads to necking, resulting in a cup-and-cone failure surface.

There are two main failure model categories generally used in numerical codes. The first type expresses failure as a result of cumulative damage, with one such example being the Johnson-Cook failure model [29], [30]. In this case, the damage function sums the cumulative plastic strain at every time step of the analysis, and failure occurs once the specified threshold is reached. The second type is a spallation failure model, which assumes

that fragmentation occurs once the spall strength[5] is reached. An example of this is the Grady spall failure model [31], [32].

2.2 Beam-Induced Damage Mechanisms

When subatomic particles interact with matter, they transfer some of the energy to the material in the form of heat. This leads to an increase in temperature of the impacted material. Such interactions may result in varying effects, depending on the deposited power density. This is a function of the timescale, amount, and distribution of energy. Various regimes are defined, as shown in Figure 9, indicating the typical response induced in a structure for a given intensity and pulse duration. Regardless of the actual material impacted and boundary conditions, the response of a structure can be approximated by considering the specific deposited energy. Three main regimes are defined: the elastic dynamic regime, plastic dynamic regime, and shock wave regime, corresponding to different levels of energy densities deposited in the material. As the names imply, dynamic responses in the elastic regime are composed of vibrations and stresses not exceeding the elastic limit of the material, whilst in the plastic regime the dynamic response induces permanent plastic deformation. In the shock wave regime, the material experiences localised changes in density, which may result in permanent damage or even fragmentation of the material. At the extreme end of the shock wave regime, hydrodynamic tunnelling may arise. In this case, the material experiences a reduction in density, resulting in the beam penetrating deeper into the material over the duration of impact [33].

[5] The spall strength is the critical tensile threshold corresponding to the ultimate strength of the material.

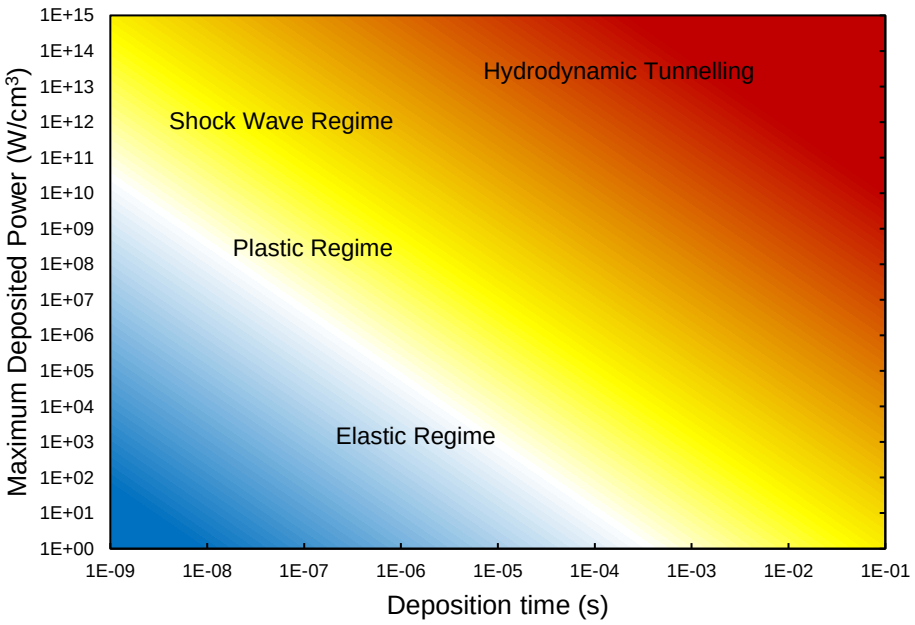

Figure 9 – Maximum deposited power in W/cm³ against pulse duration, exhibiting different dynamic response regimes induced in matter when interacting with particle beams [33].

Thermomechanical problems can be grouped into three scenarios, depending on the application rate of the thermal load. In quasistatic heating, the change in temperature with time is negligible, and the steady-state thermal and structural problems can be solved sequentially. In this case, the stress and strain fields depend on the temperature gradient. In slow-transient heating, the change in temperature with time is no longer trivial, however the rate is not high enough to warrant the consideration of dynamic effects due to mass inertia of the structure, and typically the problem can still be adequately solved sequentially. Quasi-instantaneous heating refers to heating which occurs in a very short period of time, where the material expansion is prevented by its mass inertia. In such instances, the dynamic aspect of the problem must be considered, and pressure waves, generated as a result of the rapid heating, superimpose the quasistatic stresses. Analytical solutions exist for all scenarios considered, however these can get extremely complex in dynamic scenarios with intricate geometries, especially when plasticity is involved. In this case, the problems are typically solved numerically with finite element codes. These generally include stress-strain relationships, expressed in strength models, which can also take into account strain and strain-rate dependent hardening and temperature-dependent effects.

Similar to a typical impact scenario, the rapid heating of a component can result in the generation of waves travelling from the heated volume towards the body's boundaries. As detailed, such circumstances usually involve isochoric heating, with the body's deformation being prevented by its own mass inertia. Several types of waves can originate and propagate

through the body, depending on the energy, impact duration, geometry, and boundary conditions.

2.3 Materials in Beam Intercepting Devices

2.3.1 Beam Intercepting Devices

In an ideal particle accelerator, particles are stable in their orbits and losses would not take place, however in real machines there are various mechanisms which can lead to emittance. This leads to particles drifting away from the beam core, forming what is called the primary beam halo. The beam core can be approximated by a Gaussian function, with the beam halo defined as particles at more than 3 standard deviations from the beam's central trajectory. The collimation system has to keep continuous beam losses from these particles below a defined limit [34]. The fraction of particles which escape from the collimators, the local cleaning inefficiency, is a measure of the performance of collimators in limiting these continuous losses [35].

The continuous rate of particle loss is modelled by assuming a beam lifetime (BLT)[6], with the intensity of the beam at a given time calculated by:

$$I(t) = I_0 e^{-\frac{t}{\tau}} \tag{13}$$

where I_0 is the injected intensity and τ is the defined BLT. A minimum BLT needs to be defined for the machine. This minimum, along with the quench limit of the superconducting magnets, allows for the calculation of the maximum allowable circulating intensity. If the maximum intensity is known, the maximum cleaning inefficiency can similarly be found. Relevant parameters for the LHC run 1 and 2, as well as those proposed for the HL-LHC, are given Table 1.

[6] The beam lifetime is the time interval after which the intensity of the beam reaches $1/e$ of its initial value. The beam intensity can be reduced by factors such as proton collisions at the interaction points, inelastic scattering produced by proton-gas collisions due to impurities in the ultra-high vacuum, and other machine inefficiencies.

Table 1 – Key machine parameters for LHC run I, LHC run I, and HL-LHC design [36].

Parameter	Units	LHC run I	LHC run II	HL-LHC design
Energy	*TeV*	3.5	6.5	7
Bunch spacing	*ns*	50	25	25
Bunch intensity	*p*	1.7×10^{11}	1.15×10^{11}	2.3×10^{11}
Number of bunches	*b*	1380	2808	2748
Total intensity	*p*	2.3×10^{14}	3.2×10^{14}	6.0×10^{14}
Stored energy	*MJ*	150	360	670

Various processes can cause beam losses during normal and abnormal operation of the LHC and other particle accelerators. Due to the high stored energy in the beams, these can be highly destructive; a small fraction of the full beam can in fact cause a superconducting magnet quench[7]. For this reason, a multi-stage collimation system is installed in the machine to safely dispose of beam losses. Whilst in other colliders the collimation system serves mainly to minimise experimental background, in the LHC and HL-LHC this system is required in all stages of operation, and has various roles, most importantly:

- Minimising the risk of magnet quenches by safely disposing of particle losses;
- Passive protection of the whole machine;
- Cleaning of beam collision debris at the interaction points;
- Concentration of radiation in specific areas of the machine in order to facilitate maintenance.

The collimation system is composed of a series of precisely placed blocks of material near the circulating beams. Most collimators come in pairs of movable jaws placed symmetrically around the two beams, as shown in Figure 10 [37]. The major LHC collimators are:

- *Primary collimators* (TCP), which are closest to the beam. The jaws are made from robust carbon fibre composite (CFC) and act as a scattering target for the primary

[7] A magnet quench is an abnormal termination due to the superconducting magnetic coil entering a normal resistive state (i.e., losing its superconducting state).

beam halo. Consequently, the beam halo is dispersed to then be absorbed by downstream collimators [34], [38], [39];

- *Secondary collimators* (TCSG) are also made from robust CFC, and serve the role of intercepting the secondary beam halo [34], [38], [39];
- *Shower Absorbers* are made from tungsten (which, due to its high density is ideal for absorbing scattered particles) and are divided in two categories. Long absorbers (TCLA) are placed at the end of the cleaning insertions with the aim of protecting the superconducting arcs, while tertiary collimators (TCT) are placed near the experimental insertions [34], [38], [39].

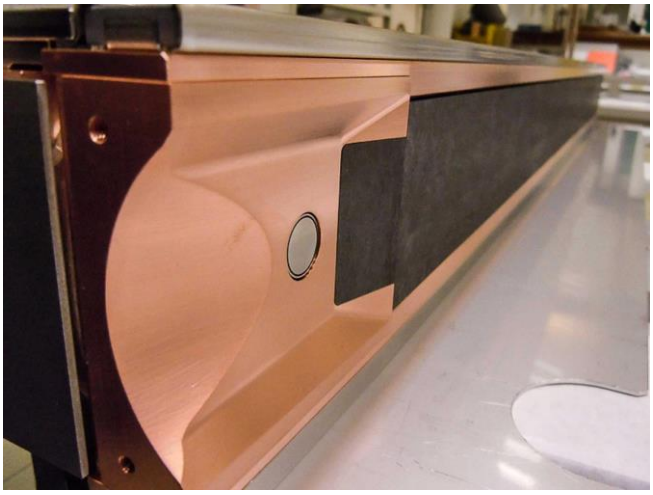

Figure 10 – Disassembled LHC collimator jaw [37].

A particle storage ring such as the LHC would ideally never lose particles, leading to a theoretically infinite beam lifetime. In practice, however, there are a number of factors which lead to beam losses, which tend to increase with an increase in beam current and luminosity. These factors include processes which manipulate the beam in preparation for collision such as injection, energy ramping and squeeze. The current collimation system deployed in the LHC has a cleaning efficiency above 99.99%, ensuring that less than 10^{-4} of beam losses (i.e., below 0.01% of the beam energy) are lost in the superconducting magnets. The LHC system was designed to withstand damage of up to 0.2 hr beam lifetime (BLT) over 10 seconds, corresponding to peak losses of 500 kW [39]. The system is designed to endure up to 7 kW in evacuated heat loads in a steady state, with a BLT of 1 hour, and up to 30 kW in transient conditions.

The full layout for the system in the LHC is shown in Figure 11, with fifty-four collimators per beam, fifty of which are movable. Two LHC insertion points are dedicated to

collimation, mainly IR3 for momentum cleaning, i.e., the removal of particles with a large energy offset, and IR7 for betatron cleaning, i.e., the continuous controlled absorption of halo particles. The losses are distributed among the collimators, ensuring no collimator is subject to single overloads [36].

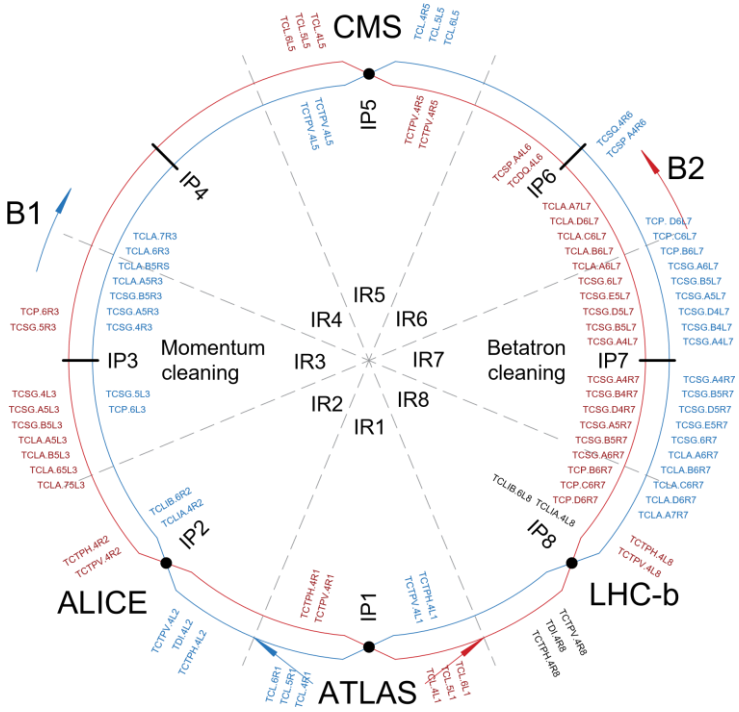

Figure 11 – The collimation system layout in the LHC (for beams 1 and 2) [36].

Being so close to the circulating beams, the collimation system additionally has an important role in the passive machine protection, in case of beam failures. Primary and secondary collimators in IR7 are designed to withstand the worst failure scenarios up to 1.15×10^{11} protons at 7 TeV [40]. The collimators' strategic positioning, coupled with the low electrical conductivity of CFC used in primary and secondry collimators, also means that the system contributes significantly to the LHC machine impedance, in turn limiting the achievable top energy [41].

2.3.2 The HL-LHC

As mentioned, the LHC is to be upgraded significantly in the 2020s in order to increase its luminosity by a factor of five, and its integrated luminosity by a factor of 10. This upgraded machine configuration will be called the High Luminosity LHC and requires various upgrades in a number of key areas, including the superconducting magnets, the superconducting RF cavities, and the beam collimation system.

The LHC margins allow for about two times the nominal design performance with regard to peak luminosity. This factor limits the statistical gain that can be achieved without major upgrades. For this reason, the upgrade in question is required to significantly increase the machine's luminosity and exploit the full potential of the existing collider. The project was initiated at the end of 2010 and a design was approved by 2013. The main objective of the HL-LHC is to identify a hardware configuration and beam parameters allowing the machine to reach a peak luminosity of 5×10^{34} $cm^{-2}s^{-1}$ and an integrated luminosity of 250 fb^{-1} per year, with the goal of a total of 3000 fb^{-1} in the twelve years following the upgrade. This target is approximately ten times the expected luminosity in the LHC lifetime. All equipment is being designed with a 50% margin, meaning that the machine can be pushed to a levelled peak luminosity of 7.5×10^{34} $cm^{-2}s^{-1}$. All hadron colliders before the LHC produced a combined integrated luminosity of around 10 fb^{-1}, while the LHC is expected to reach 300 fb^{-1} in its first 15 years of operation.

There are various systems which need to be improved, or changed, as they could become susceptible to breakdown or otherwise create a bottleneck for HL-LHC operation. These include the inner triple magnets, the cryogenic system, and the collimation system. The latter had been designed for the initial stage of LHC operation and is optimised for robustness, thus upgrades are required to take into consideration the need for lower impedance at higher beam intensities.

Particles interacting with collimators in IR7 emerge with a modified magnetic rigidity, resulting in a source of local heat deposition in the dispersion suppressor (DS) magnets downstream – these are the highest cold losses in the ring. With the increased intensities in the HL-LHC, this could result in a magnet quench. The baseline upgrade to solve this problem is the addition of collimators in the dispersion suppressors. Target Collimator Long Dispersion suppressors (TCLDs), two per side of IR7, would be required to protect the DS magnets. This necessitates the replacement of a main dipole by two shorter dipoles, with the TCLD placed between the new magnets [42].

The LHC collimators take up most of the impedance budget, and for this reason the current system has been designed in a way that facilitates upgrades in this regard. All secondary collimators in IR3 and IR7 feature an extra slot to allow for installation of new collimators with lower impedance. By the HL-LHC implementation, these slots are expected to be equipped with low-impedance collimators using novel materials and coatings.

New materials and designs for collimators are thus required to be robust against beam failure, have low impedance to reduce beam instabilities, clean the beam efficiently, and also have a high geometrical stability despite temperature changes. Among the various materials currently being studied and tested, Molybdenum Graphite (MoGr) composites are the present baseline materials for the secondary collimator upgrades [43]–[45]. Coatings with pure Mo are predicted to help in reducing the impedance to 10% that of the current CFC jaws. The validation of new materials and designs requires extensive prototyping and testing in the HiRadMat facility as well as in the LHC [41].

More advanced collimation concepts, not included in the baseline upgrade, are also being researched, mainly hollow e-lens collimation and crystal collimation [36], [46], [47]. Concepts such as halo control mechanisms, which have been used in machines such as the Tevatron, could likewise be applied in the LHC. A hollow electron beam would wrap the LHC beam, producing an electromagnetic field which only affects the halo particles above a specified amplitude. This field would control the transverse speed of halo particles, and allow for the control of loss rates, depletion of beam tails in a controlled manner, and tuning of impact parameters[8] on primary collimators. This system works in conjunction with the collimation setup in order to dispose of the particles, i.e., it is an improvement on the current system rather than a replacement [48]. On the other hand, in crystal collimation a pure bent crystal is used to steer high-energy halo particles, which get trapped between the crystal's lattice planes. This would allow the particles to be steered to a well-defined point, implying that, in theory, one single absorber per collimation plane would be sufficient. This would significantly reduce dispersive beam losses, and is also promising with regard to machine impedance, as only a small number of absorbers would be required. Additionally, the absorbers could be spaced further apart due to the relatively large bending angle of the crystal (50 μrad compared to few μrad from multiple-coulomb scattering in primary collimators). The absorber design for such a system is of paramount importance as it must resist loss rates of up to 1 MW sustained over 10 seconds, whilst in the present systems these losses are distributed among numerous collimators. A preliminary conceptual design for such an absorber indicated that a length ranging between 5 and 10 metres would be

[8] The impact parameter is the distance between the collimator edge and the particle beam impact position.

required. The design proposed consists of a combination of low and high density graphite, with a cooling system composed of CuNi pipes enclosed in a CuCrZr casing via hot isostatic pressing (HIP) [10]. The system would also be required to have mechanical stability in the sub-μrad, as misalignments could result in channelling high amounts of energy erroneously [47].

2.3.3 HiRadMat facility

The energy stored in the LHC beams will increase from 360 to 680 MJ in the upcoming HL-LHC upgrade [46]. For the Future Circular Collider [49], the beam energy is expected to be up to 8500 MJ. This beam energy increase leads to the need for high-performance components, particularly those in risk of accidental impacts, such as beam intercepting devices [44]. In the HL-LHC, asynchronous beam dumps or injection errors may result in accidental impacts leading to thermal loads surpassing energy densities of 10 kJ/cm^3 on collimator jaws [33]. Such energies may result in intense pressure waves transmitting through the impacted medium, leading to plastic deformation, fracture, and even spallation. Additionally, melting and vaporization may occur in the impacted region [50].

A number of characteristics have been identified to characterise the performance of beam intercepting devices. Along with general engineering requirements such as availability, cost, weight, and manufacturing feasibility, in the case of beam intercepting devices (BIDs) other factors need to be considered such as resistance to high temperatures, mechanical robustness, resistance to radiation, (low) contribution to RF impedance, and geometrical stability. A number of figures of merit, ranking the material performance for a specific requirement, were formulated. These are namely the thermomechanical robustness index (TRI), measuring the material's ability to withstand rapid impact from a particle beam, the thermal stability index (TSI), measuring the material's ability to maintain geometric stability in steady-state conditions, and the RF impedance index (RFI), which is proportional to the material's electrical conductivity. With regard to impedance, BIDs such as collimators are generally the components located closest to the circulating beam, and therefore have a significant contribution to the accelerator's global RF impedance. Specifically, the wall impedance is of particular interest, being impedance related to the resistive losses in materials surrounding the beam, directly correlated with the material's electrical resistivity.

A number of key properties therefore need to be optimised for BIDs to meet the requirements in high-energy particle accelerators, including:

- *Electrical conductivity* needs to be maximised so to limit the resistive wall impedance;
- *Thermal conductivity* needs to be maximised for the BID to maintain geometrical stability under steady-state losses;
- *Coefficient of thermal expansion* needs to be minimised to increase resistance to thermal shock induced by accidental beam impacts;
- *Melting/Degradation temperature* needs to be maximised so that the material can withstand high temperatures reached in the case of accidents;
- *Specific heat capacity* needs to be maximised to lower the internal temperature increase, and thus improve thermal shock resistance;
- *Ultimate strength* needs to be maximised to improve thermal shock resistance;
- *Density* needs to be balanced to limit the peak energy deposition while still maintaining an adequate cleaning efficiency;
- *Radiation-induced degradation* needs to be minimised to improve the component's lifetime under long-term particle irradiation; and
- *Outgassing rate* needs to be minimised to ensure compatibility with an ultra-high vacuum environment.

Consequently, materials developed for and subject to these intense environments necessitate extensive experimental testing, allowing the derivation of constitutive models which can be used to replicate high-energy particle beam impacts in numerical simulations. CERN's HiRadMat (High-Radiation to Materials) facility [51] was specifically designed with these kind of experiments in mind. Accelerator components and specimens can be tested in the HiRadMat facility, which delivers high-intensity beams to an irradiation area. The HiRadMat facility's location in the CERN accelerator setup is shown in Figure 12. The 440 GeV beam used is injected from the CERN SPS, has a pulse length of 7.2 μs and a maximum pulse energy of 3.4 MJ. These parameters can be adjusted to fit the beam requirements of particular experiments [52], [53].

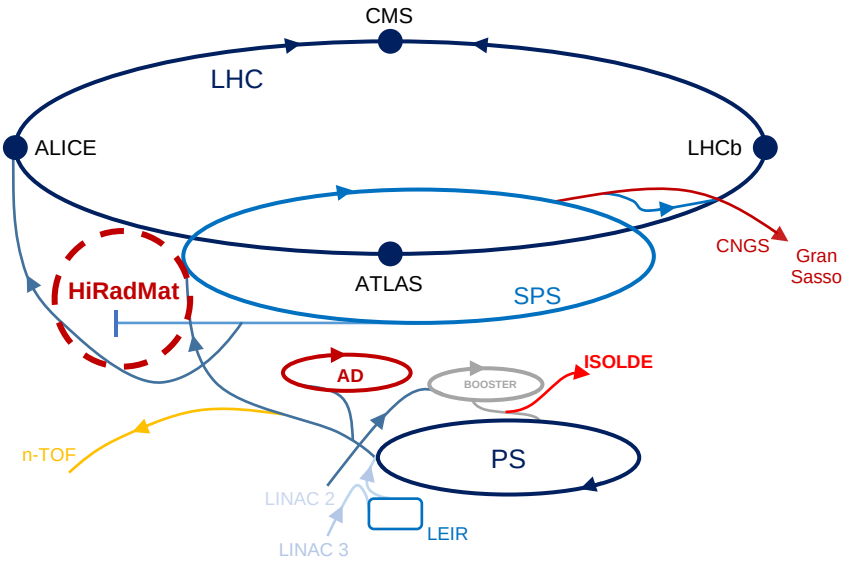

Figure 12 – HiRadMat facility location in relation to CERN accelerator setup [51].

Full-scale collimator jaws have been tested in the facility in experiments such as HRMT9, where the aim was to test three different impact scenarios on an LHC collimation jaw [44], [54], [55]. The jaw was subject to an intensity of one LHC bunch[9] at 7 TeV, after which further impacts followed in order to determine the onset of plastic damage. The final test aimed at determining the point at which the jaw, its housing, and the cooling pipes are all damaged extensively. In the HRMT14 experiment, performed in 2012 [56], specimens with uncomplicated geometries were tested to benchmark FEA results obtained from analyses conducted with numerical codes including ANSYS [57] and Autodyn [58].

The HRMT36 "MultiMat" experiment [59], [60] was conducted in October 2017 at the HiRadMat facility. Building on the experience gathered in previous experiments [56], [61], the experiment was intended to offer a reusable testbench to test novel high-performance materials for use in BIDs [62], [63].

2.3.4 HRMT36 – MultiMat

The HRMT36 experiment was named MultiMat as its main aim was to assess and validate various materials to be used for the HL-LHC upgrade. The experiment aimed to offer a

[9] The LHC beam is not a continuous string of particles, it is divided in what are called bunches, which are groups of particles a few centimetres long. Each LHC beam is made of 2808 bunches with a bunch spacing of 25 ns.

single, flexible platform which allows for the testing of specimens of a large variety of materials to be used in collimators and other BIDs exposed to high-intensity beams. The experimental testbench has dedicated target stations allowing for the assessment of the material's thermodynamic response, which can be used to derive or extend constitutive models, and applied in the simulation of full-scale setups of beam intercepting devices [59].

As can be seen in Figure 13 and Figure 14, the experimental setup consisted of 18 target stations, each having a total length of 1 m. The stations were mounted on a rotatable barrel, with each one holding material samples set up in series. The specimens were in the form of slender bars with lengths varying between 120 and 247 mm, and cross-sections between 8×8 and 12×11.5 mm^2. The decision to opt for a rectangular profile, rather than cylindrical, was driven by the testing of orthotropic graphite-based materials. The chosen geometry ensured that the graphitic plane could be easily identified, avoiding the risk of misorientation of samples in the sample holder. Additionally, the chosen geometry simplified the manufacturing process in some cases.

Some of the material specimens tested in the experiment are shown in Figure 15. The experimental vessel was cooled by forced *Ar* inert gas, which allowed for rapid cooling following each pulse, for faster pulse repetition. An actuation system allowing horizontal and vertical adjustment of samples via stepper motors was utilised. A Maltese Cross (or Geneva) mechanism allowed each target station to be rotated into the required position.

18 materials were tested for a total of 79 specimens. These were equipped with a comprehensive acquisition system based on strain gauges and thermal probes. Remote instruments included a radiation-hard high-definition camera and a Laser Doppler Vibrometer (LDV) [59]. A 3D model of the experimental setup is shown in Figure 16 and a section view with exposed specimens equipped in series can be seen in Figure 17.

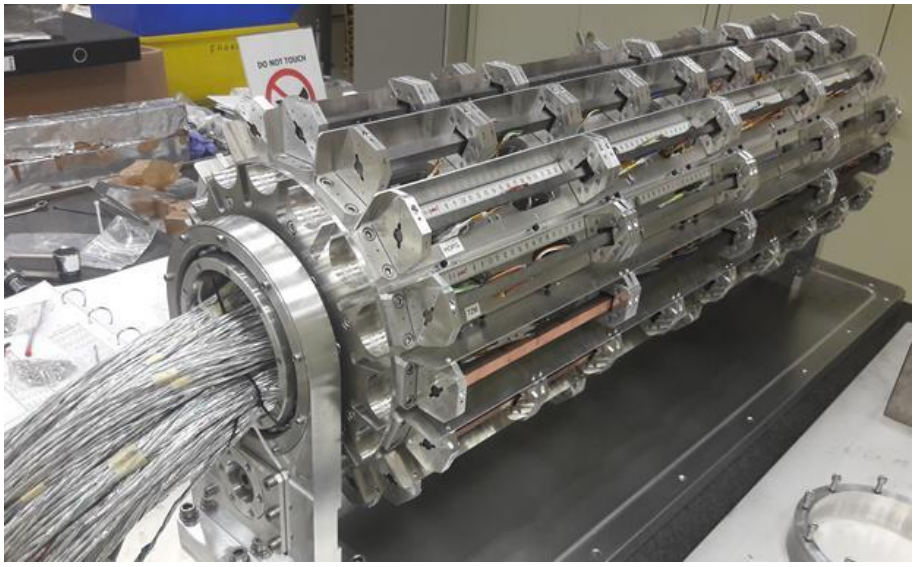

Figure 13 – Target stations mounted on the rotatable barrel with Geneva mechanism in the HRMT36 experiment test bench.

Figure 14 – Close up of material specimens set up in a MultiMat station, prior to assembly.

Figure 15 – SiC and TZM specimens tested in the HRMT36 experiment.

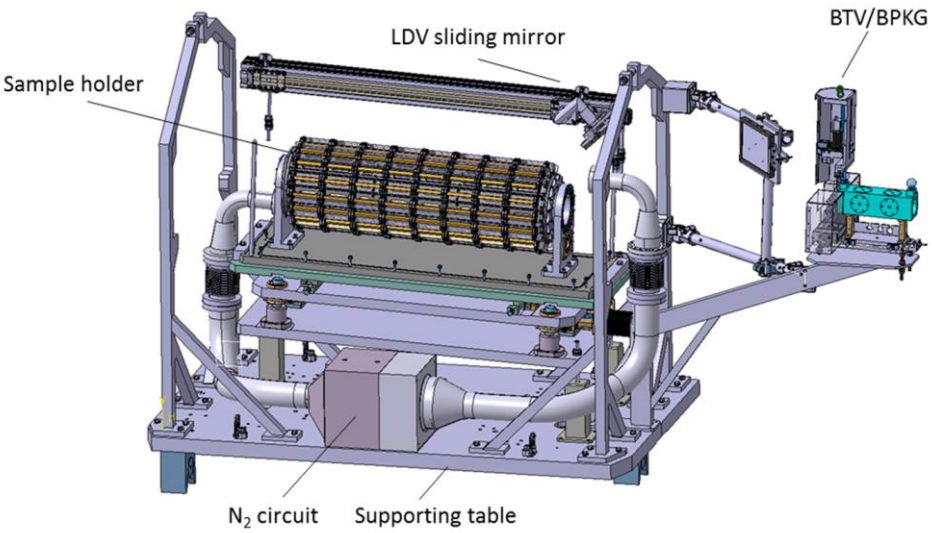

Figure 16 – 3D model of MultiMat testbench showing LDV and other monitoring equipment.

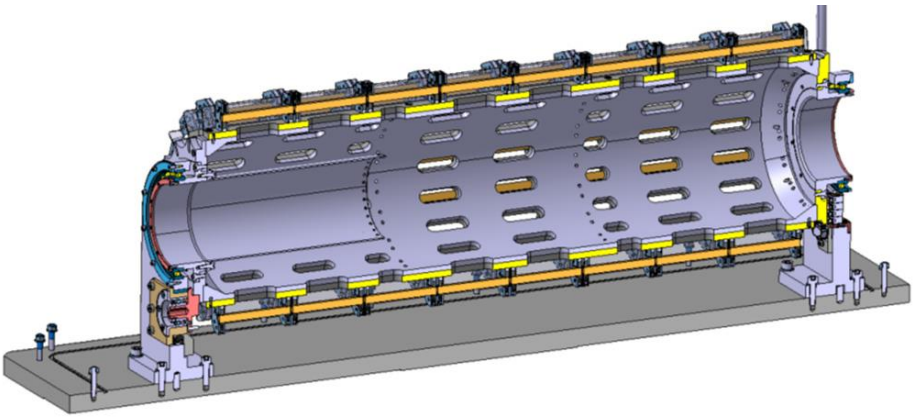

Figure 17 – Section view of sample holder showing material specimens equipped in series.

In the setup, the specimens were positioned on graphitic elastic supports, and kept in contact with an upper boundary at the two ends via a preloaded spring (in compression). The steel spring, with an original length of 14 mm, was preloaded to a length of 9 mm, compressed with a preload force of 13.57 N for a spring stiffness of 2.71 N/mm. The experimental setup at the specimen extremities can be seen in Figure 18. Modal analyses performed prior to the experiment indicated that the configuration corresponds to a simply supported system [59] and, with this in mind, initial structural analyses performed in this study consider this scenario. This is modelled by restricting movement in the vertical direction for the bottom edges of the two extremities of the sample. As will be discussed in the following chapter, experimental results showed that, in certain scenarios, the beam impact caused the specimens to lose contact with the upper support, leading to the boundary conditions differing from those initially assumed.

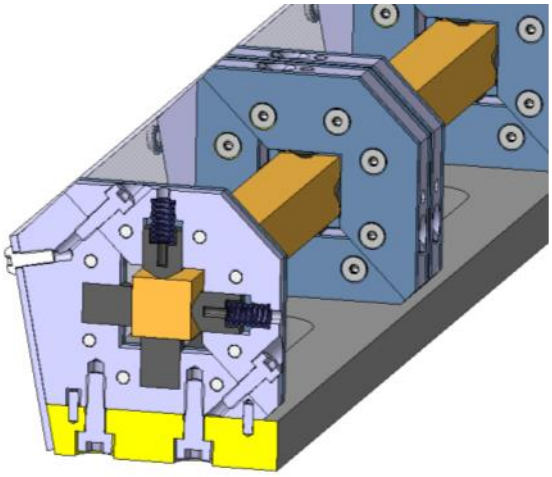

Figure 18 – Specimen setup with graphitic elastic supports supporting the extremities of each specimen with a preloaded spring.

Longitudinal strain gauges were positioned on the bottom face of specimens, with up to 5 gauges on specimens of interest. Figure 19 shows the general position of thermal probes, as well as transverse and longitudinal strain gauges. Additionally, the surface denomination and the implemented coordinate system are shown.

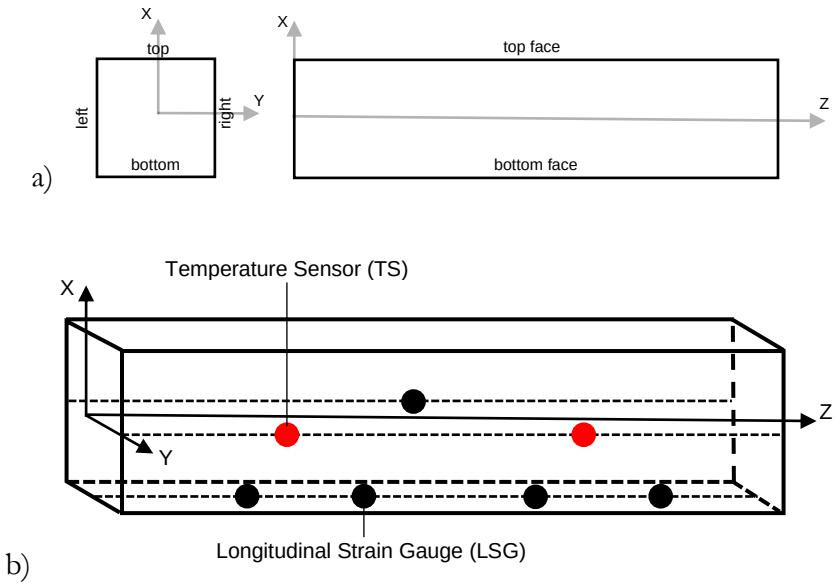

Figure 19 – Front and side view of specimens with face designation (a) and typical position of longitudinal strain gauges (black) and temperature sensors (red) on the specimens (b).

A broad range of beam scenarios were examined in the experiment, with the intensity extending up to 288 bunches, a typical bunch intensity of 1.3×10^{11} protons, and nominal beam root mean square sizes of 0.25×0.25 mm^2, 0.5×0.5 mm^2 and 2×2 mm^2. Three distinct impact types were considered, namely grazing impacts, where a coating was present, offset

impacts, and axially centred impacts. The experiment ran from the 3rd to the 17th of October of 2017, and in total 478 pulses were conducted.

This study focuses on axially centred and offset impacts. Centred impacts result in a longitudinal response, while offset impacts provoke a flexural response. These impact scenarios lead to the generation of a variety of signals, each having distinctive timescales which can be used to decouple the waveforms. The main time frames of interest include the rise time, associated with the duration of impact, which is generally in the order of 10 μs. This is followed with the generation of longitudinal waves with a trapezoidal shape, with a time period in the order of 100 μs. For impacts with transverse offsets, bending oscillations are additionally excited. These have a typical period around 1 ms [33]. Typical time periods, sampling frequencies and sensors used to detect various physical phenomena of interest are summarised in Table 2 [60].

As previously detailed, 18 different materials were tested in the MultiMat experiment, having a wide array of properties and use-cases. The materials were grouped in six main categories: pure carbon materials, metal carbide–graphite composites [63], [64], silicon carbide, titanium alloys, metal-matrix composites [65], and heavy alloys. Some specimens for carbon-based materials were additionally coated with TiN, molybdenum or copper thin films. A summary of the materials tested, their respective densities, and material coatings is shown in Table 3. The three materials studied extensively in this thesis are silicon carbide (a ceramic), titanium zirconium molybdenum (a molybdenum-based alloy), and copper diamond (a metal-matrix composite).

Table 2 – Summary of typical time period, sampling frequencies, and sensors used to detect different physical effects in the MultiMat experiment .

Physical effect	**Time Period**	**Sampling frequency**	**Sensor**
Longitudinal waves	100 μs	1 MHz	Electrical strain gauge
Bending waves	1 ms	1 MHz	Electrical strain gauge
Radial oscillations	10 μs	1 MHz	Laser Doppler Vibrometer
Temperature	/	100 Hz	PT100 Temperature Probe
Surface damage	/	/	Rad-hard camera / 4K video camera

Table 3 – Summary of materials tested in the HRMT36 MultiMat experiment.

Material	**Description** *(wt. %)*	**Density** g/cm^3	**Coating Material**	**Classification**
IT180	Inermet Tungsten Heavy Alloy	18.0	/	High Density
Ta10W	Tantalum alloy (10% Tungsten)	16.9	/	High Density
Ta2.5W	Tantalum alloy (2.5% Tungsten)	16.7	/	High Density
TZM	Titanium Zirconium Molybdenum alloy	10.0	/	High Density
CuCD IFAM	Copper Diamond	5.40	/	Medium Density
CuCD RHP	Copper Diamond	5.40	/	Medium Density
SiC	Silicon Carbide	3.21	/	Medium Density
MG-6403Fc	Molybdenum graphite (4.5% Mo, 94.95% Graphite)	2.54	5 μm TiN	Low Density
ND-7401-Sr	Molybdenum graphite	2.52	/	Low Density
MG-6530Aa	Molybdenum graphite grade (4.5% Mo, 90.5% Graphite)	2.50	2 μm Cu	Low Density
MG-6541Fc	Molybdenum graphite (4.4% Mo, 90.1% Graphite)	2.49	8 μm Mo	Low Density
HOPG	Highly ordered pyrolytic graphite	2.26	/	Low Density
TG-1100	Titanium Graphite	2.19	/	Low Density
R4550	Graphite	1.90	2 μm Cu	Low Density
CFC AC150K	Carbon Fibre Reinforced Carbon composite	1.88	8 μm Mo	Low Density
Ti6Al4V	Additively manufactured Titanium	1.62	/	Low Density
CFOAM	Carbon foam	0.40	/	Low Density
Al 6082-T651	Aluminium alloy	2.70	/	Dedicated setup

2.3.4.1 Silicon Carbide

Silicon Carbide (SiC) is a ceramic material which occurs naturally in extremely rare conditions as the mineral moissanite. It is the third hardest material on earth following diamond and boron carbide. Henri Moissan discovered silicon carbide in its natural form in meteorite fragments, and synthesised it by reducing silica with carbon in an electric arc furnace (hence the namesake moissanite) [66].

Natural moissanite is only found in very small quantities, and therefore almost all silicon carbide available is produced synthetically. The simplest process for the production of SiC is the Acheson method, which combines carbon with silica sand at temperatures up to 2500°C in an electric resistance furnace, bonding the grains by sintering to form SiC. This process results in various levels of purity, depending on the crystal's distance from the resistor heat source [67], [68]. For the production of pure silicon carbide, the Lely process is used. In this case, SiC powder is sublimed in an argon gas furnace with silicon, carbon, SiC_2 and Si_2C (silicon dicarbide and disilicon carbide), producing single crystals up to 2 cm in size, and up to 10 cm with a modified process [69], [70].

Synthetic SiC has a wide variety of thermal and mechanical applications, including use in tooling and abrasives, due to its hardness and durability, and in automotive parts such as high-performance disk brakes on account of its ability to withstand extreme temperatures. Additionally, the material is used in lightning arresters in electrical power systems because of its high electrical resistance up to a certain threshold [71].

Silicon Carbide is a polymorph and can exist in more than 250 documented crystalline polytypes [72]. The different types of SiC vary from one another in terms of the order in which planes of Si or C atoms are stacked. The most commonly encountered polytype is alpha silicon carbide (α-SiC such as 6H-SiC[10]), which has a hexagonal crystal structure and is formed at temperatures greater than 1700°C, as opposed to the cubic β-SiC (3C-SiC) polymorph produced by the chemical vapour deposition (CVD) process, which forms below this temperature [73], [74]. The typical microstructure of sintered alpha silicon

[10] In the polytype name, C, H, and R refer to the symmetrical nature of the unit cell (cubic, hexagonal, etc.), while the integer indicates the number of SiC (or C) layers in a unit cell.

carbide is shown in Figure 20 [75], [76]. The matrix is composed of small, equiaxed alpha silicon carbide grains (less than 10 μm), with embedded platelet alpha-phase silicon carbide grains (up to 400 μm in length) and no boundary phase. As can be seen, there are finely distributed microporosities and occasional macropores (1-5 μm size for the former, 10-100 μm for the latter), and the material is noted to fracture transgranularly[11].

The SiC grade tested in the HRMT36 experiment was manufactured by chemical vapour deposition by the company Microcertec SAS [78]. In the CVD process, the substrate, also referred to as the wafer, is exposed to volatile precursors which produce a deposit by reacting on its surface. Prior to the development of CVD, the production of high quality SiC polytypes had been limited to relatively small crystal dimensions, such as those produced by the Lely process. The more expensive CVD process allows for the epitaxial deposition[12] of large cubic β-SiC crystals which are free of cracks, as well as homoepitaxial and heteroepitaxial growth [80]. A schematic diagram of epitaxial growth of silicon carbide in the CVD process is shown in Figure 21.

[11] In transgranular fracture, the crack propagation does not follow grain boundaries, but travels from one grain to another through the matrix. This is in contrast with intergranular fracture, where the crack follows the grain boundaries [77].

[12] Epitaxy is the deposition of a crystalline layer on a crystalline substrate . The overlayer is called an epitaxial film or layer. An epitaxial film can either be deposited on a substrate having the same composition, in a homoepitaxial process, or on a substrate having a different composition, in a heteroepitaxial process. The term non-epitaxial growth refers to a deposition formed in a random or non-uniform orientation with respect to the substrate [79].

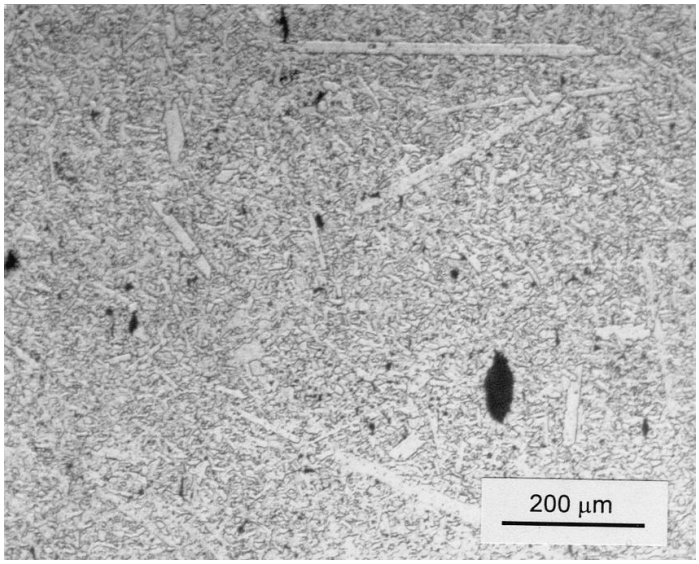

Figure 20 – Typical microstructure of sintered alpha silicon carbide [76].

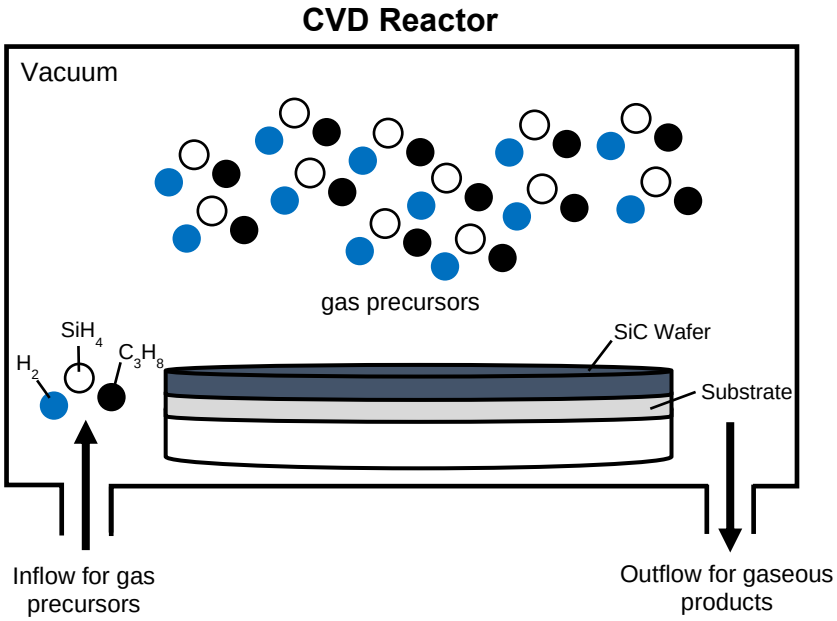

Figure 21 – Epitaxial growth of silicon carbide in the CVD process.

As opposed to sintering, the chemical vapor deposition process produces highly pure crystals which approach the theoretical density, are generally free from voids and micro-cracks, and result in a material which is both isotropic and homogeneous. A purity of up to 99.999% can be achieved. In contrast, sintered SiC will generally have a residual porosity of approximately 2.5%$_{vol}$. For these reasons, a pore-free CVD layer is generally applied in situations where SiC is used in optical faces, coating the surface of the polished sintered SiC component. The comparable coefficient of thermal expansion (CTE) of the two SiC grades allows for a good interface between the sintered SiC substrate and the CVD SiC layer, resulting in a good continuity free from defects, as seen in Figure 22 [81].

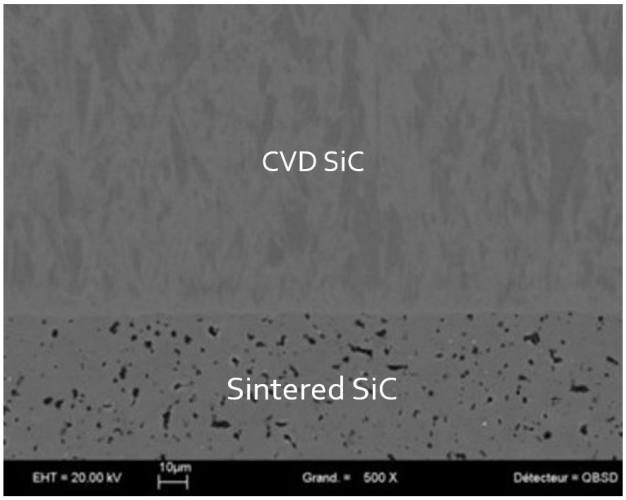

Figure 22 – SEM view of the CVD SiC (with essentially no pores) and sintered SiC interface [81].

Lower purity grades of SiC are generally used for thermal applications, while higher purity grades such as sintered and CVD SiC are used in more specialised situations requiring advanced ceramics with elevated thermal and mechanical properties. Notable properties relevant to silicon carbide's application in the field of beam intercepting devices include a low density, excellent thermal shock resistance, a low coefficient of thermal expansion, high thermal and electrical conductivities, as well as good mechanical strength [82].

Studies have been conducted with regard to the brazing of SiC with various metals such as OFE Copper, with promising results [82]. However, there is strong evidence of swelling (large and permanent volumetric expansion) under the effect of ion and neutron radiation, which can result in sudden, premature failure. This can be mitigated by operating at a high temperature, but for this reason there is limited information on the material for temperatures below 100°C, which typically is the temperature of interest for LHC collimators operating in nominal conditions. A testing campaign aiming to braze SiC with molybdenum alloys has also been carried out at CERN, based on the need for high atomic weight materials for use in absorbing cores. The brazing process is facilitated by the fact that SiC has a very similar coefficient of thermal expansion to molybdenum-based alloys such as titanium zirconium molybdenum (TZM) in temperature ranges of interest. Additionally, efforts are also being made to analyse the behaviour of Copper Diamond brazed with SiC [73].

2.3.4.2 Titanium Zirconium Molybdenum

Refractory metals include elements such as niobium, molybdenum, tantalum and tungsten, along with other elements such as titanium, zirconium, and vanadium depending on the definition. Materials classified as such generally have an elevated melting point of 2000°C or higher, high hardness at room temperature, are significantly dense, and are chemically inert. Fabrication of such types of metals is typically limited to powder metallurgy due to their high melting point [83]. Molybdenum is one such material, being a BCC metal with a high melting point of 2620°C, combined with good thermal and mechanical properties. Such properties make molybdenum an ideal material for use in applications including lighting, high-temperature furnaces, and military applications [84]–[86].

Titanium Zirconium Molybdenum is one of the most widely used molybdenum alloys, composed of 0.4-0.55% titanium, 0.06-0.12% zirconium, 0.01-0.04% carbon and molybdenum weight balance [87]. Compared with pure molybdenum, TZM exhibits higher strength and creep resistance at elevated temperatures, along with good corrosion resistance and improved ductility and weldability. Additionally, TZM has a higher resistance to recrystallisation and softening compared to unalloyed molybdenum [86], [88]. This combination of properties makes the material ideal for applications requiring high service temperature performance components that necessitate hot strength and creep resistance, such as in high-power turbines, high-temperature furnaces, as well as permanent moulding tools. Similarly, the properties described make it a promising candidate for use in beam intercepting devices in particle accelerators [89].

The high temperature and strength improvements in TZM are derived from solid solution strengthening, which involves the dissolution of alloying elements such as titanium and zirconium, along with dispersion strengthening, allowing the formation of Mo-Ti-Zr carbides [88]. The TZM grade tested in the MultiMat experiment was developed by Plansee [86], with the manufacturing process including a mixture of pressing, sintering and forming followed by additional heat treatment. Figure 23 shows the microstructure of pure, cold worked molybdenum produced by Plansee, manufactured from a fine-grained high purity powder, which is pressed and sintered at a temperature over 2000°C. This is followed by cold working up to a 50% reduction in thickness, resulting in elongated grains with almost no visible inclusions or pores [90]. This can be compared with Figure 24, which shows the microstructure of sintered TZM [91].

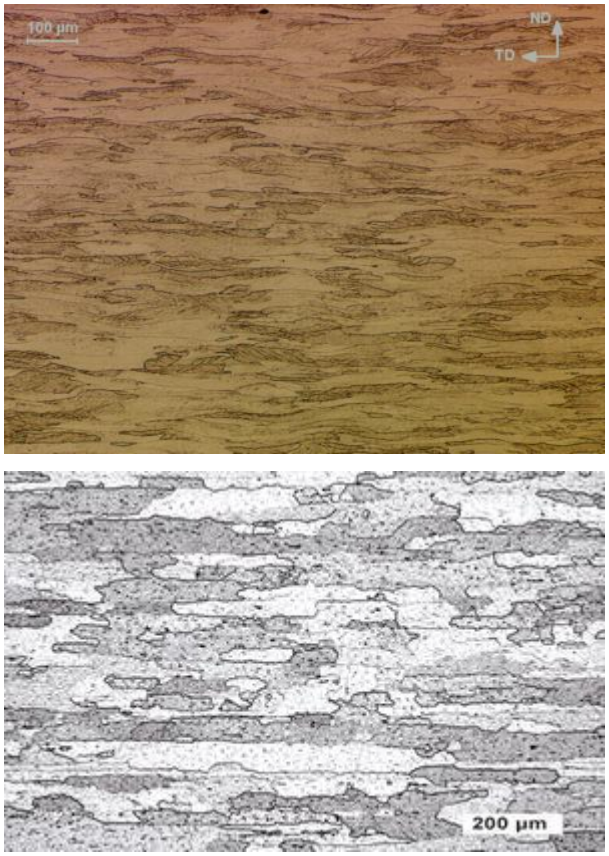

Figure 23 – Optical microscopy images of molybdenum microstructure [92].

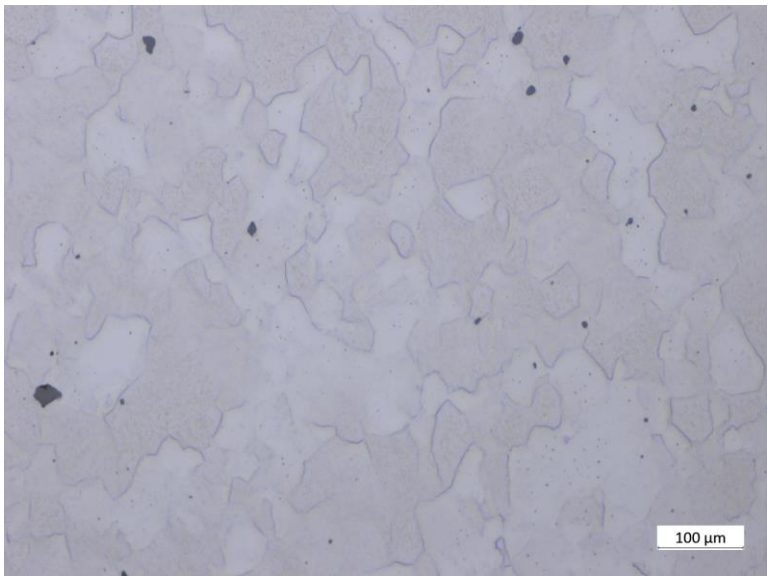

Figure 24 – Microstructure of sintered billet of a TZM alloy [91].

2.3.4.3 Copper Diamond

Copper Diamond (CuCD) is a novel composite material developed as a candidate for use in future collimators and absorbers to be implemented in the upcoming HL-LHC upgrade in CERN's LHC.

CuCD is a metal-matrix composite (MMC), specifically a particle-reinforced metal-matrix composite (PRMMC), composed of a copper matrix with diamond particles dispersed in the material. An SE micrograph of synthetic diamond particles is shown in Figure 25. The constituents are hot pressed in a spark plasma sintering process at close to the melting temperature of copper. A number of binding materials are added, including titanium, chromium, boron, zirconium and titanium. In the sintering process, these additions form carbides which aid in bonding the diamond and copper particles. The two constituents otherwise have minimal chemical affinity, which impairs mechanical strength [19].

The cost of diamond particles has decreased considerably with the advent of synthetic diamonds [93], making it possible to combine the stellar heat conduction of the material with the already high conductivity of copper. The conductivity of copper-diamond composites has consequently been studied extensively [94]–[98]. Alternative methods to the sintering process, which is expensive to conduct and requires precise control of various thermodynamic phenomena, have also been proposed, such as the electrodeposition of copper to synthetic diamonds [99].

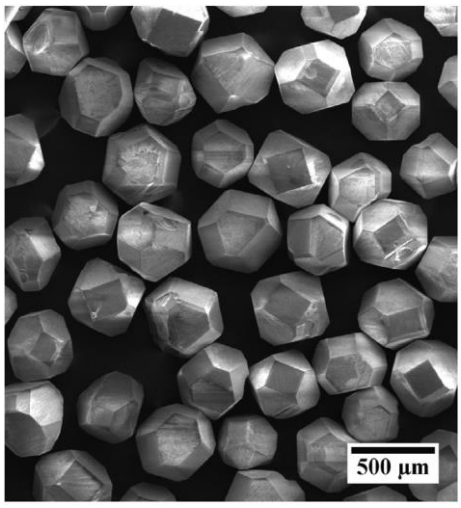

Figure 25 – SE micrograph of uncoated, synthetic diamond particles [99].

Diamond has a very high thermal conductivity (approximately 2000 W/mK, a factor of five higher than that of copper), which comes as a result of how heat is conducted in the material. In contrast with metals, in which conduction is done via electrons, the high thermal conductivity of diamond is a result of heat transfer by lattice vibrations. The copper-diamond interface plays an important role in the final CTE, thermal conductivity and mechanical properties of the final composite, and the added binding materials promote wetting and bonding of the diamond particles with the copper matrix. As mentioned, in diamonds, phonons dominate the heat conduction, while electrons dominate in copper. The thin interface layer formed by the carbide grade aids in the electron-phonon coupling and improves interfacial bonding, leading to an overlap in phonon densities of copper and diamond, which results in high thermal conductivities [100]–[102]. Best results are achieved by fast pressure-assisted sintering of powder mixtures, with an elevated heating and cooling rate (in the order of a 100 K/min). This results in conductivities in the order of 640 W/mK in CuCD composites with carbide binders, compared to thermal conductivities in the order of 400 W/mK in composites with a pure copper matrix and no additional binders [103].

Figure 26 shows an SEM image showing the carbide formations on diamond faces. The carbide interlayer has a thickness of around 100 nm, as seen in Figure 27. Similar carbide layers bridging the diamond grains with the copper matrix can be seen in Figure 28.

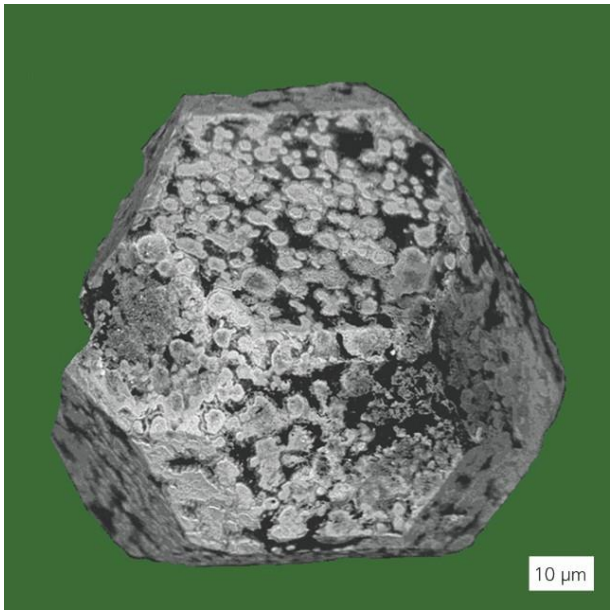

Figure 26 – SEM image showing chromium carbide formations on the diamond particle surface [103].

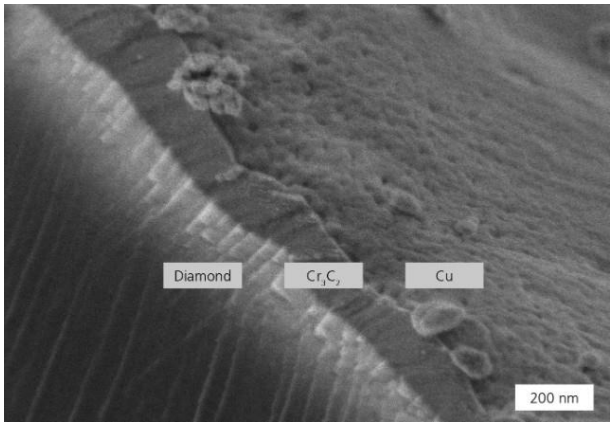

Figure 27 – SEM image of fractured surface of hot-pressed CuCD composite [103].

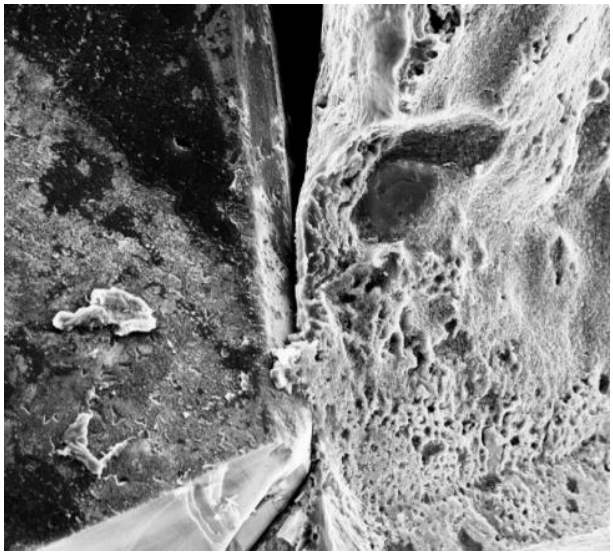

Figure 28 – Micrograph of CuCD fracture surface. Note small carbide platelet bridging diamond grain with copper matrix [104].

One of the CuCD grades tested in the MultiMat experiment, named CuCD RHP3434 for the scope of the experiment, was developed by RHP-Technology [105]. The grade is primarily composed of synthetic diamond particles ($50\%_{vol}$) dispersed in a copper matrix ($50\%_{vol}$). Such a composition would result in a theoretical density of 6.2 g/cm^3, however the actual density of the grade measures at 5.7 g/cm^3, indicating that the material has approximately $8.4\%_{vol}$ of porosity (i.e., the actual volume distribution is 8.4% porosities, 45.8% copper, and 45.8% diamond particles). The diamond particles have a bi-modal size distribution with particle sizes of approximately 194 and 115 μm.

The grade is produced by a hot-pressing process (spark plasma sintering) using a compact of cold pressed constituent powders, known as the "green". The green is composed of synthetic diamond particles, spheroidal copper, and additionally a small amount of amorphous boron as a binding element. These are sintered at pressures up to 35 MPa at a

temperature slightly below the melting point of copper, approximately 1000-1050ºC. The process is conducted in a dry hydrogen gas atmosphere, and the pressure is maintained for 1-4 hours, following which the setup is slowly cooled to 400ºC. A stress relieving heat treatment is then conducted at temperatures of around 300-400ºC for another hour [106]. The carbide B_4C (boron carbide) is formed at the interface and provides a reliable bond between the copper and diamond particles. An optical image of the copper-diamond surface at different levels of magnification is shown in Figure 29.

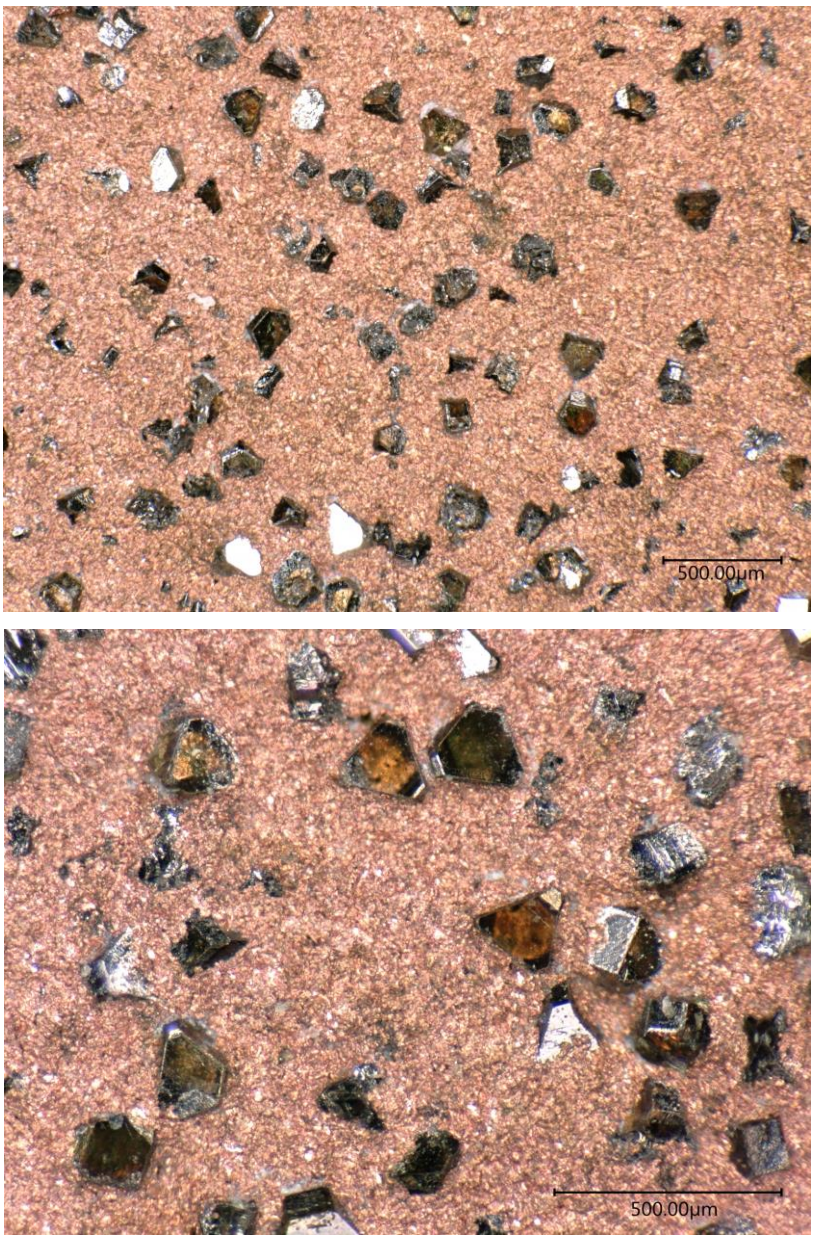

Figure 29 – Optical image of CuCD RHP3434 grade at different levels of magnification.

The blend of properties provided by the two material constituents increasingly make CuCD a material of interest in the field of BIDs. While copper delivers good thermal and electrical conductivity, the diamond particles extend thermal conductivity further and help in lowering the coefficient of thermal expansion and density.

CuCD has been chosen to replace Inermet180, a tungsten heavy alloy, for use in the HL-LHC's tertiary collimators. Compared to Inermet180, copper diamond is more robust, and is able to tolerate higher beam intensities without succumbing to extreme damage and requiring replacement. Nevertheless, the material's limitations include the difficulty and cost in machining complex shapes with precise tolerances, along with the relatively high density and CTE compared to competing materials currently being developed at CERN, such as Molybdenum Graphite (MoGr) [104]. As an example, Figure 30 shows water-jet machined CuCD specimens prepared for testing at CERN. The porosity and rough surface of the material can be clearly observed, along with marks on the material as a result of the water flow impinged on its surface [104]. Another disadvantage of the material is the low melting point of the copper matrix and the fact that, due to the high copper content, the coefficient of thermal expansion increases significantly with temperature.

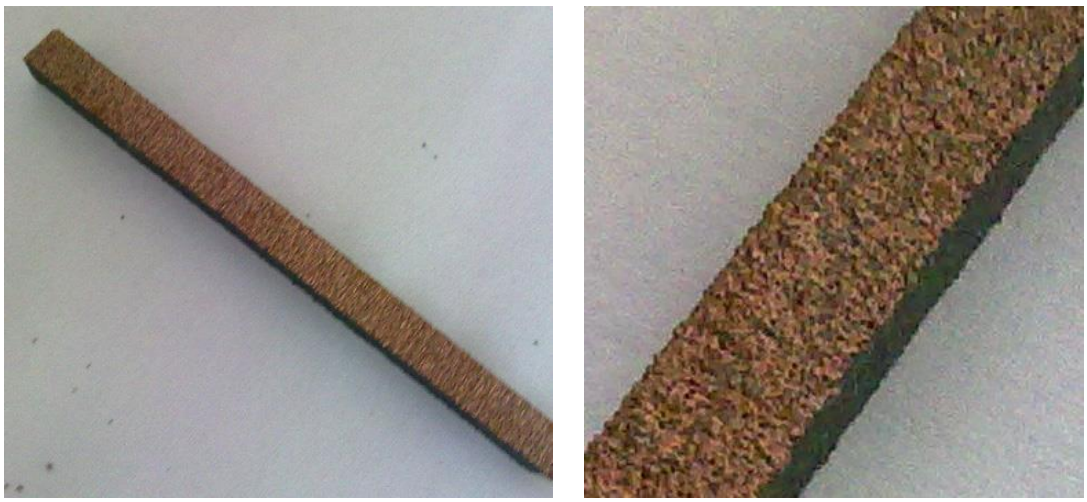

Figure 30 – CuCD samples after water-jet cutting, clearly showing porosity and marks in the water flow direction [104].

2.4 Analytical modelling of elastic stress waves in slender rods

Analytical solutions for the mathematical description of longitudinal wave propagation in long rods exposed to a quasi-instantaneous deposit of energy are available. These act as simple and efficient tools for calculating the thermal distribution following impact, and can also determine the resulting mechanical response. In the field of particle accelerators, especially in the context of beam intercepting devices, this topic is of great interest. Absorbers, such as collimators, can be modelled as one dimensional (1D) systems, subject to rapid thermal energy depositions in accidental beam scenarios.

Subatomic particles interacting with matter transfer energy to the material in the form of thermal energy. This leads to an increase in internal temperature, which results in a variety of effects based on the deposited energy density. As previously discussed, a continuous energy deposition is provoked by beam losses in particle accelerators. Such losses can last from seconds to hours. In the case of accidental impacts, energy can be deposited in nanoseconds, provoking a dynamic response [33]. As stated, many beam intercepting devices are in the shape of slender rods, thus the dynamic response of such geometries in these conditions is of great interest for high energy particle physics applications. Analytical solutions on this topic were proposed by Bargmann [107], Sievers [108], and Boley [109]. In recent years, Bertarelli *et al.* [110] have studied longitudinal and flexural phenomena.

Bertarelli [110] considers a long cylindrical rod subjected to an increase in temperature following an internal energy deposition along its axis [111]. The boundary conditions consist of a simply supported setup, with the rod's extremities free to expand. A Gaussian energy distribution covers the cross-section, having an eccentricity η and a standard deviation ϕ. A linear, elastic, isotropic material model is considered, and material properties are assumed to be independent of temperature changes.

The deposited energy is assumed to grow linearly in the duration of the thermal shock, τ, based on the hypothesis that for a diffusion time t_d which is much longer than the thermal shock duration, no heat diffusion is assumed to occur during this period of time. The system is considered adiabatic, given the relatively short time period, and therefore the total energy is constant once the energy deposition is complete. In such a rapid scenario, material inertia effects are non-negligible, and indeed play a significant role when calculating flexural and longitudinal strains and the associated stress. Radial inertia, and its influence on the dynamic longitudinal response, is not considered in this model, based on findings presented

by Graff [17]. These phenomena can result in significant effects observable in the longitudinal response, and should generally be included. In a numerical approach, as proposed in this thesis, radial inertia and dispersion phenomena can be included in the analysis.

The thermomechanical problem presented by such a scenario can be solved in two steps, starting with a thermal analysis calculating the temperature field, which feeds results into a structural analysis. If a constant temperature distribution is assumed along the longitudinal axis, along with no radial eccentricity, the analysis can be reduced to a 1D problem. The energy density at the end of the energy deposition, $U(r)$ in $\mathrm{J/m^3}$, across a specimen's cross-section for a Gaussian load distribution can be described by:

$$U(r) = U_{max} e^{-r^2/\phi^2} \tag{14}$$

Where U_{max} is the maximum energy density deposited at the beam core and r is the radial position. The increase in temperature across the specimen's radial section at the end of the energy deposition can be found by:

$$T(r) = \frac{U(r)}{\rho c_p} \tag{15}$$

Due to the adiabatic boundary conditions, the final uniform temperature increase in the specimen can simply be calculated by:

$$T_f = \frac{\int_r U(r)dr}{\rho c_p \pi R^2} \tag{16}$$

The load can be simplified further by assuming a pencil beam with a uniform circular load across the specimen's radius, rather than a Gaussian distribution. This can be justified given the large temperature gradient across the cross-section. For a load with no radial eccentricity, the energy and temperature across the specimen's cross-section can be described by:

$$U(r) = U_{max} \text{ for } r < \phi \qquad U(r) = 0 \text{ elsewhere} \tag{17}$$

$$T(r) = T_{max} = \frac{U_{max}}{\rho c_p} \text{ for } r < \phi \qquad T(r) = 0 \text{ elsewhere} \tag{18}$$

$$T_f = T_{max} \frac{\phi^2}{R^2} \tag{19}$$

where *R* is the rod's radius and ϕ is the beam's radius [112].

2.4.1 Longitudinal Phenomena

At short time scales, the body's inertia initially prevents thermal expansion, coupling inertial and thermally induced forces. In the case of a long, slender rod, with the body still in a compressive state, dynamic stress pulses propagate along its length in the form of elastic stress waves. As shown in Figure 31, the stress relaxation starts from the rod's two extremities, with the propagation of two stress waves along the rod's length, which superimpose at its centre and reflect back once reaching the opposite end [112].

Figure 31 – Compressive state of the rod following the energy deposition, resulting in the propagation of longitudinal stress waves from its extremities.

The reference stress for the propagating waves is defined by:

$$\sigma_{ref} = E\alpha T_f \tag{20}$$

The reference stress relates to the compressive axial stress induced by a uniform temperature increase T_f in a rod with fixed boundary conditions. The value is the maximum stress amplitude for each wave, meaning that a theoretical ceiling for the dynamic longitudinal stress is $2\sigma_{ref}$, which is achieved when the two propagating waves superimpose. The maximum stress is only reached in cases where there is a sufficiently short pulse duration. In fact, when the energy deposition time is significantly long, the maximum stress value may not be achieved. Figure 32 shows the typical evolution of the dynamic longitudinal stress at different locations on a long rod, normalised with the reference stress.

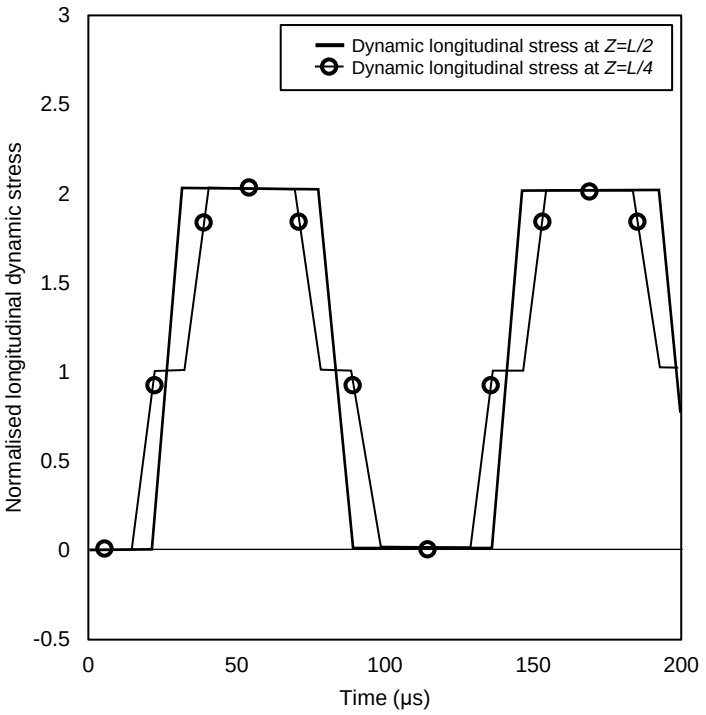

Figure 32 – Longitudinal dynamic stress at the centre of the rod and at a quarter of the length of the rod [110].

The first fundamental longitudinal frequency for elastic longitudinal waves is found by:

$$f_L = \frac{c_0}{2L} \tag{21}$$

where L is the rod's length and $c_0 = \sqrt{\frac{E}{\rho}}$ is the base velocity of longitudinal wave propagation in the material. Subsequently, the longitudinal period t_L is the inverse of the longitudinal frequency.

The thermal diffusion time, t_d, is related to the time it takes to reach a uniform distribution of temperature in a given region for a heat diffusion process:

$$t_d = \frac{B^2}{\kappa} \tag{22}$$

where B is the relevant dimension (the radius in case of cylinders) and κ is the thermal diffusivity, given by:

$$\kappa = \frac{k}{\rho c_p} \tag{23}$$

where k is the conductivity, ρ is the density, and c_p is the specific heat capacity of the material.

In hydrostatic conditions, the time period for radial waves travelling from the rod's centre in an outwards direction can be described by:

$$t_R = \frac{2R}{\sqrt{\frac{K}{\rho}}} \tag{24}$$

where R is the rod's radius and K is the impacted material's bulk modulus. Similar to longitudinal waves, radial waves are reflected inwards once they reach the rod's free surface.

In the analytical models discussed, effects on longitudinal vibrations related to radial inertia are not considered. As previously stated, this follows findings by Graff [17], who hypothesised that such effects may be neglected, provided the system's frequency is small relative to reference values. Graff studied how classical wave theory breaks down in view of dispersive effects, and found that, up to a limiting working frequency, radial inertia can in fact be disregarded. In such cases, classical wave theory can be considered for problems regarding longitudinal wave propagation in slender rods. Beyond such a frequency, classical theory is invalid and radial inertia needs to be considered. There are two phenomena relating to high-frequency effects in axial oscillations, namely cylindrical waves propagating from the centre of the rod, and wave dispersion effects due to wave-boundary interactions. In summary, the radial displacement resulting from radial waves propagating from the centre of the rod to the external surface leads to an axial component (related to the material's Poisson's ratio) and is thus captured in axial vibration measurements. Release waves caused by the interaction of axial waves with a specimen's free surface travel at lower velocities than the main wave due to wave dispersion, and this is consequently also observed as distortion in axial vibrations. High-frequency effects on longitudinal waves as a result of high intensity particle beam impacts have been further studied by the author [112], in a study where a two-pronged numerical approach was adopted. A sequentially coupled thermomechanical analysis and a modal analysis were implemented to study free surface effects on the propagating wave. The study concluded that radial effects can be mitigated or enhanced by changing the rod geometry and varying the pulse duration, allowing one to fine-tune experimental results accordingly.

2.4.2 Flexural Phenomena

In the case of a beam pulse offset in relation to the rod's longitudinal axis, an additional bending response is induced, which is superimposed on the longitudinal signal. The frequency of the first flexural harmonic is a function of the material's Young's Modulus

and density, as well as the moment of inertia of the rod's cross-section, the cross-sectional area, the specimen's length, and the boundary conditions, and can be found by:

$$f_F = \frac{a^2}{2\pi}\sqrt{\frac{EI}{\rho AL^4}} \tag{25}$$

where a is a constant dependent on the boundary conditions of the setup, equal to π for a simply supported configuration and 4.730 for a free-free configuration [113]. As will be seen in the MultiMat experiment results, while the experimental setup consisted of a simply supported configuration, contact was lost between the specimens and supports in some cases, resulting in a periodic change in boundary conditions. This resulted in the first few bending oscillations exhibiting a higher frequency corresponding to a free-free condition, with a subsequent transition into a simply supported condition. A typical dynamic flexural displacement plot, as computed in Bertarelli's study [110], can be seen in Figure 33. Note the different time scales for longitudinal and flexural phenomena, compared to the signal shown in Figure 32, i.e., in the order of microseconds for longitudinal wave propagation, and milliseconds for bending oscillations.

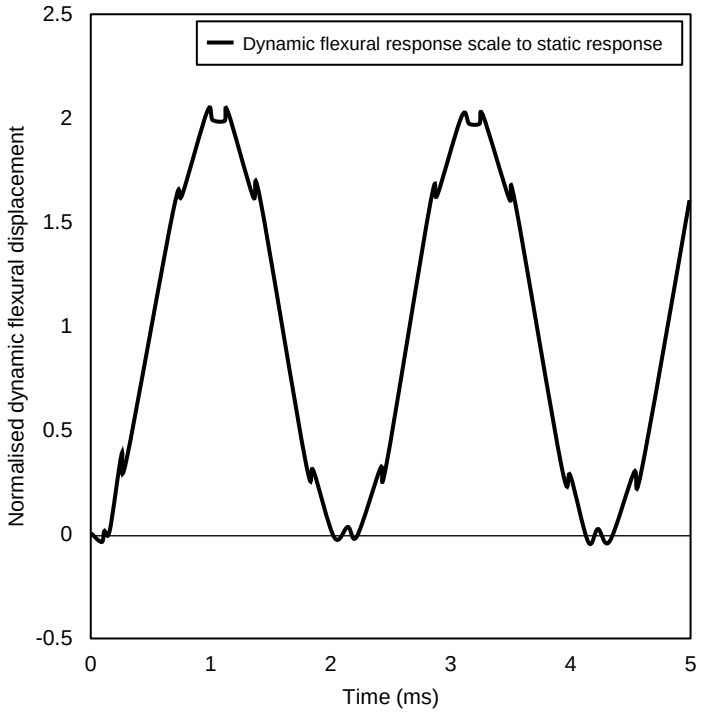

Figure 33 – Dynamic flexural response at the centre of the rod scaled to the static bending response [110].

2.5 State-of-the-art and current studies

In the context of stress waves induced by particle beam impacts, analytical solutions allow for quick calculation of factors of interest in impacted components, such as expected frequencies for a set of initial and boundary conditions, and maximum expected quasistatic and dynamic stresses. As the geometry of interest and material models available become more complex, the dynamic response becomes increasingly harder to compute. In such cases, numerical codes are essential tools for computing the required results. In recent years, there have been significant efforts in the development of numerical solutions based on the finite element method, complementing analytical solutions in order to extend the study of complex geometries in the elasto-plastic domain, as well as in the shock wave regime.

In their work, Tahir *et al.* [114] modelled a solid, cylindrical copper target subjected to 100 LHC bunches. The energy deposition was calculated with FLUKA, and the BIG-2 code was utilised to numerically model the hydrodynamic and thermodynamic response of the target in 2D, implementing a multi-phase equation of state to describe the material response when subjected to impacts leading to changes in phase [114]. A similar approach was adopted by Peroni [115], where studies were carried out in the finite element code LS-DYNA. A 2D axisymmetric geometry was implemented to model a cylindrical copper bar subjected to 8 bunches at 1.11×10^{11} protons per bunch. The deviatoric component was represented by the Johnson-Cook model with the inclusion of damage criteria and spall models, while the hydrostatic component was represented with a multi-phase tabular equation of state [116]–[119]. Results from Tahir's BIG-2 simulations and Peroni's LS-DYNA simulations were compared and achieved good agreement [115].

Dallocchio proposed a numerical method implemented in the implicit code ANSYS in order to study the structural response of prototype LHC collimators subject to rapid heat loads, validated with tests conducted in CERN's SPS ring. The prototypes were impacted with a number of full beam impacts, and experimental measurements were used to confirm the validity of the numerical simulations [120]. Similarly, Cauchi modelled a number of collimator jaw error cases resulting in the asynchronous beam dump of an LHC beam on a tertiary collimator made out of tungsten [55]. More recently, Carra compared experimental data acquired during the HRMT23 experiment, in which a number of prototype collimator jaws were tested under HL-LHC design case impacts, with results from simulations modelling the experimental setup with numerical material models of graphitic materials, obtained from an extensive characterisation campaign [19]. Once again, the numerical

analyses were performed in ANSYS's implicit solver, due to the relative simplicity of the adopted models as well as the absence of changes of phase in the studied scenarios.

In his thesis, Torregrosa discusses the limitations of implicit finite element codes in the simulation of the dynamic response of CERN's Antiproton Decelerator (AD) target in the context of the HRMT27 experiment. In the case of the AD target, an explicit numerical approach was preferred due to the high strain rates reached, as well as the strain rate dependency of the material response [89].

2.6 Summary

The purpose of the work shown in this thesis is to advance the knowledge on the thermomechanical response of novel materials developed within the context of the collimation system in CERN's particle accelerator complex. This is achieved by building material models describing the material's thermostructural behaviour under a range of conditions, which are applied in 3D models implemented in advanced numerical simulations. Specimens from the HRMT36 experiments are modelled, taking into consideration the boundary conditions resulting from the experimental setup, as well as the energy deposition on the specimens from the particle beam impact, calculated in collaboration with CERN's FLUKA team. The energy deposition is used as an input to the thermostructural analyses conduced in the implicit FE code Ansys® Academic Research Mechanical, Release 18.1, and is used to calculate the thermal load within each specimen of interest, and the resulting dynamic structural response. The numerical approach developed, consisting of simply coupled transient thermomechanical analyses, is presented in this thesis.

The studies conducted aim to narrow the knowledge gap currently present on the novel materials considered, for which only a limited amount of literature is available. This is especially true in cases where there is an intense internal heat generation as a consequence of particle beam impact. The study takes advantage of the large amount of data collected from the HRMT36 experiment, which is compared with numerical results to benchmark the material models proposed. The models are built from a combination of sources, namely manufacturer-provided material data, data obtained from literature, and commissioned characterisation campaigns conducted specifically for this study.

A number of insights are put forward in relation to observations made in the experimental campaign, such as the failure of SiC and TZM specimens, and loss of contact between the supports and tested specimens. A numerical approach is adopted to simulate such scenarios and better understand their effects.

In the final part of the thesis, developments are made on previous work [121] studying the mesoscale behaviour of particle-reinforced composites impacted by an external force. A model considering the response of such materials when subject to intense, quasi-instantaneous changes in internal temperature is proposed in this study. Additionally, a tabular equation of state for copper diamond is formulated and presented, developed from data available for the constituent materials, which can be essential for future study on the material.

Finally, a number of considerations for future work are identified in view of the current literature along with results obtained in this study. The material modelling of behaviour under intense particle beam impact requires accurate temperature and strain-rate dependent thermal and structural material data. This is especially true in cases where there are significant temperature variations, high strain-rate impacts, and considerable property dependency on these factors. A number of material characterisation tests on the SiC, TZM, and CuCD grades considered in this study have thus been commissioned or recommended, in order to obtain an improved description of the material behaviour across a wider range of conditions.

Chapter 3:

Isotropic, Homogeneous Materials: SiC and TZM

3.1 Introduction

A large amount of data was gathered in the MultiMat experiment, requiring extensive post-processing and benchmarking with results from numerical simulation. This chapter focuses on the MultiMat results for two materials, namely Titanium Zirconium Molybdenum and Silicon Carbide, two materials which, despite being very different (one is an alloy while the other is a ceramic), display a number of similarities. The two materials are isotropic and have a relatively predictable behaviour. Additionally, in both cases there were a number of anomalies observed in experimental results, namely:

- Dynamic bending frequencies measured in the experiment varied significantly from those calculated analytically; and
- Some of the specimens tested exhibited failure during the experiment.

With this in mind, this chapter aims to validate the material models available for the two materials and identify the causes of any discrepancies between experimental and numerical results. One should note that the two material models are not compared with each other in this chapter, but rather are presented together due to the similar behaviour observed.

3.2 Numerical Analysis Methodology

In order to model the material response of objects dynamically excited by thermal or mechanical means, a mathematical model is required to represent the material behaviour. In this section, the numerical modelling of such phenomena in the context of particle beam impacts is discussed. In particle beam impacts, part or all of the kinetic energy of the impacting particles, which are travelling at relativistic speeds, is transferred to the impacted body as heat. This reduces the problem at hand to one where a body is subjected to a quasi-instantaneous internal heat generation, which lasts for the duration of the beam impact. As previously discussed, the distribution of this energy deposition across the transverse direction of the body (i.e. orthogonal to the beam direction) takes the form of a Gaussian probability density function. The deposition results in a very high temperature gradient, due to the transverse size of the beam being in the order of millimetres, and the high energy densities deposited (which for experiments conducted in the HiRadMat facility is in the order of 10^5 J/cm^3) [19].

Most of the analyses carried out in this thesis are conducted in a series of steps modelling the thermomechanical process of particle beams impacting solid materials. For such phenomena to be modelled, three sets of results are of interest, namely:

1. The *energy deposition map*, describing the particle beam's interaction with the solid body, and the amount of energy transferred to the body;
2. The *temperature field*, describing the resulting internal temperature increase in the body due to the energy deposited by the beam impact; and
3. The resulting *mechanical response* in the body due to the quasi-instantaneous internal temperature rise.

A chart detailing the flow of data in most of the analyses implemented in this study is shown in Figure 34. This section will describe in detail the tools used to generate the results necessary for each step.

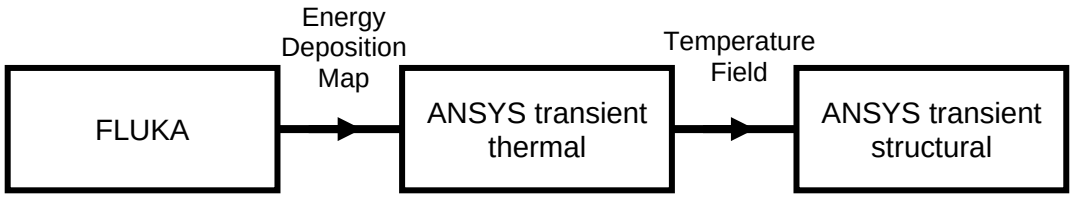

Figure 34 – Flow of data for the weakly coupled thermomechanical analysis.

Interaction and transport codes such as FLUKA, MARS and GEANT4 [122]–[124] are used to calculate the thermal energy deposited on targets. In this thesis, energy deposition maps generated by the CERN FLUKA team are used as an input for thermostructural simulations carried out. FLUKA uses a statistical code based on the Monte Carlo method to generate the energy deposition maps, which are imported in the FEM program via a dedicated algorithm in order to model a correct thermal load input. The energy distribution is rearranged in a 3D matrix aligned with the finite element model's coordinate system, following which the load is applied as an internal heat generation in W/m^3. The energy deposition is caused by the beam's particles interacting with the electrons of the target material's lattice, followed by interactions with the atoms' nuclei. This produces what is referred to as a particle shower, that is, a cascade of secondary particles. Beam interaction with high density and high atomic number materials results in higher energy densities deposited. This, in turn, means that such materials are more effective when used as beam absorbers.

The geometry implemented for thermal and structural analyses for all shots and materials considered is shown in Figure 35. The dimensions represent the specimen size tested in the HRMT36 experiment. With reference to the coordinate system defined, due to the beam impact being symmetrical across the specimen face, symmetry was implemented in the XZ plane in both thermal and structural analyses.

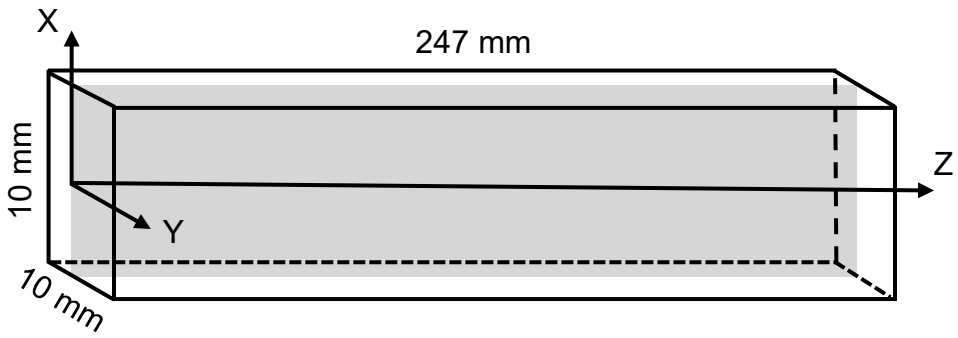

Figure 35 – Coordinate system and specimen dimensions implemented in thermal and structural analyses. Symmetry was implemented in the XZ plane for both analysis types.

In transient thermal analysis, the material specimens are modelled in 3D in the implicit finite element software Ansys® Academic Research Mechanical, Release 18.1. The modelled volume is discretised by SOLID90 elements, which are high-order 3D 20-node thermal elements. The material behaviour was represented by material models obtained from literature or from experimental campaigns. The loading conditions are defined with an ANSYS script written in the Ansys Parametric Design Language (APDL), referred to as the *FLUKA import code*. The code is composed of two parts, the first of which is applied to the load step with the aim of loading and applying the deposition to the geometry, and the second having the purpose of deleting the load from the same geometry following the end of the energy deposition. As summarised in Figure 36, the first step selects the geometry of interest, i.e., the modelled specimen, following which the coordinate system and mesh of the energy deposition are defined. The next step is importing the relevant data to the applicable specimen, after which the load is applied. The second step simply halts the energy deposition and is applied at a time equal to the energy deposition time, ensuring that the correct amount of energy is deposited in the modelled specimen.

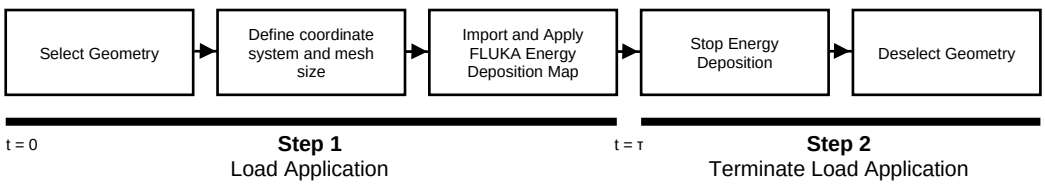

Figure 36 – Process of importing, depositing and terminating energy deposition on specimen.

The thermal analysis consists of two time-steps, the first equal to the energy deposition time for the shot being modelled, and the second having a longer duration allowing for the simulation of the temperature evolution across the specimen's volume. The relatively short time periods of interest allow for the samples to be modelled adiabatically, that is, the total energy in the system is retained throughout the analysis, following the initial influx of energy. This can be justified due to the fact that the temperature change evolution, in the order of seconds, is significantly longer than the timescale of the dynamic phenomena being observed, which are in the order of microseconds [19]. This assumption has the benefit of allowing the final uniform temperature in the analysis to be computed analytically by the methods described in Section 2.4.

For the structural analyses, the temperature field from the thermal analysis is imported as a thermal load. Again, the specimen of interest is modelled in 3D and discretised using SOLID186 elements in Ansys® Academic Research Mechanical, Release 18.1. These are higher order 3D 20-node solid elements with quadratic displacement behaviour. The structural analyses are defined by three time steps covering different phenomena of interest, namely the energy deposition, the longitudinal response, and the flexural response, in the range of nanoseconds, microseconds and milliseconds respectively. Boundary conditions modelling the experimental setup consist of restricted movement in the vertical direction of the two lower edges of the front and back faces of the specimen, simulating a simply supported configuration. The geometry, coordinate system, and boundary conditions for structural analyses are shown in Figure 37. As will be discussed in this chapter, the boundary conditions depicted are not always an accurate representation of what was observed experimentally.

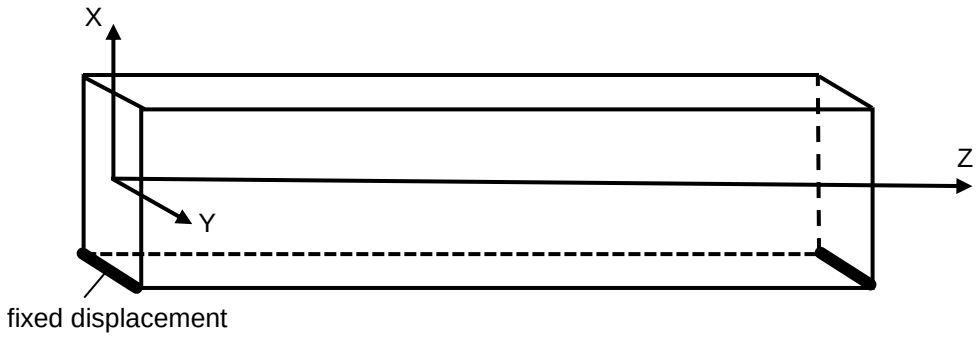

Figure 37 – Boundary conditions in a simply supported model of the experimental setup.

3.3 Material Models

The SiC grade tested in HRMT36 was produced by a chemical vapour deposition process by Microcertec SAS [78]. A linear elastic model was used to represent the material in numerical analyses, employing temperature-dependent material properties supplied by the manufacturer and verified by an external laboratory [125]. The stress-relieved TZM grade analysed was developed by Plansee [126], and consisted of a composition of 0.4-0.55% Titanium, 0.06-0.12% Zirconium and Molybdenum balance. To prepare the samples, the manufacturing process includes a sequence of pressing, sintering and forming, followed by additional heat treatment. For TZM, the manufacturer's specification sheet only included temperature-dependent information on the coefficient of thermal expansion, specific heat capacity and thermal conductivity. Thus, the material's elastic properties and a bilinear kinematic hardening constitutive model were found from literature [127], with the tangent modulus (E_t) calculated by considering the elongation at failure (ε_f), the yield strength (σ_y), the tensile strength (TS), and Young's Modulus (E) by:

$$E_t = \frac{TS - \sigma_y}{\varepsilon_f - \frac{\sigma_y}{E}} \tag{26}$$

Figure 38 and Figure 39 show the temperature-dependent properties employed for SiC and TZM respectively. The tensile strength and bilinear kinematic hardening parameters adopted for TZM, in addition to the flexural strength values for SiC, are shown in Table 4. The observed flexural strength increase at elevated temperatures for SiC could be a result of crack healing. Material properties for SiC and TZM at room temperature are summarised in Table 5.

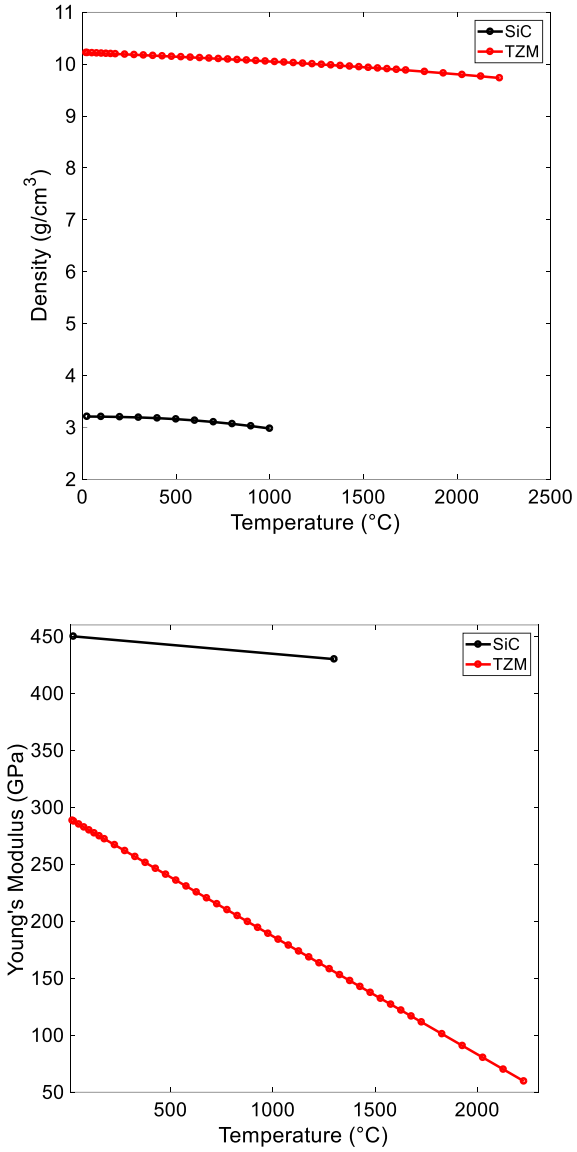

Figure 38 – Temperature-dependent values for density and Young's Modulus of SiC (black) and TZM (red). The constitutive models adopted also included a constant Poisson's ratio of 0.14 (SiC) and 0.28 (TZM).

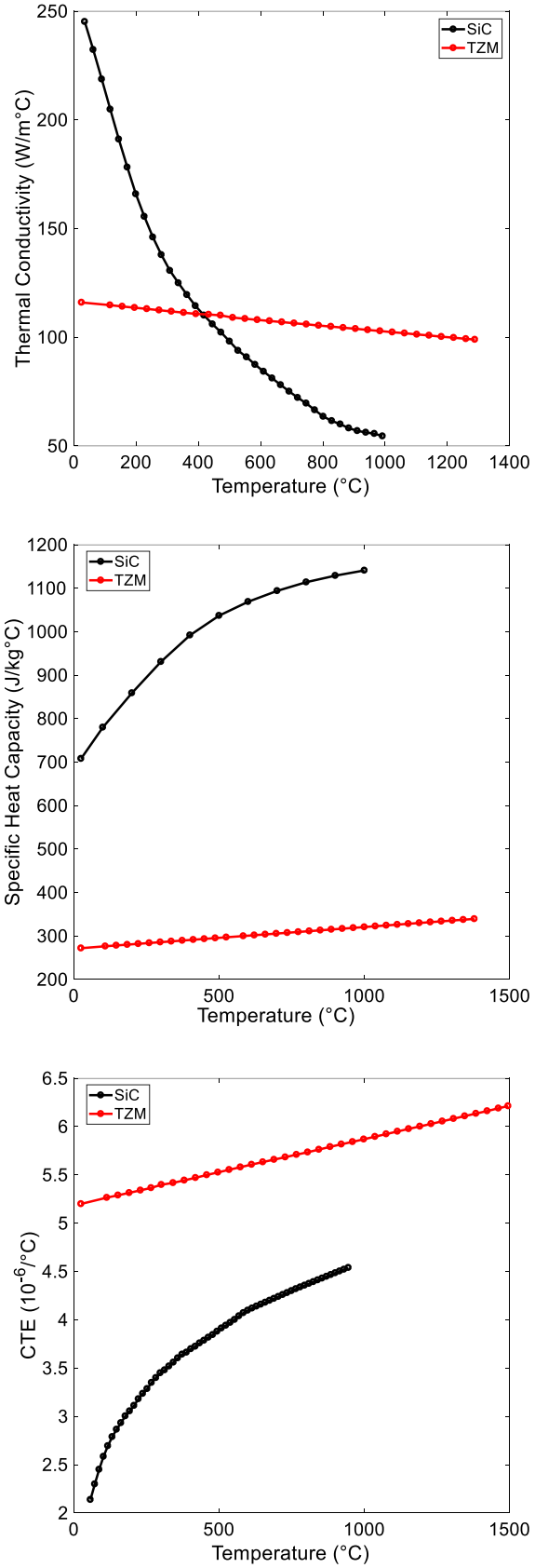

Figure 39 – Temperature-dependent values for thermal conductivity, specific heat capacity, and coefficient of thermal expansion for SiC (black) and TZM (red).

Table 4 – Bilinear kinematic hardening parameters adopted for TZM and tensile strength values [127] and flexural strength values for SiC as specified by the manufacturer [78].

Bilinear Kinematic Hardening parameters for TZM			
T	**Yield Strength**	**Tangent Modulus**	**Tensile Strength**
°C	*MPa*	*GPa*	*MPa*
20	764	2.070	965
427	660	2.468	900
829	605	8.780	690
Flexural Strength parameters for SiC			
T		**Flexural Strength**	
°C		*MPa*	
20		450	
1300		560	

Table 5 – Summary of material properties at room temperature (20°C).

Property at room temperature	**Units**	**SiC**	**TZM**
Young's Modulus	*GPa*	450	288
Poisson's Ratio	/	0.14	0.28
Thermal Conductivity	*W/m°C*	240	116
CTE	$10^{-6}/°C$	1.8	5.2
Density	kg/m^3	3210	10220
Specific Heat Capacity	*J/kg°C*	708	272
Strength	*MPa*	450 (Flexural Strength)	965 (UTS)

3.4 Benchmarking of material models

For both materials considered in this chapter, the experimental setup in the MultiMat experiment comprised of a target station holding four specimens in series, with dimensions of 10×10×247 mm^3. No coatings were present for the specimens considered.

3.4.1 Beam Parameters

During the experiment, each station was exposed to a number of particle beam impacts at increasing deposited energy levels. Additionally, the beam position was altered to incorporate a combination of grazing, offset and central impacts. In this section, two shots are studied for each material; one shot having a vertical offset and resulting in no visible damage, and a central shot which lead to the failure of one or more specimens in the target station.

For the initial scenario, a vertical beam offset was studied for the two materials, allowing the analysis of both flexural and longitudinal phenomena. For the SiC line, the shot analysed, indexed as shot 1, was a 12-bunch 300 ns pulse having a total intensity of 1.4×10^{12} protons, a 0.5 mm transverse beam size, and a vertical offset of 0.5 mm. For TZM, a 600 ns shot with 24 bunches and a total intensity of 2.64×10^{12} protons, a 2 mm transverse beam size, and a vertical offset of -2 mm was initially considered, identified as shot 2. In addition to the referenced beam pulses, which as mentioned caused no visible damage to the samples, additional shots were considered. These were believed to have resulted in the failure of the specimens, and are labelled shot 1F and 2F for SiC and TZM respectively. The described pulses and impacts are summarised in Table 6, where σ is the transverse beam size, τ is the thermal pulse duration, N_b is the number of bunches, n_{tot} is the total number of protons, and η_y is the vertical offset. One can note that shot 1F was the shot with highest intensity for SiC, and also the final shot for the material. For TZM, the highest intensity shot in the experimental campaign consisted of 36 bunches at a bunch intensity of 1.169×10^{11} protons, with a beam size of 2 mm and a pulse length of 900 ns. This latter shot was however not included in this study due to the high distortion observed in experimental readings. In Table 6, the vertical offset of the beam is quantified with respect to the defined coordinate system shown previously in Figure 13, and the deposited energy is the average on the most heated specimen.

Table 6 – Shots considered in the study of SiC and TZM samples.

Impact no.	**Material**	**τ**	**N_b**	**n_{tot}**	**σ**	**η_y**	**Peak Deposited Energy**	**Deposited energy on most heated specimen**
		ns	*b*	*p*	*mm*	*mm*	J/m^3	J/m
1	*SiC*	300	12	1.4×10^{12}	0.5	4	2.60×10^{8}	6.80×10^{3}
1F	*SiC*	900	36	4.23×10^{12}	0.5	0	7.85×10^{8}	2.05×10^{4}
2	*TZM*	600	24	2.64×10^{12}	2	-2	2.59×10^{9}	7.72×10^{4}
2F	*TZM*	300	12	1.59×10^{12}	0.5	0	6.29×10^{9}	5.28×10^{4}

Moreover, a note of interest is that shot 2F was the last in a series of shots with escalating bunch intensity, and chronologically occurred before shot 2. The effects of the specimen failure resulting from impact 2F is in fact observable in measurements from strain gauges placed on the fractured specimen in impact 2. Since each shot impacts all four specimens in a target station, following fracture of the second specimen, the remaining samples were still affected normally by ensuing shots, including shot 2. In the case of SiC, when compared

to shot 1, the total amount of energy and the peak deposited energy were both significantly higher in shot 1F. This is not the case for TZM, in which case shot 2F can be seen to have a lower total energy deposited, but a significantly higher peak compared to shot 2.

3.4.2 Numerical Modelling

With reference to equations 21 and 25, calculating the longitudinal and flexural frequency as shown in sections 2.4.1 and 2.4.2, Table 7 shows the analytically calculated first longitudinal and flexural harmonics expected for the SiC and TZM specimens tested in the MultiMat experiment. Calculations are based on a length of 247 mm and a cross-section of 10×10 mm^2, and are evaluated considering material properties at room temperature. When the specimens are in a free-free configuration, it can be seen that the flexural frequency is estimated to be more than double the frequency of a specimen in a simply supported setup.

Table 7 – First flexural and longitudinal harmonics for SiC and TZM specimens, with simply supported and free boundary conditions.

		SiC		**TZM**	
		Simply supported	*Free-Free*	*Simply supported*	*Free-Free*
Flexural Frequency	*Hz*	880	1995	410	930
Longitudinal Frequency	*kHz*	24.0		11.1	

As previously detailed, the experimental setup was simulated with a sequentially coupled thermomechanical simulation, conducted with an implicit finite-element model implemented in Ansys® Academic Research Mechanical, Release 18.1. Energy deposition maps were generated with FLUKA [122]. FLUKA provides the nodal energy deposition for a specimen impacted by a single proton. This is then imported in ANSYS and scaled to the impact's total particle intensity. The energy deposition, modelled as an internal heat generation, is the input for the thermal simulation, which is performed to calculate the temperature distribution in a specimen. During impact, a high energy density results in dense materials with a high atomic number, such as in the case of TZM. Comparatively, materials having a lower stopping power, such as SiC, absorb less energy.

The thermal analysis was made up of two steps, the first encompassing the energy deposition time, which was 300 ns for SiC's shot 1 and 600 ns for TZM's shot 2. The

second timestep modelled the evolution of temperature in the samples after the impact. For both materials, a load step lasting for approximately three flexural oscillations was implemented.

The mesh size for the thermal analysis was set to precisely capture the energy density map generated by FLUKA simulations. For SiC, the mesh consisted of 25 longitudinal divisions, 81 divisions in the X-direction, and 41 divisions in the Y-direction, with reference to the previously defined coordinate system. This resulted in a total of 83025 elements with 351508 nodes. Likewise, for TZM the mesh consisted of 41, 21 and 50 divisions in the X, Y, and Z coordinates, resulting in a total of 43050 elements with 184308 nodes.

Figure 40 and Figure 41 show the power deposited along the length of the target stations for the two materials. Additionally, the thermal analysis results at the end of the energy deposition are shown, giving the temperature along the length of the specimens. For SiC's shot 1, the third specimen can be seen to be the most loaded in terms of energy deposited. TZM is a much denser material than SiC, and consequently absorbs more energy. This can be seen in shot 2, where for TZM the first specimen in the target station is the most loaded. By equation 20, which calculates the reference longitudinal stress, the wave's amplitude is seen to be a function of the total energy deposited in the specimen. For each material, the respective most loaded specimen was thus considered, maximising the signal-to-noise ratio. The longitudinal temperature lines considered were taken along the beam impact position, that is, at a vertical offset of 4 mm for shot 1 and at -2 mm for shot 2. The amplitude of the longitudinal wave is not a function of the peak deposited energy, which reaches a maximum at a particular location, but rather the total energy. Additionally, the peak energy is not necessarily located on the most loaded specimen, but can be located on another specimen which has a lower deposited total energy. Furthermore, one can observe that various specimens exhibit a temperature gradient along their length. This leads to the resulting longitudinal waves travelling from each end having a differing maximum amplitude. This point is of particular interest when studying potential triggers causing failure in a number of specimens, as discussed in section 3.4.3.4.

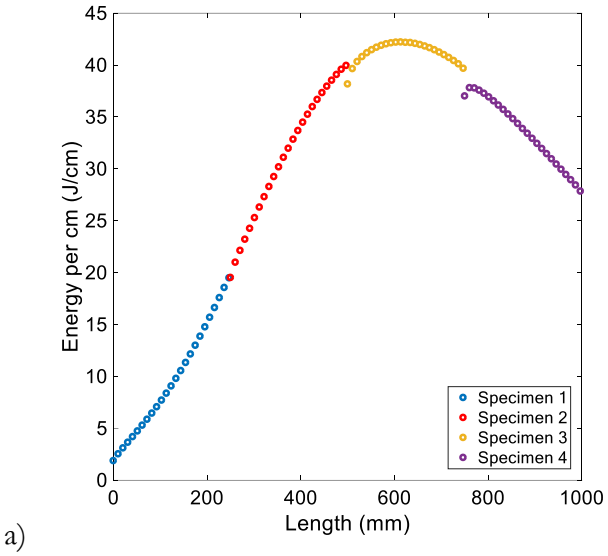

a)

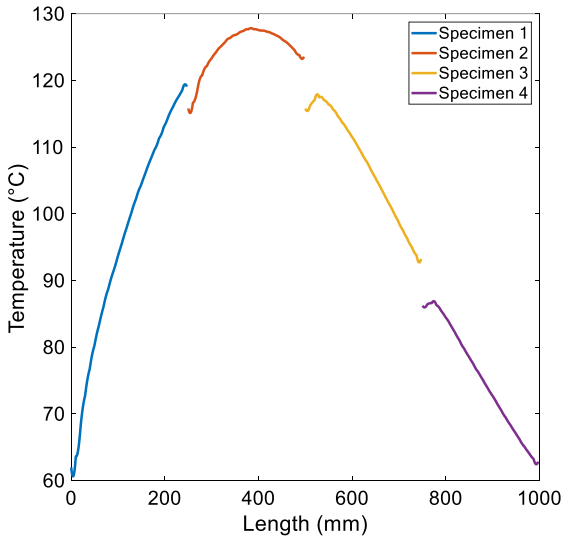

b)

Figure 40 – Power deposited along the length of the target station for SiC for shot 1 (a), and temperature along the length of the target station at the end of the energy deposition (b).

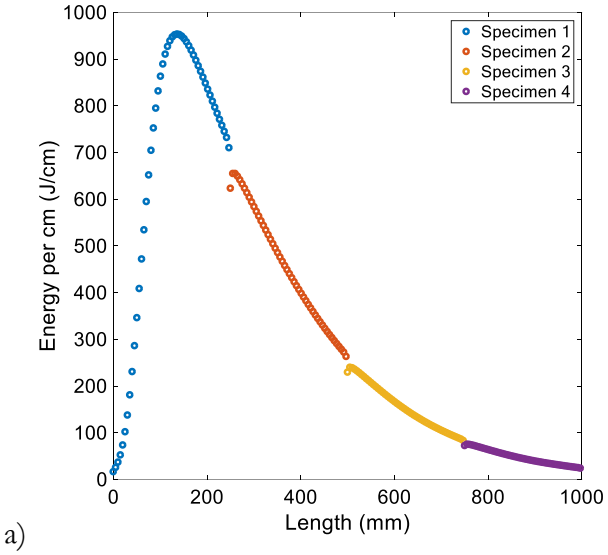

a)

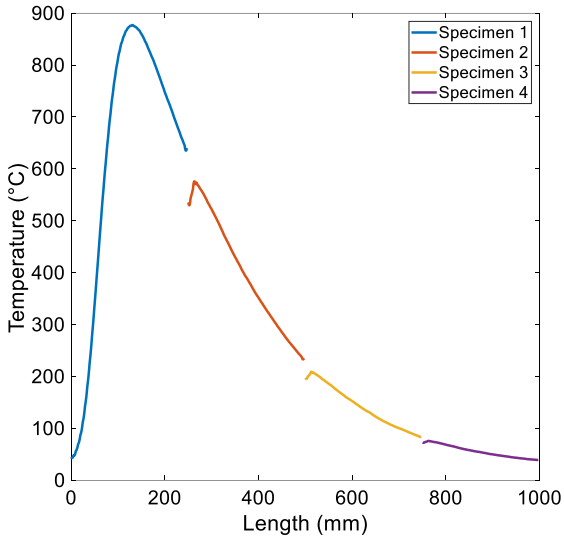

b)

Figure 41 – Power deposited along the length of the target station for TZM for shot 2 (a), and temperature along the length of the target station at the end of the energy deposition (b).

The thermal analysis results at the end of the energy deposition, i.e., at 300 ns for the SiC specimen and at 600 ns for the TZM specimen, for the most loaded specimen of each material, can be seen in Figure 42. In the SiC specimen, a maximum temperature of 118°C is experienced at a length of 26 mm from the front face of the third specimen. On the other hand, a maximum temperature of 878°C is generated in the first TZM specimen, at a length of 130 mm from its front face. For each case, thermal analysis results clearly show the beam out of line from the specimens' central axis. This offset provokes a dynamic flexural response, along with the longitudinal wave generation induced by the rapid beam impact.

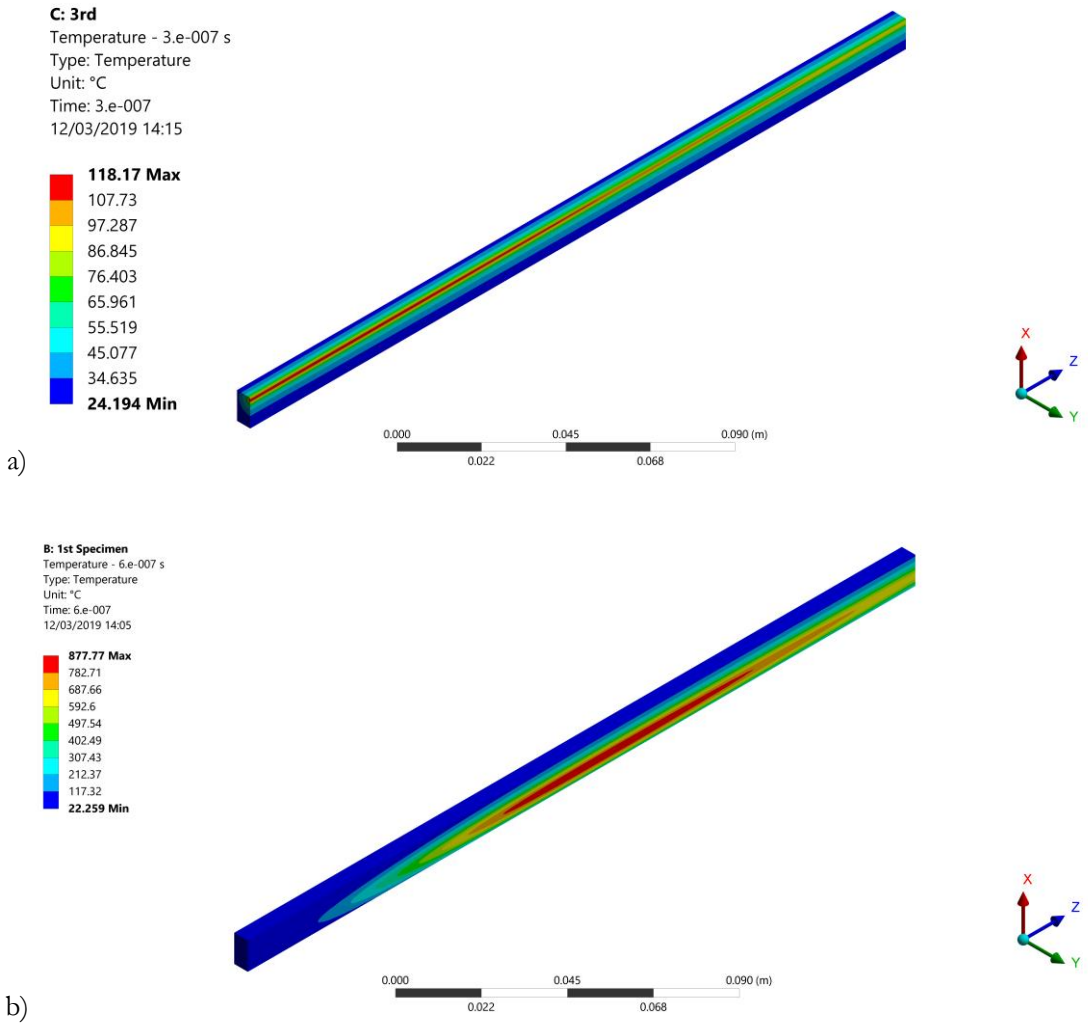

Figure 42 – Temperature profile at the end of the energy deposition in the third SiC specimen for shot 1 (a) and for the first TZM specimen for shot 2 (b).

The temperature field generated from the thermal analysis was imported in the structural analysis. This included three computation steps, the first of which modelled the deposition of energy and comprised of ten substeps. The second step modelled the dynamic longitudinal response, while the third step attempted to capture the flexural response. The time step for each phase was set accordingly to resolve each phenomenon of interest. A summary of the time interval and substep duration implemented in thermal and structural analyses is shown in Table 8. As a starting point, the substep duration was set to 1/500th of an axial wave time period to resolve the propagating axial waves. A substep equalling 1/100th of a flexural wave time period was used for flexural oscillations.

Table 8 – Summary of step time and integration time implemented in thermal and structural analyses.

	Thermal Analysis			
	SiC		**TZM**	
	Step End Time (s)	*Substep Duration (s)*	*Step End Time (s)*	*Substep Duration (s)*
Step 1	3.0×10^{-7}	3.0×10^{-8}	6.0×10^{-7}	6.0×10^{-8}
Step 2	3.6×10^{-3}	2.4×10^{-5}	6.3×10^{-3}	4.2×10^{-5}

	Structural Analysis			
	SiC		**TZM**	
	Step End Time (s)	*Substep Duration (s)*	*Step End Time (s)*	*Substep Duration (s)*
Step 1	3.0×10^{-7}	3.0×10^{-8}	6.0×10^{-7}	6.0×10^{-8}
Step 2	1.3×10^{-4}	8.9×10^{-8}	2.7×10^{-4}	1.8×10^{-7}
Step 3	3.6×10^{-3}	1.2×10^{-5}	6.3×10^{-3}	2.1×10^{-5}

For both materials, the structural analysis mesh consisted of 24000 elements with 107701 nodes. The Courant-Friedrichs-Lewy (CFL) condition was adopted to refine the time step, considering the speed of sound in each material and the element size in the direction of interest, depending on the expected wave phenomena to be observed.

The CFL condition essentially dictates that the time step must be kept at a small enough value so that the signal information propagates through all mesh elements. This implies that if the time step is too long some elements will be omitted, and information is lost. The Courant number is defined by:

$$Courant\ Number\ C = \frac{u\Delta t}{\Delta x} \tag{27}$$

Where u is the velocity of the wave, Δt is the time step and Δx is the mesh interval length in the direction of propagation. A Courant number of less than one is taken to satisfy the convergence criteria [128]. Considering longitudinal wave propagation, the Courant

number for the specified geometric and time parameters, that is, the defined sub-steps and element sizes, is given in Table 9. As can be seen, the convergence criteria were satisfied for both materials.

Table 9 – Values for u, ⊿t and ⊿x for longitudinal wave propagation in SiC and TZM rods with the defined mesh and time-step.

	Units	SiC	TZM
Longitudinal wave speed	*u (m/s)*	11163	5508
Time-step	*⊿t (s)*	8.9×10^{-8}	1.8×10^{-7}
Longitudinal element length	*⊿x (m)*	0.00206	0.00206
Courant Number	-	**0.483**	**0.482**

3.4.3 Benchmarking of Numerical Model with Experimental Results

In this section, the results achieved from thermomechanical simulations are compared against the experimental data acquired from strain gauges positioned on the specimens in the HRMT36 experiment. This was done with the aim of benchmarking and extending the proposed numerical models obtained from available literature.

3.4.3.1 Dynamic Longitudinal Response Analysis

In Figure 43a, the longitudinal strain response for the third (most loaded) SiC specimen for shot 1 is shown. Results were probed at a length of 106 mm on the bottom face of the specimen. The experimental results were imported at a cut-off frequency of 700 kHz. As previously mentioned, the frequencies of interest and their related phenomena, such as transverse, longitudinal and flexural waves, were considered when choosing the cut-off frequency. Additionally, the longitudinal response for the third TZM specimen, for shot 2, is illustrated in Figure 43b. In this case, the results were probed at a length of 165 mm, with a cut-off frequency of 600 kHz. In both instances, the general trapezoidal axial wave shape shown in the analytical model formulated by Bertarelli *et al.* [110], shown in Figure 33, is clearly visible in both experimental and numerical results. These can be seen to agree well in terms of longitudinal frequency for both SiC and TZM materials, as tabulated in Table 10, which shows results for experimental (obtained in MultiMat), numerical (simulated) and analytical (calculated with Bertarelli's equations).

The results achieved suggest that the materials' density and the Young's are reproduced well by the material models implemented, based on the fact that, as shown in equation 21, the longitudinal period is dependent on these two material properties and the rod's longitudinal length. A high noise-to-signal ratio resulted in the heavy distortion of the SiC experimental measurement. This can be attributed to the fact that, for this particular

instance, the longitudinal wave amplitude was an order of magnitude less than the amplitude of the wave travelling in the most loaded TZM specimen. Further filtering was thus employed, to isolate the fundamental frequency of interest from other frequencies.

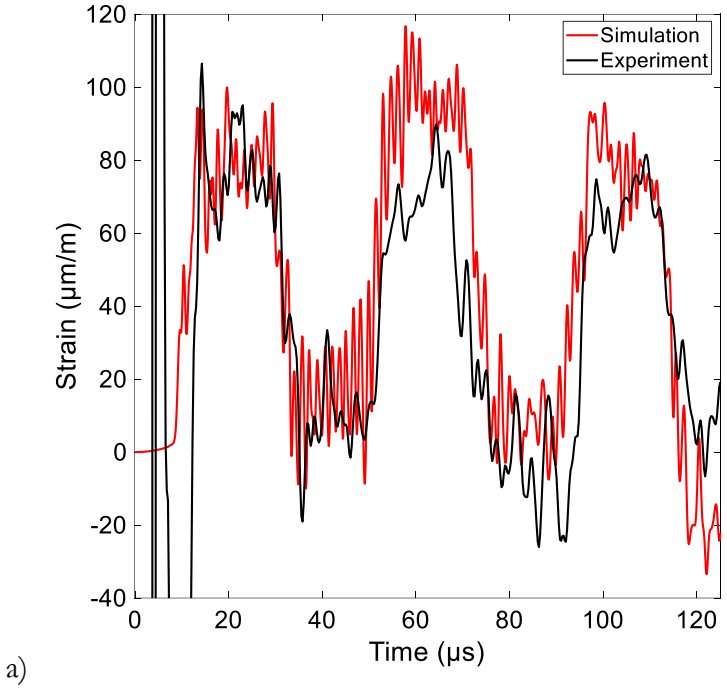

a)

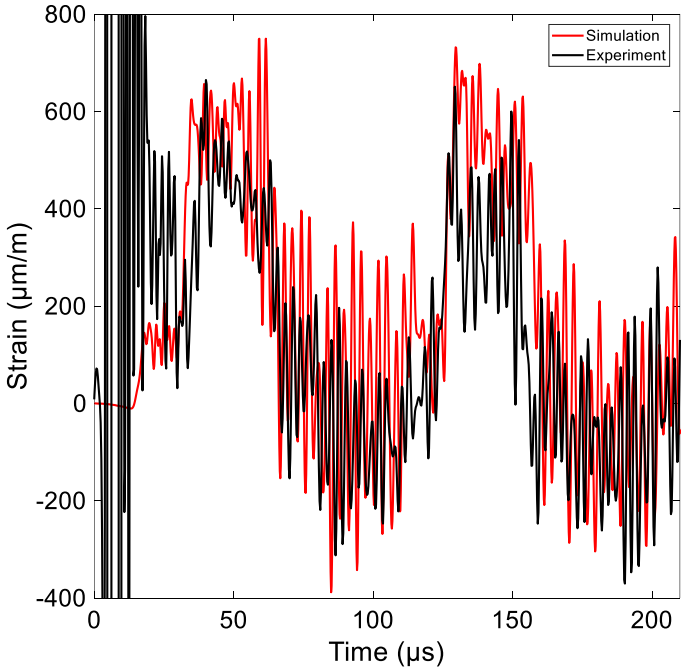

b)

Figure 43 – Experimental and numerical results for axial strain for SiC (a), and TZM (b) specimens.

Table 10 – Longitudinal wave frequencies from analytical, experimental and numerical results for tested and modelled SiC and TZM specimens.

	Units	**SiC**	**TZM**
Experiment	*kHz*	24.0	11.0
Analytical	*kHz*	24.0	11.1
Numerical	*kHz*	23.8	10.5
% difference between experimental and numerical results		0.8%	4.5%

As seen in equation 20, given a particular energy deposition, the amplitude of a longitudinal wave is dependent on the material's Young's Modulus, its coefficient of thermal expansion, as well as the specific heat capacity. For TZM, there is a 4.5% difference between numerically computed and measured experimental frequencies. The discrepancy is a results of the material properties' temperature dependency, which are not included in the material model. An in-depth thermomechanical characterisation campaign has been proposed, given the scarcity of information on the TZM grade studied. The campaign is projected to be performed at CERN facilities, and will serve to support and augment current models. A preliminary impact excitation technique (IET) test was performed on the material at room temperature conditions, from which a Young's Modulus of 320 GPa was calculated, which is significantly different (10.5%) from the value of 288 GPa currently in use.

For TZM, it is also interesting to note that experimental results from the second specimen in the target station returned a longitudinal frequency of 14.5 kHz, contrasting with the 11 kHz calculated from measurements on the other three specimens. This measurement indicated that the specimen fractured during this or a previous impact. This point is discussed in depth in section 3.4.3.4, which details the modelling and analysis of specimen failure.

3.4.3.2 Dynamic Bending Response Analysis

As previously mentioned, numerical modal analyses were carried out prior to the MultiMat experiment to design the support system implemented. Results indicated that the setup behaved in a simply supported manner, with measurements from the MultiMat experiment mostly matching up with this hypothesis. In particular scenarios, including those considered for shots 1 and 2 in this chapter, the flexural frequency probed in the first few microseconds was observed to be comparable to what one would expect from a specimen in a free condition. This phenomenon is believed to be a result of various specimens momentarily

losing contact with the supporting structure, due to the impact from the incoming beam, leading to a free configuration rather than the original simply supported setup. This loss of contact, and the consequent boundary conditions, can be attributed to the supporting spring preload being exceeded once the beam impacts the specimen. This leads to the spring compressing more than initially expected, causing the specimen to lose contact with the rigid graphitic support at the top. The phenomenon observed is shown in Figure 44, which depicts a cross-section of the specimen and supporting spring before and after beam impact.

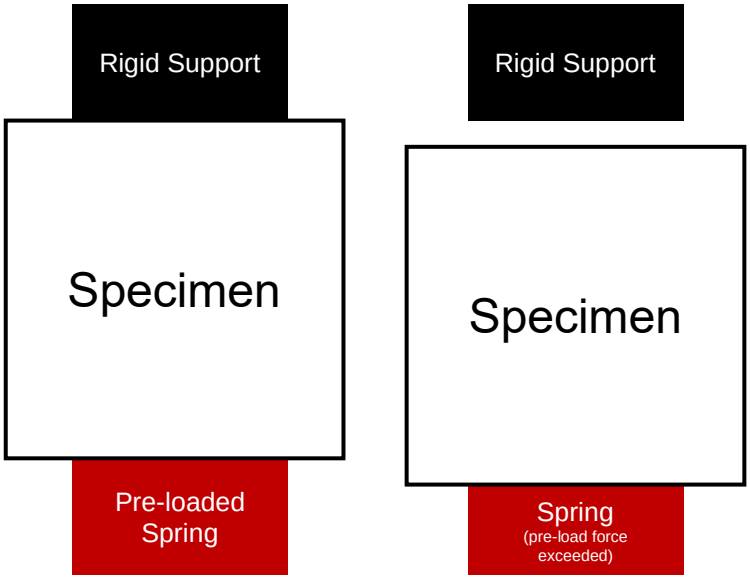

Figure 44 – Specimen in default position (left), kept in contact with the top rigid graphitic support by pre-compressed spring (in red), and specimen after offset beam impact (right), with loss of contact with the top support due to the specimen exceeding the reaction force provided by the spring support, resulting in the compression of the spring.

The described scenario is particularly evident in measurements considered for shots 1 and 2, as demonstrated in Figure 45. For SiC, strain measurements were measured at a longitudinal length of 141 mm from the third specimen's bottom face, while for TZM results were measured at a length of 82 mm from the third specimen. A frequency corresponding to a free condition is observable in the first 2 ms, after which it transitions to a lower frequency. The moment at which the specimen impacted the top support and returned to the design conditions is illustrated by an unexpected disturbance in the measured signal, at around 2 ms. The frequency measured after this point corresponds to a simply supported configuration. Comparably, in the case of TZM, in the initial 5 ms a frequency of 1050 Hz is observable, related to a free condition. The boundary conditions transition to a simply supported configuration, as characterised in subsequent time intervals by a lower frequency.

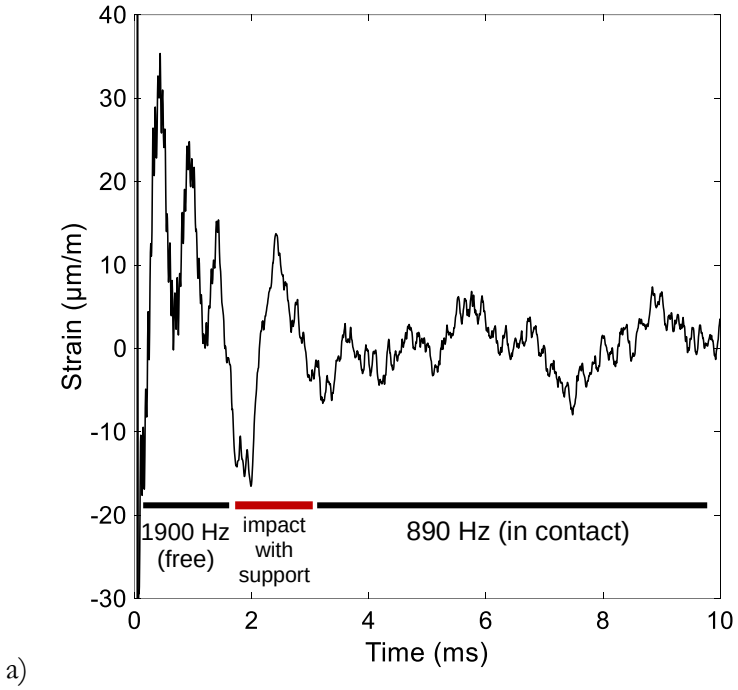

a)

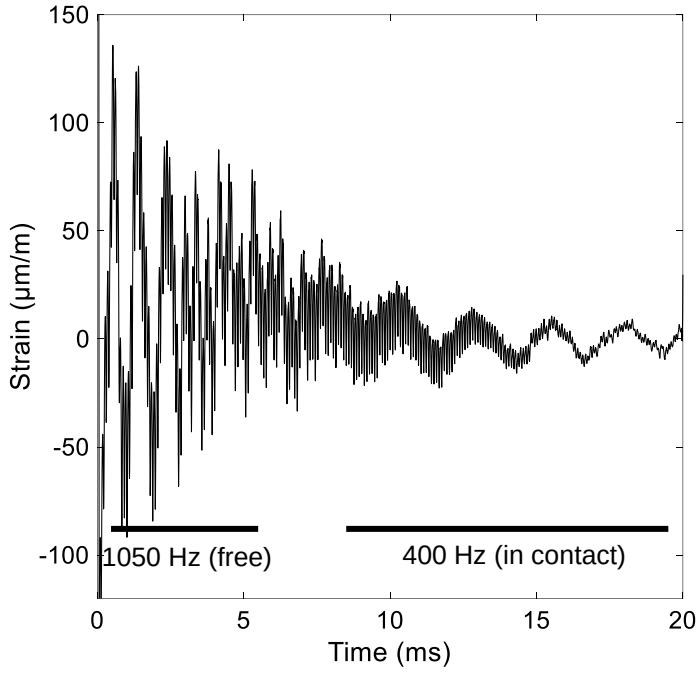

b)

Figure 45 – Experimental results for longitudinal strain exhibiting bending oscillations (superimposed on the longitudinal wave signal) for the SiC specimen (a) and for the TZM specimen (b).

To verify the observed behaviour, the experimental setup was replicated in two numerical models. The first of the two models, implemented in ANSYS, features a simply supported configuration, as implemented in the longitudinal wave analysis. This configuration attempts to replicate the experiment by constraining vertical movement at the bottom edges at the end of each specimen, as shown in Figure 46a. The second configuration, shown in

Figure 46b, attempts to simulate the boundary conditions in a more accurate manner by modelling the loss of contact between the supporting structure and the specimen. A preloaded spring at the bottom edge of both extremities and compression-only supports at the top of the specimen were implemented, simulating the same spring attributes used in the experimental configuration, with a spring preload of 13.57 N. The compression-only support behaves like a rigid constraint, limiting vertical movement beyond the supporting boundary at the sample's top edges. Thus, vertical movement is restricted to the negative X-direction, leading to loss of contact with the top support (i.e., the compression-only support) once the reaction force provided by the preload is surpassed.

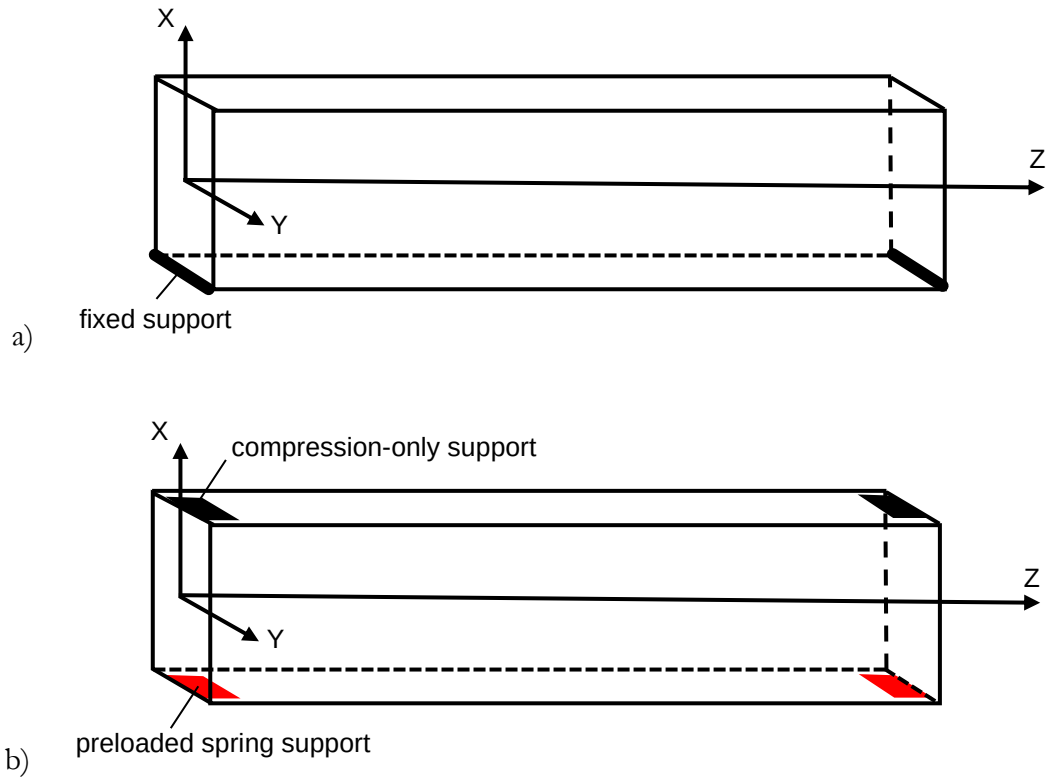

Figure 46 – Specimen model setup for the two configurations, the simply supported setup (a), with bold black edges constrained in X-direction) and the spring-loaded model (b), with compression-only supports in black and preloaded spring supports in red.

Figure 47 shows simulation results for models of the preloaded spring setup, for shots 1 and 2. The results are taken at a longitudinal length of 141.2 mm for the SiC specimen, and at a length of 123.5 mm for the TZM specimen. As can be seen, for SiC, the first millisecond of the signal reveals a fundamental bending frequency corresponding to a specimen in a free condition, resulting from loss of contact between the sample and the upper support. This can be seen to transition to 880 Hz, a frequency related to a specimen in a simply supported setup. Comparably, in the case of TZM, the results at first exhibit a relatively high frequency, once again related to the specimen's free condition. A frequency

of approximately 390 Hz can later be observed (Figure 47b), once the sample settles in its original position. Table 11 provides an overview of the observed and calculated frequencies for the two boundary conditions of interest.

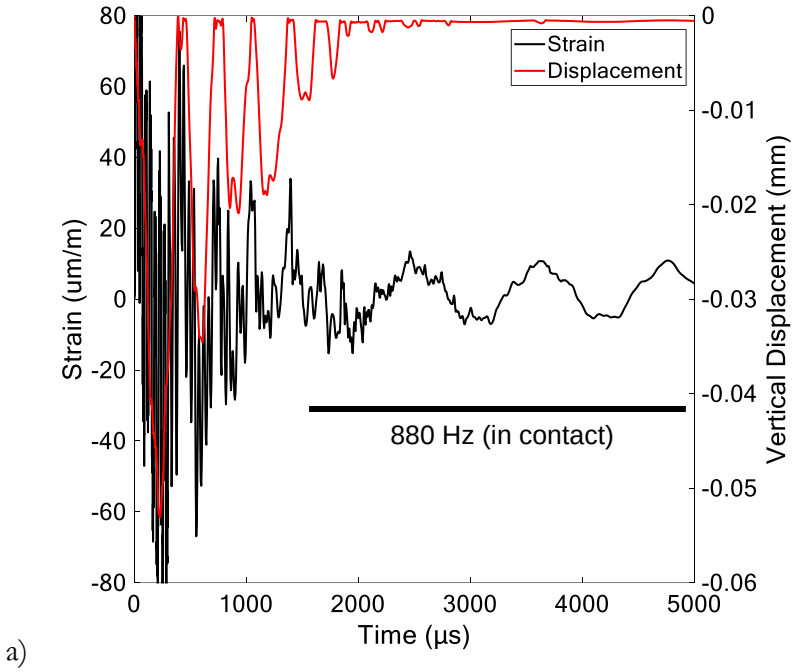

a)

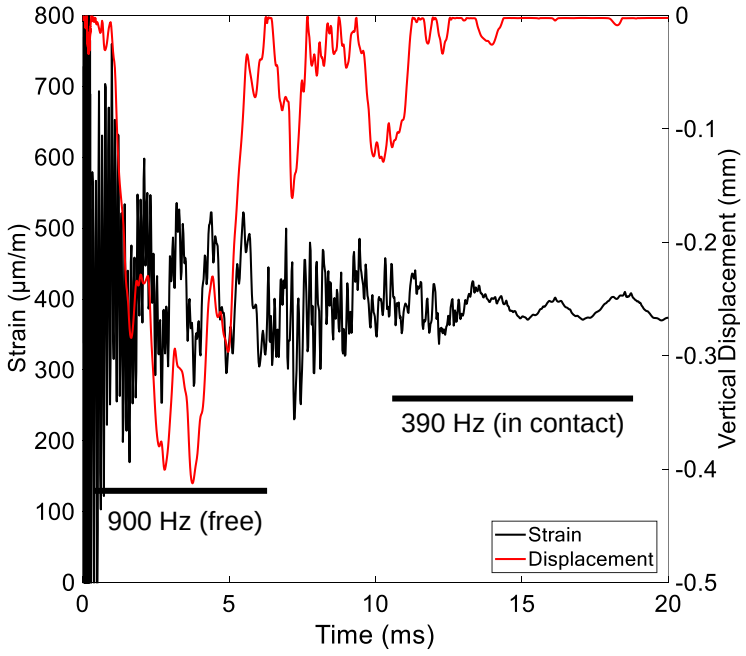

b)

Figure 47 – Numerical results for longitudinal strain showing flexural oscillations (in black) for the modelled SiC specimen (a) and TZM specimen (b) with a preloaded spring model, with superimposed vertical displacement of top edge of specimen (in red).

Table 11 – First flexural frequencies for simply supported and free-free configurations for SiC and TZM specimens from analytical, experimental, and numerical results (implementing the preloaded spring model).

	Units	SiC		TZM	
		Simply supported	*Free-Free*	*Simply supported*	*Free-Free*
Analytical	*Hz*	880	1995	410	930
Experimental	*Hz*	890	1900	400	1050
Numerical	*Hz*	880	2000	390	900

The vertical movement of one of the top edges of the sample is shown in Figure 47, superimposed on the strain signal. A negative measurement relates to the edge and the top support losing contact, thus indicating that the spring preload was exceeded. This leads to the spring compressing beyond its designed configuration. In both cases, one can see that there is loss of contact as soon as the beam impacts the material, which precedes a phase of transition where at various points contact is momentarily re-established. For both materials, the sample eventually falls back to the design configuration. At this point, there is essentially no displacement in the vertical direction.

A free-free configuration is observable in the initial 1 ms of the SiC signal, characterised by a negative vertical displacement and a flexural frequency equal to 2 kHz. This transitions to 880 Hz, a frequency once again relating to a simply supported structure. A frequency of 900 Hz was measured for TZM in the initial 6 ms, which shifted to 390 Hz. At this point in time, the vertical displacement converges to zero.

3.4.3.3 Internal Damping Effects

As observed in Figure 45, the experimental signal also exhibited wave attenuation, which can consist of internal material damping, but can also include external damping as a result of frictional effects with the supporting structure. Physically, damping is usually classified in one of three categories: viscous damping, a result of vibration in a fluid, caused by dissipation of energy due to the resistance caused by the surrounding fluid; coulomb / frictional damping, a result of sliding between two dry surfaces, a function of the normal force and the coefficient of friction; and hysteretic / structural damping, due to energy absorption and dissipation within the material itself, commonly observed in polymers.

In finite element software such as ANSYS, a damping matrix can be introduced for use in transient or harmonic analyses, which is scaled by mass (α) and stiffness (β) coefficients.

Rayleigh damping is the most common form of numerical damping and mass damping (representing frictional damping) is generally ignored. The material damping behaviour can thus be evaluated by considering the β damping parameter [129].

It is important to note that only one value of β can be input in a load step, and therefore the most dominant frequency active must be identified to calculate this value. The application of Rayleigh damping at a particular frequency thus results in the damping of both higher and lower-frequency vibrations, including noise and frequencies which may still be of interest. This, while allowing for the simulation of damping in the frequency of interest, can result in significant discrepancies between simulated results and measured values, as can be observed in the following results.

The stiffness-proportional damping constant can be defined by $\beta = \frac{\zeta}{\pi f}$, where ζ is the Rayleigh damping ratio and *f* is the frequency being considered. The logarithmic decrement δ of two successive peaks can be found from the experimental signal, thus permitting the calculation of the damping ratio [129]. The logarithmic decrement can be found by:

$$\delta = \frac{1}{n} \ln \left(\frac{x(t)}{x(t + nT)} \right) \tag{28}$$

Where *n* is an integer indicating the number of successive positive peaks, *x(t)* is the wave amplitude at a time *t*, and *x(t + nT)* is the amplitude at *n* periods from time *t*. The damping ratio can thus calculated by:

$$\zeta = \frac{1}{\sqrt{1 + \left(\frac{2\pi}{\delta}\right)^2}} \tag{29}$$

For the experimental measurements being considered, for SiC, a damping ratio of $\zeta = 0.08$ was calculated when considering the logarithmic decrement of the flexural signal. Likewise, a damping ratio of $\zeta = 0.05$ was calculated for TZM, considering experimental measurement. The calculated values were applied in numerical analyses similar to those previously described. The results were benchmarked with the observed damped response seen in the experiment. Figure 48 compares the calculated numerical results including Rayleigh damping with experimental measurements, showing a time period where the boundaries conditions had stabilised to a simply supported configuration, as opposed to

the free condition observed in the early stages of wave propagation. Results were probed at a length of 148 mm for the SiC specimen, and at 82.3 mm for the TZM specimen modelled. The damped numerical signal was consequently scaled with the measured results. As previously mentioned, the inclusion of Rayleigh damping at the bending frequency leads to the exclusion of additional high-frequency components, such as transverse or longitudinal effects. This results in numerical results having significantly different characteristics when compared to experimental results. However, one can see that the average stress value is correctly computed. The method described can also be applied to modelling damped longitudinal vibrations in the case of shots with no offset.

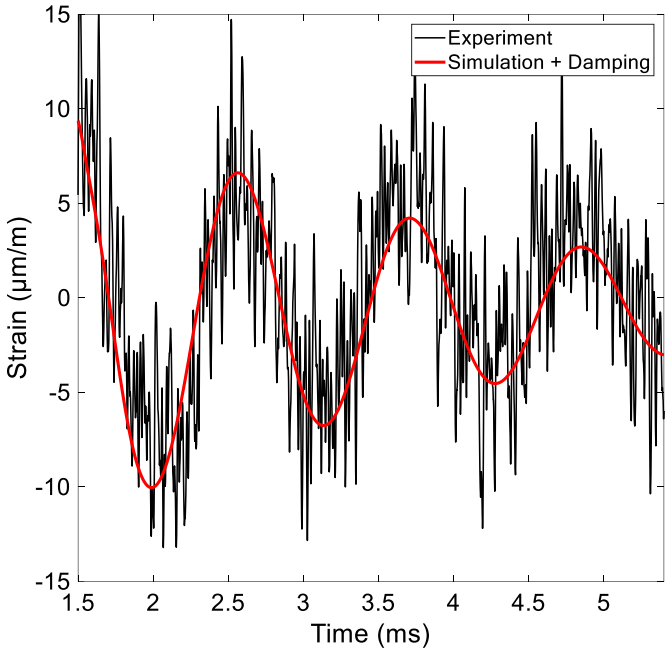

a)

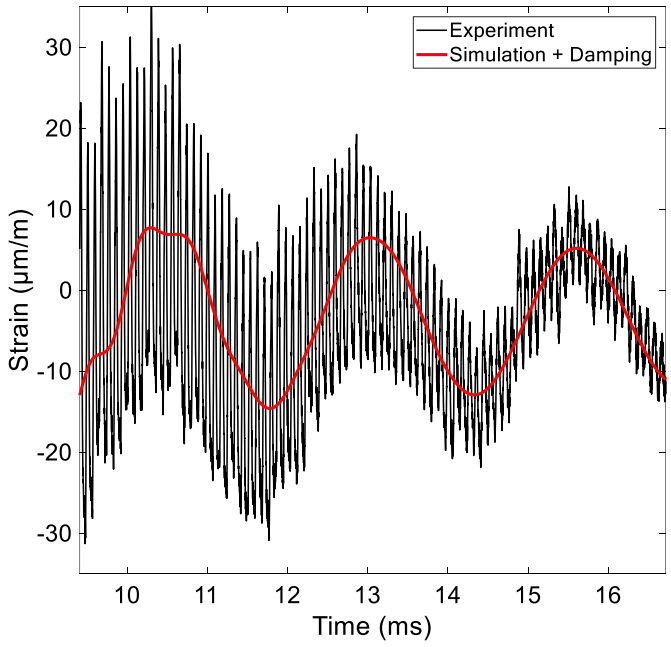

b)

Figure 48 – Comparison of experimental and numerical flexural oscillations for the second SiC specimen (a) and the third TZM specimen (b), following the implementation of Rayleigh-damping.

3.4.3.4 Failure of SiC and TZM specimens

As discussed earlier in this thesis, specimens for both SiC and TZM showed evidence of failure. For SiC, the last pulse impacting the material, that is, shot 1F, consisted of a central shot with 36-bunches and a pulse length of 900 ns, 1.175×10^{11} protons per bunch, and a beam sigma of 0.5 mm. The shot lead to the failure of two specimens, namely the second and third specimen, shown in Figure 49. These were correspondingly the first and second most loaded specimens in terms of deposited energy. Specimen 2 had two cracks at approximately $¼^{th}$ and $¾^{th}$ its length, while specimen 3 experienced a number of cracks along its longitudinal length. Indication of brittle failure can also be observed for TZM. This was caused by a pulse of 12 bunches having a bunch intensity of 1.325×10^{11} protons, a pulse length of 300 ns, a beam sigma of 0.5 mm and with no vertical offset, that is, shot 2F. In this case, a crack can be seen at a distance of 185 mm from the front face of the second specimen.

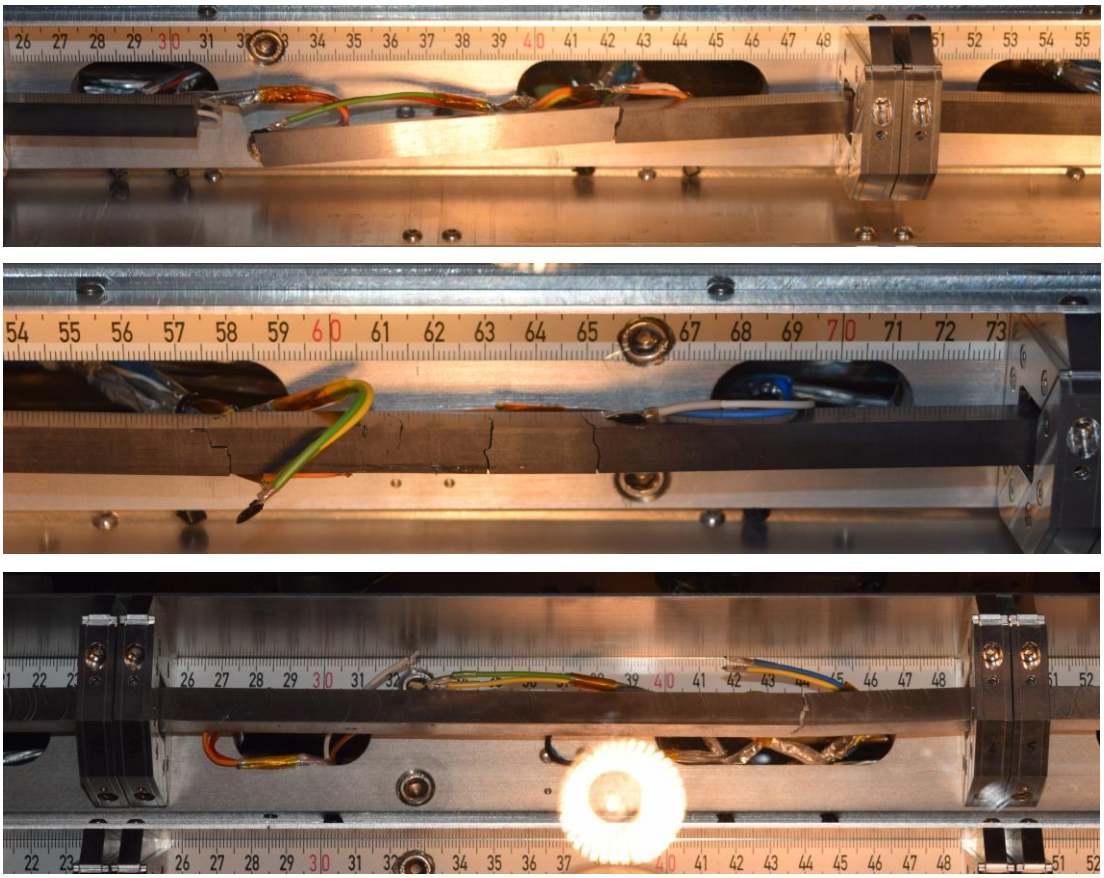

Figure 49 – Fractured SiC specimens 2 (top) and 3 (middle) and fractured TZM specimen 2 (bottom).

The fractured TZM specimen, that is, specimen 2, which was also the second most loaded in terms of deposited energy, can be seen in X-ray tomography results discussed later on in this chapter. The scans additionally exposed a number of internal cracks in the most loaded TZM specimen. Despite the extensive damage in its interior, no evidence of this can be seen when inspecting the specimen by standard means.

Images taken following the experiment clearly show specimen failure. However, as discussed, the fact that a number of samples broke during the experiment can be inferred from experimental results. A specimen fracturing in two or more pieces clearly has an effect on measurements, due to the phenomena and associated time scales of interest being related to the longitudinal dimension. The longitudinal frequency can be used to determine a specimen's length upon failure, since once a specimen breaks it still has free boundary surfaces at which longitudinal waves are reflected, allowing uninterrupted propagation. The same reasoning cannot be applied to bending oscillations, for which failure results in complex boundary conditions. If a specimen breaks into two pieces, one end will be supported by the preloaded setup previously described, while the other end will be free.

As detailed, for SiC failure occurred in two specimens, as shown in Figure 49. From experimental results, one can deduct that this failure was a result of the last impact for the station, that is, shot 1F. The third SiC sample fractured in a number of longitudinal locations, while the second broke in a symmetrical fashion at $¼^{th}$ and $¾^{th}$ its length. The specimen can be seen to have fractured into three distinct sections, with the two ends each being roughly 61.8 mm long (that is, $¼^{th}$ the specimen's initial length) and the inner section being 123.5 mm long. With the specimen at its original dimensions, the longitudinal frequency is theoretically 24 kHz when considering analytical solutions with material properties at room temperature. In the same conditions, the resulting lengths following failure lead to a frequency of 96 kHz for the shorter parts and 48 kHz for the middle section of the specimen. One should note that, for the specimen of interest, strain gauges were conveniently located at lengths of 49.4, 98.8, 148.2 and 197.6 mm along the specimen, that is, one gauge on each of the shorter ends of the fractured specimen, and two gauges on the middle section.

Specimen failure was once again simulated in the implicit code Ansys® Academic Research Mechanical, Release 18.1, by employing element birth and element death events. The code provides the option of eliminating specific elements or contact surfaces based on computed results, such as a specific value of equivalent stress, or at a particular sub-step. This permits

for the modelling of specimen failure at a particular time instance, or when a limiting value is reached. The element death function was thus executed in ANSYS and used to eliminate (by reducing the selected elements' respective stiffness matrix contribution to zero) two slices of elements at longitudinal lengths of 61.8 mm and 185.3 mm, as observed in post-irradiation images shown in Figure 49, at a particular point in time. The longitudinal positions at which the model was sliced are shown schematically in Figure 50, marked A at 61.8 mm and B at 185.3 mm. The four strain gauges and their position on the specimen are also indicated. Another approach to simulating failure is to use contact elements and partition the specimen in three individual parts, again with two slices at a length of 61.8 mm from each end, and a middle part with a resulting length of 123.5 mm. In this case, a bonded contact is first applied to the pre-sliced sections. The contact surface is then removed at the time corresponding to failure. The two described methods, i.e., element and contact killing, were implemented, with a similar outcome achieved in both cases.

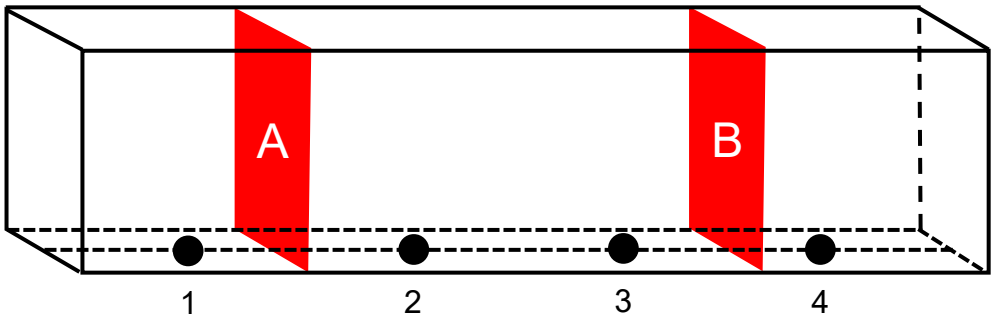

Figure 50 – Location of fracture (A and B) and strain gauges (1, 2, 3, and 4) on the SiC specimen.

Figure 51 shows the longitudinal strain measurements for the probe at 98.8 mm, i.e., strain gauge 2, plotted along with the simulation results employing element death at 20 µs. The experimental signal is seen to heavily distort at 20 µs, after which a frequency of around 47 kHz was measured. This corresponds to a specimen with half the length of the original. The simulation replicates the new longitudinal frequency adequately, with a frequency of 47.5 kHz once failure occurs, corresponding to the new length following failure. Difference in amplitude can be observed between experimental and numerical results. The simulation is seen to retain the wave's previous amplitude, and does not account for energy lost in the process of failure.

For shot 1F, thermal analysis results for the second SiC specimen showed that it experienced internal temperatures varying from room temperature up to a maximum of 316°C. At this temperature, the flexural strength of the material is in the order of 475 MPa,

assuming a linear fit between the two available data points. In structural analyses conducted, the computed equivalent stress can be seen to reach up to 480 MPa, indicating that the material's internal stress exceeded its strength limits. The flexural strength referenced was found in a static 4-point bending experiment, however one should note that in experimental results, strain rates were in the order of 500 s^{-1}.

As briefly discussed in previous sections, it is believed that in this particular scenario, failure was a result of the propagating longitudinal waves, travelling from the two rod ends, hence the symmetrical nature of failure. It has, however, proven difficult to determine the exact cause for failure occurring at these particular locations (at ¼ the rod's length), instead of at a location closer to the two extremities.

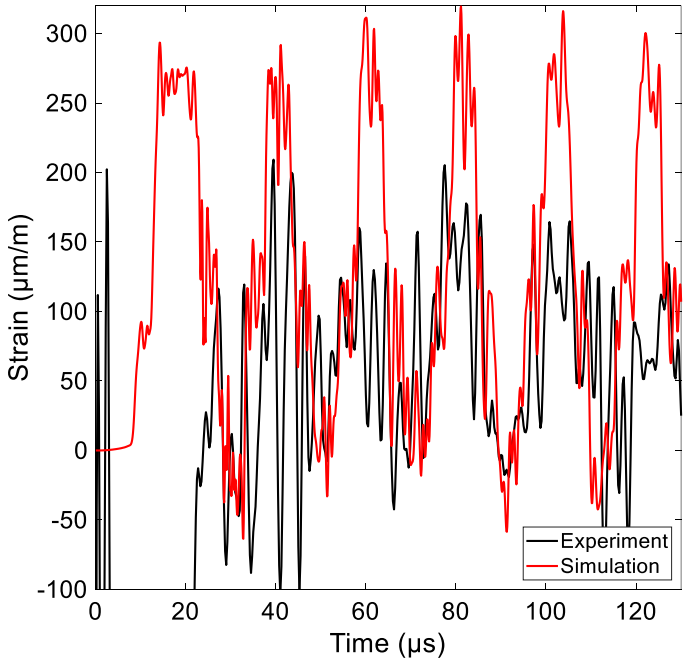

Figure 51 – Comparison of experimental results from the strain gauge at 98.8 mm for SiC specimen 2 with numerical model simulating failure at 20 μs.

For TZM, a change in longitudinal frequency is observed in both shot 2F, which caused the specimen's failure, and in succeeding shots, such as in the previously reviewed shot 2. Similarly to what was seen for SiC, the measured longitudinal frequency at various points on the fractured specimen was higher than that expected, that is, the frequency measured from the other undamaged specimens (having a length of 247 mm). As discussed, this frequency relates to the new length of each specimen portion subsequent to its failure. In this case, the specimen was observed to have broken at a distance of around 185 mm from the left-hand side, leading to it being broken in two seperate parts of 185 mm and 62 mm length.

Following failure, strain gauges on each separate piece of the specimen are therefore expected to measure a longitudinal frequency of 14.5 kHz and 45 kHz for each respective length. The TZM specimen had four strain gauges positioned along its length, similar to the SiC specimen discussed previously. Two strain gauges were positioned on the bottom face of the specimen at longitudinal lengths of 148.2 and 197.6 mm respectively, i.e., on opposite sides of the point of failure. Their position is shown schematically in Figure 52, marked 3 and 4, along with the two other strain gauges and the point of failure, marked A. Figure 53 shows the experimentally acquired longitudinal strain signal for the second TZM specimen for shot 2F, measured from gauge 3 at 148 mm, and gauge 4 at 198 mm. In other words, the two strain gauges of interest are positioned on the left-hand and right-hand sides of the failure point respectively. One should note that, for the specimen in question, there was a temperature gradient along the longitudinal axis, resulting in longitudinal waves propagating from each extremity of the rod having differing amplitudes. The right half of the rod, i.e., the part on which gauge 4 is located, had less energy deposited and therefore, prior to the time of failure, the wave initially originating from this extremity had a lower amplitude compared to that originating from the left end of the specimen.

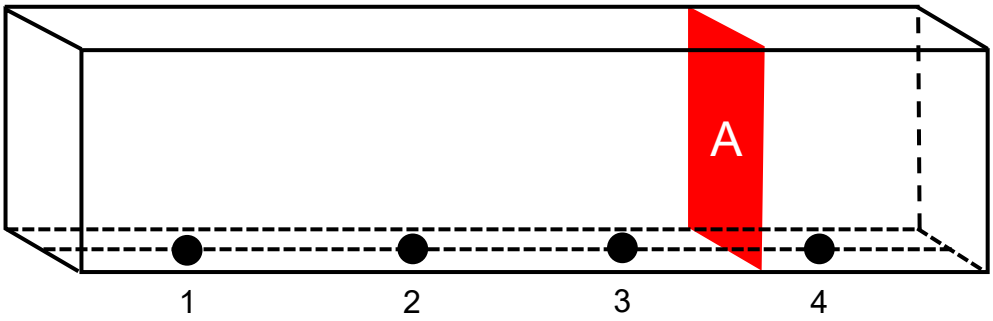

Figure 52 – Location of fracture (A) and strain gauges (1, 2, 3, and 4) on the TZM specimen.

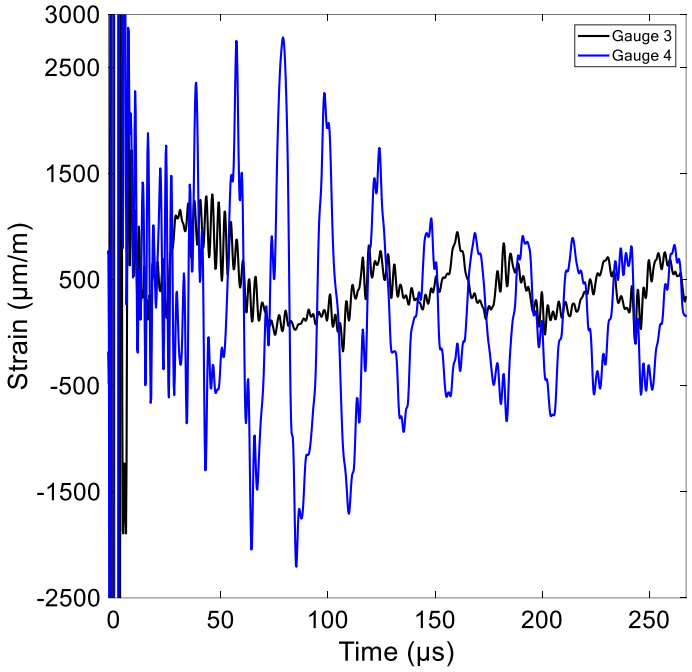

Figure 53 – Experimental results for the second TZM specimen for shot 2F.

The longitudinal wave period for the rod with original length of 247 mm, which was measured in results for unbroken specimens, is approximately 90 μs. As can be seen by the change in frequencies in the experimental signals shown in Figure 53, the specimen fractured at a point in time which is significantly shorter than the time it takes for the longitudinal wave to propagate across the sample and returns to the originating location. Considering that the fracture location is at a longitudinal length of 185 mm, while the speed of sound in TZM is roughly 5500 m/s, following the beam impact, the longitudinal wave with smaller amplitude travelling from the edge nearest to location of fracture (that is, travelling from the right-hand end) takes 11 μs to cross 62 mm of material and reach this point. Similarly, the high-amplitude wave travelling from the left-hand end requires 34 μs

to reach the same location. As shown in Figure 53, the signal measured by strain gauge 4 has a larger amplitude compared to the wave probed at gauge 3. Additionally, the measured signal's frequency reveals the new length for this part of the specimen following failure (62 mm for the specimen portion on which gauge 4 was situated).

An element death event was implemented once more in a thermomechanical analysis, and used to eliminate a elements at a longitudinal length of 185 m. Employing this method, two situations were modelled:

1. Specimen failure at 11 μs at the onset of the lower-amplitude right-hand wave arriving; and
2. Specimen fractures at 45 μs into the simulation, following the arrival of the higher-amplitude left-hand wave.

The results for the two simulated conditions, probed at lengths of 148 mm and 198 mm, are shown in Figure 54. In the case of failure occurring at 11 μs, the high-amplitude wave can be seen to never reach gauge 4, a result of the sample failing prior to the wave making it to the failure location. Results displayed in Figure 54a show a wave with a relatively small amplitude calculated at the probe modelling gauge 4, varying from the measured scenario demonstrated in Figure 53.

Figure 54b shows the results from the analysis modelling failure at 45 μs. For the initial 45 μs, the results are indistinguishable to those from a model where failure is not included, given that the failure event is only executed at 45 μs. The lower-amplitude longitudinal wave can be clearly seen travelling from the right side of the specimen, eventually reaching the location of gauge 4 at around 11 μs, shown in blue. The maximum stress at this location is reached as soon as the two waves superimpose, when the higher-amplitude longitudinal wave travelling from the left side reaches this position. To model this scenario, the time of failure was set to 45 μs, resulting in waves with two distinct frequencies on each end of the specimen, relative to the length of each fractured piece of the sample. The two frequencies measured/calculated are 14.5 kHz at gauge 3, and 45 kHz at gauge 4. The simulation results probed at gauge 4 for this scenario can be seen to be relatively similar to experimental measurements, when compared to the simulation with failure at 11 μs. This suggests that, in fact, the sample did indeed fail due to the higher-amplitude wave travelling from the left-hand end. This results in a portion of the wave's energy being transmitted to the right-hand side of the sample. The wave is consequently confined to this area, hence the high-

amplitude waveform observed in experimental measurements from gauge 4. The cause of failure of the specimen is thus hypothesised to be a result of a void or defect in the material, which resulted in the specimen only exhibiting failure upon the arrival of a stress wave with a higher amplitude than the wave travelling from the right-hand side.

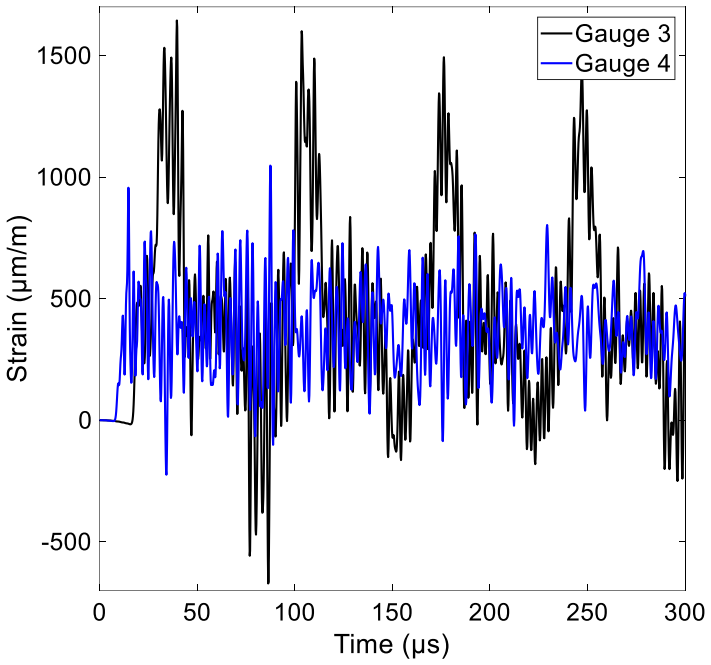

a)

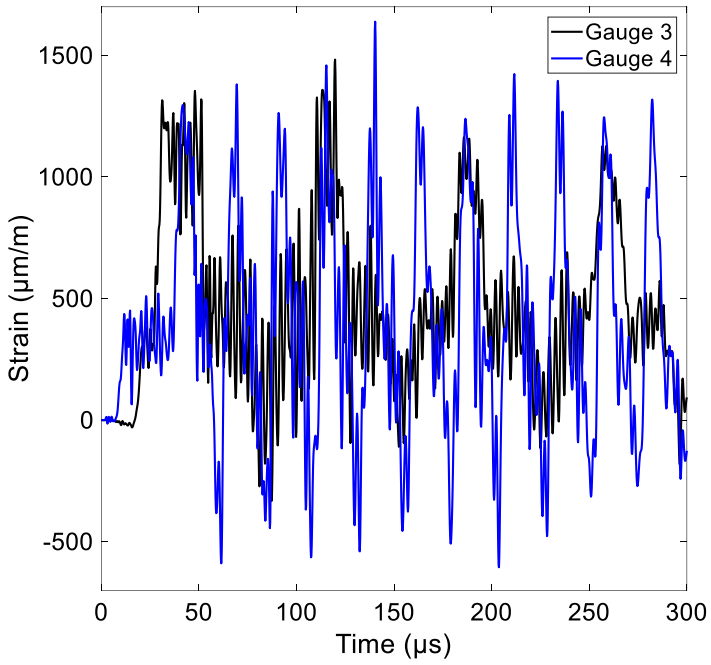

b)

Figure 54 – Numerical results for the second TZM specimen for shot 2F, for scenario 1 [element killing at 11 μs] (a), and for scenario 2 [element killing at 45 μs] (b).

Figure 55 schematically shows the propagation of waves originating from each end of the rod, and how each wave behaves following failure of the TZM sample for the second scenario (failure at 45 μs). The figure at the top indicates the location of each wavefront at 11 μs. At this instance, the wave travelling from the right-hand end reaches the point of eventual failure. The diagram in the middle depicts the location of the propagating waves at 34 μs. At this time, the wave travelling from the left-hand side, which has a larger amplitude, has reached the length of 185 mm, and consequently triggers failure. The final image shows that a portion of the wave's energy is transmitted to the right-hand side of the sample. Subsequently, this end breaks off from the rest of the specimen, while a part of the incoming wave is reflected back at this newly formed boundary. The two strain gauges placed on the specimen at 148 mm and 198 mm are respectively indicated in black and blue.

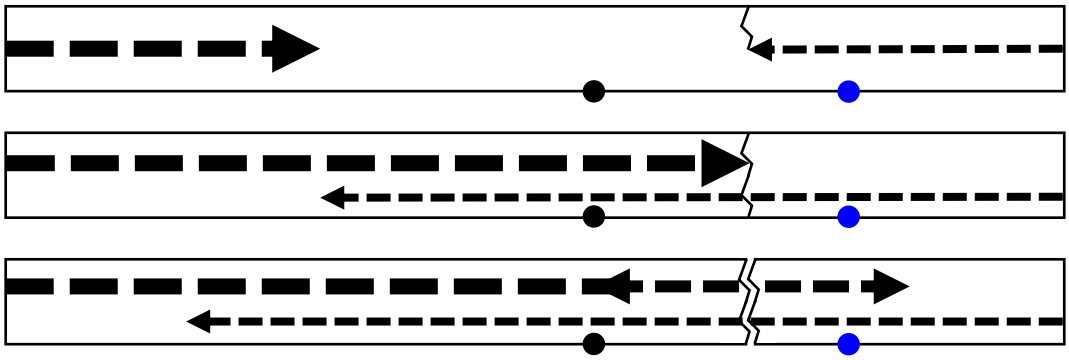

Figure 55 – Left and right-hand side wave propagation along the TZM specimen's length, and its subsequent failure on the arrival of the higher amplitude wave from the left-hand side, i.e., following the hypothesis of fracture at 45 μs as per top right results. Strain gauges 3 and 4 are shown in black and blue respectively.

As discussed, the failed specimen was the second most loaded in terms of total energy deposited, while the most loaded specimen appeared to remain intact upon visual inspection. For shot 2F, simulation results indicate that the most loaded specimen experienced temperatures up to 400°C in its core, whilst the failed specimen reached a maximum temperature of 362°C at the point of failure. By the time the specimen is believed to have fractured, the maximum temperature had already decreased to 200°C in this area of the sample. The relatively low temperature of the second most loaded specimen, compared to the most loaded, results in the specimen being more brittle, due to the material's ductile-to-brittle transition temperature (DBTT). This may have been the reason why this specimen failed, and the most loaded did not. Hiraoka *et al.* studied the ductile-to-brittle transition characteristics of pure molybdenum and molybdenum alloys such as TZM, observing that the DBTT in impact tests was higher than that measured in static tests, signifying that lower loading rates may lead to brittle failure at reduced temperatures [130].

Considering the bilinear kinematic constitutive law for TZM implemented in the numerical analysis simulating the MultiMat experiment, the internal stress in specimens reached 900 MPa, significantly surpassing static yield and UTS figures specified for the material. While the quasistatic strength is surpassed in both first and second most loaded TZM samples, only the second one was seen to fail, indicating that the material model implemented needs additional enhancement, such as inclusion of temperature and strain-rate dependent data. Strain rates in experimental signals measured at 1000 s^{-1}, reaching regimes were material behaviour is believed to diverge substantially from static conditions.

Knowledge on the material's performance at the specified strain-rates is limited, however studies have been performed on the modelling and simulation of the behaviour of pure molybdenum at elevated temperatures and strain-rates. The mechanical response of Mo across a broad range of conditions, including conditions leading to brittle failure, are presented [90], [131]. Given the lack of literature available, the information on pure molybdenum was used as a qualitative benchmark, with the caveat that TZM can display substantially different behaviour at high-strain rates, notwithstanding the relatively minor discrepancies in composition of the two materials. Findings on pure Mo showed that brittle failure can be seen at conditions with low temperatures and high strain-rat [131]. Such conditions are similar to those produced in the HRMT36 experiment in the case of TZM. The results indicate that the tested specimen could have been at conditions consistent with those resulting in brittle failure. In addition to quasistatic tests, additional experimental campaigns, such as one utilising the Hopkinson Bar setup, are therefore required in order to accurately model the material behaviour across a wide range of impact scenarios.

3.4.3.5 Post-Irradiation Campaign

A post-irradiation examination consisting of computed tomography imaging was conducted in the CERN laboratories to assess the condition of material specimens following the impacts subjected to them in the MultiMat experiment, with particular focus on specimens which experienced failure.

As previously discussed, preliminary visual assessment of tested TZM samples in the wake of the experimental campaign indicated that only the second most loaded specimen was damaged. The experimental test-bench was relocated to a storage area upon completion of the experiment, and was accessed at the start of 2019 when the radiation dose rate decreased to safe amounts. This was followed by a post-irradiation X-ray tomography campaign

performed on a number of tested samples. The tests indicated that the most loaded TZM also exhibited various internal cracks, as shown in Figure 56a.

X-ray microtomography has a wide range of applications in a wide array of fields, including in the biomedical [132], and food [133] industries. In material science, the process is widely used for microstructure and failure investigation of ceramics and ceramic-metal composites [134]. The post-irradiation imaging system utilised at CERN's metrology department is a closed X-ray system, i.e., the X-ray scanner is shielded, meaning that X-rays may not escape or leak out as is the case for open systems, and therefore the operator does not require any special protective clothing. The system utilises a cone-beam reconstruction system, utilising an electronic X-ray source and a 2D X-ray detector, as opposed to a 1D detector which is used in fan-based reconstruction systems. This method allows the generation of projection images which are then used to reconstruct the cross-section of the tested specimen. A standard charge-coupled device (CCD) camera is used, focused on the scintillator material which converts X-ray radiation, emitted from the X-ray source across from the detector, into visible light which can be detected and recorded by the camera. Projections are obtained from different angles by placing the specimens on a rotatable table, allowing images to be taken from a 360° angle of view [135]. The images obtained from the microtomography scanner are isotropic, i.e., once the images are obtained it is possible to build up a 3D volume by means of stacking each individual slice taken. This allows the possibility to display the generated volume from different angles of view, rather than being constrained by the angle from which the images are taken. Specialised software is used to generate a volumetric rendering of the subject, made up of a number of volumetric elements (voxels) obtained by sampling the area surrounding each respective voxel [112], [113].

As can be seen in Figure 56a, a long crack is clearly visible along the whole length of the most loaded TZM specimen, along with various cracks across the cross-section. Images from the scans on the second TZM specimen, Figure 56b, clearly show the point of failure, while a top view of the most loaded SiC specimen, shown in Figure 57, allows for a clear view of the various cracks near the centre of the sample.

a)

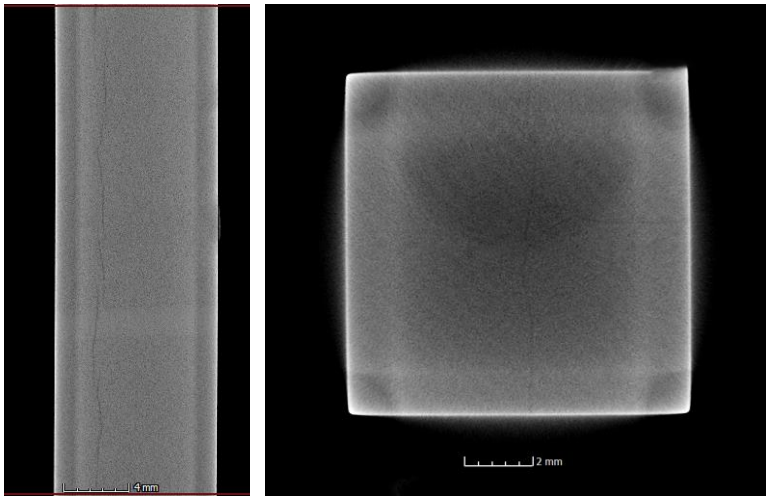

b)

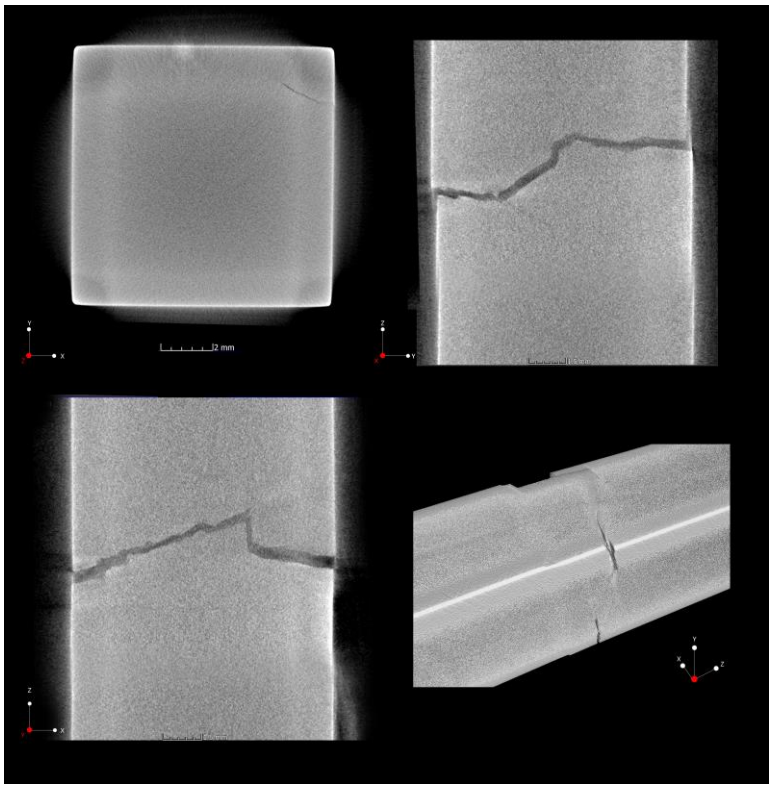

Figure 56 – X-ray tomography scans of the most loaded TZM specimen (a), showing a crack along its length (left) and various cracks across its cross-section (right), and of the second most loaded TZM specimen (b), showing the point of failure from various angles.

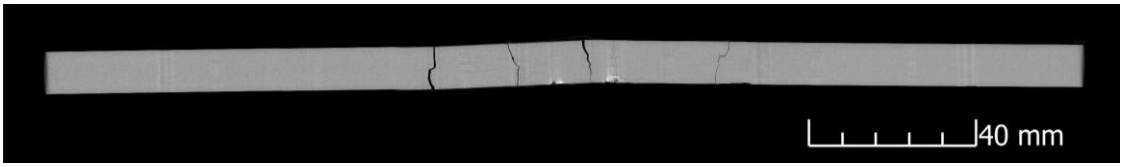

Figure 57 – X-ray tomography scan of the most loaded SiC specimen, showing various cracks near the centre of the sample.

3.5 Summary

This chapter focused on the modelling of Titanium Zirconium Molybdenum and Silicon Carbide, two materials of great interest for application in BIDs such as absorbers and collimators. The material models for the two materials were benchmarked with experimental data detailing the materials' thermal and mechanical response, collected in the MultiMat experiment. The study presented concentrates on dynamic flexural and longitudinal phenomena generated by particle-matter impacts. A number of aspects related to such events are discussed, including the observed frequencies and wave amplitudes of the measured perturbations, effects related to internal damping, and interactions with boundary-conditions. Additionally, instances were material specimens experienced failure are discussed, along with the likely scenario resulting in these conditions.

The experimental setup was simulated by implementing a simply coupled transient thermomechanical finite element analysis implemented in the FEA code Ansys® Academic Research Mechanical, Release 18.1. Energy deposition maps generated in FLUKA were input in thermal analysis to model the resulting temperature field in impacted specimens. This was used as a thermal load in structural simulations modelling the dynamic response provoked. The measured experimental results were found to accurately match the computed longitudinal response when considering the wave's amplitude, frequency and general trapezoidal shape. Offset impacts were similarly modelled to study the flexural response of tested specimens. An accurate portrayal of the complex experimental boundary conditions was simulated. This was deemed as an important aspect to consider, following observations of a different flexural frequency to that initially expected, a result of loss of contact between the specimen and the upper graphitic supports. The preloaded springs and upper (compression-only) supports were thus modelled, and the loss of contact and subsequent variation in bending frequency successfully simulated. Additionally, Rayleigh damping was included in the modelling of bending phenomena.

Lastly, a discussion on the failure of tested specimens was presented, along with simulation results. Element birth and death events were introduced to model fracture in SiC and TZM samples, prompted by longitudinal wave propagation. In some cases, failure was detected in experimental results when the measured longitudinal wave frequencies varied significantly from those expected. SiC specimens were observed to fail in a symmetrical fashion, indicating that this was a result of the passing of longitudinal waves originating

from the two extremities of the rod. The nature of failure, at ¼ the length of the specimen, is not yet fully understood and is proposed as a potential topic of interest for future study of the material. A number of findings related to various specimens, believed to have remained undamaged following preliminary visual inspections, were made as a result of the X-ray tomography campaign conducted following a cooling down period.

A summary of the material models adopted can be seen in Table 12. A combination of properties provided by the manufacturers and found in literature was used. This information proved to be appropriate to effectively simulate a number of experimental scenarios. Strength data available was used as a means of comparison with computed stress results, which revealed that the specified material limits had, in some cases, been exceeded. For TZM, additional temperature dependent mechanical testing and measurements are scheduled to be performed in order to extend the currently available models and validate existing data. IET tests for the estimation of dynamic elastic properties are to be conducted, along with testing for the material's density, conductivity, coefficient of thermal expansion, and specific heat capacity.

For both materials considered in this chapter, failure to include strain-rate related behaviour proved to be the main shortcoming of the models utilised in this study. Robust strength and failure models are thus required to correctly simulate the material response over a wider range of conditions, as experienced by BIDs in nominal and accidental conditions. Consequently, a Split-Hopkinson bar experiment has been proposed to derive dynamic strength behaviour, which will be used to supplement material data from quasistatic tests.

A summary of the study's main findings is shown below:

- The present material models available for the Titanium Zirconium Molybdenum and Silicon Carbide grades assessed in the HRMT36 experiment effectively reproduce dynamic flexural and longitudinal phenomena, when implemented in a simply coupled thermomechanical simulation;
- The dynamic boundary conditions observed in experimental measurements was also successfully simulated, as shown by the modelling of the free to simply supported condition observed in probed measurements;
- The material models currently available for the two materials can be seen to work well for modelling of the harmonic and general structural response of the structure,

but do not simulate or predict failure. Additional characterisation is essential in order to accurately model the material response at elevated temperatures and strain-rates, and effectively simulate failure and spallation.

Table 12 – Summary of material properties at room temperature.

Property at room temperature	**Units**	**SiC**	**TZM**
Young's Modulus	*GPa*	450	288
Poisson's Ratio	/	0.14	0.28
Thermal Conductivity	$W/m°C$	240	116
CTE	$10^{-6}/°C$	1.8	5.2
Density	kg/m^3	3210	10220
Specific Heat Capacity	$J/kg°C$	708	272
Strength	*MPa*	450[13]	965[14]

[13] Flexural Strength.

[14] Ultimate Tensile Strength.

Chapter 4:

Characterisation and benchmarking of CuCD RHP3434

4.1 Introduction

This chapter presents the characterisation campaign conducted at CERN and related analyses of the Copper Diamond grade (CuCD RHP3434) tested in the MultiMat experiment. The characterisation campaign included a number of temperature-dependent measurements for the specific heat capacity, density, coefficient of thermal expansion and conductivity. Additionally, IET tests were conducted for the computation of the material's elastic constants. Testing on a four-point bending setup was carried out for the evaluation of the stress-strain performance of CuCD in elastoplastic conditions. The formulated material model was subsequently applied in a transient thermostructural simulation implemented in an implicit FEA code. Various beam impacts on CuCD specimens from the MultiMat experiment were modelled. Strain gauge and thermal probe measurements from the MultiMat experiment were used to benchmark the material model.

As previously illustrated in section 2.3.4.3, CuCD RHP3434 is a recently developed composite material grade, proposed as the material of choice for application in tertiary collimators in the forthcoming HL-LHC upgrade. Precisely, the material has been chosen as a substitute for Inermet180. The CuCD RHP3434 grade discussed in this chapter was created by RHP-Technology [105]. The material consists of a copper matrix with dispersed diamond particles. The mixture is hot pressed in a spark plasma sintering process [138], [139]. Several binding elements are introduced in the process to form carbides, which aid in binding the diamond particles with the matrix [103].

The CuCD RHP3434 grade comprises of an equal by volume distribution of copper and diamond, and a porosity of 8.4%. The two constituents provide a mix of qualities which make CuCD particularly suitable for application in BIDs. Copper has good electrical and electrical conductivity, whereas diamond contributes to improve thermal conductivity further, while aiding to decrease the material's CTE and density [19]. Copper Diamond is regarded as more robust than Inermet180, and is able to endure higher intensities without succumbing extreme damage [140]. That said, a number of limitations have been identified. The diamond-copper interface has been observed to degrade when temperatures exceed 250-300°C. This is mainly a consequence of the discrepancy in CTE between the two constituents, resulting in diamond particles separating from the matrix and consequently causing a permanent reduction in thermal diffusivity [141]. The temperature sensitivity of

the material is discussed further in section 4.2.4.

4.2 Material Testing and Characterisation

As detailed, a material testing campaign was carried out at CERN[15], in order to develop a material model for the CuCD RHP3434 grade. This consisted of:

- A thermomechanical characterisation comprising of measurements for CTE, conductivity, specific heat capacity and density;
- An IET test, used to calculate the material's dynamic elastic properties;
- A 4-point bending test, for determining the elastoplastic stress-strain response; and
- A temperature sensitivity test to measure the degradation of material temperatures at elevated temperatures.

4.2.1 Thermomechanical Characterisation

A thermomechanical characterisation campaign was conducted, measuring material properties as a function of temperature. Measurements were made for the coefficient of thermal expansion, density, specific heat capacity, and conductivity of the material. The measurements were limited up to a temperature of approximately 300°C, above which the boundary between the diamond particles and the copper matrix was found to degrade irreversibly, resulting in a regression in thermal properties [141].

For the measurement of the linear coefficient of thermal expansion, a Netzsch DIL 402E dilatometer was utilised. Measurements were made for the expansion, in the heating phase, and shrinkage, in the cooling phase, of CuCD specimens. These were made with reference to the ASTM E228-17 standard *"Standard Test Method for Linear Thermal Expansion of Solid Materials with a Push-Rod Dilatometer"* [142], [143]. Measured values for the coefficient of thermal expansion are shown in Figure 58. Note that the error bars shown in this figure and subsequent plots refer to the standard deviation between measurements for different samples. The strain measurement dL/L_0, i.e., change in length with respect to the original

[15] All experiments and measurements were conducted at CERN facilities with remote input from the author. IET test conducted during author's visit to CERN facilities.

length, were conducted in a temperature range between 25°C and 320°C for the heating phase, and from 330°C to 55°C for the cooling phase. The linear CTE is defined as the induced change in the strain, that is, the relative expansion for a given temperature change, and can therefore easily be calculated from the measurements. In total, three samples were tested, and the average result used to characterise the material.

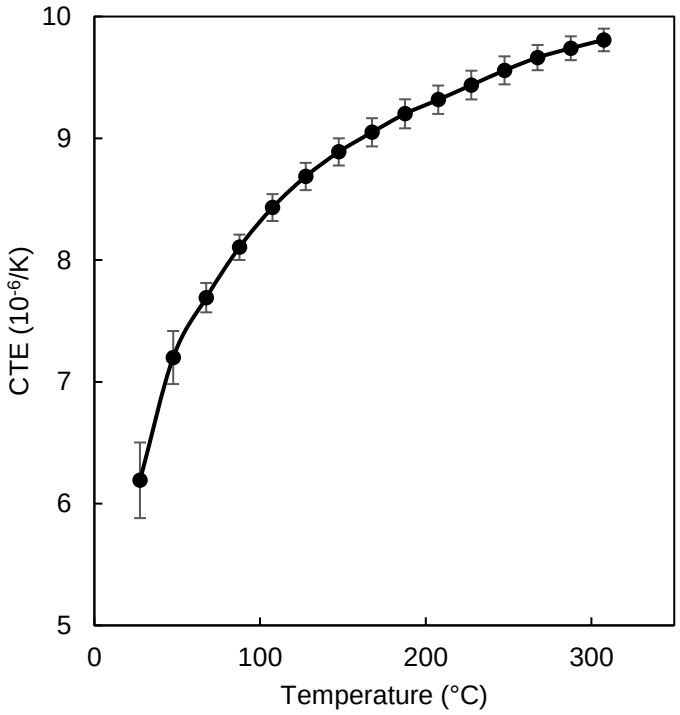

Figure 58 – Linear coefficient of thermal expansion of CuCD RHP3434. Error bars represent standard deviation between measurements on different specimens.

Initial tests for the calculation of density were carried out using the Archimedes principle, where the specimen is immersed in a liquid and its volume is determined by the displacement of liquid. The mass of the specimen can then be measured to calculate the density [144]. Due to the high porosity of the CuCD grade being tested, the alcohol in which the specimen was submerged in infiltrated the material's pores, resulting in an overestimation of the density calculated. The density was thus calculated from measurements of the specimens' dimensions and weight. Three specimens of varying dimensions were measured and weighed, and the results averaged to achieve a final value of density at room temperature (ρ_0), equal to 5700 kgm^{-3}. Taking into consideration the volumetric coefficient of thermal expansion $\beta = 3\alpha$ (where α is the linear CTE), the density can be expressed as a function of temperature by considering temperature-dependent measurements for the coefficient of thermal expansion, as shown in equation 30.

$$\rho\ [kgm^{-3}] = \frac{\rho_0}{1 + \beta(T - T_0)} \tag{30}$$

Where ρ_0 is the measured density at ambient temperature conditions, T is the temperature, and T_0 is the ambient temperature. The measured dimensions and mass of the specimens and the resulting average density are shown in Table 13, while the results for the density as a function of temperature, plotted in Figure 59.

Table 13 – Measured values for specimen dimensions and weight, and calculated density.

Measurement	Units	Specimen 1	Specimen 2	Specimen 3	Average
Thickness	*cm*	0.50	0.50	0.49	0.49
Length	*cm*	2.01	2.01	2.02	2.01
Width	*cm*	1.53	1.52	1.52	1.52
Mass	*g*	8.59	8.59	8.59	8.59
Volume	cm^3	1.53	1.52	1.51	1.52
Density	$\boldsymbol{g/cm^3}$	5.63	5.64	5.69	5.66 ± 0.03 **≈ 5.7**

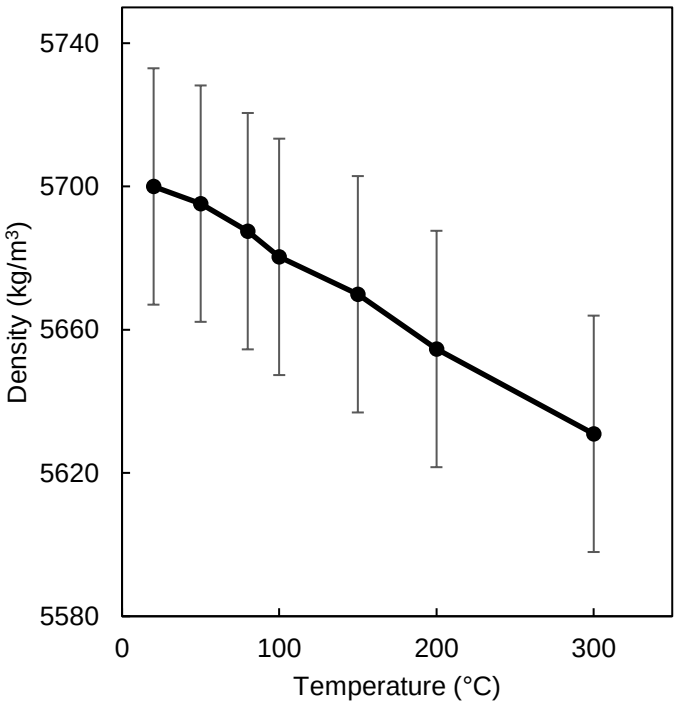

Figure 59 – Density of CuCD RHP3434.

The specific heat capacity was determined via the ratio method [145] with the use of a Differential Scanning Calorimeter (DSC). For each test sample, three measurements were performed, the first test being a "baseline" which records system characteristics and allows removal of the system bias from experimental data. After a repeatable baseline was recorded, a reference material was tested, following which the experimental sample was tested in exactly the same way as the reference [146] [147]. The specific heat capacity measurements for the CuCD RHP3434 grade are shown in Figure 60.

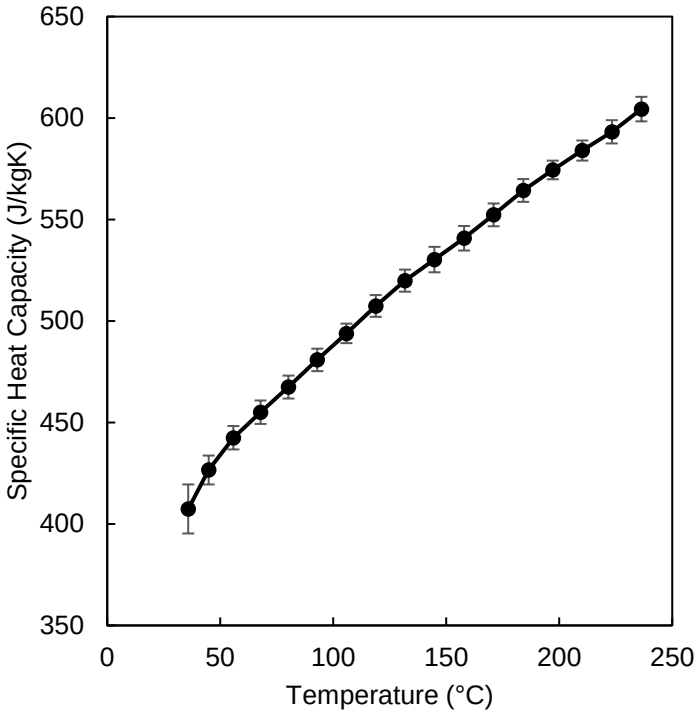

Figure 60 – Specific heat capacity of CuCD RHP3434.

The thermal diffusivity was measured by a Laser Flash Apparatus (LFA), which shoots a short laser pulse onto one of the specimen's faces and measures the temperature on the opposite face with the use of an optical pyrometer. Knowing the specimen's thickness, the thermal diffusivity across a range of temperatures was computed from these readings, following which the material's conductivity was found by multiplying the diffusivity, the density and the specific heat capacity, as shown in equation 31 [148]. The calculated thermal conductivity results are shown in Figure 61.

$$\mathrm{k}\,[Wm^{-1}K^{-1}] = \kappa \cdot \rho \cdot c_p \tag{31}$$

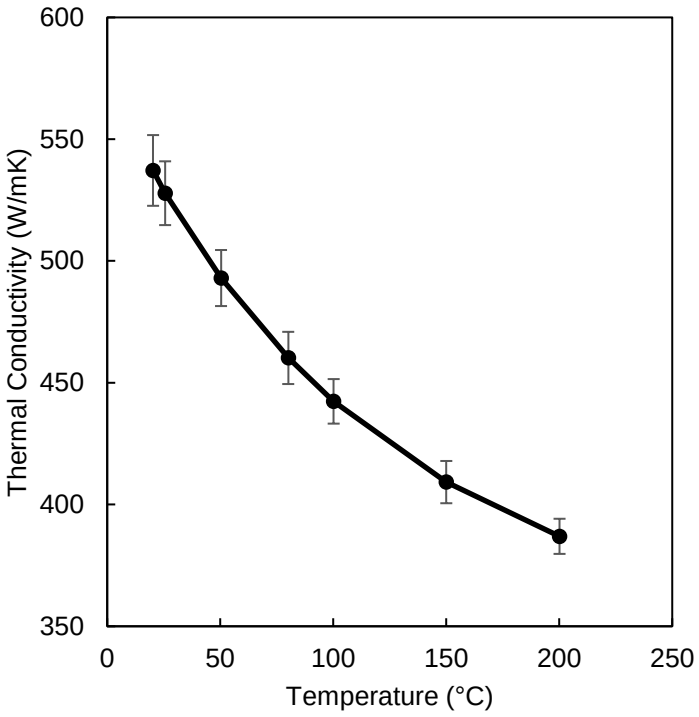

Figure 61 – Thermal conductivity of CuCD RHP3434.

Measured values for the CTE, density, specific heat capacity, and thermal conductivity at room temperature are summarised in Table 14.

Table 14 – CuCD RHP3434 material properties at room temperature.

Property at room temperature	Units	Value	Standard Uncertainty
Density	kg/m^3	5700	± 33
Specific Heat Capacity	$J/kg°C$	407	± 12
Thermal Conductivity	$W/m°C$	537	± 15
Coefficient of Thermal Expansion	10^{-6} °C	6.19	± 0.2

4.2.2 Impulse Excitation Technique

The impulse excitation technique test (IET) is a dynamic, non-destructive material characterisation technique which measures the resonant frequencies of a material specimen at room temperature or at elevated temperatures. The measured frequencies are subsequently used to calculate the material's elastic constants at the tested temperature. Dynamic methods of measurement, such as the IET and ultrasound spectroscopy, provide an advantage over static methods, such as four-point bending tests, due to their relative simplicity and quickness, as well as generally involving small elastic strains. The IET is therefore suitable for refractory metals, ceramics, and particle-reinforced composites,

which tend to be porous and brittle. Additionally, test samples can be very small in size, and the experimental setup can be easily modified for testing properties at high temperatures [149]. The technique can also be used for difficult to grip specimens which cannot be set up in tensile test machines.

The test consists of hitting a sample with a hammer and recording the induced vibration modes by means of a microphone. Alternatively, a piezoelectric sensor, an accelerometer, or a laser vibrometer can be used. The advantage of using a microphone over the former is that it does not need to be in contact with the specimen. The vibrational signal measured in the time domain is converted to the frequency domain by a Fast Fourier Transform (FFT), from which the resonant frequencies can be determined, allowing for the calculation of the elastic properties of the material by considering classical beam theory, by taking into consideration the dimensions at hand.

Different natural frequency modes, or resonant frequencies, can be excited in the specimen, and are mainly dependent on the specimen's geometry and material properties. The specific frequencies which are excited and measured can be controlled by the position of the support wires, the mechanical impulse, and the measuring device. With regard to the elastic properties of the material, the two most important resonant frequencies are the flexural and torsional frequencies, which are respectively dependent on the Young's and Shear moduli, for isotropic materials. The specimen's elastic properties can be calculated by considering the dimensions and geometry, weight, and the measured resonant frequencies, in accordance with the ASTM E1876-15 "*Standard Test Method for Dynamic Young's Modulus, Shear Modulus, and Poisson's Ratio by Impulse Excitation of Vibration"* [150]. Similarly, ASTM C1259 *"Standard Test Method for Dynamic Young's Modulus, Shear Modulus, and Poisson's Ratio for Advanced Ceramics by Impulse Excitation of Vibration"* describes the standard for the same method specifically for advanced ceramic materials [151] [152].

The natural flexural frequency, denoted f_f, is characteristic of the dynamic Young's modulus, E. For the measurement of this frequency, the specimen is supported at the nodes, where the amplitude of vibration is zero, and is excited at one of the anti-nodes at either end of the rod in order to provoke maximum vibration, as shown in Figure 62a. Following the flexural frequency measurement, the Young's Modulus can be calculated by:

$$E = 0.9465\left(\frac{m \cdot {f_f}^2}{b}\right)\left(\frac{L^3}{t^3}\right)R_f \tag{32}$$

Where m is the mass, b, t and L are the width, thickness and length of the specimen, f_f is the measured flexural frequency and R_f is a geometrical correction factor which compensates for the aspect ratio of the specimen, dependent on the thickness and length of the specimen:

$$R_f = 1 + 6.585\left(\frac{t}{L}\right)^2 \tag{33}$$

As can be seen, the mass and dimensions of the sample need to be measured accurately for reliable calculation of the Young's Modulus.

The natural torsional frequency, denoted f_t, is characteristic of the shear modulus. In this case, the specimen is supported along both longitudinal and transverse axes, as can be seen in Figure 62b, while the mechanical excitation is performed at one corner, inducing a twisting motion in the beam, rather than flexing it. Following the torsional frequency measurement, the Shear Modulus can be calculated by:

$$G = \frac{4 \cdot L \cdot m \cdot {f_t}^2}{b \cdot t} R_t \tag{34}$$

Where f_f is the measured flexural frequency and R_t is a geometrical correction factor similar to R_f, found by:

$$R_t = \left[\frac{1+\left(\frac{b}{t}\right)^2}{4-2.521\frac{t}{b}\left(1-\frac{1.991}{e^{\pi\frac{b}{t}}+1}\right)}\right]\left[1+\frac{0.0085b^2}{L^2}\right] - 0.06\left(\frac{b}{L}\right)^{\frac{3}{2}}\left(\frac{b}{t}-1\right)^2 \tag{35}$$

Following the calculation of the Young's and Shear Moduli, the Poisson's Ratio can also be calculated, as shown in equation 36. In addition, the material damping due to internal friction can also be characterised by considering the logarithmic decrement of the decaying amplitude of vibration [153] [154].

$$\nu = \frac{E}{2G} - 1 \tag{36}$$

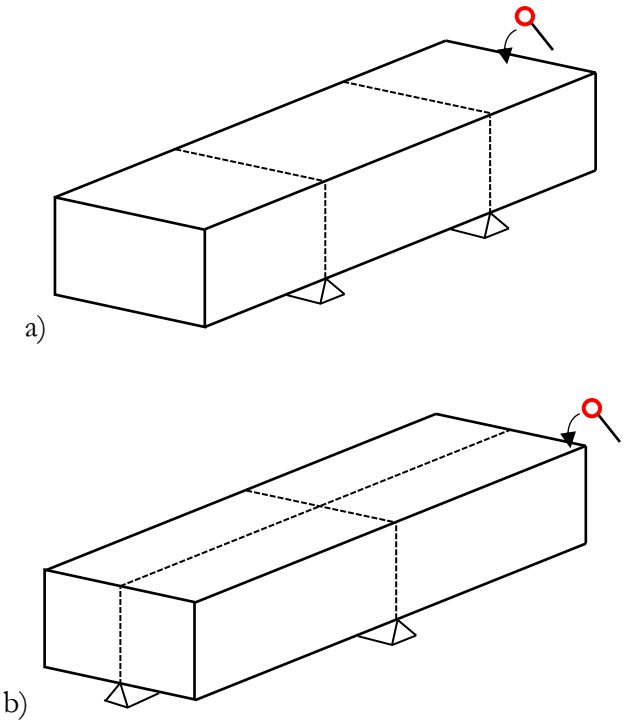

Figure 62 – IET set-up for flexural (a) and torsional (b) mode excitation with indicated position of hammer impact.

While the defined analytical solutions provide adequate results for elastic properties, a numerical approach encompasses the triaxiality of the problem, and facilitates the optimisation of the elastic constants, allowing for reverse engineering of these values from the measured frequencies with great accuracy. In addition, a numerical approach has the benefit of allowing the calculation of elastic constants for anisotropic bodies. The following section describes the numerical approach adopted in this study to determine the elastic properties of the tested CuCD grade. For a specimen with a square cross-section and made of an isotropic material, measurements of resonant frequencies in different transverse planes, referred to as in-plane and through plane, are identical, since the orientation of the specimen does not have an effect on the material properties. Whilst the method described in the following section refers to isotropic bodies, as is the case for CuCD, it can easily be extended to anisotropic bodies by considering flexural and torsional mode measurements for both in-plane and through-plane conditions.

The finite element analysis optimisation was again implemented in ANSYS, using a modal FEM analysis which, for a defined geometry, calculates the resonant frequencies for the given elastic properties and density. Arbitrary elastic properties are initially input, which are then optimised with the resonant frequencies measured from the IET experiment. During pre-processing, the geometry is divided into sub-blocks, allowing the definition of several lines and surfaces which can be constrained to force the excitation of a particular resonance

mode, similar to what is done physically in the IET experiment. The density value input in the simulation is also of particular importance, given that the frequency response is directly dependent on this property. For a given set of properties and dimensions, a higher density results in lower excited frequencies, and vice-versa. The experimentally derived density values detailed in section 4.2.1 were used for the CuCD grade in question, i.e., 5700 kg/m^3 at room temperature, since the test was conducted in ambient conditions.

During the simulation setup, the flexural mode in the direction of interest is forced by defining the central plane in the direction of interest as a frictionless support. The plane is allowed to move freely within the planar direction, but movement is blocked in the direction perpendicular to the plane. Considering the two possible orientations of flexural oscillations, the direction excited in the experiment needs to be chosen. This is relevant if the specimen has a rectangular cross-section, rather than a square profile as was the case for those tested.

For the excitation of the torsional mode, the longitudinal and transverse axes are fixed by setting the displacement on these lines equal to zero, blocking movement of the axes in all directions. Thus, the mode of interest is easily promoted. It is important to note the orientation of the specimen during the experiment when determining the axis on which the two central lines are fixed. In addition, to promote a natural torsional behaviour where the two faces at the extremities of the specimen rotate in opposite directions, a constraint equation is applied to the faces defining this behaviour. The relevant boundary conditions for the two analyses are shown in Figure 63.

Once the initial simulations are set up and completed, utilising the approximated values for elastic constants, the resulting first flexural and torsional frequencies are parametrised and optimised to the experimental results. The variables influencing the two natural frequencies of interest, flexural and torsional, are the Young's Modulus and Poisson's Ratio (the Shear Modulus is calculated from the two other properties). A range of acceptable results is defined for each parameter to streamline the process.

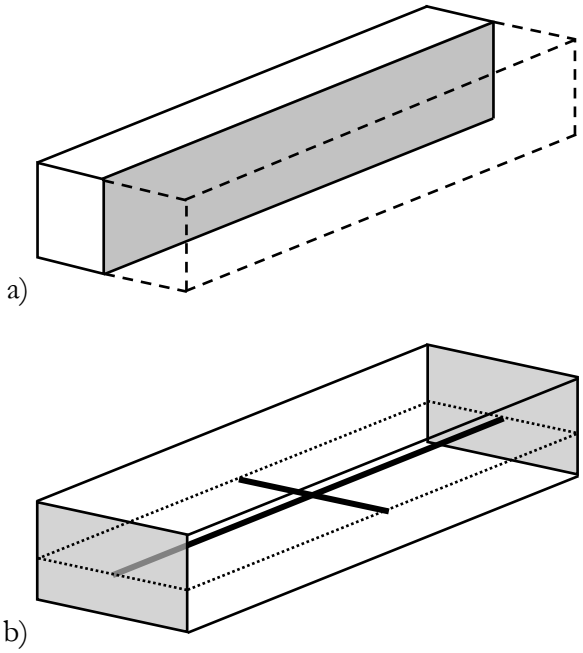

Figure 63 – Boundary conditions forcing mode of interest: (a) symmetry plane promoting flexural vibration and (b) fixed central lines promoting torsional vibration, and a constraint equation limiting motion of the two extremities of the specimen to rotate in opposite directions.

The IET test was carried out on a specimen with length, width and thickness of 247 × 12.41 × 10.35 mm^3. A spectrogram showing the intensity of the excited frequencies measured from the tested specimen set-up in the configuration shown in Figure 62a, is shown in Figure 64. The slender nature of the specimen made it difficult to excite the torsional mode, however this was still be observed when testing for the flexural resonance frequency. As can be seen in the spectrogram, there are various excited frequencies in the measured range. In order to identify the modes of interest, using initial values of 208 GPa for the Young's Modulus and a Poisson's ratio of 0.22, the first flexural and torsional modes were calculated by equations 32 and 34 as a first approximation. The resulting frequencies, shown in Table 15, allow for the identification of the first torsional and flexural modes from the various unwanted frequencies excited in the experiment.

Table 15 – Calculated flexural and torsional modes with E = 208 GPa *and* ν = 0.22.

Specimen Dimensions *length × width × thickness*	**Flexural Mode**	**Torsional Mode**
mm^3	kHz	kHz
247 × 12.41 × 10.35	1.047	7.054

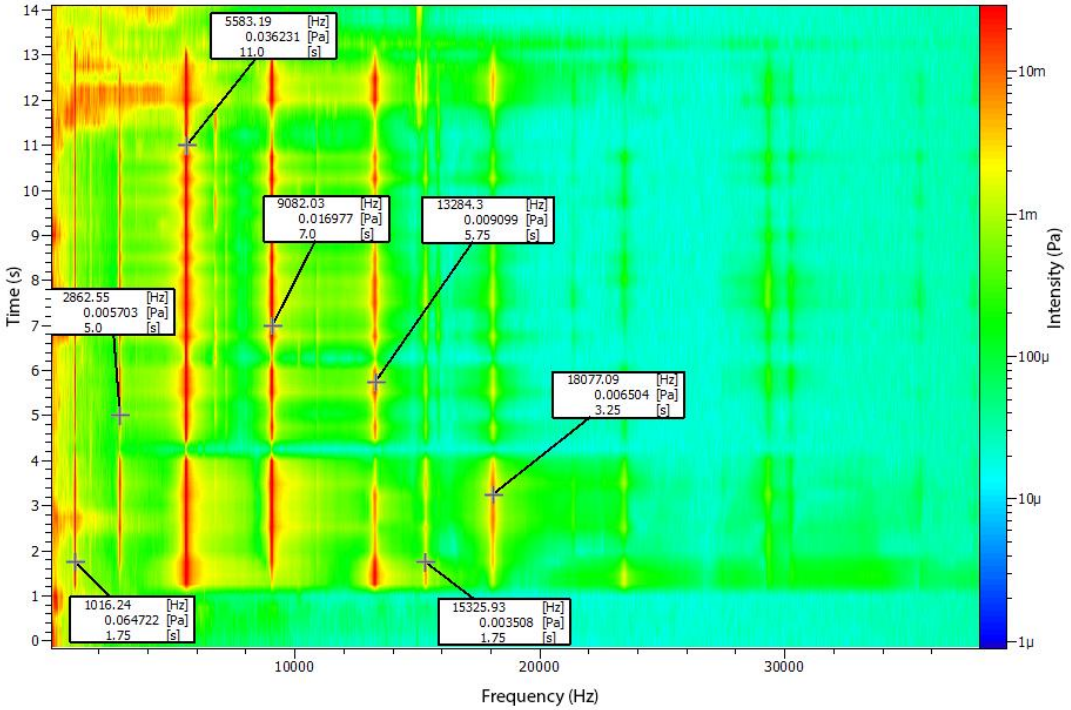

Figure 64 – Spectrogram showing the IET test frequency measurement as a function of time.

From the experimental results, the first flexural frequency can be easily identified, with a peak at 1.016 kHz. Two possible frequencies corresponding to the torsional mode were identified, at 6.794 kHz and 7.238 kHz (two faint lines between the 5.583 kHz and 9082 kHz readings).

Following the identification of the first flexural mode and the two possible torsional modes, the estimated values for the Young's Modulus and Poisson's Ratio (208 GPa and 0.22 respectively) were used as a primary input, along with the density of the material, in the optimisation procedure. A first estimation of the expected flexural and torsional modes was computed for the given material properties, improving on the estimated frequencies calculated analytically, which did not consider triaxiality. The first flexural and torsional modes determined by the modal analyses are shown in Figure 65. As can be seen, additional 'undesired' modes, such as the first longitudinal harmonic, can also be excited, since movement in this direction is unrestricted.

Following the initial modal analysis with estimated properties, the computed frequencies were parametrised and optimised with the frequencies measured in the experiment. The Young's Modulus was constricted to a range between 187 and 229 GPa, while the Poisson's ratio was restricted to values ranging from 0.1 to 0.3. The optimisation procedure adjusts

these two values, attempting to match the computed frequencies with the measured values in the experiment.

The relatively minor difference (11%) in the two measured frequencies identified for the torsional mode resulted in a significant effect on the computed Poisson's ratio. For f_f = *1.016 kHz* and f_t = *6.794 kHz*, the Young's Modulus is computed at 193.7 GPa, with a Poisson's ratio of 0.248, while for f_f = *1.016 kHz* and f_t = *7.238 kHz*, the Young's Modulus is calculated at 193.6 GPa, with a Poisson's ratio of 0.104. Considering previous data on other CuCD grades, the value of $\nu = 0.248$ was retained, along with a Young's Modulus of 194 GPa, as potential values to be used in the material model. A summary of the results is shown in Table 16.

Table 16 – Young's Modulus and Poisson's Ratio results determined by the preliminary IET optimisation procedure.

Property	Symbol	Value	Uncertainty	Units
Young's Modulus	E	194	± 32	*GPa*
Poisson's Ratio	ν	0.248	± 0.002	-

The IET process was repeated with a number of specimens of equal dimensions to verify the experiment's repeatability. Seven specimens with average dimension 45.4×4.5×3.1 mm^3 were tested in the flexural (in-plane) configuration, with the average Young's Modulus found to be 220 GPa. The specifications for the tested specimens, along with the calculated Young's Modulus, are shown in Table 17. The final value for Young's Modulus adopted for the constitutive model describing the CuCD RHP3434 grade, along with the Poisson's Ratio, is shown in Table 18. This value was implemented in the simulations presented in section 4.3 along with the previously measured value of 194 GPa.

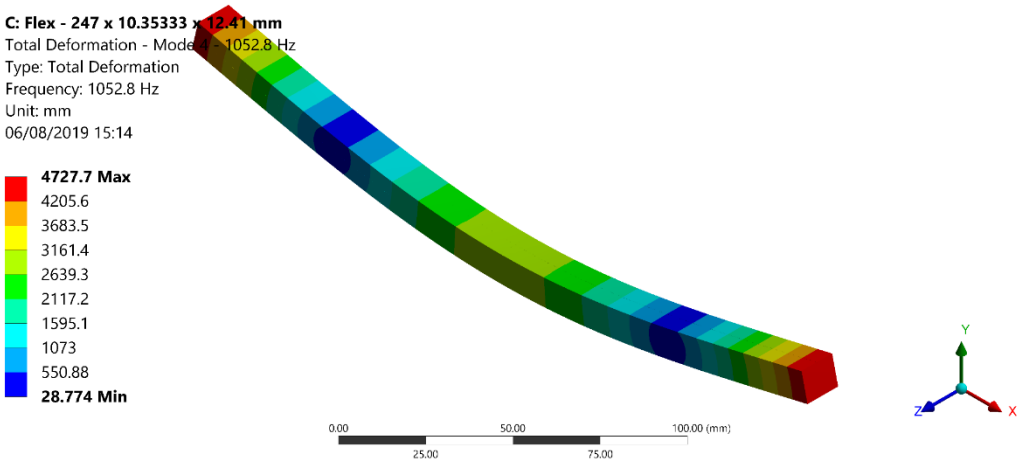

a)

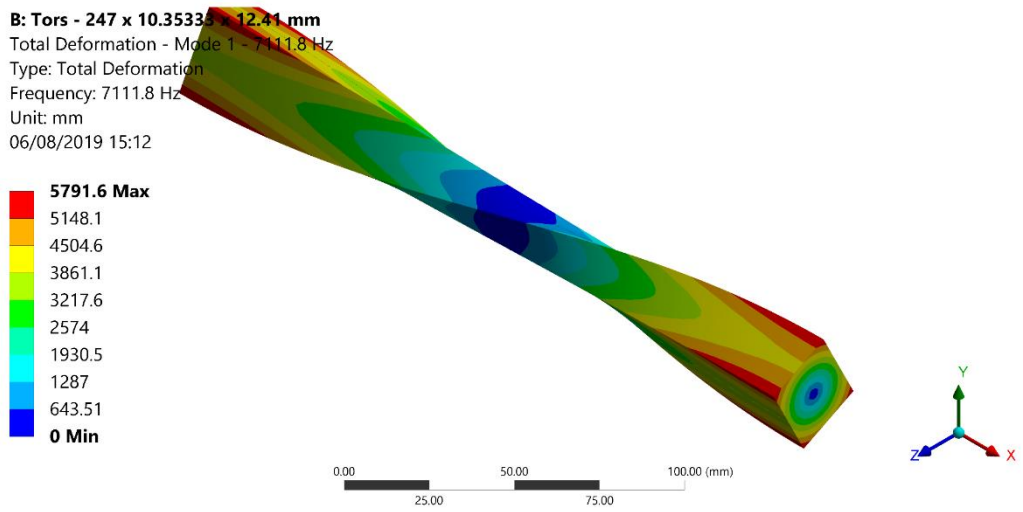

b)

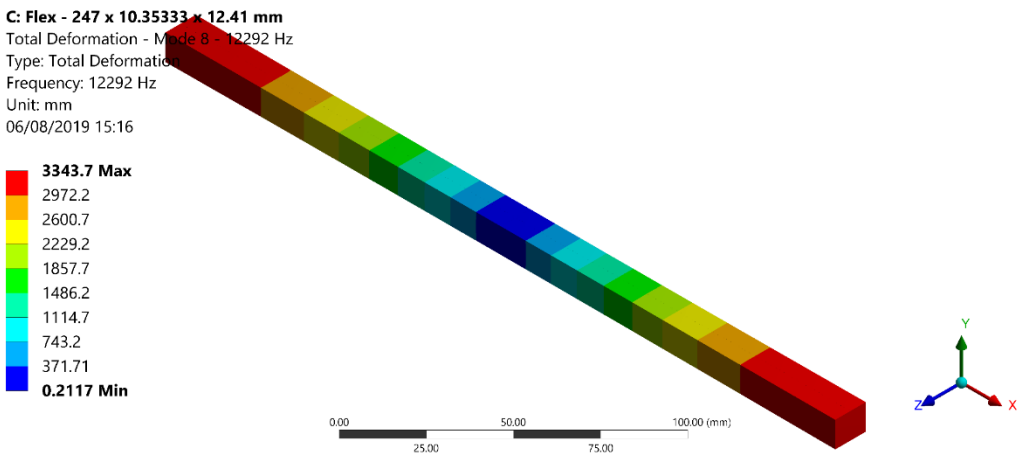

c)

Figure 65 – First flexural and torsional modes simulated with estimated material properties (a and b) and additional modes such as the first longitudinal frequency (c).

Table 17 – Specifications for tested specimens, measured flexural frequencies, and calculated Young's Modulus.

Specimen	**m**	**L**	**b**	**t**	**f_f**	**E**
	g	*mm*	*mm*	*mm*	*kHz*	*GPa*
1	3.23	45.42	4.48	3.15	10.17	*218.8*
2	3.37	45.59	4.57	3.18	10.19	*220.8*
3	3.19	45.26	4.50	3.06	10.16	*230.5*
4	3.18	45.34	4.50	3.09	9.93	*214.8*
5	3.22	45.45	4.53	3.16	10.36	*221.8*
6	3.28	45.43	4.54	3.02	9.87	*234.9*
7	3.12	45.43	4.44	3.00	9.67	*222.7*

Table 18 – Final Young's Modulus and Poisson's Ratio measurements for CuCD RHP3434.

Property	**Symbol**	**Value** (± *standard uncertainty*)	**Units**
Young's Modulus	*E*	220 ±7	*GPa*
Poisson's Ratio	*ν*	0.248 ± 0.002	-

The beam impact scenarios in accelerators can lead to significantly high temperatures in beam intercepting devices. For this reason, a material model which describes the material behaviour over a range of temperatures is ideal in order to model experimental scenarios accurately and reliably. The impulse excitation technique can be implemented at high temperatures with the use of a purpose-built furnace, which houses specimens to be heated to the required temperature of measurement and allows for the striking hammer and microphone to still be unobstructed. When performing the IET test at high temperatures, one should consider the temperature range in which the specimen retains its chemical integrity. Some materials, such as Mo in TZM, might exhibit oxidisation at high temperatures, while in the case of CuCD the copper matrix has a relatively low melting temperature [155]. An IET test conducted at elevated temperatures is scheduled to be conducted on a number of CuCD samples, allowing for modelling of the elastic behaviour of the material at these temperatures.

4.2.3 Plasticity – 4-Point Bending test

To model the material behaviour beyond the elastic regime, a four-point bending test was performed, allowing for the implementation of a multilinear hardening model in numerical analyses, expressed in terms of plastic strain and equivalent stress. A Zwick/Roell Z400 universal testing machine was used for the 4-point flexural test in accordance with the

ASTM C651 standard *"Flexural Strength of Carbon and Graphite by Four-Point Loading"* [156]. With this experimental setup, as shown in the schematic in Figure 66, the bending force is applied at two points along the length of the specimen, which is supported at its extremities. The bending force is progressively increased, with the corresponding induced strain in the specimen measured with strain gauges glued to its surface.

The 4-point bending test was repeated three times on three different specimens, with an average length of 30 mm, width of 5.3 mm and thickness of 5.1 mm. The results for the first specimen tested were used and processed, shown in Figure 67.

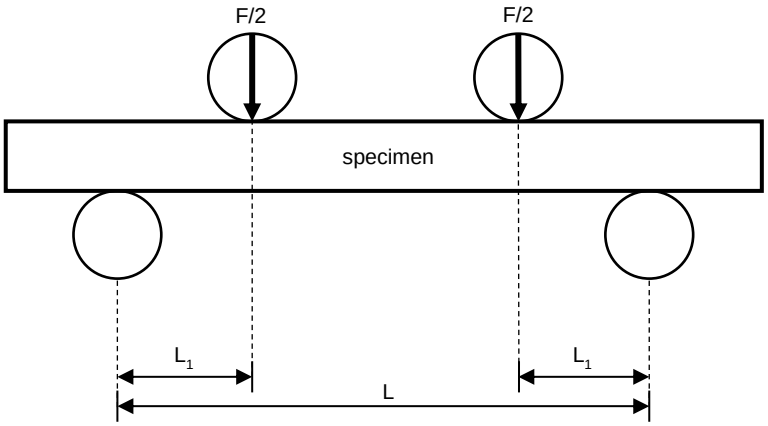

Figure 66 – 4-point bending experimental setup.

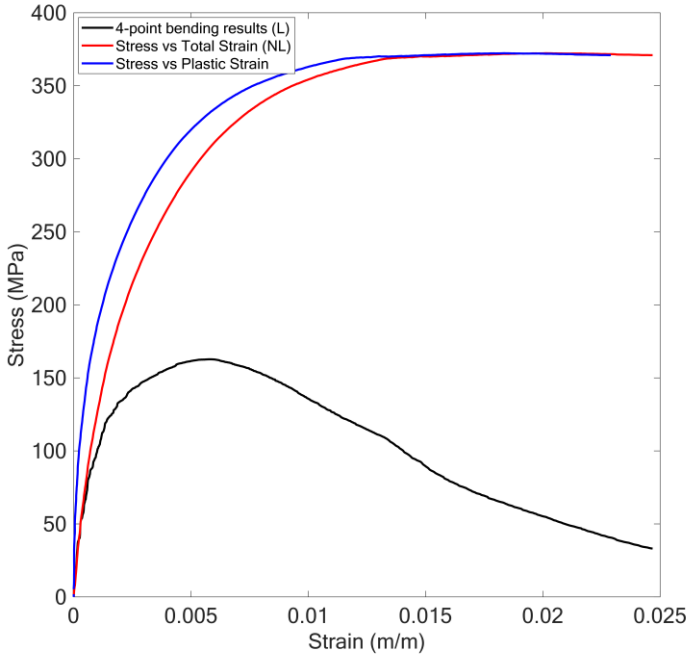

Figure 67 – Stress-Strain plots obtained from 4-point flexural test and processed stress-strain relationships.

The procedure to convert these values into the plastic strain against equivalent stress plot required to be input in numerical analyses follows three main steps, namely converting engineering stresses and strains into true stresses and strains, reconstructing the non-linear bending moment from the true stress, and converting the total equivalent strain into plastic strain [157].

In tensile tests, true stresses and strains are different from the engineering stress and strain due to the change in section area and length of the specimen. While engineering stress and strain relate the internal force and deformation to the original cross-sectional area and length of the specimen, in reality these are changing with an increase in load (the cross-sectional area is decreasing, and the overall length of the specimen is increasing). The true stress and strain consider these actual values, and are to be used when inputting material data in numerical analyses such as those performed in ANSYS. For a uniaxially loaded member, the true stress and strain can be derived from the engineering stress and strain by:

$$\varepsilon_{true} = ln\left(1 + \varepsilon_{eng}\right) \tag{37}$$

$$\sigma_{true} = \sigma_{eng}\left(1 + \varepsilon_{eng}\right) \tag{38}$$

In a tensile test, the true strain is therefore less than the engineering strain, while the true stress is larger than the measured engineering stress, resulting in the true stress-strain curve displacing upwards and to the left in relation to an engineering stress-strain curve [157].

The maximum bending moment is deduced from the force F and the distance between the load application and the supports, $M = L_1F/2$. In the linear elastic domain, the stress distribution through the sample thickness can be shown to be linear, and the maximum can be calculated by $\sigma = Mh/2I$, where I is the flexural moment of inertia and is equal to $bt^3/12$ for a rectangular section, where b is the width and t is the thickness of the specimen.

However, the Force-Strain relation measured in the experiment is non-linear, indicating that there is a non-linear stress distribution across the thickness of the specimen, as shown in Figure 68. The maximum stress thus has to be calculated taking into consideration this non-linearity. For small curvatures, the axial strain can be considered to be linearly distributed through the thickness [141].

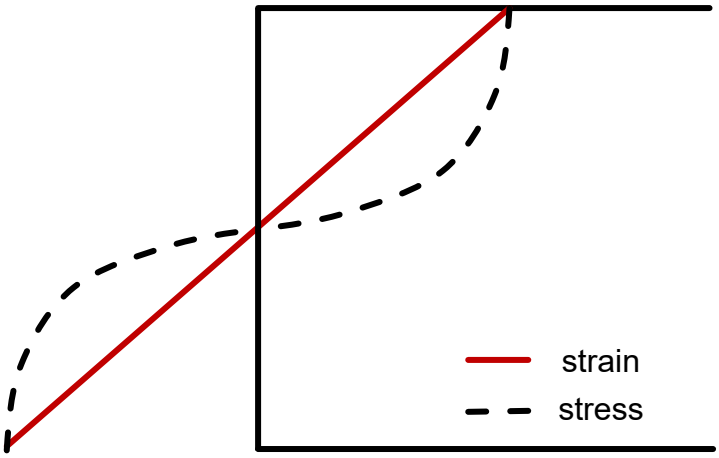

Figure 68 – Axial strain (linear) and stress (non-linear) distribution through the sample thickness.

The stress must therefore be calculated out of the general moment-strain relationship. The moment can be expressed as an integration of the stress distribution through the thickness by:

$$M = b\int_{-t/2}^{t/2}\sigma_z(x)xdx \tag{39}$$

Where x is the vertical coordinate from the neutral axis, b is the specimen's width, and t is its thickness (height, i.e., along x). The moment can be expressed in terms of the measured strain as:

$$M(\varepsilon_{max}^{tot}) = 2b\int_{0}^{t/2}\sigma_z(\frac{2x}{t}\varepsilon_{max}^{tot})xdx \tag{40}$$

Where $\sigma_z(\frac{2x}{t}\varepsilon_{max}^{tot})$ indicates the stress-strain curve which can be numerically derived, given the applied moment $M(\varepsilon_{max}^{tot})$ and the measured strain ε_{max}^{tot}. The problem can be solved for each measured value of force and strain, resulting in a piecewise stress-strain relationship, i.e., a multi-linear hardening curve describing the plastic behaviour of the material, shown in Figure 69. The material can be seen to quickly lose linearity, and undergoes a significant amount of plastic deformation as a result of the highly ductile copper matrix.

One aspect which is not considered in the model is the compression behaviour of the material, which is assumed to be identical to that in tension. This assumption may not be valid at high compressive strains, at which point the diamond particles may come in contact. In contrast, when the material is loaded in tension, the bond between the diamond particles and the copper matrix may be lost.

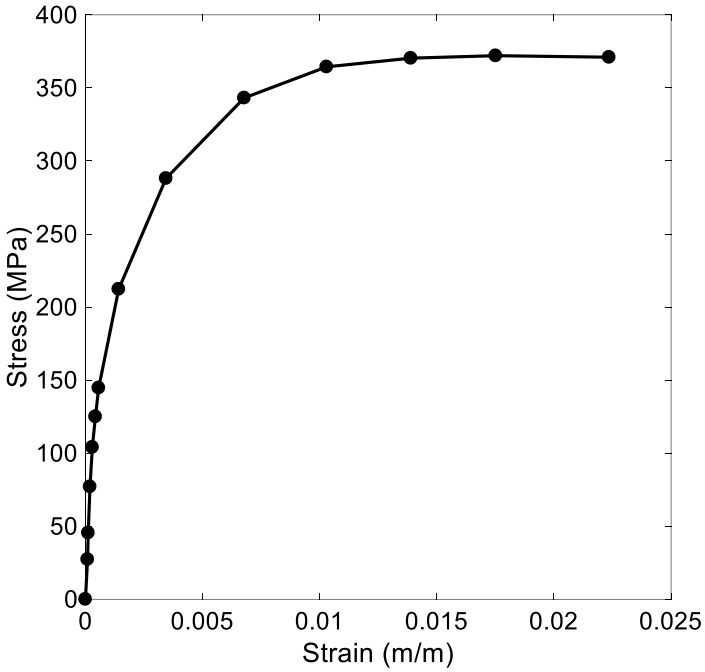

Figure 69 – Stress-strain diagram for CuCD RHP3434 obtained from four-point bending test.

The multilinear hardening model was implemented in finite element software, as is described in Section 4.3. This required the equivalent stresses to be expressed as a function of the plastic strain, rather than total strain. This was calculated by simply subtracting the elastic strain from the equivalent total strain, i.e., $\varepsilon_p = \varepsilon_{tot} - \varepsilon_{el}$, where $\varepsilon_{el} = \sigma/E$.

The reconstruction of the non-linear bending moment across the specimen thickness was implemented in a MATLAB script, which first calculates the moments from the flexural stress values obtained in the experiment, assuming a linear distribution across the specimen's thickness, which is then scaled for a non-linear distribution. This is followed by the conversion of engineering stress and strain into true stress and strain, and the final output is the plastic strain and the equivalent stress, which can be input in FEA software to describe the plastic behaviour of the material in a multilinear hardening model.

4.2.4 Temperature Sensitivity Testing

Previous studies have reported a limitation in CuCD related to the degradation of the copper-diamond interface as a result of elevated temperatures in the range of 250-300°C. This is believed to be a result of a significant mismatch between the coefficient of thermal expansion of the two materials making up the composite. This results in irreversible damage in the material once it reaches the limiting temperatures, due to the detachment of diamond particles from the copper matrix, leading to inefficiencies in thermal diffusivity [141].

A number of tests were carried out at CERN to quantify this degradation. The first test comprised of a long heat treatment of a CuCD specimen, consisting of three 48-hour cycles at an elevated temperature of 250°C. After each 48-hour cycle, the specimen was brought to room temperature. The thermal diffusivity was measured throughout the experiment. As can be seen in the results shown Figure 70 and summarised in Table 19, the thermal diffusivity at room temperature gradually decreases with each thermal cycle, decreasing by up to 21.5% of the original measured value following the third and final cycle.

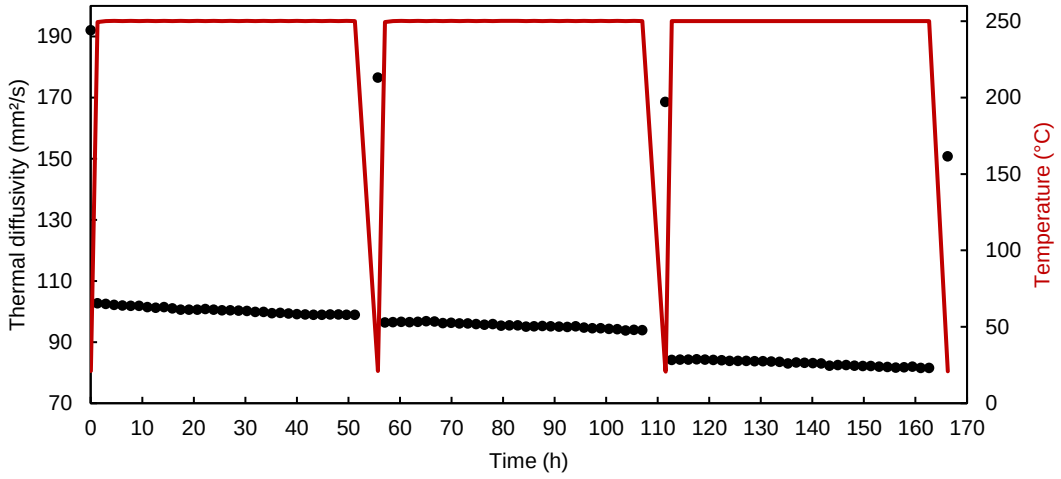

Figure 70 – Long heat treatment test temperature cycles (red line) and measured diffusivity (black dots) following each 48-hour cycle at 250°C.

Table 19 – Diffusivity measurements at room temperature for CuCD following 48-hour temperature cycles, as shown in Figure 70, and percentage decrease in diffusivity from initial measured value.

	Diffusivity at room temperature	**Decrease in Diffusivity**
	mm^2/s	-
Initial value	192.0	*N/A*
48h at 250°C	176.5	8.1%
96h at 250°C	168.6	12.2%
144h at 250°C	150.8	21.5%

A similar test was performed, where a specimen's temperature was gradually increased from room temperature up to a temperature of 300°C. In this case, once the specimen reached certain temperatures, it was cooled to room temperature, before repeating the process and increasing the temperature to a higher threshold. As can be seen in the results in Figure 71, summarised in Table 20, up to 200°C the decrease in thermal diffusivity is relatively minor at 2.4%. This value, however, increases to a change of 6.7% from the original value following the final temperature cycle up to 300°C. This is still relatively minor compared to

the 21.5% decrease observed in the previous test, suggesting that the degradation process is significantly time dependent.

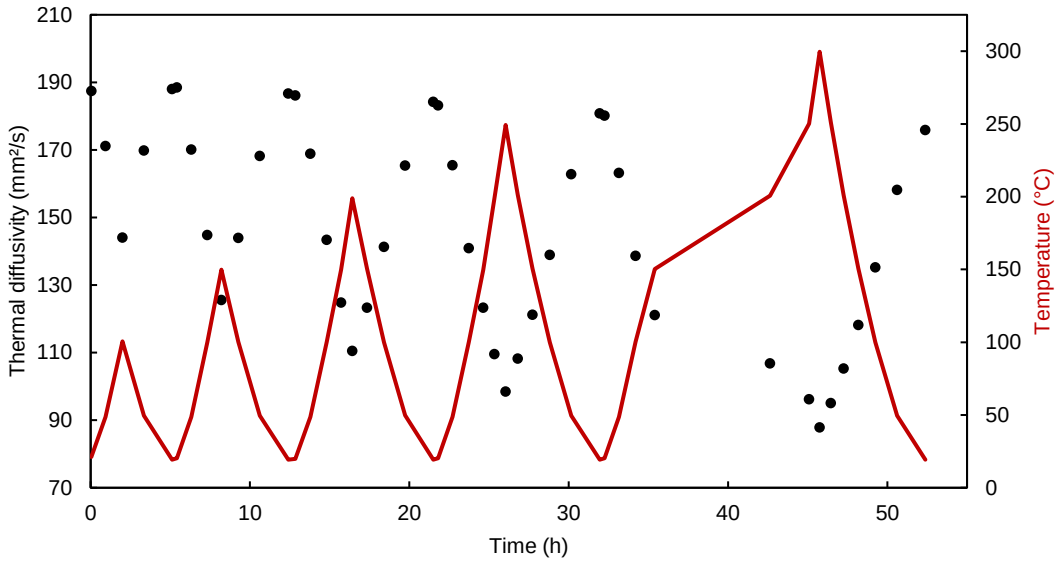

Figure 71 – Diffusivity measurements (black dots) for temperature cycling (red line) with gradual increase in temperature up to a maximum of 300°C.

Table 20 – Diffusivity measurements for CuCD at room temperature following temperature cycles up to a maximum of 300°C (as shown in Figure 71), and percentage difference from initial value.

Maximum temperature cycle	Diffusivity at room temperature	Decrease in Diffusivity
°C	*mm^2/s*	-
20	188.0	*N/A*
100	188.1	0.0%
150	186.1	1.0%
200	183.5	2.4%
250	180.3	4.1%
300	175.5	6.7%

4.3 Benchmarking of material model

The material model for the CuCD RHP3434 grade, consisting of the measured thermomechanical temperature-dependent properties, dynamic elastic constants from the IET test, and multilinear hardening curve from the 4-point bending test, was included in a simply coupled, implicit thermomechanical simulation performed in Ansys® Academic Research Mechanical, Release 18.1, similar to analyses on SiC and TZM presented in this thesis in section 3.4.

For copper diamond, two pulses from the MultiMat experiment were modelled, utilising FLUKA energy deposition maps [122] as an input in the thermal simulation, allowing the determination of the thermal load in each specimen. The thermal load was imported in the structural analysis to model dynamic phenomena as tested and measured in the MultiMat experimental campaign. In the MultiMat experiment, the target station hosting the CuCD RHP3434 samples consisted of 4 specimens in series, each having a length of 247 mm, with a 3 mm space in-between specimens. The specimens had a square cross-section with an edge length of 10 mm. All four specimens were equipped with longitudinal strain gauges to measure dynamic phenomena induced by the particle beam impacts, as shown in Figure 72. BF, LF and RF notations respectively refer to the bottom, left and right faces of the specimens.

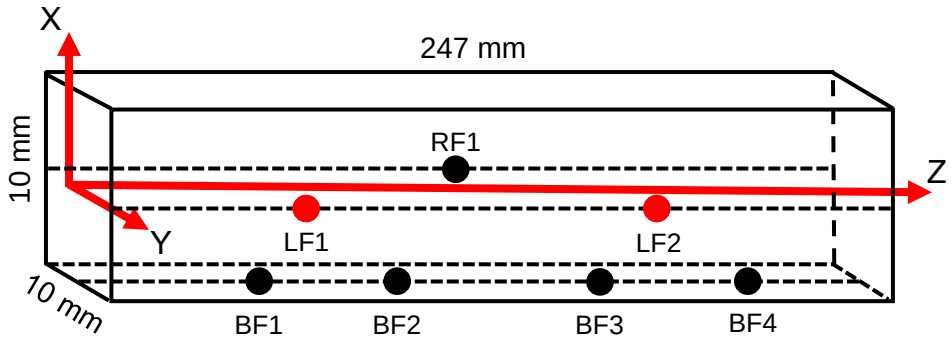

Figure 72 – Dimensions of CuCD specimens along with positions of strain gauges (in black) and temperature probes (in red) on the specimens of interest.

Similar to previously presented analyses for SiC and TZM, the thermomechanical analysis started with the calculation of the energy deposition map in the specimens as a result of the pulses impacting the specimens equipped in the target station [122]. This was used to map the internal heat generation in the transient thermal analyses, allowing for the computation of the internal temperature of the specimens during and following the beam impact. The mesh adopted for the thermal analysis consisted of 50 longitudinal divisions and 60 divisions across the cross-section, for a model of 379,181 3D 20-node high-order elements. The thermal analysis consisted of two steps, one modelling the energy deposition, and a longer step to compute the thermal evolution in the specimens. The computed time-dependent thermal field was imported as a thermal load in the structural analysis, which consisted of three steps covering the energy deposition, longitudinal effects, and flexural effects respectively. The substep for each step was set according to the phenomenon of interest, considering the CFL condition to determine whether the element size is

appropriate. For longitudinal vibrations, considering a longitudinal wave speed of 6200 m/s, a time step of 5×10^{-8} s, and a longitudinal element length of 2.06 mm, the Courant number equated to 0.150 (safely below the limiting value of 1). The structural analysis utilised a mesh having 15,350 3D 20-node solid elements with quadratic displacement behaviour. The specimens were modelled in a simply supported configuration as in this case, as opposed to what was observed in SiC and TZM specimens, the experimental supports did not exhibit any loss of contact during the experiment.

The material model adopted was built from measurements presented in section 4.2. Temperature-dependent values for the linear coefficient of thermal expansion, density, specific heat capacity, and thermal conductivity were adopted, along with Young's Modulus and Poisson's Ratio obtained from the IET tests performed. A multilinear kinematic hardening model describing the plastic behaviour of the material was adopted following the 4-point bending test carried out. The material properties used in the thermomechanical model at room temperature are summarised in Table 21.

Table 21 – Summary of material model for CuCD RHP3434 at room temperature. Temperature-dependent properties were adopted where available.

Property	Value	Uncertainty	Units
Density	5700	± 33	$kg \cdot m^{-3}$
Specific Heat Capacity	407	± 12	$J \cdot kg^{-1} \cdot K^{-1}$
Thermal Conductivity	537	± 15	$W \cdot m^{-1} \cdot K^{-1}$
Coefficient of Thermal Expansion	6.19	± 0.2	$10^{-6} \cdot K^{-1}$
Young's Modulus	194	± 32	*GPa*
Poisson's Ratio	0.248	± 0.002	-

Information on the two experimental scenarios modelled in numerical simulations is shown in Table 22. The first shot consisted of 1 bunch having a total intensity of 1.433×10^{11} protons, and a vertical offset of 3 mm. The second shot consisted of a longer, central, 12-bunch shot with a total intensity of 6.880×10^{12} protons. Modelling two distinctly different pulses allows one to test the ability of the formulated material model to simulate different scenarios. The energy deposited along the length of the specimens, along with the temperature along the length of the specimens following beam impact (i.e., at 25 ns for shot 128, and at 300 ns for shot 132), can be seen in Figure 73. Note that the temperature line was probed along the beam impact position, i.e., at a vertical offset of 3 mm for shot 128 and along the longitudinal axis of the specimen for shot 132, with no offset.

The most loaded CuCD specimen can be seen to be the second in the target station – this

specimen was chosen to model the dynamic phenomena in the structural analysis, due to the lower signal-to-noise ratio achieved as a result of the higher deposited energy, and subsequent larger amplitudes in the propagating waves. Figure 74 shows experimental measurements obtained from a thermal probe positioned on the outer surface of the second specimen at a length of 82.3 mm, LF1 in Figure 72, compared with thermal analysis results for the modelled specimen, probed at the same location. The thermal probe has a reaction time in the order of seconds, and is not capable of capturing variations of temperature in the order of microseconds. This, coupled with issues related to contact resistance between the thermal probe and the tested specimens, results in a delay in experimental measurements to reach the maximum temperature, when compared to the numerical analysis. The simulation can otherwise be seen to accurately predict the maximum temperature at the surface of the specimen.

Table 22 – Shot information for the studied impacts (pulse 128 and pulse 132).

Pulse No.	**Pulse Duration**	**No. of bunches**	**Bunch intensity**	**Total intensity**	**σ**	**η_y**
	ns	*b*	*p/b*	*p*	*mm*	*mm*
128	25	1	1.433×10^{11}	1.433×10^{11}	0.5	3
132	300	12	5.733×10^{11}	6.880×10^{12}	0.5	0

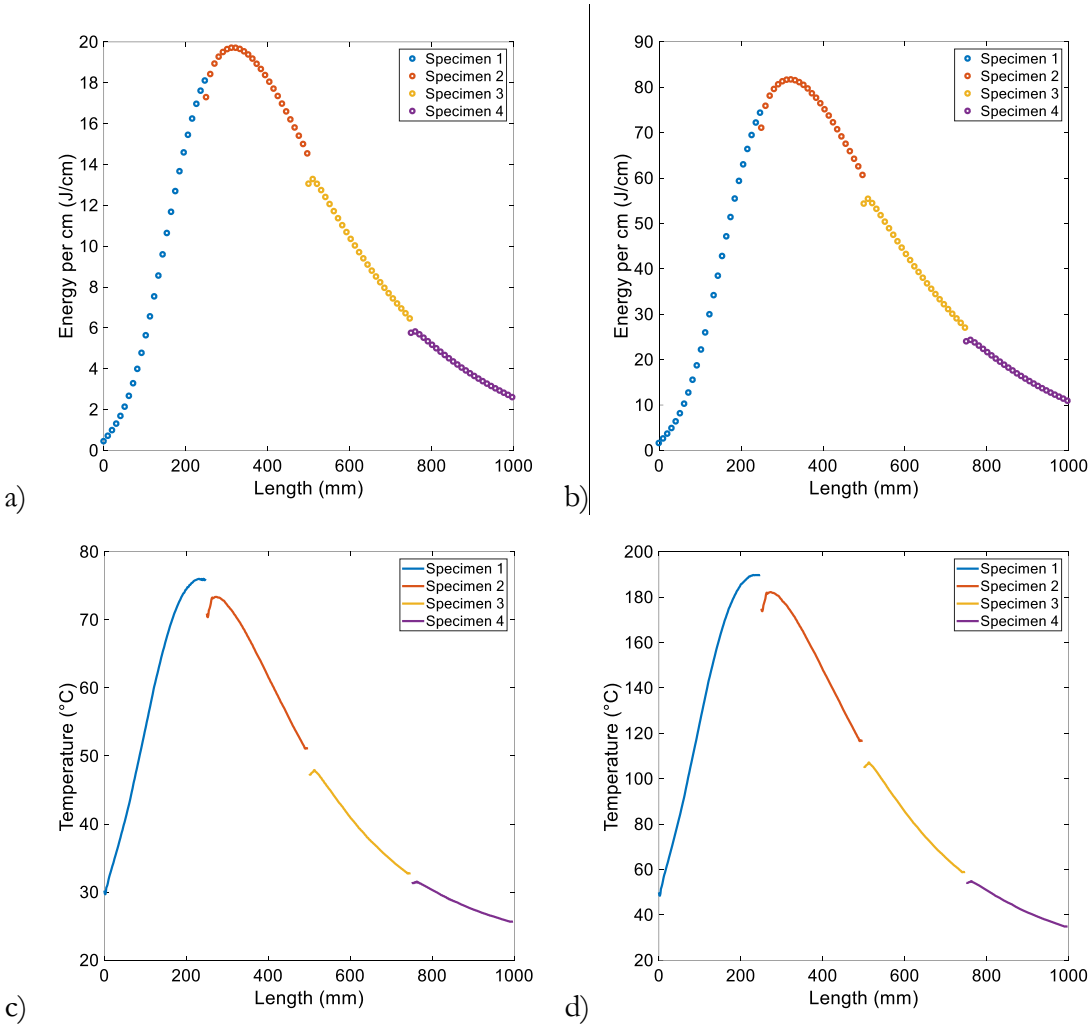

Figure 73 – Energy deposited along the length of the specimens in the CuCD RHP target station for shots 128 (a) and 132 (b), and temperature along the length of specimens for each respective shot (c and d).

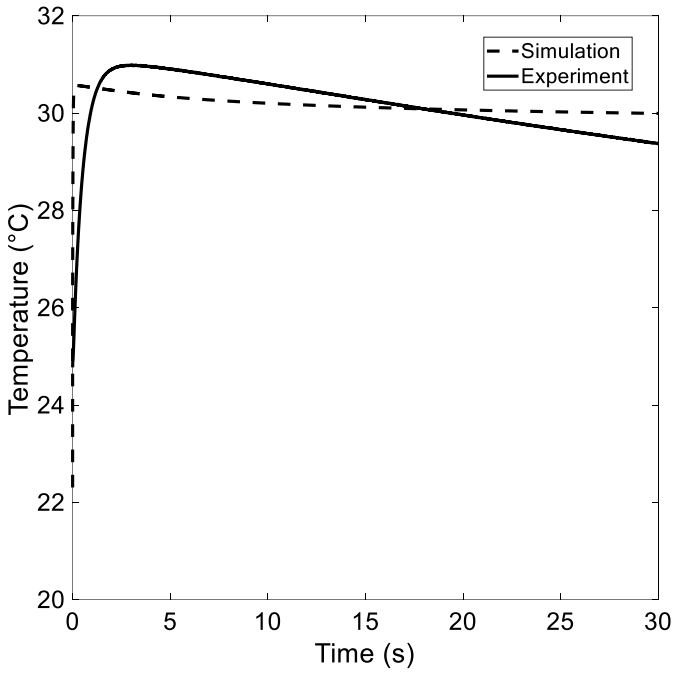

a)

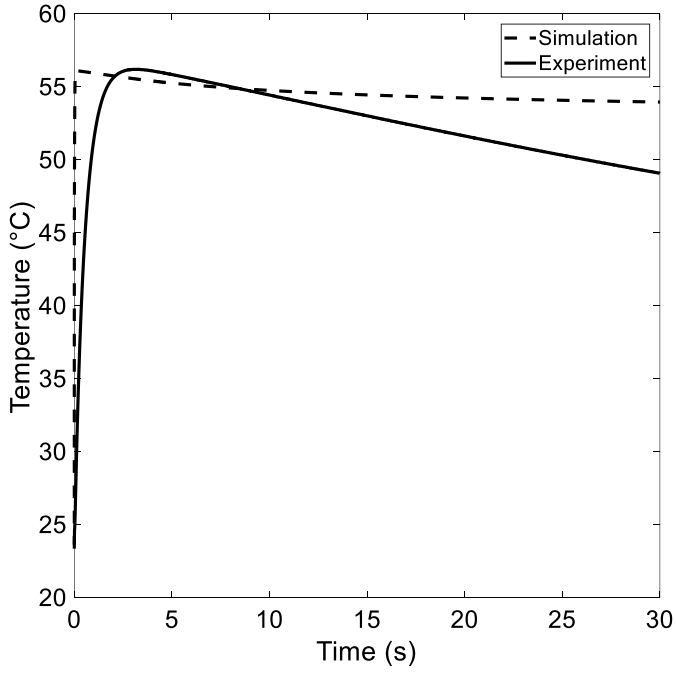

b)

Figure 74 – Thermal analysis results compared with experimental results for shot 128 (a) and shot 132 (b), probed on the surface of the second specimen at a length of 82.3 mm.

4.3.1 Benchmarking of Multilinear Hardening Model

The temperature field obtained from the thermal analyses was imported in a structural analysis modelling the material's dynamic behaviour upon beam impact. The dynamic longitudinal and flexural response were modelled by considering a simply supported specimen, simulating the experimental setup. The second specimen in the target station, being the most loaded, was modelled, and results were probed at a length of 154 mm at a point at the centre of the specimen's bottom face. These results were compared with experimental results obtained from a longitudinal strain gauge attached to the specimen at the same position.

The dynamic longitudinal response for shot 128, obtained with the application of the material model described in the study with a Young's Modulus of 194 GPa, as initially measured, is compared with experimental results in Figure 75. Along with a measurable difference in amplitude, the main discrepancy between the two signals can be seen to be in the longitudinal frequency, with the numerical result having a frequency of 11.8 kHz, compared to an experimental result of 13.0 kHz (9% difference), suggesting that the Young's Modulus implemented in the simulation underestimated that of the material. With this in mind, the material model was updated with a higher Young's Modulus of 220 GPa obtained from further testing performed on smaller CuCD samples, as described in section 4.2.2. The increase in Young's Modulus provides the best fit for longitudinal and flexural frequencies between experimental and numerical data. All other properties were retained. One should also note that a Young's Modulus of 208 GPa was used in previous studies for this material [60]. Simulation results compared with experimental results for the updated model are shown in Figure 76. The general wave shape and amplitude can be seen to remain unchanged, which is expected, as the increase in Young's Modulus only results in a 'compression' of the waveform, i.e., an increase in frequency. This leads to a better fit with experimental data, with a longitudinal frequency of 12.6 kHz (3% difference). The benefits of using a multilinear hardening model, rather than an elastic model, can be clearly see in Figure 77, which shows the result for a linear elastic material model, i.e., not multilinear and no plasticity, with a Young's Modulus of 220 GPa. It can be seen that, with the application of the elastic model, the longitudinal frequency is retained to a certain extent, but the model fails to correctly simulate the high frequency content of the signal, which can be seen to have a much higher amplitude than the one observed in the experiment. The introduction of plasticity can thus be seen to contribute to the replication of energy dissipation in the material, observable as wave attenuation in the measured and computed signals.

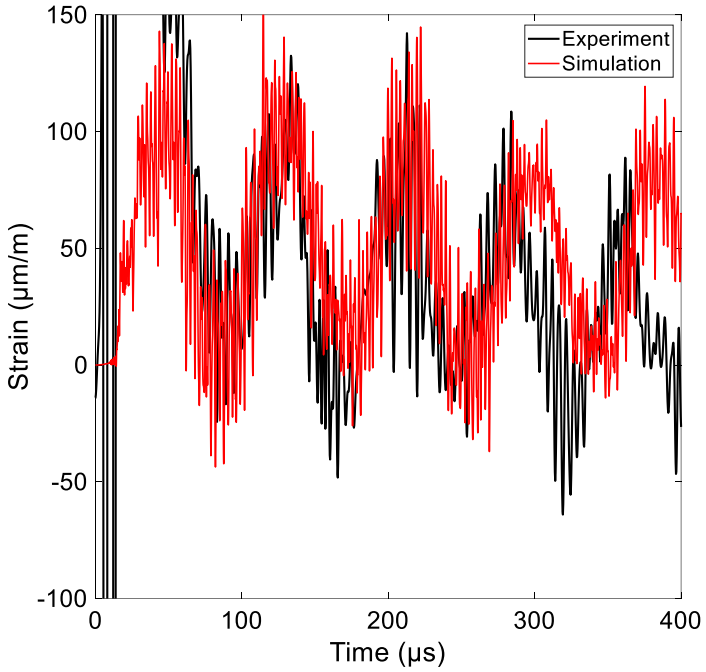

Figure 75 – Longitudinal strain for shot 128, probed at a length of 154 mm on the bottom face of the second specimen. Numerical model with a Young's Modulus of 194 GPa and multilinear hardening model.

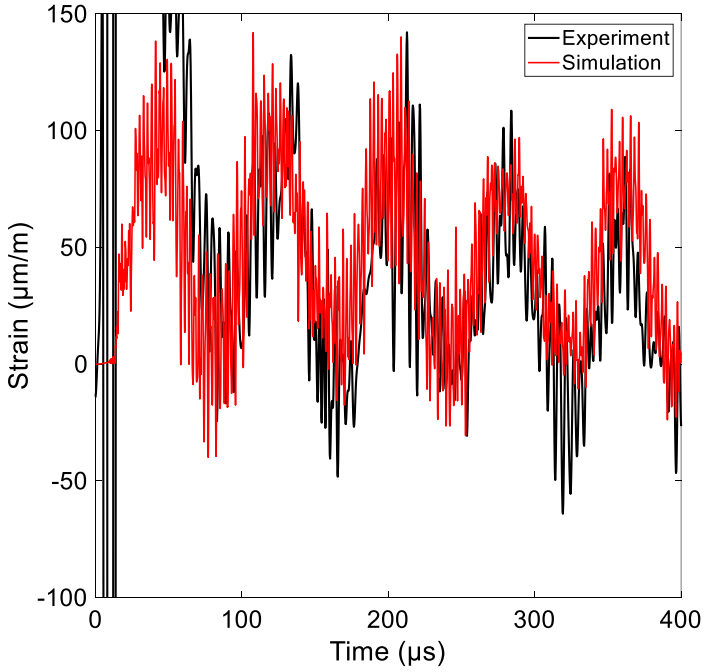

Figure 76 – Longitudinal strain for shot 128, probed at a length of 154 mm on the bottom face of the second specimen. Numerical model with a Young's Modulus of 220 GPa and multilinear hardening model.

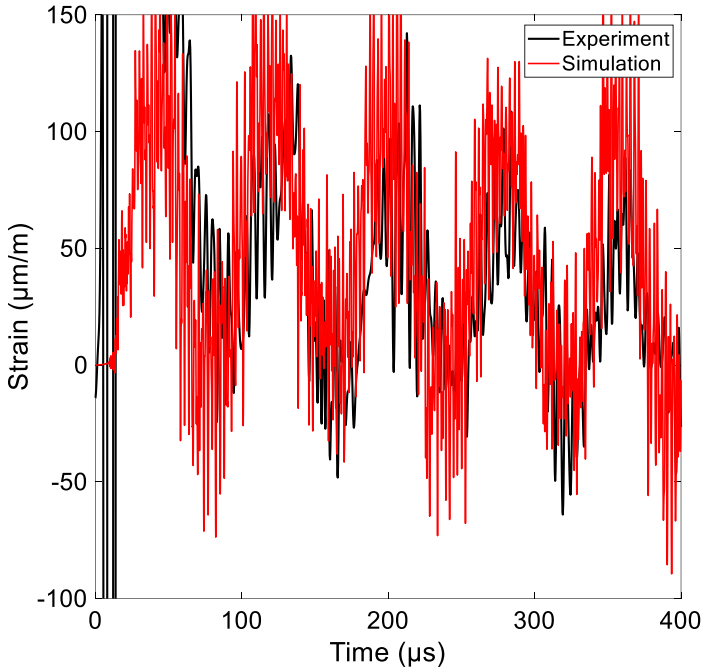

Figure 77 – Longitudinal strain for shot 128 with a linear elastic model (E=220 GPa), plotted against experimental data measured at a length of 154 mm on the bottom face of the second specimen.

In respect of the flexural response, shown in Figure 78 for the same beam impact, the numerical result, with multilinear hardening model and a Young's Modulus of 220 GPa, can be seen to overestimate the amplitude of oscillation. This is addressed by the introduction of Rayleigh damping to the analysis, with a Rayleigh damping ratio of ζ = 8.61% at 450 Hz, i.e., the flexural frequency, for a stiffness coefficient $\beta = 6.088 \times 10^{-5}$. The resulting waveform can be seen to closely follow the experimentally measured signal. With the implementation of Rayleigh damping at the flexural frequency, one can observe that information at higher frequencies is lost. The implementation of the multilinear hardening model already produced a decay in amplitude of numerical results, as a result of dissipation, in the longitudinal response, as could be observed by comparing the numerical results with different implemented models. Similarly, for the flexural response, the numerical results without the application of Rayleigh damping can also be seen to exhibit a reduction in amplitude in both the lower frequency flexural oscillations as well as in the higher frequency content. A possible improvement to the model could be the application of a hardening law inducing an earlier and more significant plasticisation, thus replicating signal dissipation without requiring the need to resort to numerical damping. A summary of the longitudinal and flexural frequencies obtained through the different models implemented is shown in Table 23.

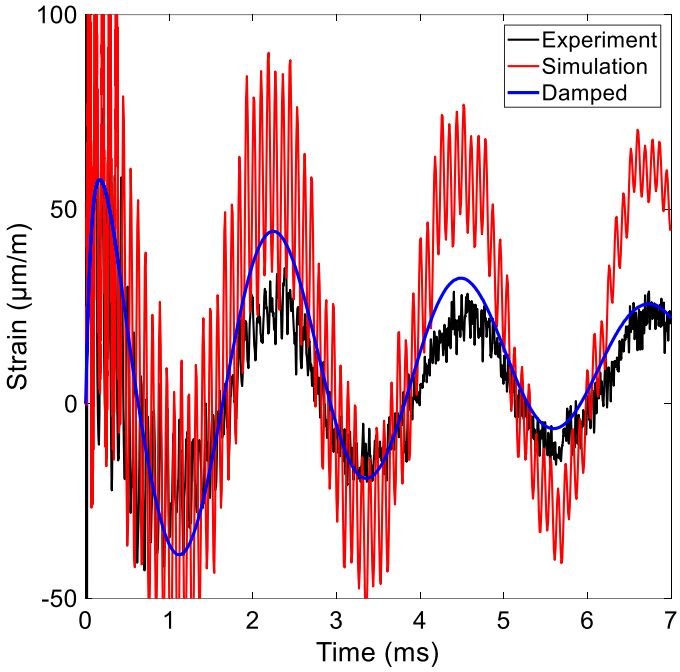

Figure 78 – Flexural response for multilinear model with and without included material damping for shot 128.

Table 23 – Comparison of measured experimental frequencies with and numerical results from perfectly elastic and multilinear hardening models with varying Young's Modulus.

	Longitudinal Frequency	**Flexural Frequency**
	kHz	*Hz*
Experiment	**13.0**	**452**
Simulation Multilinear hardening model, E=194 GPa	11.8	434
Simulation Elastic model, E=220 GPa	12.2	444
Simulation **Multilinear hardening model, E=220 GPa**	**12.6**	**455**
% difference between experimental and numerical results with ML model and E=220 GPa	3.1%	0.7%

The repeatability of the multilinear kinematic hardening model adopted was tested by simulating a higher intensity shot, pulse no. 132 in Table 22. Experimental and numerically computed results for shot 132 are shown in Figure 79. Similar to the previously modelled pulse, the simulation follows the experimental result with a good degree of accuracy in terms of wave shape, amplitude and frequency for the longitudinal wave. The model can be seen to underestimate the amplitude of high frequency content in the signal – this can indicate that the hardening curve adopted is overstating the dissipation of energy at higher

intensities. An additional factor, which needs to be considered when looking at this discrepancy, is the inhomogeneity of the material's microstructure, which is composed of diamond particles dispersed in a copper matrix. On a microscopic level, the diamond particle size is an important factor, especially when compared to the wavelength of the travelling wave, since internal reflections in the material can become significant and have an effect on the high frequency content observed in the measured signal.

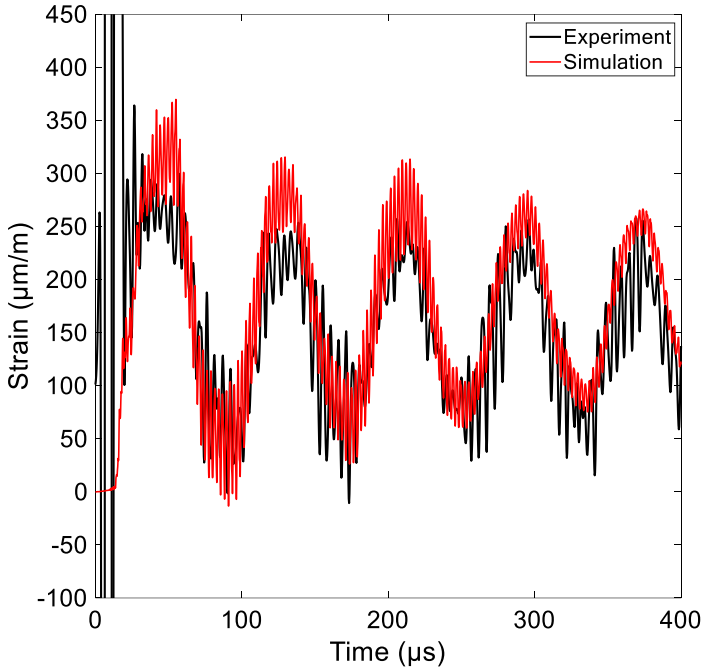

Figure 79 – Longitudinal response for simulation with hardening model against experimental data for shot 132.

4.4 Summary

Copper Diamond is the baseline material chosen for use in tertiary collimators in the upcoming HL-LHC upgrade, as a replacement of Inermet180. This chapter presents the thermomechanical characterisation campaign carried out at CERN for the measurement of various material properties of the CuCD RHP3434 grade, which was one of the CuCD grades recently tested in the MultiMat experiment conducted in CERN's HiRadMat facility. The campaign comprised of measurements for density, specific heat capacity, conductivity, and coefficient of thermal expansion, as well as impulse excitation technique testing for the computation of elastic constants. Additionally, a 4-point bending test was carried out, along with temperature sensitivity testing. The measurements conducted at CERN were used to build a mathematical model describing the material behaviour, which was applied in thermostructural analyses simulating various beam shots from the MultiMat experiment. Measurements from thermal probes and strain gauges from this experiment were used to

benchmark the material model.

The multilinear hardening material model obtained through the thermomechanical characterisation campaign described in this chapter proved accurate in replicating the shape of the signal obtained experimentally, improving on the purely elastic model in terms of longitudinal wave shape and amplitude relative to the experimental results. Despite this, one can see that the Young's Modulus computed from initial impulse excitation technique test measurements, equal to 194 GPa, underestimates the value observed in the MultiMat experiment measurements, resulting in a lower computed longitudinal frequency, with a 9% difference between the two values. The measurements were repeated on a number of specimens, showing that the Young's Modulus is actually significantly higher, as seen in comparisons between experimental and numerical results using the different elastic constants computed. The drastic difference in measurements is believed to be a result of the variability exhibited by different batches of the material, due to the relatively high level of porosity present.

Differences between the longitudinal wave results obtained experimentally and those generated numerically can be observed in terms of high frequency dissipative effects, which manifest as a loss of amplitude in the longitudinal wave. This discrepancy suggests that the hardening model adopted does not encompass the full range of behaviour of the material, which is represented as a homogeneous entity in the analyses conducted. On a smaller scale, the material is composed of diamond particles dispersed in a copper matrix, which results in stress waves propagating through the material having to travel from one medium to another. This leads to the propagating wave splitting into respective transmitted and reflective portions in accordance with the shock impedance of the two constituents. The longitudinal signal in experimental results can be seen to reduce in amplitude significantly following the first oscillation, which could similarly be related to this phenomenon.

The model proposed in this chapter can be seen to accurately predict the structural response of specimens tested in the MultiMat experiment. This is especially true in the calculation of flexural and longitudinal harmonics, with a 3.1% difference between experimental and numerical results in the longitudinal frequency, and only a 0.7% difference in the flexural frequency. The inclusion of a multilinear hardening curve to model the material's behaviour when loaded plastically can be seen to contribute significantly to improving the model's performance, aiding in producing numerical results which are closer to experimentally observed signals. The model is additionally able to replicate the longitudinal wave amplitude

in the scenarios considered, and is able to compute results relatively quickly due to its homogeneous nature, compared to more complex models discussed in the upcoming chapter. In the homogeneous model considered, loss of energy and wave dissipation are handled through the application of damping and the modification of the material's yield stress. This is fundamentally different from the wave-particle interaction discussed in section 5.1.4, where the mechanism in play is wave dispersion at the particle-matrix interface. Three main considerations are hence proposed for further study of the material, two of which are addressed in the next chapter, namely:

- *Modelling of internal material effects*

Longitudinal strain signals measured experimentally can be seen to decay as the wave propagates through the material. This phenomenon is believed to be a result of the inhomogeneous mesoscale structure of CuCD, which is composed of diamond particles with particle size ranging between 40 and 200 μm in a copper matrix, resulting in the stress waves propagating through the medium being split into transmitted and reflected portions, depending on the shock impedance of the two materials, resulting in the perceived decay of the signal. While such a phenomenon conserves the total energy of the system, dissipative effects related to internal friction are also believed to be contributing to this decay. The effects related to the microstructure of the material can be studied by modelling the diamond particles on a mesoscale level, continuing on the work proposed by Carra [19].

This phenomenon is the main topic discussed in Chapter 5, in which a homogeneous model and a mesoscale model are compared, with the former (i.e., the one used in this chapter) assuming a constant material behaviour across the geometry, and the latter attempting to model the structure of the composite on a mesoscale level, i.e., diamond particles dispersed in a copper matrix.

- *Strain-rate and temperature-dependent testing*

The presented thermomechanical characterisation campaign tested the material in quasistatic conditions at room temperature, which can result in a difference in material behaviour compared to the dynamic conditions induced by sudden particle beam impacts. The Split-Hopkinson bar test is designed to characterise material behaviour at elevated strain-rates and temperatures [158], allowing for the formulation of strength models, such as the Johnson-Cook and Zerilli-Armstrong models, which describe the material behaviour at these extreme conditions. Additional CuCD RHP3434 samples are to be produced by

RHP Technology and a Split-Hopkinson Bar test is planned to be conducted at the *Politecnico di Torino* at a later stage. Initial tests carried out on three sample specimens indicated that there could be some issues with measuring and disentangling the propagating signals, as a result of the roughness of the CuCD surface.

- *Formulation of the equation of state of the material*

While the strength model describes the deviatoric contribution to the stress tensor, the hydrostatic response of shocked materials is described by the equation of state (EOS). The EOS describes the state of matter in a given set of conditions, such as pressure, density, temperature, etc. The Mie-Grüneisen equation of state is used to describe the relationship between pressure, volume and temperature of shock-compressed solids, and can be derived for CuCD by considering the Shock-Hugoniot curves available for copper and diamond provided by LANL [159]. This topic is discussed further in Chapter 5.

Chapter 5:

Mesoscale modelling of Copper Diamond

5.1 Wave-Particle Interactions in Copper Diamond

So far, in this study, CuCD has been represented by isotropic homogeneous elastic and elastic-plastic models, with the assumption that diamond particles are uniformly distributed and small with respect to the dimensions of the body. Based on the results achieved in Chapter 4, the composite structure of the material is believed to have a significant impact on material behaviour, limiting the accuracy of homogeneous models in wave propagation applications. This chapter aims to investigate the mesoscale behaviour of the material and determine the advantages and limitations of modelling the structure of the composite on a mesoscopic level. The calculation of the Mie–Grüneisen equation of state for Copper Diamond is presented later on in the chapter, calculated from the Shock Hugoniot data available for the constituent materials.

5.1.1 Stochastic Media and Copper Diamond

The structure of many real, non-idealised media is quite complicated, and thus the idealisation of such media as a homogeneous continuum is generally only valid up to a limiting scale of magnitude. Classical elasticity theory is typically applied to metals, which on a microscale level are polycrystalline in nature, i.e., they are made up of a number of randomly oriented anisotropic crystals. Similarly, material composites are comprised of a mixture of different materials with varying properties, leading to complex heterogeneity which sometimes cannot be accurately idealised as a homogeneous continuum.

Copper Diamond is one such example of a composite material made up of a mixture of two constituents, namely diamond particles encased in a copper matrix. The material can thus either be described as a homogeneous medium, which is the case when testing for material properties using conventional tools such as the 4-point bending test, or as a stochastic heterogeneous medium composed of a random distribution of diamond particles in copper. The diamond particles have thermomechanical properties which are significantly different from those of the surrounding material. The composition is similar to what is seen in plastic composites, where small spherical particles are commonly added to increase sound absorption and stiffness. Comparably, metal solutions frequently separate in distinct phases, which can be globular, such as spheroidised steel-carbide spheres in a ferrite matrix.

Wave propagation in stochastic media has been studied extensively by Sobczyk [160], who considered scalar and vector waves such as elastic waves in stochastic solids, thermoelastic

waves, as well as wave scattering at stochastic surfaces. Wave propagation in inhomogeneous media is intrinsically coupled with the phenomenon of scattering, which gives rise to a number of interesting physical effects such as wave attenuation, that is, the loss of energy of a propagating wave and the resulting reduction in the strength of the recorded signal. This phenomenon is closely related to the dispersion of energy caused by wave distribution to a larger volume of material as it propagates radially through a material.

Most studies on the subject of wave propagation in stochastic media are based on various simplifications and assumptions of physical hypotheses, one such assumption being that the studied stochastic medium is only weakly inhomogeneous, i.e., fluctuations of properties are relatively small. This is not always the case, especially when characteristic lengths of the propagating wave, such as the wavelength, approach those of the material's inhomogeneities, as is the case for diamond particles in CuCD.

5.1.2 Composites containing dispersed spherical inclusions

5.1.2.1 Analytical methods

One of the fundamental problems of mixture theory is the determination of gross material properties from those of its respective constituents. For simplicity's sake, one can consider the propagation of one-dimensional elastic waves in a two-phase elastic material composed of the matrix and rigid spherical inclusions. The average static material properties for such a two-phase elastic material were found by Hashin [161], perhaps most famous for his publication on failure criteria for unidirectional fibre composites [162]. Hashin developed a system to compute the elastic properties, thermal expansion and strength of composite materials for military and aerospace applications. However, the calculated average modulus was limited to low-frequency wave applications, and such a method is not ideal for the determination of the dispersive effects of waves in inhomogeneous media.

Dynamic effects in elastic fibre composites, i.e. layered materials or dispersed rods, have also been researched by Herrmann and Achenbach [163], who studied wave propagation in the layered direction. While dispersion effects were observed for harmonic waves, the study did not observe any wave attenuation. This was believed to be a result of the periodic nature of layering, as well as what is referred to as the boundedness of the body in the direction normal to the wave propagation direction, which results in the confinement of energy.

Micropolar elasticity theories have also been formulated, attempting to incorporate local motions of structured solids through the inclusion of additional constitutive constants. While such theories are able to provide a certain level of consistency and rigor, the additional constants cannot be completely determined from the material properties of the material constituents [164].

The topic of wave propagation in composite materials having dispersed spherical inclusions was studied extensively by Moon and Mow [165], who built on previous solutions for the scattering of elastic compressional waves from rigid inclusions in elastic media [166], [167]. The work namely describes the problem in a number of steps: the general motion of a rigid inclusion, a homogenised model of an elastic mixture, and wave propagation in such a material. Pao and Mow's solution for the equation of motion for a spherical inclusion takes the form of a damped oscillator with memory, similar to a homogeneous viscoelastic spring [166]. This solution, and its implications for wave scattering, is used by Moon and Mow as the basis for the construction of a model of an elastic matrix with randomly distributed spherical inclusions. As discussed in their study, while in periodic inclusion distributions the scattered waves will either reinforce or cancel each other in certain patterns, forming cut-off bands in the frequency spectrum, this is not necessarily the case in a stochastic medium. Instead, their research aimed to formulate a model which could be used to determine the dispersion and attenuation properties of harmonic longitudinal waves taking into consideration the size of the inclusions, their volumetric distribution in the material, and the elastic properties of the matrix. The study concludes that if the wavelength is large compared to the radius of inclusions, the matrix obeys the wave equation, and the average density of the composite may be used to calculate the resulting wave speed. Otherwise, for wavelengths which are similar in length to the inclusion radius, the material will be both dispersive and dissipative.

The implication of dispersion is that the wave velocity depends on the frequency of vibration. Given that pulsed waves are composed of a spectrum of frequencies, the propagation of such a pulse in a dispersive medium results in spreading, with each frequency component travelling at its own phase velocity. Pao and Mow's model allows for the prediction of the damping time constant for longitudinal motion by considering the thickness and material properties of the matrix, the inclusion density, and the inclusion size.

As detailed, attenuation is the measure of the energy loss of propagating acoustic waves.

This is a result of the fact that most media are viscous and non-ideal. This thus implies that there is thermal consumption of energy as an acoustic wave travels through the material, as a result of the medium's viscosity. For an inhomogeneous medium such as CuCD, acoustic scattering additionally contributes to the reduction in acoustic energy [168]–[170]. The acoustic attenuation coefficient for various porous and viscoelastic materials can be expressed in terms of frequency as a power law:

$$P(\mathrm{x}+\Delta\mathrm{x}) = P(x)e^{-\alpha(\omega)\Delta\mathrm{x}}, \alpha(\omega) = \alpha_0\omega^{\eta} \tag{41}$$

Where P is the pressure, $\Delta\mathrm{x}$ is the wave propagation distance, ω is the angular frequency, $\alpha(\omega)$ is the attenuation coefficicent, α_0 is a frequency-dependent exponent, and η is a material parameter obtained by fitting experimental data, ranging from 0 to 2 [171]–[173]. η is equal to 2 for many metals, crystalline materials, and water, i.e., they are frequency-squared dependent. For viscoelastic materials, this value is generally less than 2 – for example, for rock and soil η is roughly equal to 1 [174], [175]. In the case of porous and dispersed-particle composites, one could additionally add an exponent considering the wavelength of the propagating wave, depending on its length relative to the porosities or dispersed particles.

5.1.2.2 Numerical methods

In finite element analyses, composite materials are generally modelled by performing experimental testing to determine the global, i.e., homogeneous, material properties, which can be both costly and time consuming. The numerical simulation of complete composite structures is particularly challenging due to the different length scales involved, with the composite structure being much smaller than the actual component. In theory, FEM could be used to structurally simulate such a system on all scales, however this is not computationally practical, requiring an incredibly large number of elements and contact points. Such multi-scale simulations, or fully coupled numerical analyses, model all dimension ranges of the material's structure, i.e. there is a separate microscopic finite element analysis for each integration point on a macroscopic level [176].

The issue of multi-scale simulations being so computationally expensive is solved through the process of homogenisation, where material properties of the different constituents making up the composite are averaged to obtain homogenised material data which can then be used to simulate the structure on a macroscopic scale. Homogenisation can be done

through an analytical approach, as described in the previous sections, using methods such as the rule of mixtures or mean-field homogenisation [177]. Numerically, solutions have been proposed to determine more accurate homogenised material properties of composites, by considering the material properties of representative elements of the material structure. ANSYS Material Designer is one such program which facilitates the modelling and parametrisation of composites to determine their material properties. The software is readily-available, being a component system in ANSYS Workbench [178].

Material Designer and similar software packages perform a single pre-processing step which results in the calculation of homogenised material data, thus allowing for the simulation on a macroscopic level. This can only be done if there is significant scale separation, that is, the macroscale structure must be significantly larger than the microscale [179]. The composite material is assumed to have a representative microscale structure, referred to as a representative volume element (RVE), which is still large enough to exhibit the material's macroscopic properties. The RVE can be described as a sample of a heterogeneous material which is typical of the whole mixture on average, and one that represents a composite statistically [180], [181]. Thus, the volume should include a sample of all microstructural inhomogeneities of the composite material, such as inclusions, voids and fibres. In general, the required size for an RVE increases with an increase in the mismatch in material properties between the different constituents.

For periodic materials, an RVE can be identified as a unit cell which repeats itself in all directions, as shown in Figure 80. For non-periodic materials, a more complex approach needs to be adopted in order to determine a large enough volume where any further changes to the representative element do not change the macroscopic properties significantly [182]. Once the RVE is modelled, the material properties of the constituent materials can be defined, and the geometry can be meshed for finite element analysis. The RVE is subsequently exposed to a number of macroscopic load cases, which are followed by the calculation of the structural response of the structure. This allows one to calculate the homogenised material data of the material, as visualised in Figure 81.

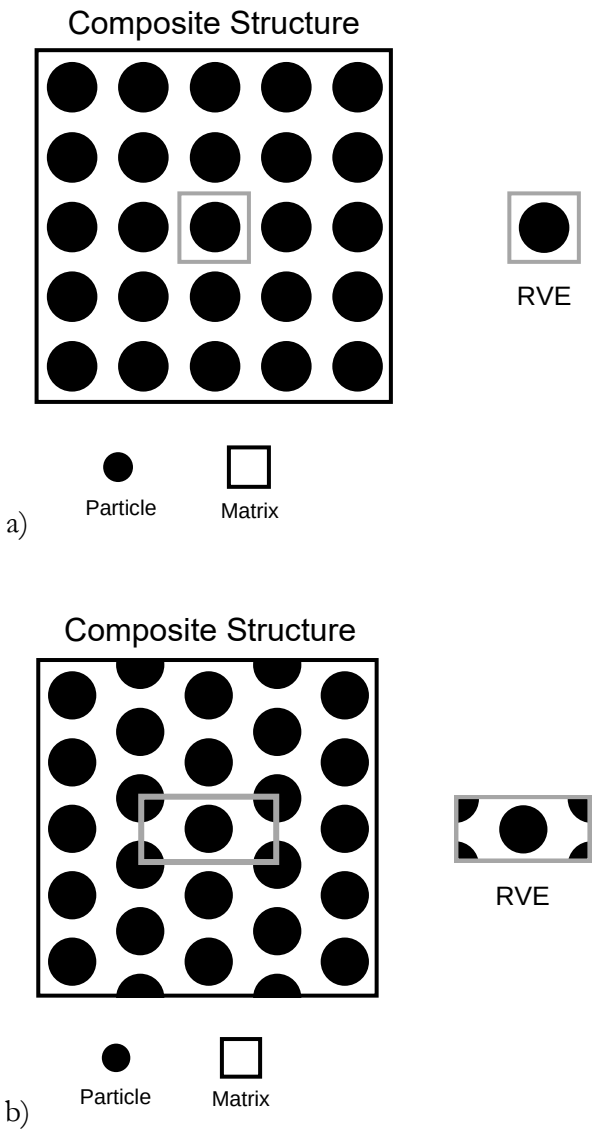

Figure 80 – Representative Volume Element for a periodic composite composed of a matrix with spheroidal particles organised in a square array (a) and in a hexagonal array (b).

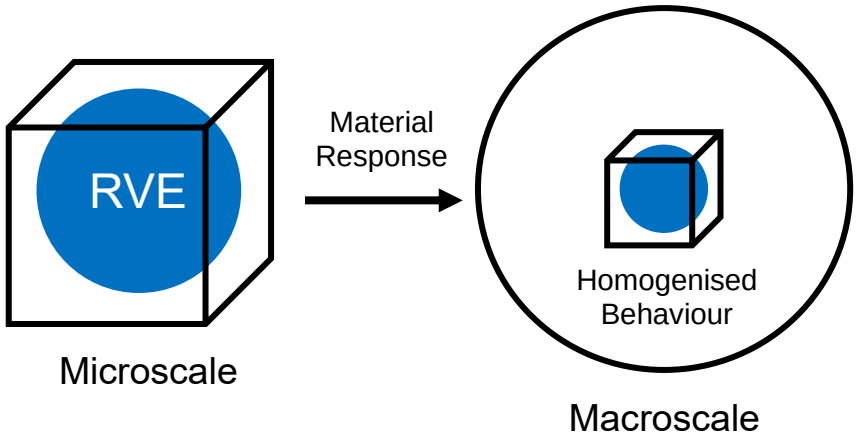

Figure 81 – Representative Volume Element of a simple periodic composite in the microscale, from which the material response is determined to compute the macroscopic homogenised behaviour of the material.

5.1.3 Wave attenuation effects in Copper Diamond

Wave attenuation in Copper Diamond is a topic which has not been studied extensively in the context of particle accelerator technology and wave propagation induced by particle beam impacts [19]. In the HRMT23 experiment conducted at CERN's HiRadMat facility, an accidental scenario equivalent to an HL-LHC asynchronous beam dump was tested on a CuCD absorber composed of ten 10 cm blocks in series, for a total length of 1 metre [183]. The thermomechanical scenario was also modelled in ANSYS Mechanical, along with additional components such as the clamping system and related pre-tension, Glidcop housing, and cooling pipes. Two material models were tested, one purely elastic model and an elasto-plastic model. The elastic model was observed to drastically overestimate the dynamic strain values measured experimentally, while the elastoplastic model provided a better fit with experimental data. However, the experimentally measured strain signal was observed to quickly decay following a few oscillations, contrasting with the wave propagation in the numerical elastoplastic model, where stress waves decayed in amplitude down to the elastic limit, following which no further energy dissipation occurred. One should also note that this analysis was extended to include modelling of the collimator jaw casing and clamping. This was found to have little effect on the reduction in strain amplitude with time, reinforcing the idea that the rapid decay in amplitude was not caused by the introduction of frictional contacts with the surrounding structure, but rather due to internal material effects. As discussed in the study, Kolsky [184] used the general term "internal friction" to refer to such dissipative phenomena in materials.

On a mesoscopic level, CuCD has a highly inhomogeneous structure which is composed of diamond particles of approximately 100 μm in diameter, embedded in the copper matrix. A material's shock impedance, found by multiplying the density with the speed of sound in the material, is a measure of the interaction between shock waves and a material's interface. Due to the material's high speed of sound, the shock impedance for diamond is approximately two times more than that of copper (61.8 MPa.s.m^{-1} vs 33.8 MPa.s.m^{-1} in the case of an elastic wave in uniaxial conditions) [19]. Assuming that the wavelength of the travelling wave is small compared to the diamond particles, the relative amplitude of transmitted and reflected waves travelling through a copper-diamond interface can be calculated. Carra examined the effect of this particle impedance mismatch by modelling in 2D an infinitely long bar submitted to a sinusoidal excitation in a transverse direction [121]. Three main models were considered, namely a mesoscale model with polygonal diamonds in a copper matrix, and two homogeneous CuCD models with a purely elastic and a viscoelastic material model. The model was restricted to diamonds occupying 30% of the total volume to minimise computation time, the diamond particles were scaled to 2 mm in width, and the sinusoidal excitation had a wavelength in the order of 7 mm for a pulse length of 2 μs. The mesoscale model showed a strong dispersion in the signal as the wave progressed through the material, as a result of the continuous wave-particle interaction at the copper-diamond interface. This was not captured in the homogeneous elastic model, which showed only a slight decay as a result of dispersive phenomena. The homogeneous viscoelastic model, being time-dependent, showed a combination of both dispersion and dissipation and consequently exhibited a larger amplitude decay compared to the elastic model. A similar analysis was conducted with a pulse length of 10 μs, and consequently a wavelength in the order of 35 mm. For the mesoscale model, this resulted in less dissipative effects due to particle-wave interactions. In this case, the viscoelastic model was closer to the mesoscale model in terms of the modelled amplitude decay.

It is interesting to note that, despite the fact that signal damping effects seem to be mostly evident in cases where wavelengths are close to the diamond particle diameter, the dominating frequencies in beam intercepting devices are a result of the structure's geometry, which amplifies frequencies that correspond to the block dimensions. In truth, the harmonic response is a result of a combination of factors, one of which is indeed the geometry, and the other being the beam parameters, most importantly the pulse duration, which determines the input spectrum to which the rod is subjected to, which theoretically includes an infinite number of frequencies.

5.1.4 Mesoscale Modelling of Copper Diamond

Building on the previous studies on mesoscale effects in material composites discussed in the previous section, this study aims to better understand how the mesoscopic structure of the CuCD RHP3434 grade tested in the MultiMat experiment affects the dynamic response of the material. In the thermomechanical simulations carried out in section 4.3, the material was treated as being homogeneous in nature, and the material model was built by considering data collected from standard mechanical tests which represent the material behaviour as a whole. In most scenarios, this results in acceptable calculations which closely match experimental measurements. As explained in section 5.1.3, in dynamic scenarios, especially in cases where the wavelength of propagating waves is similar to the diamond particle diameter in the composite, the inhomogeneous nature of the material is believed to result in significant disparities between experimental data and results achieved with a homogeneous model, even when plasticity is included.

As previously detailed, the CuCD grade considered in this study and tested in the MultiMat experiment, referred to as CuCD RHP3434, consists of a 50-50 volume percentage of copper matrix and diamond particles, hot pressed in a spark plasma sintering process. The mixture also includes a small percentage of carbide-forming binding elements, which aid in binding the diamond particles with the copper matrix. The material has a measured porosity of approximately 8%, calculated by considering the ideal density of the material mixture and the measured density. The diamond particles range between 40 and 200 μm in size.

A number of numerical models were considered to analyse the mesoscale behaviour of the material, and how this compares to homogeneous material models presented in this thesis . As a starting point, a 1 mm by 0.5 mm specimen was modelled in 2D. The model assumes an infinitely long rod (i.e., in plane strain) subjected to an external force on one of its shorter sides. The model was similarly implemented in plane stress conditions, with comparable results achieved. Both scenarios do not model the physical problem perfectly, but serve as an adequate benchmark for comparison between homogeneous and mesoscale momdels. A schematic of homogeneous and mesoscale models adopted is shown in Figure 82. The mesoscale model is composed of a 50-50 distribution between the copper matrix and the dispersed circular diamond particles, which have diameters ranging from 40 to 200 μm. The rod is free to move, bar for a symmetry line on the lower edge which restricts vertical movement. An external impact with a rectangular pulse and an amplitude of 100 N is applied to the left side of the model, for a period of 20 ns. Three material models were

initially tested, namely a purely elastic homogeneous model, an elastoplastic homogeneous model, and a mesoscale model with relevant elastic constituent data for the copper and diamond.

A summary of structural material properties at room temperature used for the CuCD homogeneous elastic model, as well as the constituent material data for diamond and copper used in the mesoscale model, are shown in Table 24.

Table 24 – Elastic material properties for the modelling of an internal heat generation in copper diamond for homogeneous and mesoscale models [185].

	E	**ν**	**ϱ**	**CTE**	**C_p**	**k**	**c_0**
	GPa	-	*kgm^{-3}*	*10^{-6} K^{-1}*	*$Jkg^{-1}K^{-1}$*	*$Wm^{-1}K^{-1}$*	*ms^{-1}*
Copper Diamond	220	0.248	5700	6.7	395	537	6200
Pure Copper	130	0.3	8900	17	385	398	3800
Carbon (Diamond)	1143	0.0691	3530	1	520	1000	18000

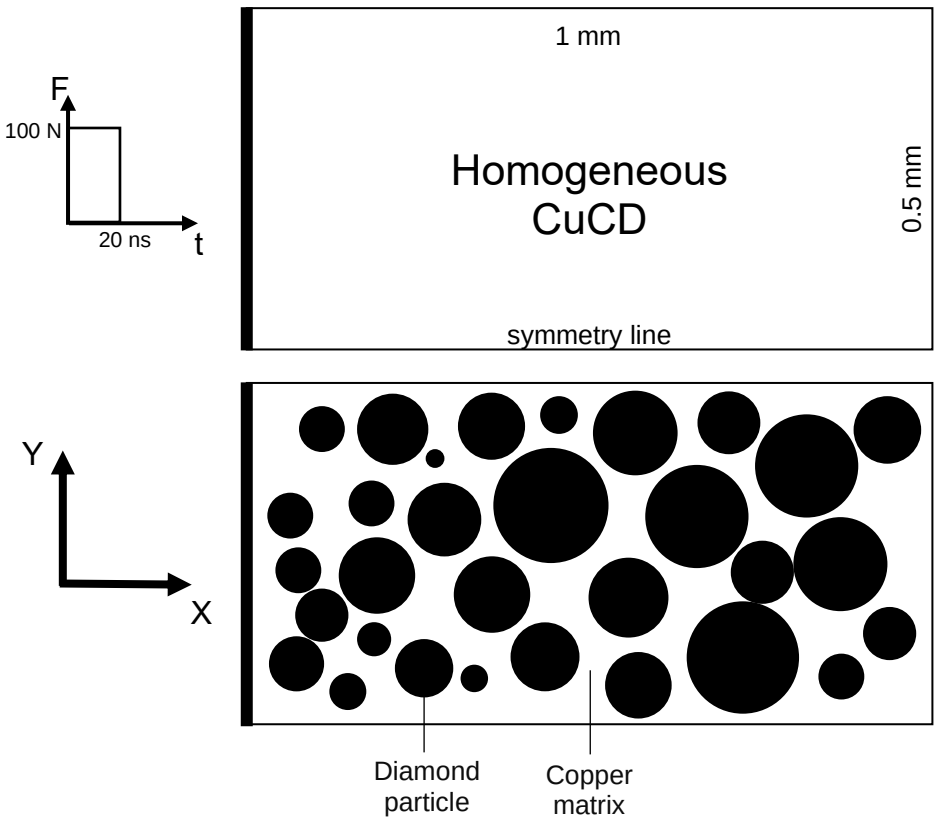

Figure 82 – Homogeneous CuCD geometry (top) and mesoscale copper-diamond geometry (bottom). 100 N force applied in the X-direction to the left side of each model with a rectangular pulse duration of 20 ns.

The resultant stress wave travelling through each specimen can be seen by considering the stress along the centreline at different timepoints, as shown in Figure 83. In the case of the homogeneous elastic model, there is only a very slight decay in the signal related to dispersive phenomena, while the homogeneous elastoplastic model introduces a degree of dissipation as a result of plasticity. This is observed in the stress wave travelling through the material, which decays heavily as it traverses the length of the specimen. The mesoscale model, which is composed of purely elastic constituents, can also be seen to result in a significant decay in the stress wave, which can be attributed to the signal dispersion caused by the continuous reflection of the wave at the copper-diamond interface. Considering the speed of sound in copper diamond, the wavelength of a 20 ns pulse is in the order of 120 μm, which is in the range of sizes of the diamond particles. A longer pulse, with a period of 100 ns and a wavelength in the order of 600 μm, was similarly modelled, the results of which are shown in Figure 84. In this case, as expected, there is a less pronounced decay in the signal from the mesoscale model, although wave dispersion is more prominent.

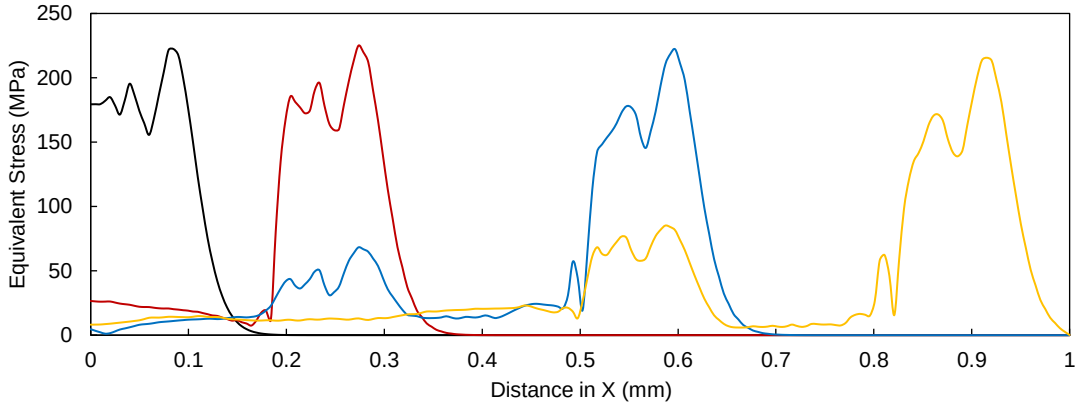

(a)

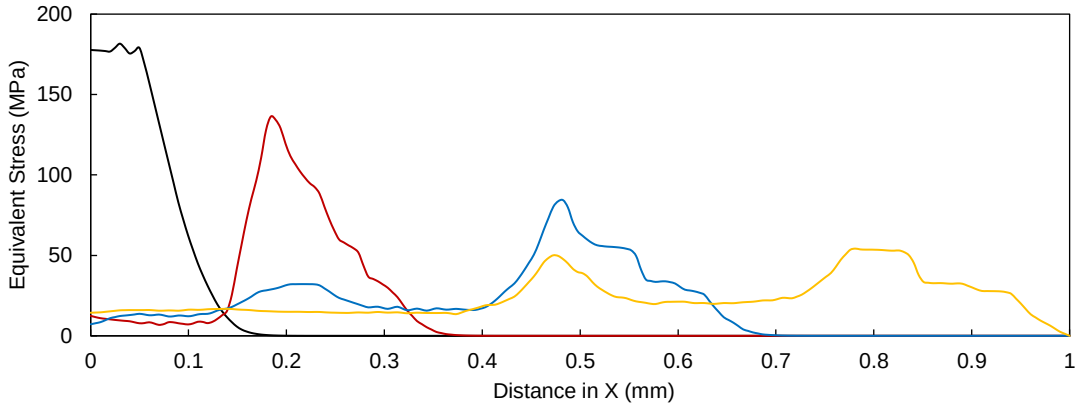

(b)

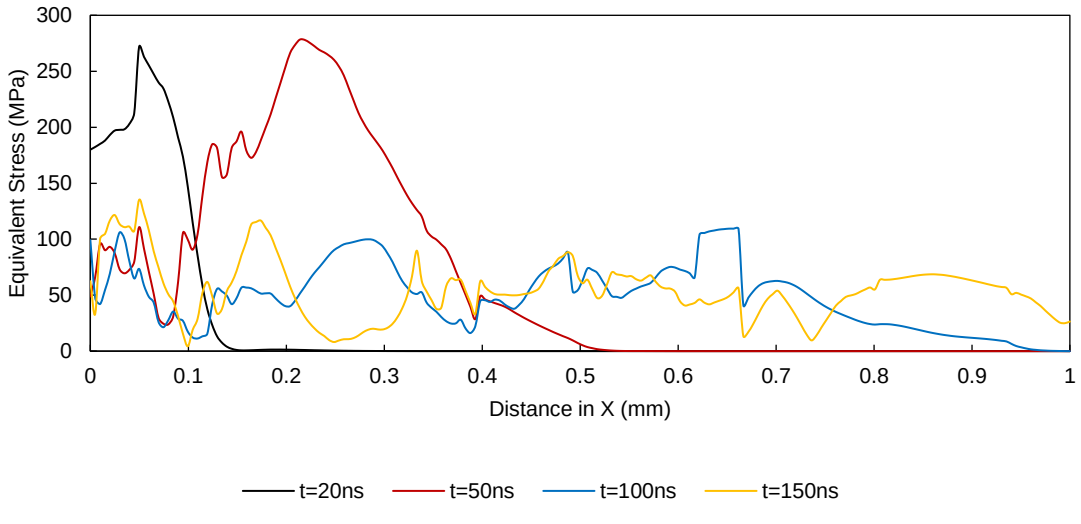

(c)

Figure 83 – Stress wave with 20 ns time period travelling through homogeneous elastic (a), homogeneous elastoplastic (b), and mesoscale CuCD (c) specimens.

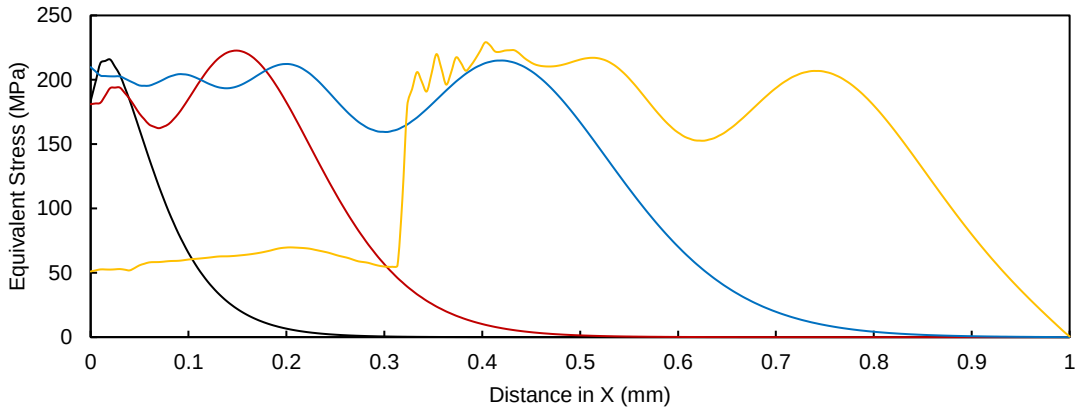

(a)

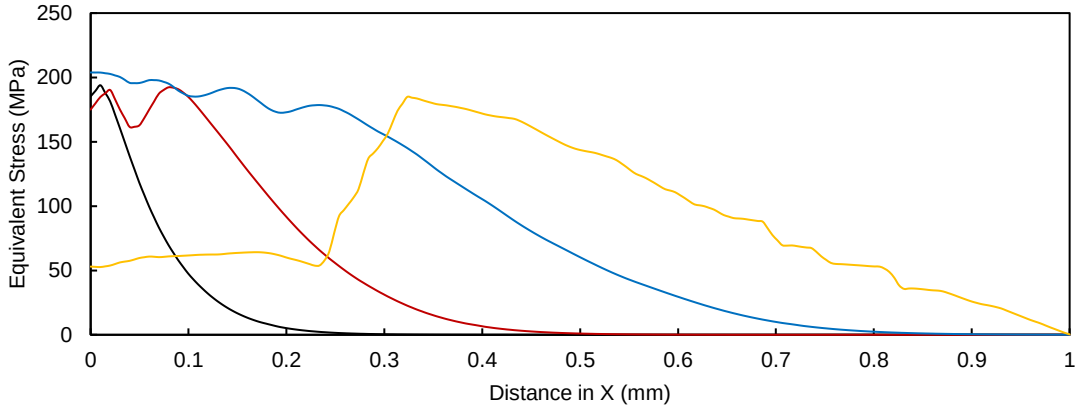

(b)

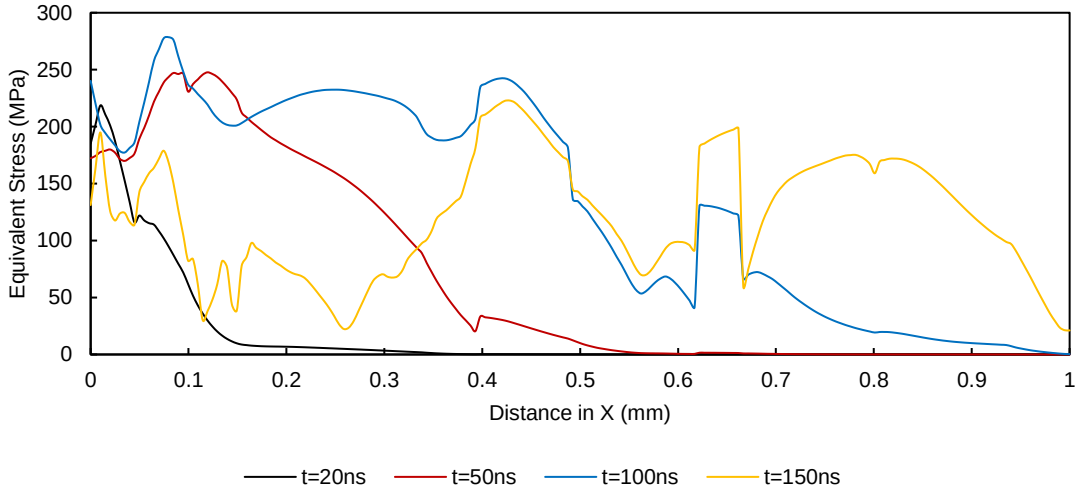

(c)

Figure 84 – Stress wave with 100 ns time period travelling through homogeneous elastic (a), homogeneous elastoplastic (b), and mesoscale CuCD (c) specimens.

Since the application of interest for copper diamond in this work is related to beam intercepting devices, where the material is subjected to sudden increases in internal temperature as a result of the interaction between subatomic particles and the material, an attempt was made to model such a scenario on a mesoscale level.

Similar to the structural analyses described above, two main types of models were tested, namely a homogeneous model and a mesoscale model. A specimen measuring 6 mm by 1 mm, with symmetry for a total effective length of 12 mm, was once again modelled in 2D, as shown in Figure 85. The mesoscale model consisted of a copper matrix with 375 diamond particles each having a diameter of 100 μm, for a 50-50 percentage area distribution. The same material models described in the previous analysis (shown in Table 24) were utilised. Note that for a length of 12 mm, the fundamental period for vibrations for Copper Diamond is $t_L = 2L/c_0 = 3.9\,\mu s$, where L is the length (12 mm) and c_o is the speed of sound (approximately 6200 m/s for CuCD).

The simulation, conducted in ANSYS Mechanical, consisted of a simply coupled thermomechanical analysis, starting with a 2D thermal analysis which consisted of an internal heat generation throughout the specimen, aiming to achieve maximum temperatures comparable to those experienced in specimens tested in the MultiMat experiment. This results in a uniform temperature increase in the homogeneous model, but, due to the different thermal properties of copper and diamond, there is a different temperature increase in the two materials. The results from the thermal simulation were applied as a thermal load in a 2D (plane strain) structural analysis.

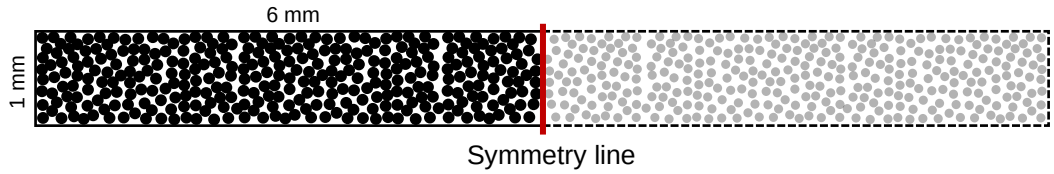

Figure 85 – Mesoscale models adopted for the modelling of an internal heat generation and its effects.

Two pulses were considered, namely 300 ns and 20 ns long, corresponding to typical energy depositions in the MultiMat experiment for CuCD samples. For the 300 ns shot, an intensity of 10^{15} W/m^3 was applied in the thermal analysis. The 20 ns shot was modelled with a scaled intensity of 1.5×10^{16} W/m^3, resulting in an equal total deposited energy for the two scenarios considered. As mentioned, the energy deposition for both scenarios results in an internal temperature similar to that achieved in the MultiMat experiment. For

the 300 ns shot, the maximum temperature in the homogeneous model was equal to a uniform 138°C in the geometry. For the mesoscale model, the diamond particles reached a maximum of 185°C, while the copper matrix reached 107°C following the energy deposition (for an average temperature of 146°C at the end of the energy deposition). Similar results were achieved for the 20 ns shot, with slightly higher maximum temperatures and lower minimum temperatures due to the faster energy deposition (and therefore less time for heat to dissipate throughout the body during the pulse duration). Thermal analysis results at 300 ns and 20 ns for the two shots considered are shown in in Figure 86.

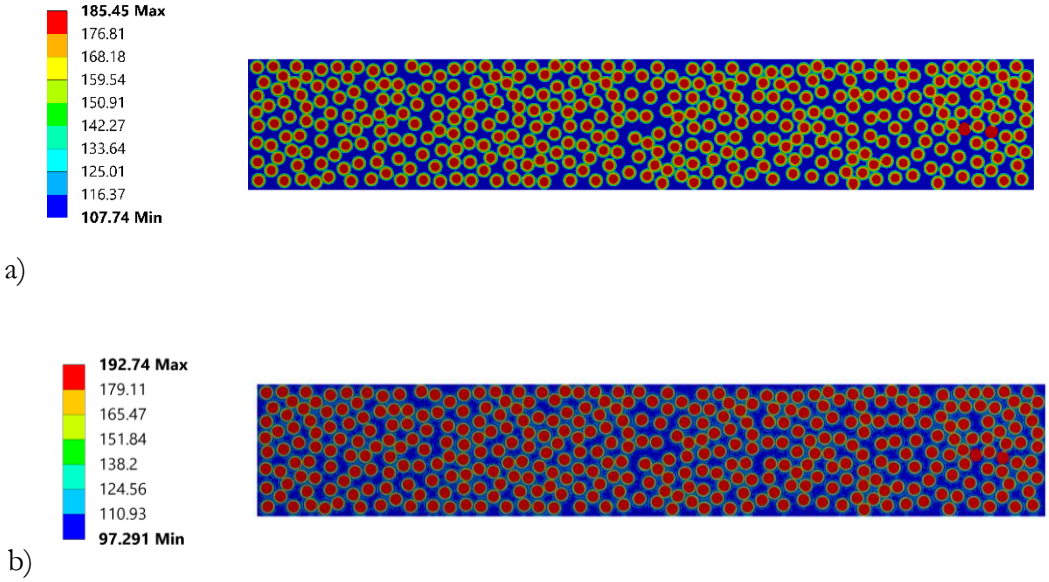

Figure 86 – Temperature reached (in °C) in the mesoscale model at the end of the energy deposition for the two shots considered (a, at 300 ns) and (b, at 20 ns) with total intensity of 10^{15} W/m^3 and 1.5×16^5 W/m^3 respectively.

For the structural analysis, the material model used for the copper matrix was updated to include a bilinear kinematic hardening model for the inclusion of plasticity, with a yield strength of 200 MPa and a tangent modulus of 160 MPa. Four scenarios were thus considered:

- Homogeneous CuCD model with elastic material properties;
- Homogeneous CuCD model with plasticity (multilinear hardening curve);
- Mesoscale model with elastic material properties;
- Mesoscale model with plasticity in the copper matrix.

The resulting respective expected wavelengths for the two shots, considering the geometry of the modelled samples, along with the points on the model at which results of interest were probed, are shown in Figure 87.

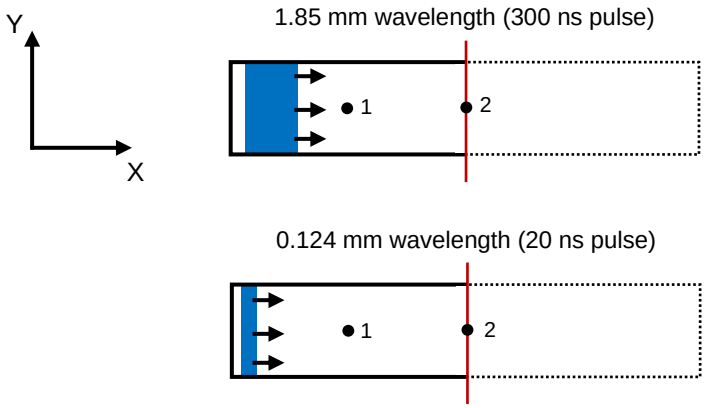

Figure 87 – Position of probe points on specimen, and wavelength (in blue) and direction for 300 and 20 ns pulses (not to scale).

Figure 88 and Figure 89 respectively show the longitudinal strain results probed at the centre of the simulated specimen (i.e., at a longitudinal length of 6 mm and a transverse length of 0.5 mm) for the modelled 300 ns and 20 ns shots respectively. The figures show results for the four simulated models, namely a homogeneous model with elastic properties, a homogeneous model with the inclusion of elastoplastic properties (the multilinear hardening curve obtained through a four-point bending test), a mesoscale model with 100 µm diamond particles with elastic properties, and a mesoscale model with an elastoplastic model for the copper matrix.

All elastic models can be seen to have very similar frequencies, indicating that the homogeneous model's elastic properties manage to average the material's mesoscale behaviour well in terms of wave propagation effects. As can be seen, the inclusion of plasticity in the copper matrix of the mesoscale structure results in a significant decrease in the amplitude of the propagating wave, when compared to the same model with elastic properties. For the 300 ns shot, results from the mesoscale model with plasticity (blue) are comparable to those for the homogeneous elastic model (black), with the amplitude maintained for various oscillations. In contrast, in the homogeneous elastoplastic model energy dissipation (as a result of the included plasticity) results in an observable decay in amplitude, as well as a significant reduction in frequency due to the change in stiffness. For the 20 ns shot, one can observe a significant increase in high-frequency content. While this can be explained by the magnitude of the wavelength, which is approximately the same size as the diamond particles, the disturbances can also be observed in the homogeneous elastic model, suggesting that these are dispersive effects as a result of wave-boundary interaction.

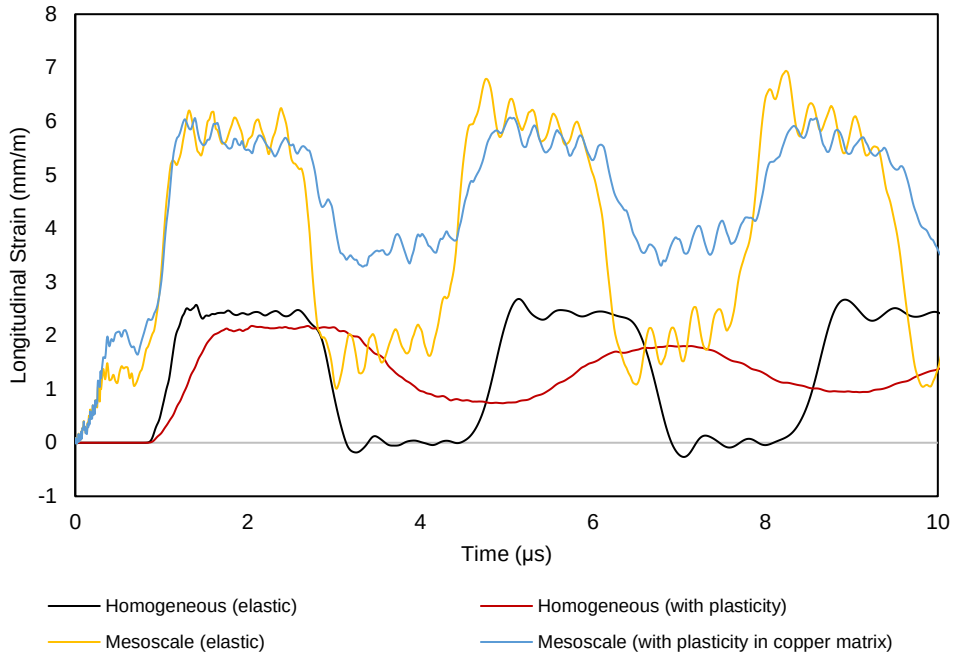

Figure 88 – Normal strain results for the 300 ns shot at the centre point of the specimen.

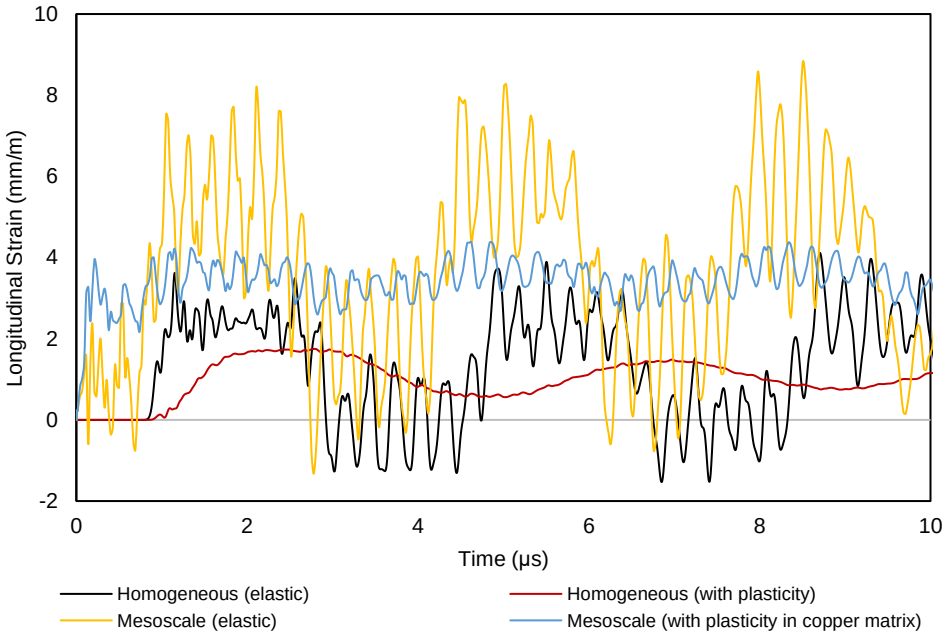

Figure 89 – Normal strain results for the 20 ns shot at the centre point of the specimen.

The state of longitudinal strain in the geometry at different time intervals for the 300 ns shot is shown in Figure 90, Figure 91 and Figure 92 for the homogeneous elastic, mesoscale elastic, and mesoscale with plasticity in the copper matrix models respectively. The state of longitudinal strain in the geometry at different time intervals for the 20 ns shot is shown in Figure 93, Figure 94, and Figure 95 for the homogeneous elastic, mesoscale elastic, and mesoscale with plasticity in the copper matrix models respectively.

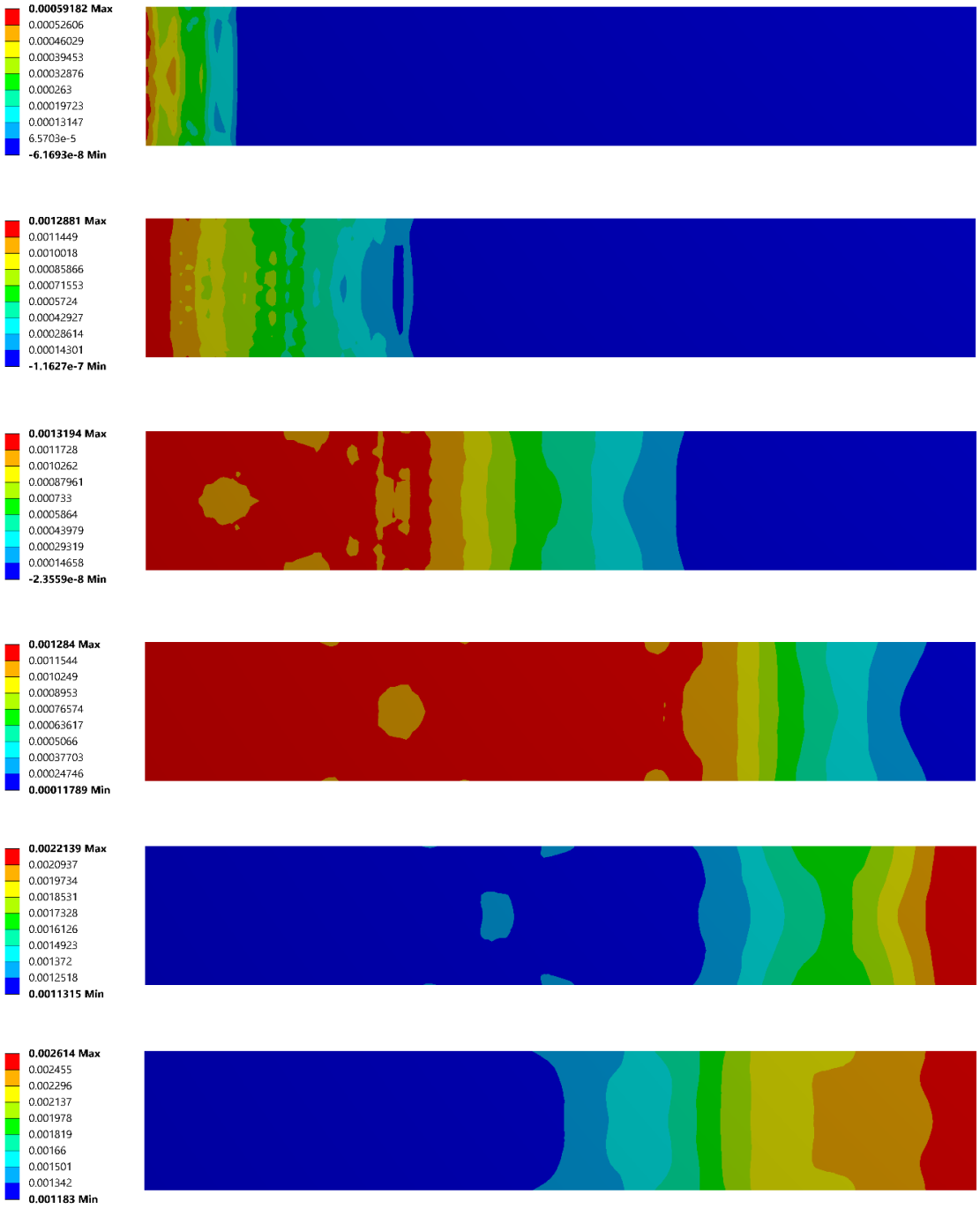

Figure 90 – Longitudinal strain state at 100, 300, 600, 900, 1200 and 1400 ns (respectively from top to bottom) for the homogeneous elastic model, subjected to 300 ns internal heat generation.

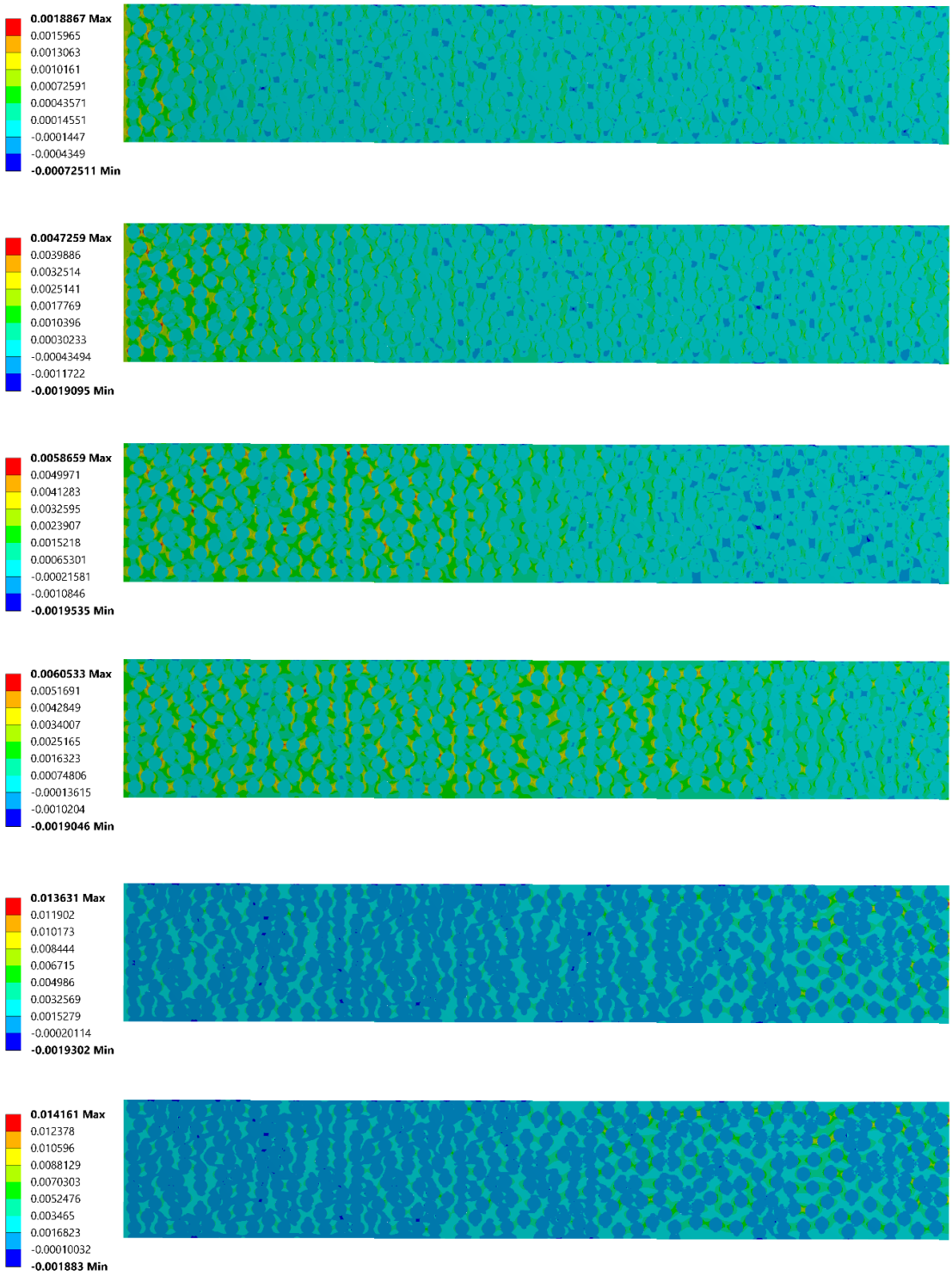

Figure 91 – Longitudinal strain state at 100, 300, 600, 900, 1200 and 1400 ns for the mesoscale model with elastic properties, subjected to 300 ns internal heat generation.

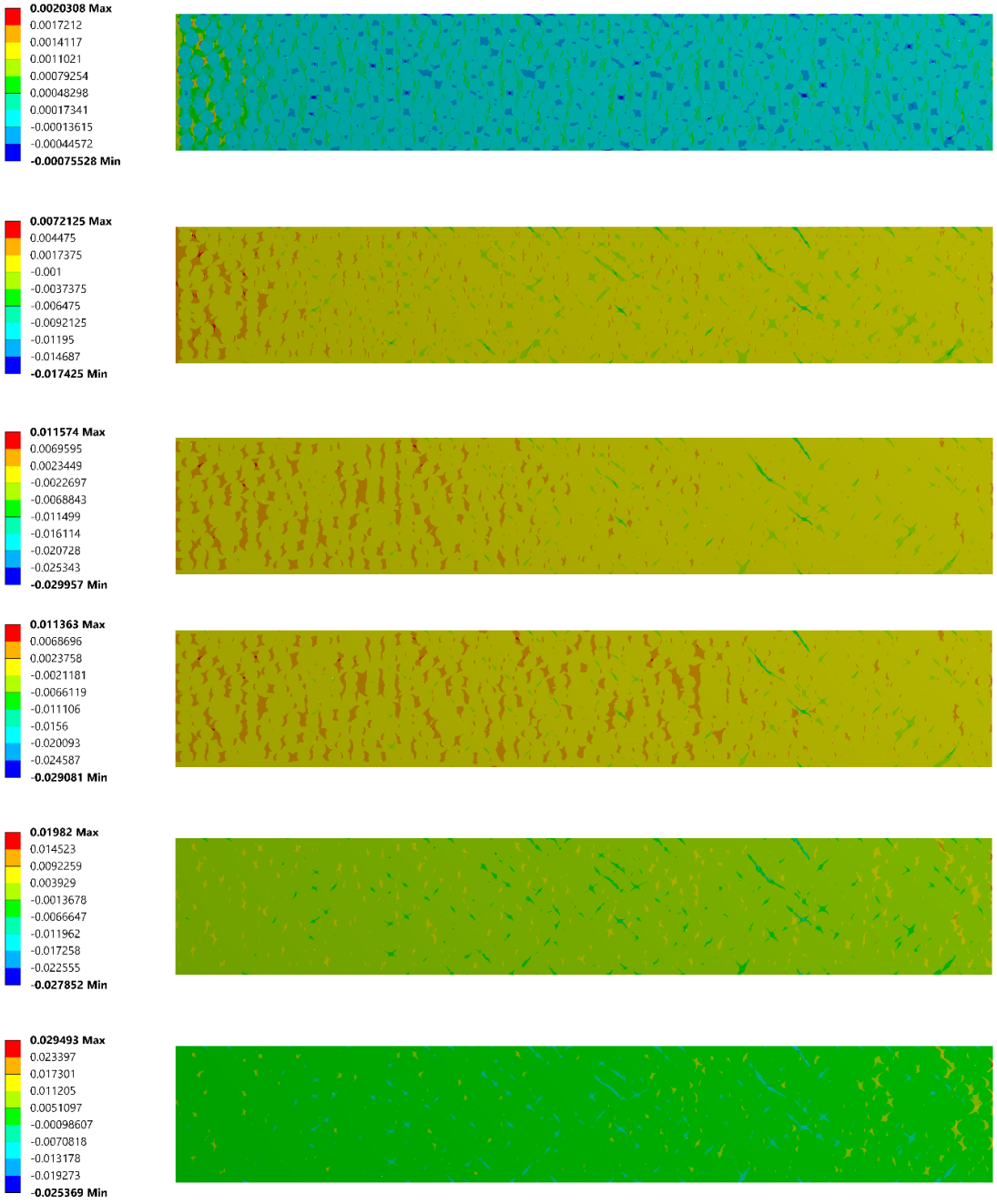

Figure 92 – Longitudinal strain state at 100, 300, 600, 900, 1200 and 1400 ns for the mesoscale model with plasticity in the copper matrix, subjected to 300 ns internal heat generation.

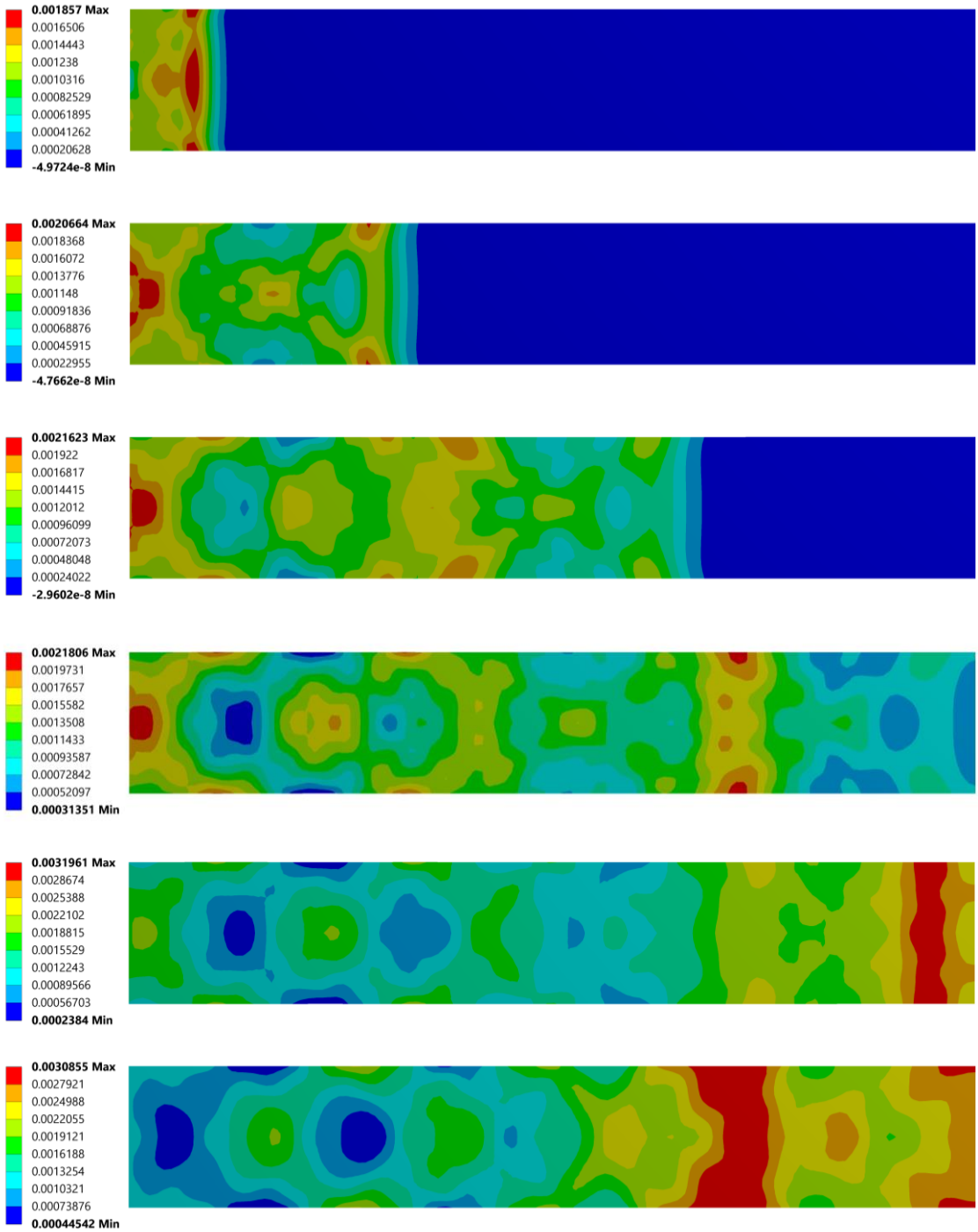

Figure 93 – Longitudinal strain state at 100, 300, 600, 900, 1200 and 1400 ns for the homogeneous elastic model, subjected to 20 ns internal heat generation.

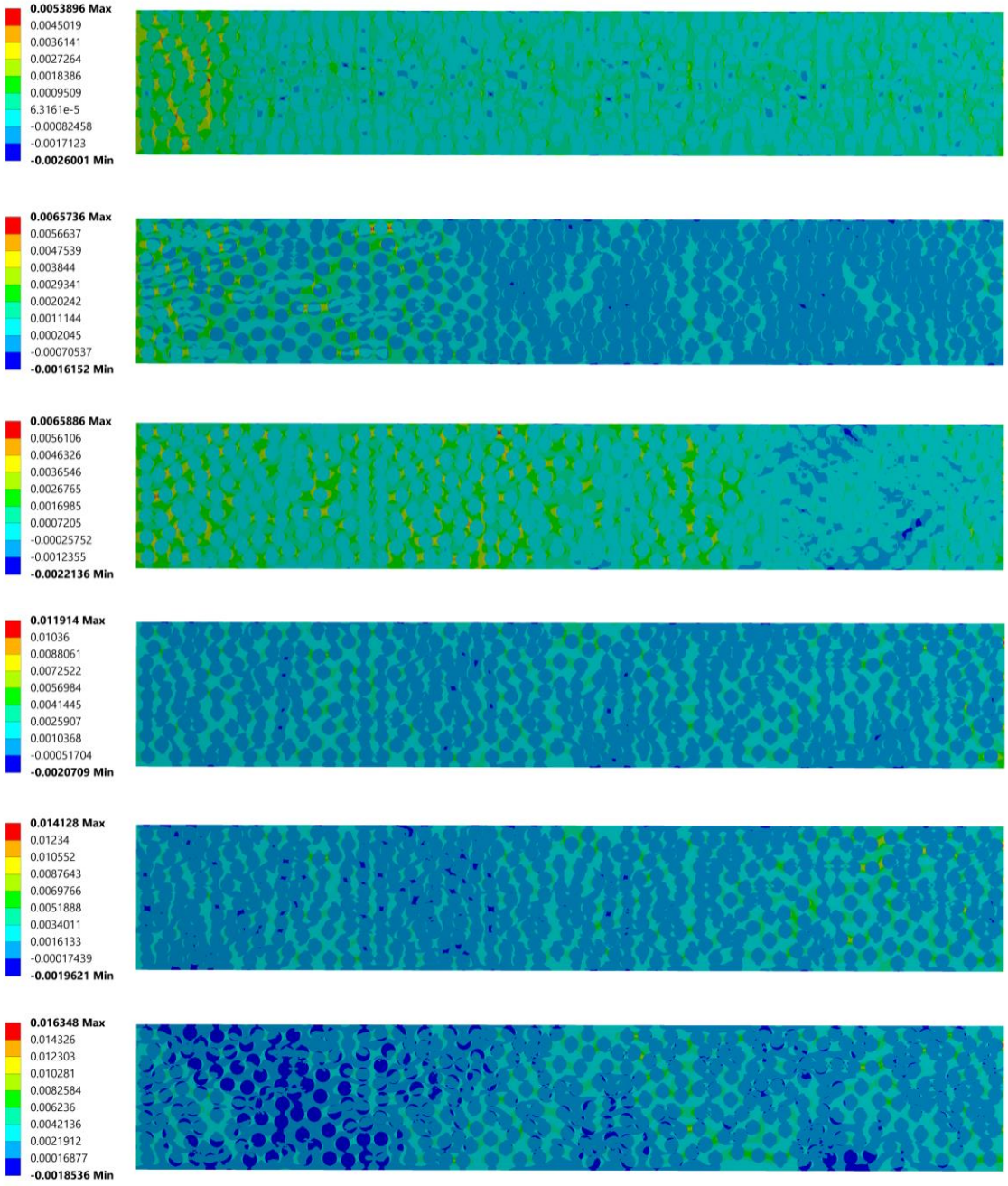

Figure 94 – Longitudinal strain state at 100, 300, 600, 900, 1200 and 1400 ns for the mesoscale model with elastic properties, subjected to 20 ns internal heat generation.

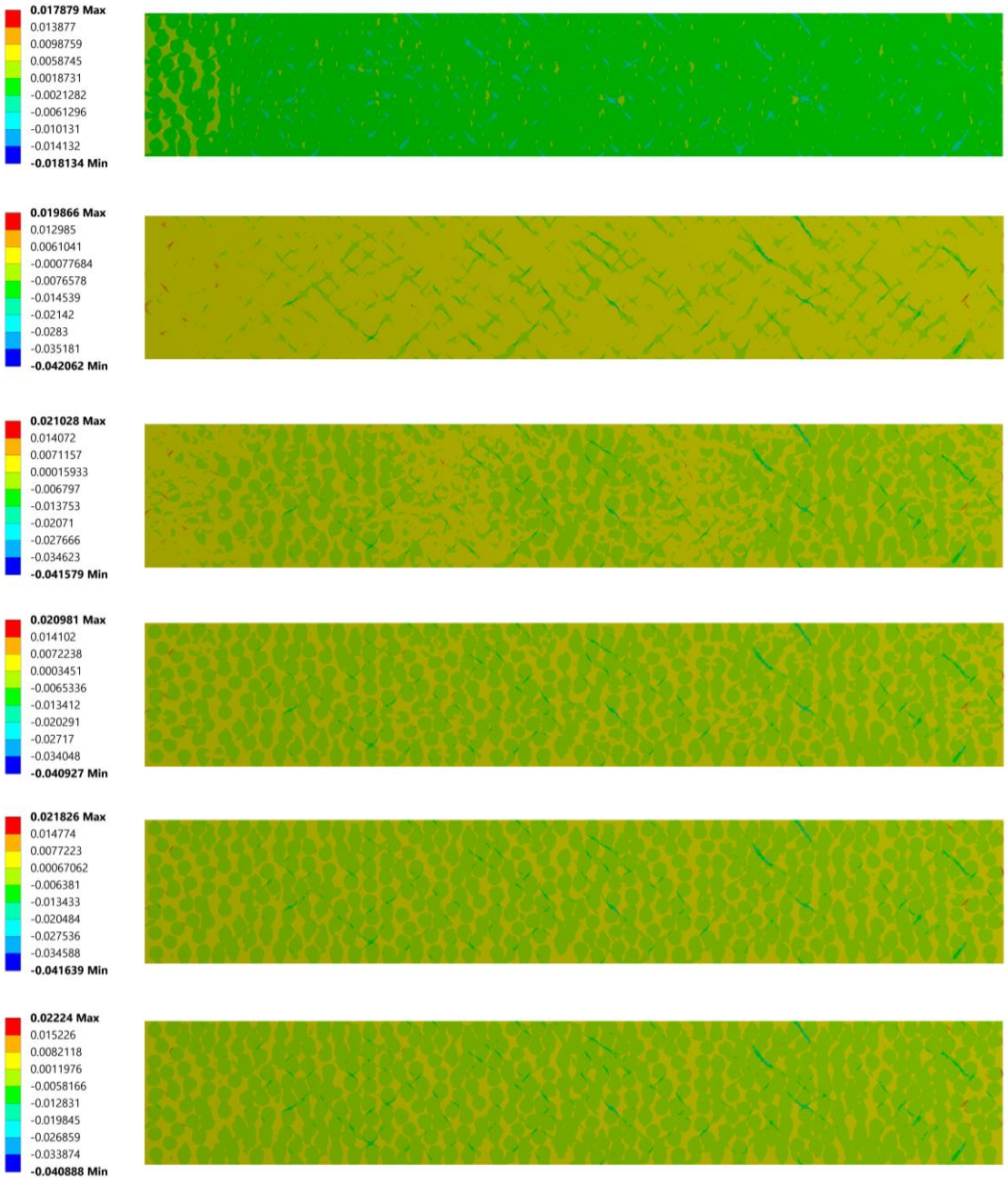

Figure 95 – Longitudinal strain state at 100, 300, 600, 900, 1200 and 1400 ns for the mesoscale model with plasticity in the copper matrix, subjected to 20 ns internal heat generation.

5.1.5 Discussion

In this section, the numerical study of wave propagation effects in a stochastic Copper Diamond composite was presented, aiming to compare and contrast differences between a model considering the mesoscale structure of the composite and another trying to capture the material behaviour through a homogenised model. The homogenised model was built through standardised material characterisation techniques, as presented in Chapter 4, including a 4-point bending test to determine the stress-strain relationship of the material. The mesoscale model was built by considering the material data for the two constituents making up the composites.

The problem was modelled in 2D by considering a small, slender specimen in plane strain. The size considered was based on computational limitations, while the geometry chosen aimed to mimic the slender nature of beam intercepting devices. Two scenarios were considered for each model, the first consisting of an external impact one side of the modelled specimen, which results in a stress wave propagating through the material. The second scenario, similarly, consisted of a thermomechanical simulation where the specimen was dynamically loaded with a thermal pulse, with an energy deposition time in the order of nanoseconds, which also results in a dynamic structural response. The two cases successfully modelled the propagation of the stress wave throughout the different models tested.

The wavelength of stress waves propagating through the material can be seen to have a significant effect on results. In the study, two pulse durations were considered, namely 20 ns and 300 ns. These correspond to typical impact times of shots tested in experiments such as the HRMT36 MultiMat experiment. For Copper Diamond, such pulse durations result in wavelengths of approximately 0.12 and 1.85 mm respectively. Wave-particle interaction was observed to increase substantially as the wavelength approaches the size of the diamond particles modelled, which for the CuCD grade in is in the order of 0.1 mm.

To conclude, the homogeneous model adopted for Copper Diamond can be seen to be able to capture wave propagation effects within the material, and is improved with the inclusion of plasticity behaviour of the material. Limitations are particularly apparent in the case of wavelengths which approach the particle size of diamond particles. Given the computational requirements of a full-scale, 3D mesoscale model, such an analysis would not be feasible to model a scenario such as a whole LHC tertiary collimator or a specimen

of similar dimensions to those tested in the HRMT36 experiment. For the 6 mm × 1 mm 2D model considered in this chapter, the computation time for the mesoscale models was approximately two orders of magnitude higher than that for the homogeneous models, with the mesoscale model requiring a significantly large amount of elements and contact points between the copper matrix and modelled diamond particles.

5.2 Equation of State for Copper Diamond

As discussed throughout this study, the interaction of high-energy, high-intensity particle pulses with matter leads to a quasi-instantaneous temperature rise within the material, which results in large thermal deformations in a very short period of time. In the cases considered in this study, the dynamic effects considered were in energy ranges in the elastic and plastic regimes. High-energy impacts can result in the propagation of intense pressure waves which, in turn, lead to possible extensive plastic deformation, changes in phase, spallation and material fragmentation. In such instances, the material strength models fail, and the material can be treated as a fluid, and thus represented by a hydrostatic curve: an Equation of State (EOS) which describes the material's behaviour under such extreme conditions.

The EOS describes the material state with four variables, namely the density, pressure, internal energy, and particle velocity. Equations of State are generally semi-empirical, i.e., they use a combination of statistical mechanical models and experimental data. The ideal gas law, shown in equation 42, is a typical and simple EOS, expressing the relationship between temperature, density and pressure of a gas. Additionally, the specific heat capacity, which expresses the relationship between energy and temperature of the material, or specifically the required energy for a unit change in temperature of a unit mass of the material, is required to express the temperature as a function of internal energy.

$$P = \rho RT \tag{42}$$

Where R is the specific gas constant $R = c_p - c_v$.

5.2.1 Calculation of Mie–Grüneisen Equation of State for Copper Diamond

The LASL Shock Hugoniot Data document [159], produced by the Los Alamos Scientific Laboratory, is a collection of Huganiot data accumulated over more than 5000 experiments, which originated following the second world war using P. W. Bridgman's method [186]. Bridgman calculated the states by considering isotherms from known thermodynamic

relations and shock states. The data was extended from pressures of 10 GPa up to 50 GPa by the technique developed by Walsh and Christian [187] and Goranson *et al.* [188], where thermodynamic relations were again used to determine the locus of single-shocked states, the Hugoniot locus, and used to calculate states off the Hugoniot.

The determination of the Hugoniot locus of a material does not require the direct measurement of thermodynamic parameters behind the shock front, namely pressure P, specific volume V or density ϱ, and specific internal energy E. Instead, the shock wave parameters, shock velocity U_s and mass / particle velocity U_p, are determined directly or indirectly. The relationship between thermodynamic and shock wave parameters can be determined by applying conservation of mass, momentum and energy across the shock front, otherwise known as the Rankine-Hugoniot equations.

Assuming the material is originally at rest, the mass, momentum and energy conservation equations are:

Mass conservation
$$V/V_0 = (U_s - U_p)/U_s \tag{43}$$

Momentum conservation
$$P - P_0 = \rho_0 \, U_s \, U_p \tag{44}$$

Energy conservation
$$E - E_0 = 1/2 \ (P + P_0) \ (V_0 - V) \tag{45}$$

Where V_0 P_0 E_0 ϱ_0 are the initial states (at rest). Note that the specific volume V is the reciprocal of the density ϱ.

The LASL SH Data document presents the SH data for various materials in the form of data tables, which are divided in ten sections depending on the type of material. The materials covered in the data sheets range from metal alloys to minerals, plastics, liquids, and explosives, among others. The tables give values of ϱ_0, U_s, U_p, P, V, ϱ and V/V_0, in order of increasing particle velocity. Most of the Hugoniot data in the tables was obtained through the impedance-match technique. In this method, specimens are shocked through base plates, whose EOS are known in detail, with the shock energy source being either a high explosive or an accelerated reservoir light-gas gun. Equations of State contain information about the relationship between different thermodynamic variables of materials, such as the temperature, density, and Helmholtz free energy, and tabular EOS store this data in a grid, such as a temperature-density matrix. In this case, each point in the grid

would be a value of the Helmholtz free energy, thus providing a relationship between the three variables. The tables can be expressed in terms of other thermodynamic variables from these fundamental identities, i.e., the pressure can also be expressed in terms of temperature and density.

The SESAME EOS is primarily composed of the Helmholtz free energy data as a function of the density and temperature. While experimentally the pressure and temperature are easier to control and measure, suggesting that the Gibbs free energy *G(P,T)* would be more adequate as a measure of thermodynamic potential, statistical mechanics for condensed matter was mainly developed with density and temperature as the independent variables, thus making the Helmholtz free energy the ideal thermodynamic potential to refer to. Additionally, all other thermodynamic functions can be directly derived from this value. A tabular EOS for pure elements additionally contains the following basic parameters: the atomic number *Z*, the atomic weight *A*, and the reference density, defined as the density of the material at ambient conditions, i.e., 1 atm and 298 K. For mixtures, an average atom approach is taken, considering a weighted average of the composition ratios of the constituents. Copper Diamond is a relatively novel material and, as one would expect, is not included in the SH data libraries. The properties of the material's constituents, i.e., copper and diamond, are both found in the library. The properties and SH data for these materials can be combined using the rule of mixtures in order to derive the SH data and the equation of state for this material.

In Figure 96 and Figure 97, the plots for pressed carbon (diamond) with a density of 3.191 g/cm^3 and pure copper with a density of 8.924 g/cm^3, as found in the LASL Shock Hugoniot Data document, are shown, displaying the variation of the shock velocity with the particle velocity along the Hugoniot, along with the corresponding pressure and specific volume for each respective point. An extract of the tabular EOS for pressed carbon [159], [189], [190] and pure copper [159], [190]–[196] can be seen in Table 25 and Table 26.

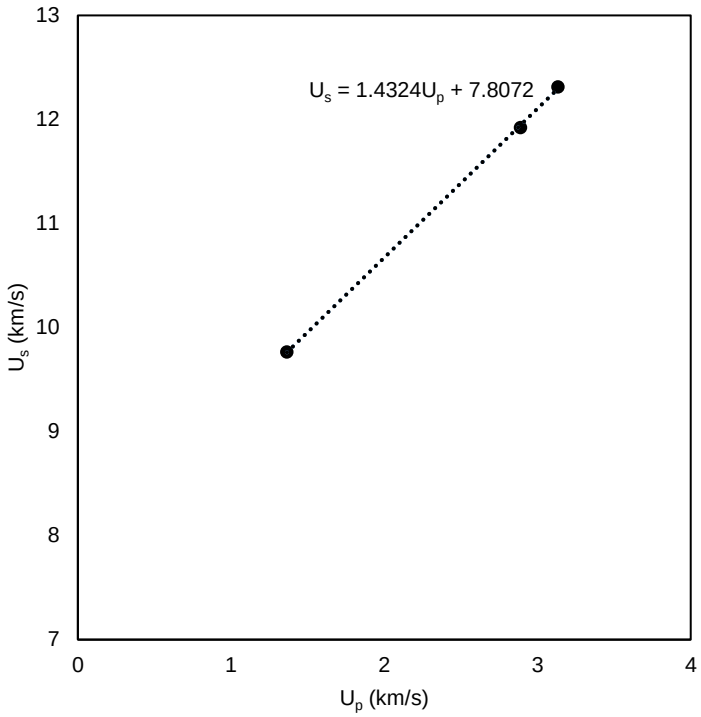

a)

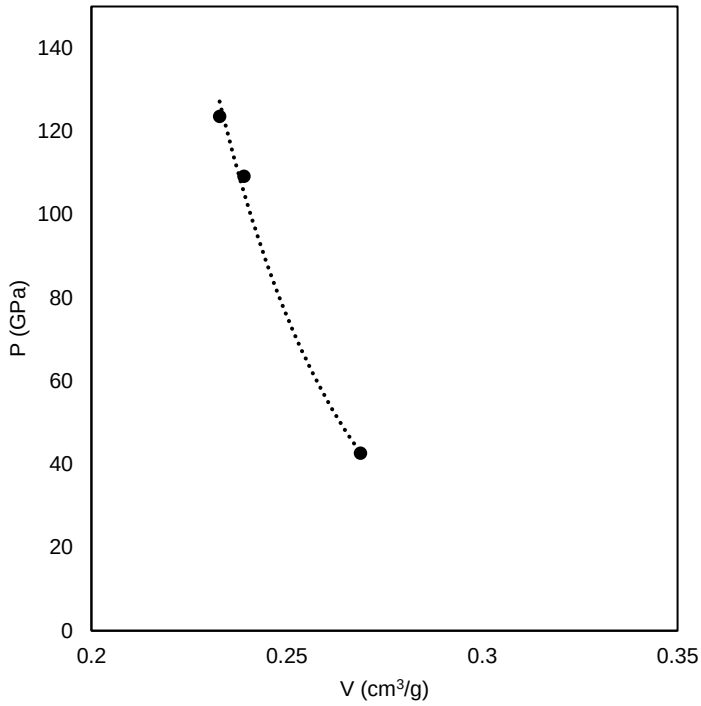

b)

Figure 96 – Particle and shock velocity plot (a) and pressure and specific volume plot (b) for pressed carbon (diamond) [159].

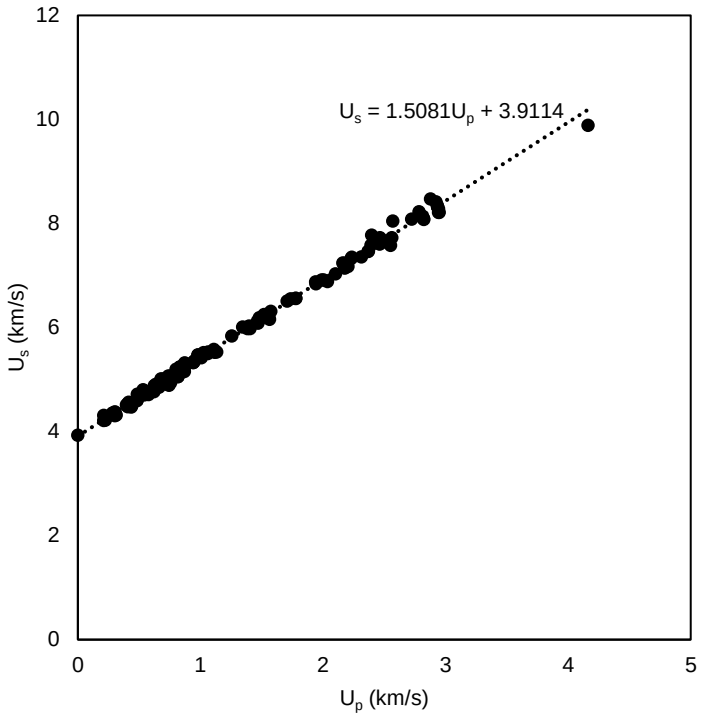

a)

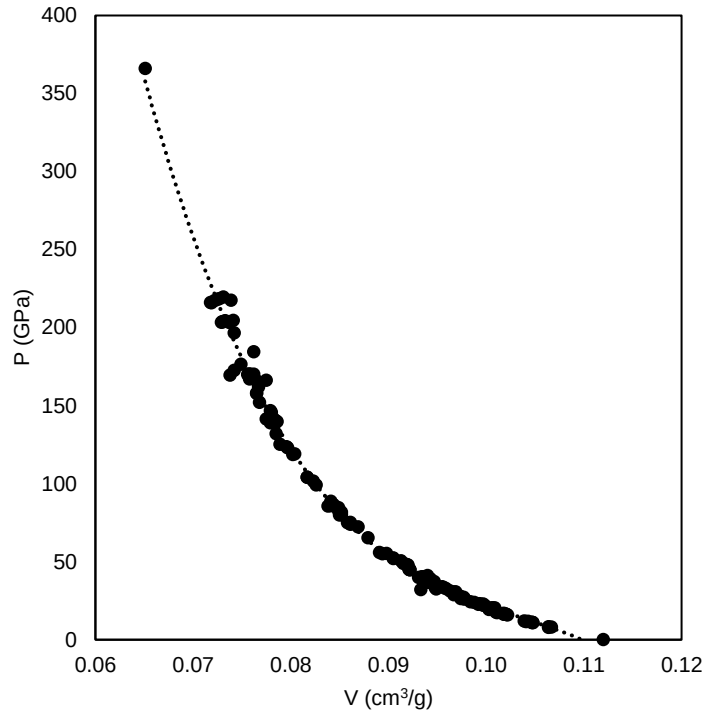

b)

Figure 97 – Particle and shock velocity plot (a) and pressure and specific volume plot (b) for pure copper [159].

Table 25 – Tabular EOS for pressed carbon (diamond), as per the LASL Shock Hugoniot Data document. Average density ρ_0 of 3.191 g/cm³ [159].

ρ_0	U_s	U_p	P	V	ρ	V/V_o
g/cm³	*km/s*	*km/s*	*GPa*	*cm³/g*	*g/cm³*	-
3.2	9.764	1.364	42.618	0.2688	3.72	0.86
3.17	11.923	2.889	109.192	0.239	4.184	0.758
3.203	12.314	3.133	123.571	0.2328	4.296	0.746

Table 26 – Extract of tabular EOS for pure copper, as per the LASL Shock Hugoniot Data Document. Average density ρ_0 of 8.924 g/cm³, longitudinal sound velocity of 4.76 km/s, shear sound velocity of 2.33 km/s [159].

ρ_0	U_s	U_p	P	V	ρ	V/V_o
g/cm³	*km/s*	*km/s*	*GPa*	*cm³/g*	*g/cm³*	
8.929	3.927	0.000	0.000	0.1120	8.929	1.000
8.920	4.314	0.210	8.081	0.1067	9.376	0.951
…	…	…	…	…	…	…
8.895	9.89	4.161	366.05	0.0651	15.355	0.579

For both materials, the relationship between the shock velocity and the particle velocity can be estimated to be linear. The relationship can be described by the following equations (in m/s):

$$\textit{Diamond} \qquad U_s = 7810 + 1.43U_p$$

$$\textit{Copper} \qquad U_s = 3910 + 1.51U_p$$

The rule of mixtures can be used to combine these two equations and derive the U_s-U_p relation for copper diamond. The Copper-Diamond grade (CuCD3434) studied in this work is made up of approximately equal parts of diamond and copper, with densities at room temperature of 3.191 g/cm^3 and 8.924 g/cm^3 respectively. While additional binding materials are negligible, the material has a measured porosity of 8.4%$_{vol}$. This results in a mass distribution of 26.3%$_{mass}$ diamond and 73.7%$_{mass}$ copper. The intercept (C) and the gradient (S) of the relation can then be determined by simply applying a mass-weighted average of the values obtained from the LASL SH Data document, as shown in Table 27. The resultant U_s-U_p plot for copper diamond is shown in Figure 98.

Table 27 – C and S values for copper diamond derived from material constituent data.

Material	C	S
	m/s	-
Diamond	7810	1.43
Copper	3910	1.51
Copper Diamond	4937	1.49

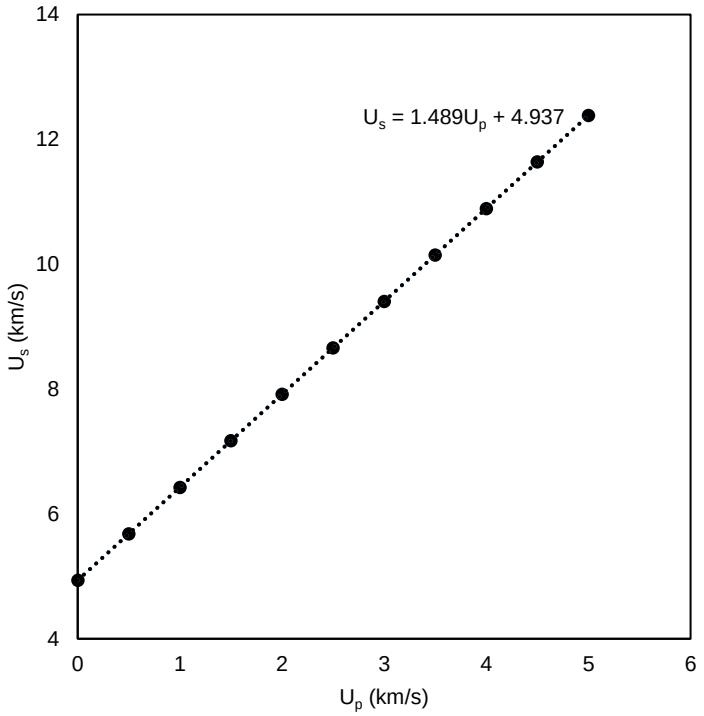

Figure 98 – Particle and shock velocity plot for copper diamond.

The EOS of a material is generally conveyed as an equation of pressure as a function of density and temperature, with three main contributions to the pressure, as by:

$$P(\varrho,T) = P_c(\varrho) + P_N(\varrho,T) + P_e(\varrho,T) \tag{46}$$

The first term, $P_c(\varrho)$, is the pressure at $T = 0$, commonly referred to as the *cold curve*. This is due to the electronic forces which bind individual atoms into a solid. The second term, $P_N(\varrho,T)$, is the pressure due to the vibrational excitation of the nuclei, while the third term, $P_e(\varrho,T)$, is the pressure due to the electron's thermal excitation. The cold curve is generally modelled by empirical formulae such as the Lennard-Jones and Morse potentials, along with Thomas-Fermi-Dirac theory, while the vibrational contribution for solids is modelled with the Debye theory, along with Monte Carlo methods to calculate the relevant pressures as a function of temperature and density. The pressure due to electron excitations can be

modelled using Thomas-Fermi-Dirac theories [197].

With the material data in hand, along with material constitutive data obtained from experimental characterisation (namely specific heat capacity at constant pressure, coefficient of thermal expansion, density and conductivity as a function of temperature), a step-by-step approach can be taken to derive the Mie–Grüneisen equation of state of the material and other values of interest.

The Grüneisen parameter[16], γ, is defined by:

$$\gamma = \frac{\alpha_v K}{\rho c_p} \tag{47}$$

where K is the bulk modulus of the material, in this case defined by $\mathrm{K} = \rho C^2$ (with C being the intercept in the material's SH curve as defined) and α_v is the volumetric coefficient of thermal expansion, related to the linear coefficient of thermal expansion by $\alpha_v = 3\alpha_L$. Note that the bulk modulus is sometimes denoted by B (B^T for isothermal bulk modulus, B^S for isentropic bulk modulus) – in this case, compressibility is denoted by K = 1/B.

The specific heat capacity at constant volume can then be found by:

$$c_v = \frac{c_p}{1 + \gamma^2 \frac{c_p}{C^2} T} \tag{48}$$

Note that at low temperatures c_v and c_p are practically equal, with a slight divergence at elevated temperatures.

The Mie-Grüneisen equation relates two equilibrium points attainable by a body. Knowing one state allows for the derivation of the other. We are generally interested in analysing after-shock states, and therefore the SH curve, which describes a collection of after-shock points attainable for different initial conditions, can be used to derive the neighbouring

[16] The Grüneisen parameter describes the effect of change in temperature and the resulting volume change of the crystal lattice of a material on its vibrational properties.

equilibrium states. The Mie-Grüneisen equation of state can be defined by:

$$p(\rho,T) = \frac{\rho C^2 \chi\left(1-\frac{\gamma\chi}{2}\right)}{(1-S\chi)^2} + \gamma\rho\int_{T_0}^{T} c_v dT \tag{49}$$

Where $\chi = 1 - \varrho_0/\varrho = U_p/U_s$.

Assuming a linear variation of pressure with density (i.e., $p(\varrho,E) = K(\varrho/\varrho_0 - 1)$), a linear equation of state can be described by:

$$p(\rho,\mathrm{T}) = \mathrm{K}\left(\frac{\rho}{\rho_0}-1\right) + \gamma\rho\int_{0}^{T} c_v dT \tag{50}$$

To complete a full SESAME (tabular) equation of state to be included in the ANSYS's Autodyn solver, the values for specific internal energy *E* and the specific Helmholtz free energy *H* need to be computed. These are described by:

$$E(T) = \int_0^T c_v dT \tag{51}$$

$$H(T) = \int_0^T \int_0^T -\frac{c_v}{T} dT\, dT \tag{52}$$

The specific internal energy, sometimes also called the energy density, describes the internal energy per unit mass of the system (J/kg), which can be increased by the introduction of heat or by doing thermodynamic work on the system, but does not include the potential energy due to external forces, or the kinetic energy of the system's motion [198], [199].

The specific Helmholtz free energy is the thermodynamic potential measuring the useful work per unit mass that is obtainable from a closed thermodynamic system at isothermal and isochoric (constant pressure and volume) conditions [200]. During an isochoric process, the negative of the change in Helmholtz free energy is equivalent to the maximum amount of work that the system can perform. Alternatively, the Gibbs free energy (also known as free enthalpy) is the thermodynamic potential used to calculate the maximum reversible work that can be performed in a system at isothermal and isobaric (constant temperature and pressure) conditions [201]. To summarise, both the Helmholtz and Gibbs

free energy are a measure of thermodynamic potential, however the former is useful in cases where the system is at constant volume (as is generally the case in high-energy beam impacts resulting in the propagation of shock waves), while the latter is more commonly used for applications occurring at constant pressure. Note that the change in entropy is defined as the integral of the change in heat in a system divided by the absolute temperature from a process's initial state to its final state. For an isochoric process, this can be expressed by:

$$\Delta S = \int_{T_0}^{T} \frac{dQ}{T} = c_v ln \frac{T}{T_0} \tag{53}$$

Where the change in heat dQ is equivalent to $c_v dT$. A MATLAB script was implemented to compute the Mie-Grüneisen EOS for copper diamond, along with the linear EOS, specific internal energy, and specific Helmholtz free energy, using data from the relevant copper and diamond constituents described earlier in this section. This allowed for the calculation of all four parameters, i.e., two pressure plots and two specific energy plots, as a function of temperature and density, along with the specific heat capacity at constant pressure and volume, as described by equations 47-52. The plots showing the calculated values are shown in Figure 99, Figure 100, and Figure 101.

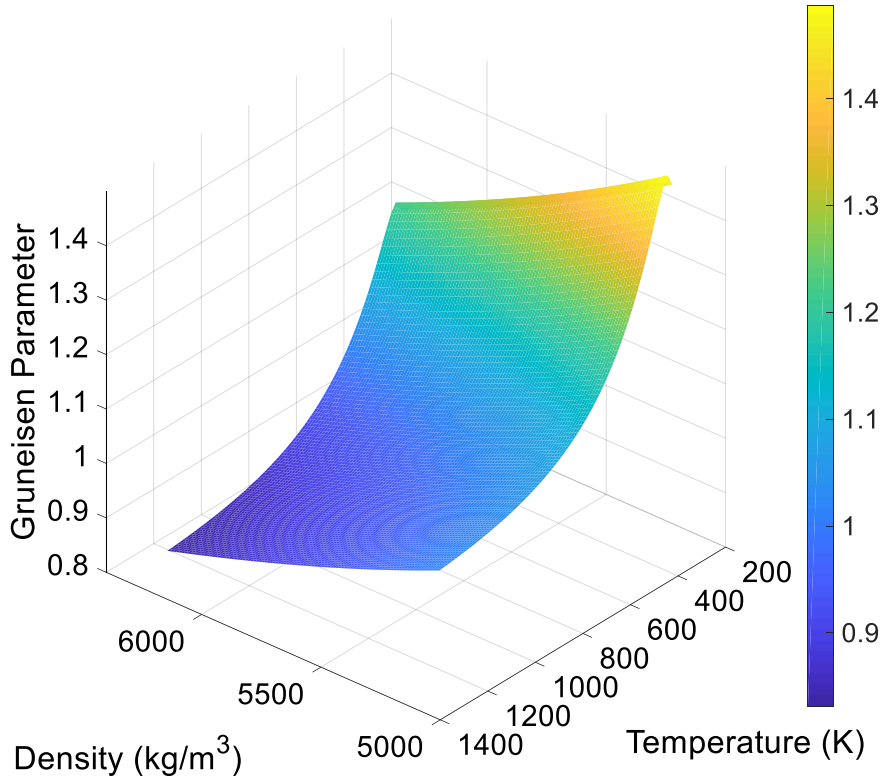

a)

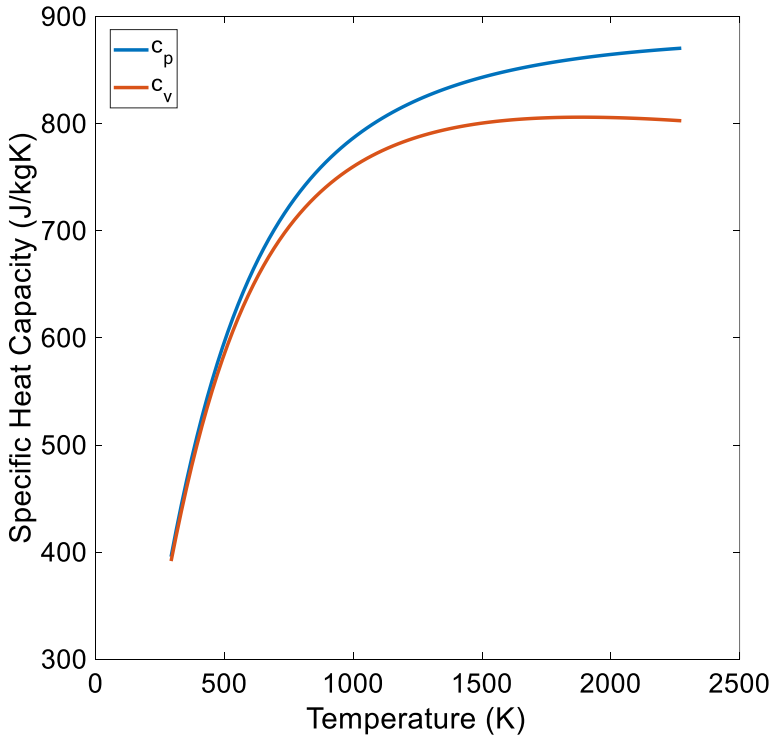

b)

Figure 99 – Grüneisen parameter, γ, as a function of density and temperature (a) and specific heat capacity at constant pressure (c_p) and constant volume (c_v) as a function of temperature (b).

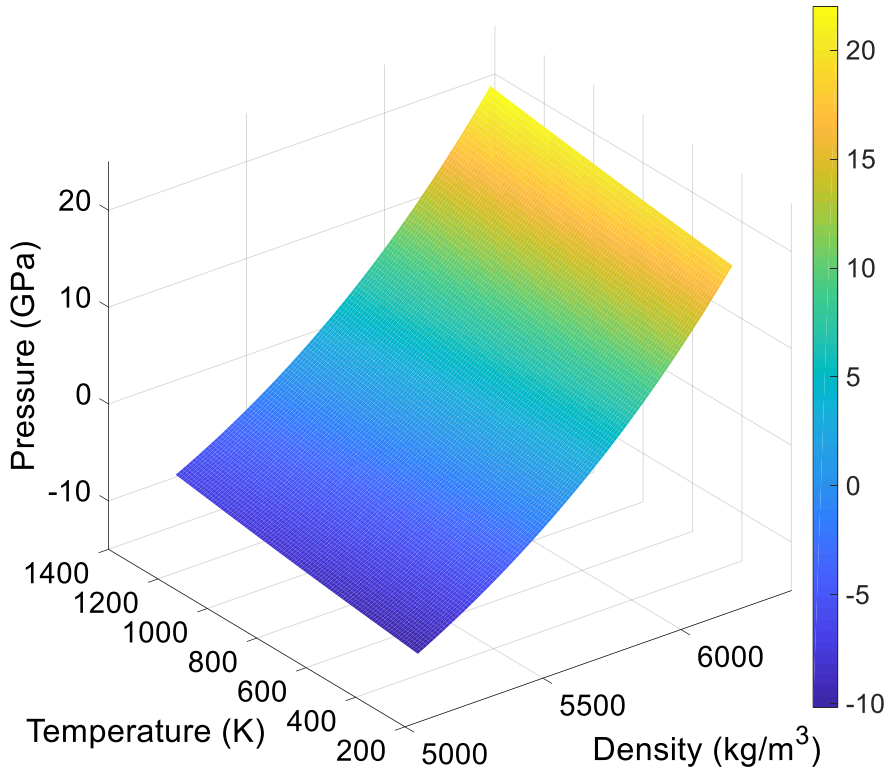

a)

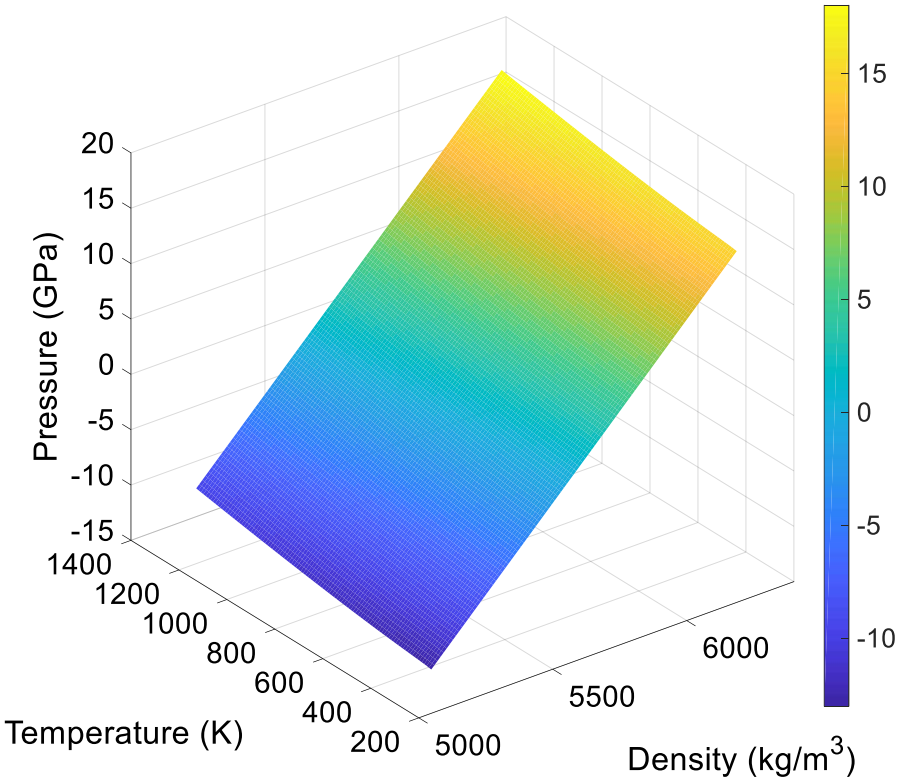

b)

Figure 100 – Mie-Grüneisen EOS (a) and Linear EOS (b) for CuCD.

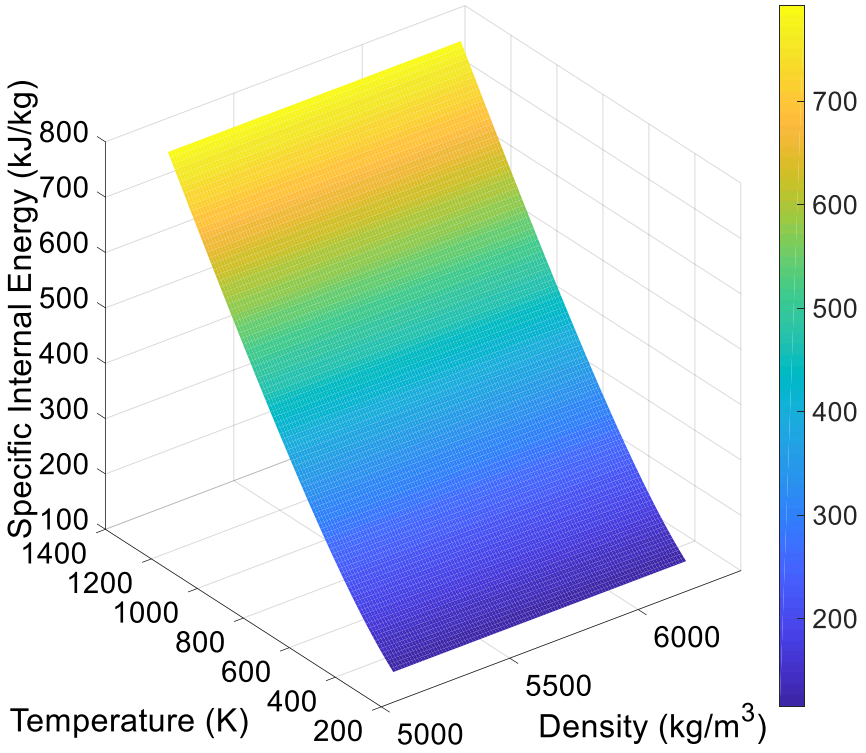

a)

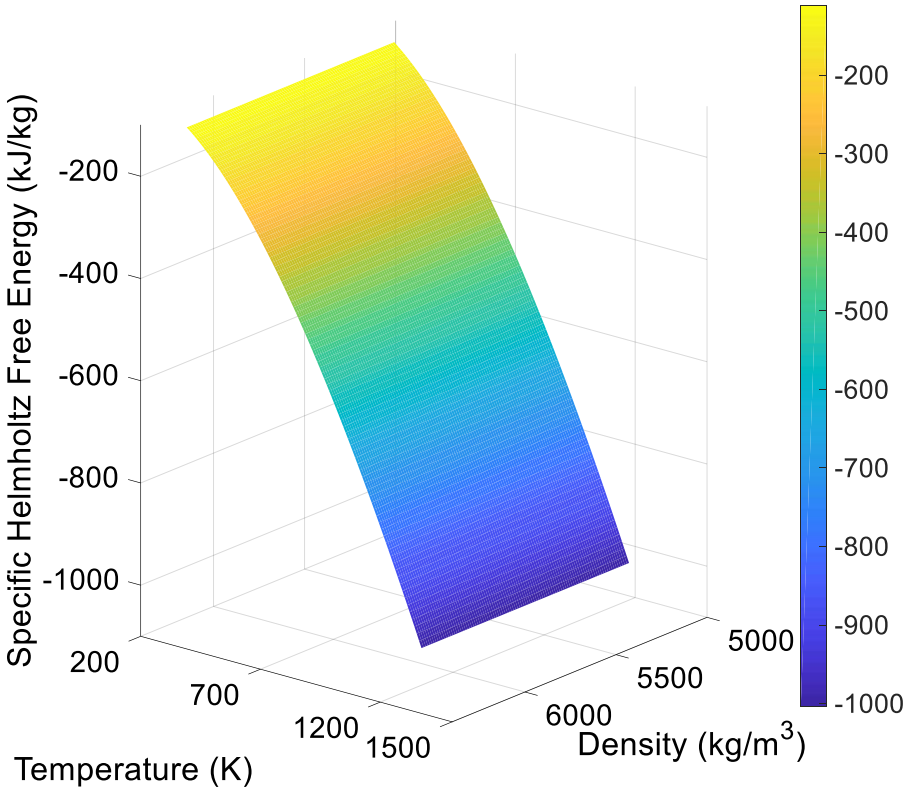

b)

Figure 101 – Specific Internal Energy, E, (a) and Specific Helmholtz Free Energy, H, (b).

5.3 Summary

In this chapter, a continuation on the work and observations on Copper Diamond shown in Chapter 4 is presented. The mesoscale behaviour of the material is investigated through the 2D modelling of the diamond-copper structure in finite element analyses. A number of scenarios are considered, namely the case of an external impact on a body, and the case of a quasi-instantaneous internal heat generation. In both cases, the material behaviour was simulated by considering various models, namely:

- A homogeneous model with elastic properties;
- A homogeneous model with plasticity;
- A mesoscale model with elastic properties for copper and diamond; and
- A mesoscale model with plasticity in the copper matrix.

In the modelled scenario for an external impact, qualitatively, the homogeneous elastoplastic model can be seen to provide a reasonable middle ground between the homogeneous elastic and mesoscale models. The homogeneous elastic model, while being the most computationally efficient, fails to model the signal decay as the sound wave propagates through the material from the impact position. The elastoplastic model introduces signal dissipation as a result of plasticity, while in the mesoscale model the decay can be mostly attributed to dispersion as a result of interaction between the travelling wave and the diamond-copper interface. The analyses modelling an internal heat generation featured a larger, rod-shaped geometry, roughly mimicking the shape of LHC collimators, with the main limitation being the computation resources and time required to simulate full-scale components in such level of detail. Here, wave-particle interaction in wavelengths similar to the size of dispersed diamond particles was again apparent, along with the influence of plasticity on calculated results. The 2D models adopted to simulate the mesoscale behaviour of the material were seen to be highly computationally expensive, limiting the size of specimens modelled. A summary of the number of elements and computation time required for various models of comparable dimensions simulated is shown in Table 28.

Table 28 – Summary of number of elements, nodes, and computation time for the various models tested. Simulations performed on a 4-core, 8-thread Intel i7-7700 CPU clocked at 3.60 GHz, with 16 GB of RAM.

	Model			
	Homogeneous Elastic	*Homogeneous Elastoplastic*	*Mesoscale Elastic*	*Mesoscale Elastoplastic*
No. of elements	2340	2340	39804	39804
No. of nodes	7295	7295	135199	135199
Computation Time (min)	12	22	1411	1471

Intense, high-energy impacts can result in the generation of shock waves which can lead to changes in phase and extensive plastic deformation. In such instances, the material behaviour cannot be simply modelled with a strength model, as the material essentially behaves as a fluid. An equation of state is thus required to describe the material behaviour in these extreme conditions. Copper Diamond is a fairly novel and niche material and, as such, there are no EOS available for the material in literature. The rule of mixtures was thus applied, considering the shock data available for the constituent materials, i.e., copper and (carbon) diamond, making up the composite, made available publicly by the Los Alamos Scientific Laboratory. This allowed for the calculation of the shock and particle velocity relationship in Copper Diamond. Additionally, material data for CuCD gathered and presented in Chapter 4, such as the density and specific heat capacity, was used to calculate a tabular EOS for Copper Diamond, namely the Grüneisen parameter, the Mie-Grüneisen and Linear EOS, and the specific internal energy and specific Helmholtz free energy as a function of temperature and density.

Following the work presented in this chapter, a number of considerations are proposed for future work on the subjects discussed. The mesoscale behaviour of Copper Diamond is extremely interesting in the context of beam intercepting devices. Simple, analytical solutions for the calculation of the dynamic behaviour of the material in the context of wave-particle interaction would aid in quickly analysing the influence of parameters such as particle size, wavelength, and dimensions on the amplitude of the propagating waves. This can be combined with numerical methods to characterise the material behaviour of complex, 3D composites from available material properties for the constituent materials.

Additionally, the tabular equation of state proposed for Copper Diamond can be applied in explicit analyses modelling intense impacts resulting in the propagation of shock waves in the material. In the context of this study, the HRMT36 MultiMat experiment only consisted of relatively low-intensity impacts which did not lead to the generation of shock

waves in the material. A dedicated experiment purposely designed to test the material behaviour in such conditions would thus be required to benchmark this data.

Chapter 6:
Conclusions

6.1 Discussion

The LHC's multi-stage collimation system is made out of long blocks of material distributed around the LHC tunnel, surrounding the two circulating beams. The collimation system's main function is beam cleaning, where particles which deviate from the correct beam trajectory during normal operation are absorbed by the collimators, which are placed strategically to protect sensitive equipment such as the superconducting magnets. In this case, energy is deposited continuously on the collimators. Additionally, the collimators serve the role of protecting such components in the case of accidental impacts, where energy is instead deposited in a very short period of time.

The work presented in this study focuses on the latter scenario in the context of the HRMT36 MultiMat experiment conducted in CERN's HiRadMat facility, where a number of materials were tested under beam impacts in the order of nanoseconds to microseconds, achieving beam intensities similar to the ones achieved in the LHC and HL-LHC. Experiments such as HRMT36 are essential in the development of accurate and reliable mathematical models which allow for the simulation of full-scale scenarios, such as accidental beam impact with collimator jaws.

In this study, a numerical finite element approach was developed to model the MultiMat experimental scenario, consisting of implicit, transient, thermomechanical simulations modelling the thermal deposition as a result of particle beam impact, and the resulting dynamic response of tested specimens. The study focuses on three materials tested in the MultiMat experiment, namely a Silicon Carbide developed by Microcertec, a Titanium Zirconium Molybdenum grade developed by Plansee, and a CuCD grade developed by RHP Technology. All materials were modelled in the elastoplastic domain. A number of impacts of interest from the experiment were considered, with the experimentally measured data used to benchmark the material models adopted.

For SiC and TZM, elastoplastic literature-based models were adopted, and their performance benchmarked with experimental data. A number of central and offset impacts were correctly modelled, basing time step and mesh size on standardised gauging techniques such as the Courant criterion, as well as phenomena and timescales of interest, such as impact duration, longitudinal wave period, and flexural bending period. The analyses found good agreement between simulations and measurements in terms of longitudinal wave amplitude and frequency, indicating that the materials' stiffness and

density were well represented in the material models adopted. In the case of the bending response, boundary condition effects resulting from loss of contact between the specimens and the support were successfully modelled, allowing for the simulation of the correct frequency of interest depending on the type of boundary condition present at a particular moment in time. This is of particular interest in the first few microseconds following the beam impact, at which point loss of contact between the specimen and support is most likely to occur. Additionally, the internal damping in both materials was successfully modelled, along with the simulation of instances where failure occurred. A post-irradiation campaign was conducted, and it was observed that some specimens showed evidence of internal cracking, which was not seen in initial visual inspections. In general, the material models adopted for SiC and TZM were found to replicate the material behaviour well in the cases tested, however there is a clear knowledge gap at high strain-rates and temperatures that should be addressed in future work.

For CuCD, a dedicated thermostructural characterisation campaign with temperature-dependent measurements was presented. This allowed for the modelling of the material behaviour with a multilinear elastoplastic material model, with temperature-dependent material behaviour. Two scenarios of differing intensity were modelled to verify the repeatability of the model. The low intensity shot considered was well replicated by the material model, both in terms of amplitude and frequency. Differences in longitudinal wave amplitude in the case of high-intensity shots were attributed to the mesoscale structure of the material, which is believed to result in the wave attenuation observed in experimental results. This observation prompted a detailed study on the effect of wave-particle interaction on waves propagating in particle-reinforced composites, which compared results from simulations utilising homogeneous and mesoscale models of Copper Diamond. The homogeneous model was found to provide satisfactory results for wavelengths much larger than the diamond particle diameter. In cases where the wavelength approached the diamonds' dimensions, the two models considered were seen to diverge. The inclusion of plasticity in the copper matrix of the mesoscale model resulted in a better agreement, in terms of wave amplitude, with the elastoplastic homogeneous model. The mesoscale model is however highly computationally expensive, thus limiting its application significantly, especially in 3D analyses.

Additionally, the Mie–Grüneisen equation of state for CuCD was formulated from constituent data made available by the Los Alamos Scientific Laboratory, which can be used in future explicit analyses modelling intense beam impacts resulting in the propagation of shock waves in the material.

6.2 Main Contributions

This thesis has presented the analysis and benchmarking of the performance of a number of material models of novel materials with applications in particle accelerator technology and other thermomechanical scenarios. Adopted models were implemented in implicit finite element thermostructural simulations, modelling various pulses from the HRMT36 experiment. Data collected from the experiment was used to validate the models presented. This allowed for a more in-depth understanding of the material behaviour in the elastic and plastic regimes. Additionally, the study allowed for a better understanding of failure phenomena in slender specimens exposed to accidental beam impact, as well as the strain, strain-rate, and temperature-dependency of the materials. The work presented also shed light on less-known phenomena, such as the relationship between particle size and wave attenuation in particle-reinforced composites.

The main contributions of this thesis to the research field are as follows:

- *Formulation of material models for SiC and TZM*

Material models for SiC and TZM grades tested in the HRMT36 experiment were built from data obtained from previously commissioned characterisation campaign, allowing for the modelling of the material behaviour under beam impact. The material models were benchmarked and validated with results from the HRMT36 experiment. This contribution allows for the application of such material models in more complex analyses modelling large-scale components such as collimator jaws. The study additionally concluded that the field would benefit from additional material testing of TZM at high strain-rates and temperatures, a subject on which there is a clear knowledge gap.

- *Development and application of FE models for the simulation of HRMT36 impacts*

A simple, fast and effective numerical model was developed and adopted successfully to simulate a number of pulses from the HRMT36 experiments, for a variety of materials. The analysis consisted of a weakly coupled thermostructural simulation, which was deemed

appropriate for the cases modelled due to the relatively short timescales and energy densities, which do not result in changes of phase or significant change in material behaviour. The model was applied for shots concerning SiC and TZM, and a similar approach was adopted for the modelling of the material response in CuCD. Such an approach can be easily adopted for future experiments, such as the upcoming follow-up experiment to HRMT36, MultiMat-2.

- *FE modelling of boundary condition effects in experiments testing materials under beam impact*

An FE model was developed to compliment the standard model implemented, focusing on the simulation of the complex boundary conditions present in HRMT36 and similar experimental testbenches. The model was successfully implemented to simulate the first few microseconds of shots which resulted in loss of contact between specimens and supports.

The work conducted on the above three points has been published in a peer-reviewed publication in *Mechanics and Materials* [202].

- *Thermostructural characterisation of a novel CuCD grade*

Thermal and structural characterisation tests were commissioned for a novel CuCD grade, under varying temperatures conditions. The results obtained were utilised to build a material model for the copper diamond grade CuCD RHP3434, and implemented in numerical analyses modelling various scenarios in the MultiMat experiment. This proved to be an essential contribution to research on this material, given its importance in the field due to the grade in question being chosen as a baseline material for use in tertiary collimators in the HL-LHC upgrade.

The work on the characterisation and validation of a material model for CuCD has been published as a peer-reviewed article in *Shock and Vibration* [185].

- *Modelling of wave-particle interactions in Copper Diamond*

A numerical FE model was implemented for the study of wave-particle interactions in particle-reinforced metal-matrix composites such as CuCD. The model attempted to simulate the stress-strain response of specimens when subjected to external impacts, as well as intense internal heat generation resulting in the propagation of stress waves through the

material. The results proved useful in furthering the knowledge on a subject which has been sparsely studied in the context of wave propagation induced by intense particle beam impacts.

The work presented on the mesoscale modelling of wave-particle interactions in CuCD has been submitted for peer-review.

- *Equation of State for CuCDRHP3434*

The equation of state of CuCD has been developed from constituent data available in literature. This development is a crucial step in the modelling of the material behaviour when subjected to intense impacts resulting in the propagation of shock waves in the material.

6.3 Proposed Future Work

- *Strain-rate dependent testing of SiC, TZM, and CuCD*

This study has presented a number of elastic and elastoplastic material models for the Silicon Carbide, Titanium Zirconium Molybdenum and Copper Diamond grades tested in the MultiMat experiment. All materials would benefit from further testing with varying strain-rates and temperatures. In the case of SiC and TZM, such tests would help in getting a better understanding of phenomena in play which led to the failure of a number of specimens in the MultiMat experiment. For TZM, additional metrology measurements and thermomechanical testing, including IET testing across a range of temperature, have been proposed, and are scheduled to be conducted at CERN.

For CuCD, the viscoelastic and viscoplastic behaviour of the material is particularly interesting with regard to the damping behaviour of the material at high strain-rates. As mentioned, a Split-Hopkinson bar experiment for CuCD has been proposed, and is planned to be conducted at the *Politecnico di Torino*, provided that manufacturing issues related to the flatness of the specimen surface are resolved.

- *3D modelling of CuCD mesoscale structure*

The 2D modelling of the mesoscale structure of CuCD provided some interesting insights in the context of wave propagation in particle-reinforced composites. The presented model does have a number of limitations related to its 2D nature, which can be solved by

modelling the specimen in 3D, allowing for the realistic simulation of wave-particle interactions. Such a process would require extensive computational resources since, as was seen in the 2D analysis, the mesoscale model requires significantly more computation time to solve problems compared to homogeneous models. Additionally, a study focusing on the homogenised dynamic behaviour of the material through the application of representative volume elements could be beneficial when designing novel grades of the material. This could allow for optimisation and relatively straightforward analysis of the effect of size and distribution of inclusions and porosities on the material behaviour.

- *Post-irradiation analysis of CuCD specimens*

In this study, X-ray tomography scans for SiC and TZM were presented, showing how the specimens tested experienced internal cracking in addition to the catastrophic failure observed. A post-irradiation campaign on CuCD specimens would similarly allow one to analyse whether the impacted samples experienced any permanent damage at the diamond-copper interface as a result of extended exposure to elevated temperatures and dynamic strains.

- *Application of CuCD EOS in explicit analyses*

The equation of state for CuCD presented in this study can be used in future analyses modelling shock wave propagation through the material. This is especially relevant in the modelling of accidental scenarios for the HL-LHC tertiary collimators, where change of phase and spallation can occur.

- *Anisotropy in CuCD*

The manufacturing process of CuCD includes pressing, which can result in some anisotropy in the material. An experimental campaign is scheduled to be conducted at the CERN laboratories to determine whether there is a significant amount of anisotropy in the material's behaviour.

- *The MultiMat-2 experiment*

An experimental continuation on the HRMT36 MultiMat experiment, adequately titled MultiMat-2, will be conducted at CERN's HiRadMat facility in the second half of 2021. The MultiMat-2 experiment will reuse the same testbench adopted for the HRMT36 experiment, which was designed with reusability in mind.

The experiment will again test slender rods under beam impact, with a similar size to that tested in the MultiMat experiment (approximately 10×10×200 mm^3). The main objective will be to validate the HL-LHC baseline collimation materials, primarily the MoGr NB-8404Ng grade produced by Nanoker for the primary collimators, as well as the same grade coated with an Mo layer via the high-power impulse magnetron sputtering (HIPIMS) technique for the secondary collimators. Additionally, backup materials such as Mo or Cu-coated isotropic graphite are to be tested in the experiment. An energy density peak comparable to that expected in the HL-LHC will be achieved by reducing the beam spot size with the maximum beam intensity available, and a maximum average energy equivalent to the HL-LHC will once again be achieved by decreasing the specimens' cross-sectional area. A summary of the beam parameters proposed for the MultiMat-2 experiment is shown in Table 29.

Table 29 – Proposed beam parameters for the MultiMat-2 experiment.

Particle type	Protons
Bunches/pulse	1 to 288
Intensity/pulse	Up to 1.2×10^{11} protons
Spot size	Down to 0.25 mm
No. of pulses	250
Integral intensity	2×10^{15} protons

In regard to instrumentation, a similar approach to that adopted in the MultiMat experiment is to be adopted, utilising strain gauges, temperature probes, LDVs, etc. Additionally, the number of transverse strain gauges will be increased, allowing for better decoupling of the longitudinal and transverse stresses.

References

[1] 'CERN', *CERN official website*. http://home.cern/about (accessed Oct. 30, 2019).

[2] G. Aad *et al.*, 'Observation of a new particle in the search for the Standard Model Higgs boson with the ATLAS detector at the LHC', *Phys. Lett. B*, vol. 716, no. 1, pp. 1–29, Sep. 2012, doi: 10.1016/j.physletb.2012.08.020.

[3] S. Chatrchyan *et al.*, 'Observation of a new boson at a mass of 125 GeV with the CMS experiment at the LHC', *Phys. Lett. B*, vol. 716, no. 1, pp. 30–61, Sep. 2012, doi: 10.1016/j.physletb.2012.08.021.

[4] S. S. McPherson, *Tim Berners-Lee: inventor of the World Wide Web*. Minneapolis: Twenty-First Century Books, 2010.

[5] 'Tim Berners-Lee's proposal', *CERN official website*. http://info.cern.ch/Proposal.html.

[6] S. & T. F. Council, 'CERN Accelerator Complex'. http://www.stfc.ac.uk/research/particle-physics-and-particle-astrophysics/large-hadron-collider/cern-accelerator-complex/.

[7] O. Bruning *et al.*, 'LHC Design Report', CERN, Geneva, 2004. [Online]. Available: http://cds.cern.ch/record/782076.

[8] 'The ATLAS Experiment'. http://cern60.web.cern.ch/en/exhibitions/atlas-experiment (accessed Jan. 10, 2020).

[9] 'Interim summary report on the analysis of the 19 September 2008 incident at the LHC', CERN, Geneva, 2008.

[10] M. Portelli, 'Preliminary thermo-mechanical design of a high-power absorber for HL-LHC crystal collimation', MSc, University of Malta, Malta, 2017.

[11] M. Meyers, 'Dynamic Deformation and Waves', in *Dynamic Behavior of Materials*, University of California, San Diego: John Wiley & Sons, Inc., 1994, p. 1.

[12] M. Meyers, *Dynamic Behavior of Materials*. University of California, San Diego: John Wiley & Sons, Inc., 1994.

[13] M. Meyers, 'Elastic Waves', in *Dynamic Behavior of Materials*, University of California, San Diego: John Wiley & Sons, Inc., 1994, pp. 25–26.

[14] F. Carra, 'Modelling of phenomena associated to quasi-instantaneous heating', in *Thermomechanical Response of Advanced Materials under Quasi Instantaneous Heating*, Italy: Politecnico di Torino, 2017, pp. 138–140.

[15] P. He, 'Measurement of acoustic dispersion using both transmitted and reflected pulses', *J. Acoust. Soc. Am.*, vol. 107, no. 2, pp. 801–807, 2000.

[16] L. Pochhammer, 'On the propagation velocities of small oscillations in an unlimited isotropic circular cylinder', *J. Pure Appl. Math.*, vol. 81, 1876.

[17] K. F. Graff, *Wave Motion in Elastic Solids*. New York: Dover Publications Inc., 1991.

[18] J. W. S. Rayleigh, *The theory of sound. Vol. 1:* ..., Repr. of 2. ed. rev. and enl.1894. New York: Dover Publ, 1969.

[19] F. Carra, 'Thermomechanical Response of Advanced Materials under Quasi Instantaneous Heating', PhD Thesis, Politecnico di Torino, Italy, 2017.

[20] R. Skalak, 'Longitudinal impact of a semi-infinite circular elastic bar', *J. Appl. Mech.*, vol. 24, no. 1, pp. 59–64, 1957.

[21] M. Meyers, 'Plastic Waves', in *Dynamic Behavior of Materials*, University of California, San Diego: John Wiley & Sons, Inc., 1994, pp. 66–97.

[22] M. Meyers, 'Shock Waves', in *Dynamic Behavior of Materials*, University of California, San Diego: John Wiley & Sons, Inc., 1994, pp. 98–123.

[23] 'Representing Stress as a Tensor'. https://www.doitpoms.ac.uk/tlplib/metal-forming-1/stress_tensor.php.

[24] R. Menikoff, 'Mie-Grüneisen Equation of State', Los Alamos National Laboratories, Tech. Report LA-UR-16-21706., 2016.

[25] S. P. Lyon and J. D. Johnson, 'SESAME: The Los Alamos National Laboratory Equation of State Database', Los Alamos National Laboratories, Tech. Report LA-UR-92-3407.

[26] G. R. Johnson and W. A. Cook, 'A constitutive model and data for metals subjected to large strains, high strain rates and high temperatures', in *Proceeding of 7th International Symposium on Ballistics*, 1983, pp. 541–547.

[27] F. J. Zerilli and R. W. Armstrong, 'Dislocation-mechanics-based constitutive relations for material dynamics calculations', *J. Appl. Phys.*, vol. 61, no. 5, pp. 1816–1825, Mar. 1987, doi: 10.1063/1.338024.

[28] P. S. Follansbee and U. F. Kocks, 'A constitutive description of the deformation of copper based on the use of the mechanical threshold stress as an internal state variable', *Acta Metall.*, vol. 36, no. 1, pp. 81–93, Jan. 1988, doi: 10.1016/0001-6160(88)90030-2.

[29] G. R. Johnson and W. H. Cook, 'Fracture characteristics of three metals subjected to various strains, strain rates, temperatures and pressures', *Eng. Fract. Mech.*, vol. 21, no. 1, pp. 31–48, Jan. 1985, doi: 10.1016/0013-7944(85)90052-9.

[30] M. Murugesan and D. Jung, 'Johnson Cook Material and Failure Model Parameters Estimation of AISI-1045 Medium Carbon Steel for Metal Forming Applications', *Materials*, vol. 12, no. 4, p. 609, Feb. 2019, doi: 10.3390/ma12040609.

[31] D. E. Grady, 'INCIPIENT SPALL, CRACK BRANCHING, AND FRAGMENTATION STATISTICS IN THE SPALL PROCESS', *J. Phys. Colloq.*, vol. 49, no. C3, pp. C3-175-C3-182, Sep. 1988, doi: 10.1051/jphyscol:1988326.

[32] N. Ma'at *et al.*, 'Modelling Dynamic Behaviour and Spall Failure of Aluminium Alloy AA7010', *J. Phys. Conf. Ser.*, vol. 914, p. 012033, Oct. 2017, doi: 10.1088/1742-6596/914/1/012033.

[33] A. Bertarelli, 'Beam-Induced Damage Mechanisms and their Calculation', CERN, 0007–8328, 2016. Accessed: Feb. 06, 2018. [Online]. Available: https://e-publishing.cern.ch/index.php/CYR/article/view/234.

[34] R. Assmann *et al.*, 'LHC Collimation: Design and Results from Prototyping and Beam Tests', in *Proceedings of the 2005 Particle Accelerator Conference*, Knoxville, TN, USA, 2005, pp. 1078–1080, doi: 10.1109/PAC.2005.1590664.

[35] H. Burkhardt, S. Jakobsen, S. Redaelli, B. Salvachua, and G. Valentino, 'Collimation down to 2 sigmas in special physics runs in the LHC', presented at the IPAC2013, Shanghai, China.

[36] D. Mirarchi, 'Crystal collimation for LHC', PhD Thesis, Imperial College, London, 2015.

[37] 'The collimation system: defence against beam loss', *CERN Courier*, Aug. 19, 2013. https://cerncourier.com/a/the-collimation-system-defence-against-beam-loss/ (accessed Oct. 14, 2020).

[38] A. Bertarelli *et al.*, 'Mechanical Design for Robustness of the LHC Collimators', in *Proceedings of 2005 Particle Accelerator Conference*, Knoxville, Tennessee, 2005, pp. 913–915, doi: 10.1109/PAC.2005.1590608.

[39] R. Assmann *et al.*, 'The final collimation system for the LHC', presented at the European Particle Accelerator Conference, May 2006.

[40] 'HL-LHC Parameters'. https://espace.cern.ch/HiLumi/PLC/_layouts/15/WopiFrame.aspx?sourcedoc=%2FHiLumi%2FPLC%2FSiteAssets%2FParameter%20Table%2Exlsx&action=view.

[41] N. Mounet, 'Transverse impedance in the HL-LHC era', presented at the 3rd HiLumi Annual Meeting, Daresbury, 2013.

[42] L. Rossi, 'Review of 11 T dipoles and cold collimation', CERN, Geneva, 2011. Accessed: Jan. 13, 2020. [Online]. Available: https://indico.cern.ch/event/155408/.

[43] C. Accettura *et al.*, 'Ultra-High Vacuum characterization of Molybdenum-Carbide Graphite for HL-LHC collimators', *J. Phys. Conf. Ser.*, vol. 1350, p. 012085, Nov. 2019, doi: 10.1088/1742-6596/1350/1/012085.

[44] F. Carra *et al.*, 'Mechanical engineering and design of novel collimators for HL-LHC', *IPAC2014*, doi: 10.18429/JACoW-IPAC 2014-MOPRO 116.

[45] A. Bertarelli *et al.*, 'Dynamic Testing and Characterization of Advanced Materials in a New Experiment at CERN HiRadMat Facility', *J.Phys.Conf.Ser.*, vol. 1067, no. 8, 2018, doi: 10.18429/JACoW-IPAC2018-WEPMF071.

[46] G. Apollinari *et al.*, 'High-Luminosity Large Hadron Collider (HL-LHC) Technical Design Report', CERN, Geneva, Vol. 4, 2017. [Online]. Available: http://dx.doi.org/10.23731/CYRM-2017-004.

[47] W. Scandale, 'Crystal-Based collimation in Modern Hadron Colliders', in *Charged and Neutral Particles Channeling Phenomena*, Erice, Italy, Apr. 2010, pp. 144–159, doi: 10.1142/9789814307017_0013.

[48] M. Fitterer *et al.*, 'Hollow electron beam collimation for HL-LHC - effect on the beam core', Fermilab, United States, FERMILAB-CONF-16-387-AD, 2016.

[49] M. Benedikt and M. Zimmerman, 'Future Circular Colliders', *Proc Int Sch Phys Fermi 194*, pp. 73–80, 2016, doi: 10.3254/978-1-61499-732-0-73.

[50] A. Bertarelli *et al.*, 'Behaviour of advanced materials impacted by high energy particle beams', *J. Phys. Conf. Ser.*, vol. 451, no. 1, p. 012005, 2013, doi: 10.1088/1742-6596/451/1/012005.

[51] I. Efthymiopoulos *et al.*, 'HiRadMat: A New Irradiation Facility for Material Testing at CERN', San Sebastián, Spain, 2011, pp. 1665–1667.

[52] 'HiRadMat Beam Parameters', *CERN official website*. https://espace.cern.ch/hiradmat-sps/Wiki%20Pages/Beam%20Parameters.aspx.

[53] 'High-Radiation to Materials (HiRadMat) Facility of CERN/SPS', *CERN official website*. https://espace.cern.ch/hiradmat-sps/Wiki%20Pages/Home.aspx.

[54] A. Bertarelli *et al.*, 'Permanent Deformation of the LHC Collimator Jaws Induced by Shock Beam Impact: an Analytical and Numerical Interpretation', p. 3, 2006.

[55] M. Cauchi *et al.*, 'High energy beam impact tests on a LHC tertiary collimator at the CERN high-radiation to materials facility', *Phys. Rev. Spec. Top. - Accel. Beams*, vol. 17, no. 2, p. 021004, Feb. 2014, doi: 10.1103/PhysRevSTAB.17.021004.

[56] A. Bertarelli *et al.*, 'High Energy Tests of Advanced Materials for Beam Intercepting Devices at CERN HiRadMat Facility', p. 5, 2012.

[57] ANSYS, Inc., *Ansys® Academic Research Mechanical, Release 18.1*.

[58] ANSYS, Inc., *Autodyn® Nonlinear dynamic analysis software, Release 18.1*.

[59] F. Carra *et al.*, 'The "Multimat" experiment at CERN HiRadMat facility: advanced testing of novel materials and instrumentation for HL-LHC collimators', in *Journal of Physics: Conference Series*, Copenhagen, Denmark, 2017, vol. 874, doi: 10.1088/1742-6596/874/1/012001.

[60] M. Pasquali *et al.*, 'Dynamic response of advanced materials impacted by particle beams: the MultiMat experiment', *J. Dyn. Behav. Mater.*, 2019.

[61] A. Bertarelli *et al.*, 'An experiment to test advanced materials impacted by intense proton pulses at CERN HiRadMat facility', *Nucl. Instrum. Methods Phys. Res. Sect. B Beam Interact. Mater. At.*, vol. 308, pp. 88–99, Aug. 2013, doi: 10.1016/j.nimb.2013.05.007.

[62] E. Quaranta, 'Investigation of Collimator Materials for the High Luminosity Large Hadron Collider', Politecnico di Milano, Italy, 2017.

[63] A. Bertarelli, F. Carra, N. Mariani, and S. Bizzaro, 'Development and testing of novel advanced materials with very high thermal shock resistance', EuCARD-2 Scientific Report CERN-ACC-2014-0306, 2014. Accessed: Feb. 06, 2018. [Online]. Available: https://cds.cern.ch/record/1973365/files/CERN-ACC- 2014-0306.pdf.

[64] A. Bertarelli *et al.*, 'Innovative MoC – graphite composite for thermal management and thermal shock applications', Mar. 2015, pp. 56–59, doi: 10.1109/SEMI-THERM.2015.7100140.

[65] A. Bertarelli, G. Arnau Izquierdo, F. Carra, A. Dallocchio, M. Gil Costa, and N. Mariani, 'Research and development of novel advanced materials for next-generation collimators', presented at the 2nd International Particle Accelerator Conference, San Sebastian, Spain, 2011.

[66] J. Anthony, R. Bideaux, K. Bladh, and M. Nichols, 'Moissanite', in *Handbook of Mineralogy*, Mineralogical Society of America.

[67] Y. Zhong, L. Shaw, M. Manjarres, and M. F. Zawrah, 'Synthesis of Silicon Carbide Nanopowder Using Silica Fume', *J. Am. Ceram. Soc.*, vol. 93, no. 10, pp. 3159–3167, 2010, doi: 10.1111/j.1551-2916.2010.03867.x.

[68] G. L. Harris, 'Properties of Silicon Carbide', Institution of Engineering and Technology, 2005, pp. 19, 170–180.

[69] J. A. Lely, 'Darstellung von Einkristallen von Silicium Carbid und Beherrschung von Art und Menge der eingebauten Verunreinigungen', *Berichte Dtsch. Keram. Ges.*, vol. 32, pp. 229–236, 1955.

[70] 'Lely SiC Wafers', *Nitride Crystals*. http://www.nitride-crystals.com/Lely-Wafers.htm.

[71] J. Whitaker, 'The electronics handbook', CRC Press, 2005.

[72] R. Cheung, 'Silicon carbide microelectromechanical systems for harsh environments', Imperial Colege Press, 2006, p. 3.

[73] R. Blanchon, 'Caractérisation du Carbure de Silicium pour application au projet Collimateurs Phase II du LHC', CERN, Geneva, Jul. 16, 2009.

[74] H. Rashid, A. Koel, T. Rang, R. Gähwiler, M. Grosberg, and R. Jõemaa, 'Nanoscale and microscale simulations of N-N junction heterostructures of 3C-4H Silicon Carbide', Tallinn, Estonia, Jun. 2017, pp. 235–248, doi: 10.2495/MC170241.

[75] Saint-Gobain, 'Hexoloy SA SiC Material'. https://www.refractories.saint-gobain.com/hexoloy/sa-grade (accessed Sep. 05, 2018).

[76] G. D. Quinn and J. A. Salem, 'Effect of Lateral Cracks on Fracture Toughness Determined by the Surface-Crack-in-Flexure Method', *J. Am. Ceram. Soc.*, vol. 85, no. 4, pp. 873–880, Dec. 2004, doi: 10.1111/j.1151-2916.2002.tb00186.x.

[77] H. Wu, 'Understanding residual stresses and fracture toughness in ceramic nanocomposites', in *Residual Stresses in Composite Materials*, Woodhead Publishing, 2014, p. 404.

[78] Microcertec, 'Matériaux : Carbure de silicium (SiC)'. http://www.microcertec.com/fiche-materiaux-fr-9-carbure-de-silicium-sic.html.

[79] A. Bakin, 'SiC Homoepitaxy and Heteroepitaxy', in *SiC Materials and Devices*, vol. 1, World Scientific, 2006, pp. 43–76.

[80] K. Byrappa and T. Ohachi, 'Crystal Growth Technology', Springer, 2003, pp. 180–200.

[81] Michel Bougoin, Jérôme Lavenac, Alexandre Gerbert-Gaillard, and Dominique Pierot, 'The SiC primary mirror of the EUCLID telescope', Sep. 2017, vol. 10562, [Online]. Available: https://doi.org/10.1117/12.2296073.

[82] M. Delonca, C. Maglioni, M. Gil Costa, and A. Vacca, 'Use of Silicon Carbide as Beam Intercepting Device Material: Tests, Issues and Numerical Simulation', presented at the IPAC14, Dresden, Germany, Jun. 2014.

[83] 'International Journal of Refractory Metals and Hard Materials'. https://www.journals.elsevier.com/international-journal-of-refractory-metals-and-hard-materials/.

[84] J. A. Shields, 'Applications of Molybdenum Metal and its Alloys', IMOA International Molybdenum Association, 2013, p. 27.

[85] E. L. Baker, 'Development of Molybdenum Shaped Charge Liners', in *Proceedings of the TMS Symposium on Molybdenum and Molybdenum Alloys*, 1988, p. 27.

[86] Plansee High Performance Materials, 'Mechanical Properties of Molybdenum and its Alloys'. https://www.plansee.com/en/materials/molybdenum.html.

[87] R. Smallwood, 'TZM Moly Alloy', in *ASTM special technical publication 849: Refractory metals and their industrial applications: a symposium*, ASTM International, p. 9.

[88] L. B. Lundberg, 'A Critical Evaluation of Molybdenum and Its Alloys for Use in Space Reactor Core Heat Pipes', Los Alamos National Laboratories, LA-8685-MS, 1981.

[89] C. Torregrosa, 'Comprehensive Study for an Optimized Redesign of the CERN's Antiproton Decelerator Target', Universitat Politecnica de Valencia, Valencia, 2018.

[90] M. Scapin, C. Fichera, F. Carra, and L. Peroni, 'Experimental investigation of the

behaviour of tungsten and molybdenum alloys at high strain-rate and temperature', *EPJ Web Conf.*, vol. 94, p. 01021, 2015, doi: 10.1051/epjconf/20159401021.

[91] P. Hu *et al.*, 'High temperature mechanical properties of TZM alloys under different lanthanum doping treatments', *J. Alloys Compd.*, vol. 711, pp. 64–70, Jul. 2017, doi: 10.1016/j.jallcom.2017.03.346.

[92] N. Mariani, 'Development of Novel, Advanced Molybdenum-based Composites for High Energy Physics Applications', PhD Thesis, Politecnico di Milano, Milan, Italy, 2014.

[93] A. S. Barnard, *The Diamond formula: diamond synthesis - a gemmological perspective*. London: NAG Press, 2008.

[94] S. Kidalov and F. Shakhov, 'Thermal Conductivity of Diamond Composites', *Materials*, vol. 2, no. 4, pp. 2467–2495, Dec. 2009, doi: 10.3390/ma2042467.

[95] K. Chu *et al.*, 'Thermal conductivity of SPS consolidated Cu/diamond composites with Cr-coated diamond particles', *J. Alloys Compd.*, vol. 490, no. 1–2, pp. 453–458, Feb. 2010, doi: 10.1016/j.jallcom.2009.10.040.

[96] Th. Schubert, B. Trindade, T. Weißgärber, and B. Kieback, 'Interfacial design of Cu-based composites prepared by powder metallurgy for heat sink applications', *Mater. Sci. Eng. A*, vol. 475, no. 1–2, pp. 39–44, Feb. 2008, doi: 10.1016/j.msea.2006.12.146.

[97] K. Yoshida and H. Morigami, 'Thermal properties of diamond/copper composite material', *Microelectron. Reliab.*, vol. 44, no. 2, pp. 303–308, Feb. 2004, doi: 10.1016/S0026-2714(03)00215-4.

[98] Y. Zhang, H. L. Zhang, J. H. Wu, and X. T. Wang, 'Enhanced thermal conductivity in copper matrix composites reinforced with titanium-coated diamond particles', *Scr. Mater.*, vol. 65, no. 12, pp. 1097–1100, Dec. 2011, doi: 10.1016/j.scriptamat.2011.09.028.

[99] H. J. Cho, Y.-J. Kim, and U. Erb, 'Thermal conductivity of copper-diamond composite materials produced by electrodeposition and the effect of TiC coatings on diamond particles', *Compos. Part B Eng.*, vol. 155, pp. 197–203, Dec. 2018, doi: 10.1016/j.compositesb.2018.08.014.

[100] P. T. Jochym, K. Parlinski, and M. Sternik, 'TiC lattice dynamics from ab initio calculations', *Eur. Phys. J. B*, vol. 10, no. 1, pp. 9–13, Jul. 1999, doi: 10.1007/s100510050823.

[101] R. M. Mazitov *et al.*, 'Density of phonon states in nanostructured copper', *JETP Lett.*, vol. 92, no. 4, pp. 238–243, Aug. 2010, doi: 10.1134/S0021364010160095.

[102] J. Xie, S. P. Chen, J. S. Tse, S. de Gironcoli, and S. Baroni, 'High-pressure thermal expansion, bulk modulus, and phonon structure of diamond', *Phys. Rev. B*, vol. 60, no. 13, pp. 9444–9449, Oct. 1999, doi: 10.1103/PhysRevB.60.9444.

[103] T. Weißgärber, 'Copper/diamond Composites for Heat Sink Applications', *Fraunhofer IFAM*, 2019. https://www.nanoanalytik.fraunhofer.de/en/library/CS1.html.

[104] A. Bertarelli *et al.*, 'Novel materials for collimators at LHC and its upgrades', East-Lansing, MI, USA, 2014.

[105] 'RHP-Technology GmbH', 2019. http://www.rhp-technology.com/.

[106] M. Kitzmantel, 'Developments and Novelties in Thermal Management by RHP-Technology', presented at the EuCARD-2 Workshop on Applications of Thermal

Management Materials, CERN, Geneva, Nov. 2015, [Online]. Available: http://indico.cern.ch/event/400452/.

[107] H. Bargmann, 'Dynamic Response of External Targets Under Thermal Shock', CERN Technical Note No. LAB II/BT/Int/73-3, 1973.

[108] P. Sievers, 'Elastic Stress Waves in Matter Due to Rapid Heating by an Intense High-Energy Particle Beam', CERN Technical Note No. LAB II/BT/74-2, 1974.

[109] B. A. Boley, 'Approximate analyses of thermally induced vibrations of beams and plates', *J. Appl. Mech.*, vol. 24, no. 3, pp. 413–416.

[110] A. Bertarelli, A. Dallocchio, and T. Kurtyka, 'Dynamic Response of Rapidly Heated Cylindrical Rods: Longitudinal and Flexural Behavior', *J. Appl. Mech.*, vol. 75, no. 3, Apr. 2008, doi: 10.1115/1.2839901.

[111] M. Cauchi *et al.*, 'Thermomechanical assessment of the effects of a jaw-beam angle during beam impact on Large Hadron Collider collimators', *Phys. Rev. Spec. Top. - Accel. Beams*, vol. 18, Feb. 2015, doi: 10.1103/PhysRevSTAB.18.021001.

[112] M. Portelli, A. Bertarelli, F. Carra, L. K. Mettler, P. Mollicone, and N. Sammut, 'Numerical simulation of long rods impacted by particle beams', *Phys. Rev. Accel. Beams*, vol. 21, no. 6, Jun. 2018, doi: 10.1103/PhysRevAccelBeams.21.063501.

[113] S. M. Han, H. Benaroya, and T. Wei, 'Dynamics of Transversely Vibrating Beams using Four Engineering Theories', *J. Sound Vib.*, vol. 225, no. 5, pp. 935–988, Sep. 1999, doi: 10.1006/jsvi.1999.2257.

[114] N. Tahir *et al.*, 'Simulation Studies of Impact of SPS Beam with Collimator Materials', in *Proceedings of the 11th European Particle Accelerator Conference*, Genoa, Italy, Jun. 2008, pp. 2689–2691.

[115] M. Scapin, L. Peroni, and A. Dallocchio, 'Thermo-Mechanical Modelling of High Energy Particle Beam Impacts', in *Numerical Modeling of Materials Under Extreme Conditions*, 1st ed. 2014., Berlin, Heidelberg: Springer Berlin Heidelberg, 2014, pp. 87–106.

[116] M. Scapin, L. Peroni, A. Dallocchio, and A. Bertarelli, 'Shock Loads Induced on Metal Structures by LHC Proton Beams: Modelling of Thermo-Mechanical Effects', *Appl. Mech. Mater.*, vol. 82, pp. 338–343, Jul. 2011, doi: 10.4028/www.scientific.net/AMM.82.338.

[117] M. Scapin, L. Peroni, and A. Dallocchio, 'Effects induced by LHC high energy beam in copper structures', *J. Nucl. Mater.*, vol. 420, no. 1, pp. 463–472, Jan. 2012, doi: 10.1016/j.jnucmat.2011.10.036.

[118] L. Peroni, M. Scapin, and A. Dallocchio, 'Thermo-mechanical modelling of metal structures subjected to high energy particle beam impacts', p. 4.

[119] M. Scapin, L. Peroni, and A. Dallocchio, 'Damage evaluation in metal structures subjected to high energy deposition due to particle beams', *J. Phys. Conf. Ser.*, vol. 305, p. 012062, Jul. 2011, doi: 10.1088/1742-6596/305/1/012062.

[120] A. Dallocchio, 'Study of thermo-mechanical effects induced in solids by high energy particle beams: Analytical and Numerical methods', Politecnico di Torino, 2008.

[121] F. Carra, 'Numerical analyses of novel materials under quasi-instantaneous heat deposition', in *Thermomechanical Response of Advanced Materials under Quasi Instantaneous Heating*, Italy: Politecnico di Torino, 2017, pp. 138–140.

[122] A. Ferrari, P. R. Sala, A. Fassò, and J. Ranft, 'FLUKA: A multi-particle transport code (program version 2005)', CERN, Geneva, 2005.

[123] O. E. Krivosheev and N. V. Mokhov, 'A new MARS and its applications', Tsukuba, Japan, FERMILAB-CONF-98-043, 1998.

[124] S. Agostinelli *et al.*, 'Geant4—a simulation toolkit', *Nucl. Instrum. Methods Phys. Res. Sect. Accel. Spectrometers Detect. Assoc. Equip.*, vol. 506, no. 3, pp. 250–303, Jul. 2003, doi: 10.1016/S0168-9002(03)01368-8.

[125] W. Hohenauer, 'Thermophysical Characterisation of CVD-SiC: thermal diffusivity and specific heat', Austrian Institute of Technology, 2.04.000766.1.19-10.

[126] Plansee, 'Molybdenum'. https://www.plansee.com/en/materials/molybdenum.html.

[127] H. Shinno, M. Kitajima, and M. Okada, 'Thermal stress analysis of high heat flux materials', *J. Nucl. Mater.*, no. 155–157, pp. 290–294, 1988.

[128] R. Courant, K. Friedrichs, and H. Lewy, 'Über die partiellen Differenzengleichungen der mathematischen Physik', *Math. Ann.*, vol. 100, no. 1, pp. 32–74, 1928.

[129] D. J. Inman, 'Engineering Vibration', 3rd ed., Upper Saddle, New Jersey: Prentice Hall PTR, 2017, pp. 43–48.

[130] Y. Hiraoka, H. Kurishita, M. Narui, and H. Kayano, 'Fracture and Ductile-to-Brittle Transition Characteristics of Molybdenum by Impact and Static Bend Tests', *Mater. Trans. JIM*, vol. 36, no. 4, pp. 504–510, 1995.

[131] M. Scapin, L. Peroni, and F. Carra, 'Investigation and Mechanical Modelling of Pure Molybdenum at High Strain-Rate and Temperature', *J. Dyn. Behav. Mater.*, vol. 2, no. 4, pp. 460–475, Dec. 2016, doi: 10.1007/s40870-016-0081-3.

[132] J. Duan, C. Hu, and H. Chen, 'High-Resolution Micro-CT for Morphologic and Quantitative Assessment of the Sinusoid in Human Cavernous Hemangioma of the Liver', *PLoS ONE*, vol. 8, no. 1, p. e53507, Jan. 2013, doi: 10.1371/journal.pone.0053507.

[133] G. van Dalen, H. Blonk, H. van Aalst, and C. Luengo Hendriks, '3-D Imaging of Foods Using X-Ray Microtomography', *G.I.T. Imaging & Microscopy*, 2011. https://web.archive.org/web/20110719140749/http://www.cb.uu.se/~cris/Documents/GIT2003.pdf.

[134] D. A. H. Hanaor *et al.*, 'Compressive performance and crack propagation in Al alloy/Ti2AlC composites', *Mater. Sci. Eng. A*, vol. 672, pp. 247–256, Aug. 2016, doi: 10.1016/j.msea.2016.06.073.

[135] C. C. Shaw, Ed., 'Cone beam computed tomography', in *Imaging in medical diagnosis and therapy*, Boca Raton: CRC Press, Taylor & Francis Group, 2014, p. 35.

[136] W. van Aarle *et al.*, 'The ASTRA Toolbox: A platform for advanced algorithm development in electron tomography', *Ultramicroscopy*, vol. 157, pp. 35–47, Oct. 2015, doi: 10.1016/j.ultramic.2015.05.002.

[137] W. van Aarle *et al.*, 'Fast and flexible X-ray tomography using the ASTRA toolbox', *Opt. Express*, vol. 24, no. 22, p. 25129, Oct. 2016, doi: 10.1364/OE.24.025129.

[138] J. Guardia-Valenzuela, 'Development and characterisation of novel graphite-matrix composite material for thermal management applications', Escuela de Ingenieria Y Arquitectura, Universidad de Zaragoza, Spain, MSc Thesis, 2015.

[139] J. Guardia-Valenzuela, A. Bertarelli, F. Carra, N. Mariani, S. Bizzaro, and R. Arenal,

'Development and properties of high thermal conductivity molybdenum carbide - graphite composites', *Carbon*, vol. 135, pp. 72–84, Aug. 2018, doi: 10.1016/j.carbon.2018.04.010.

[140] R. Bruce and S. Redaelli, 'CuCD-based tertiary collimator', presented at the HL-LHC TCC Meeting, CERN, Geneva, Jul. 04, 2019.

[141] F. Carra, J. G. Valenzuela, P. Gradassi, and L. K. Mettler, 'Results on simulations of new materials and composites', CERN, CERN, Geneva, EuCARD2 WP11 Deliverable 11.1, 2016. [Online]. Available: https://edms.cern.ch/document/1325252/3.

[142] 'DIL 402 Expedis Classic'. https://www.netzsch-thermal-analysis.com/en/products-solutions/dilatometer/dil-402-expedis-classic/.

[143] ASTM International, 'Standard Test Method for Linear Thermal Expansion of Solid Materials With a Push-Rod Dilatometer', ASTM International, Standard ASTM E228-17. doi: 10.1520/E0228-17.

[144] 'Sartorius Quintix Analytical Balance 224-1x'. https://www.northernbalance.co.uk/product/sartorius-quintix-analytical-balance-224-1x/ (accessed Oct. 22, 2019).

[145] DIN, 'Thermal analysis - Differential thermal analysis (DTA) and differential scanning calorimetry (DSC) - General Principles', DIN, Standard DIN 51007:2019-04, 2019. doi: 10.1520/E1876-15.

[146] J. Guardia-Valenzuela, 'Mathematical model and extrapolation for thermal diffusivity and specific heat', EDMS No. 1540215.

[147] T. Burchell, 'Graphite: Properties and Characteristics', *Compr. Nucl. Mater.*, no. 2, pp. 285–305, 2012, doi: 10.1016/B978-0-08-056033-5.00020-3.

[148] D. R. Lide, 'CRC Handbook of Chemistry and Physics', 90th ed., Boca Raton, Florida: CRC Press, 2009, pp. 2–65.

[149] M. Borg *et al.*, 'Thermostructural characterization and structural elastic property optimization of novel high luminosity LHC collimation materials at CERN', *Phys. Rev. Accel. Beams*, vol. 21, 2018, doi: 10.1103/PhysRevAccelBeams.21.031001.

[150] ASTM International, 'Standard Test Method for Dynamic Young's Modulus, Shear Modulus, and Poisson's Ratio by Impulse Excitation of Vibration', ASTM International, Standard ASTM E1876-15. doi: 10.1520/E1876-15.

[151] ASTM International, 'Standard Test Method for Dynamic Young's Modulus, Shear Modulus, and Poisson's Ratio for Advanced Ceramics by Impulse Excitation of Vibration', ASTM International, Standard ASTM C1259-15. doi: 10.1520/C1259-15.

[152] 'Methods of test for refractory products - Part 1: Determination of dynamic Young's modulus (MOE) by impulse excitation of vibration', ISO/TC 33 Refractories, ISO 12680-1:2005, 2005. Accessed: Jan. 10, 2020. [Online]. Available: https://www.iso.org/standard/37670.html.

[153] G. Roebben, B. Bollen, A. Brebels, J. Van Humbeeck, and O. Van der Biest, 'Impulse excitation apparatus to measure resonant frequencies, elastic moduli, and internal friction at room and high temperature', *Rev. Sci. Instrum.*, vol. 68, no. 12, pp. 4511–4515, Dec. 1997, doi: 10.1063/1.1148422.

[154] N. Traon, T. Tonnesen, and R. Telle, 'Estimation of Damage in Refractory Materials after Progressive Thermal Shocks with Resonant Frequency Damping Analysis', *J.*

Ceram. Sci. Tech., no. 02, 2016, doi: 10.4416/JCST2015-00080.

[155] G. Roebben, B. Basu, J. Vleugels, J. Van Humbeeck, and O. Van der Biest, 'The innovative impulse excitation technique for high-temperature mechanical spectroscopy', *J. Alloys Compd.*, vol. 310, no. 1–2, pp. 284–287, Sep. 2000, doi: 10.1016/S0925-8388(00)00966-X.

[156] ASTM International, 'Standard Test Method for Flexural Strength of Manufactured Carbon and Graphite Articles Using Four-Point Loading at Room Temperature', ASTM International, Standard ASTM C651-15. doi: 10.1520/C0651-15.

[157] ASTM International, 'Standard Test Methods for Tension Testing of Metallic Materials', ASTM International, Standard ASTM E8 / E8M-16a, 2016. doi: 10.1520/E0008_E0008M-16A.

[158] G. T. Gray, 'Classic Split-Hopkinson Pressure Bar Testing', in *ASM Handbook Volume 8: Mechanical Testing and Evaluation*, vol. 8, ASM International, 2000, pp. 462–476.

[159] *LASL Shock Hugoniot Data*. Los Alamos Scientific Laboratory: University of California Press, 1980.

[160] K. Sobczyk, *Stochastic wave propagation*. Amsterdam; New York: Elsevier, 1985.

[161] Z. Hashin, 'Theory of Mechanical Behavior of Heterogeneous Media', University of Pennsylvania, Technical Report 3, Jul. 1963. Accessed: Jul. 09, 2020. [Online]. Available: https://apps.dtic.mil/sti/pdfs/AD0412503.pdf.

[162] Z. Hashin, 'Failure Criteria for Unidirectional Fiber Composites', *J. Appl. Mech.*, vol. 47, no. 2, pp. 329–334, Jun. 1980, doi: 10.1115/1.3153664.

[163] G. Herrmann and J. Achenbach, 'On Dynamic Theories of Fiber Composites', presented at the 8th Structural Dynamics and Materials Conference, Palm Springs,CA,U.S.A., Mar. 1967, doi: 10.2514/6.1967-1112.

[164] A. C. Eringen, 'Linear Theory of Micropolar Elasticity', Office of Naval Research, US, AD664271, Jun. 1967.

[165] F. C. Moon and C. C. Mow, 'Wave Propagation in a Composite Material Containing Dispersed Rigid Spherical Inclusions', United States Air Force Project RAND, RM-6139-PR, Dec. 1970.

[166] Y. Pao and C. C. Mow, 'Scattering of Plane Compressional Waves by a Spherical Obstacle', *J. Appl. Phys.*, vol. 34, no. 3, pp. 493–499, Mar. 1963, doi: 10.1063/1.1729301.

[167] C. C. Mow, 'On the Effects of Stress-Wave Diffraction on Ground-Shock Measurements: Part I', The Rand Corporation, RM-4341-PR, Jan. 1965.

[168] Y. Chen and J. Ma, 'Random noise attenuation by *f-x* empirical-mode decomposition predictive filtering', *GEOPHYSICS*, vol. 79, no. 3, pp. V81–V91, May 2014, doi: 10.1190/geo2013-0080.1.

[169] Y. Chen, G. Zhang, S. Gan, and C. Zhang, 'Enhancing seismic reflections using empirical mode decomposition in the flattened domain', *J. Appl. Geophys.*, vol. 119, pp. 99–105, Aug. 2015, doi: 10.1016/j.jappgeo.2015.05.012.

[170] Y. Chen, 'Dip-separated structural filtering using seislet transform and adaptive empirical mode decomposition based dip filter', *Geophys. J. Int.*, vol. 206, no. 1, pp. 457–469, Jul. 2016, doi: 10.1093/gji/ggw165.

[171] T. L. Szabo and J. Wu, 'A model for longitudinal and shear wave propagation in

viscoelastic media', *J. Acoust. Soc. Am.*, vol. 107, no. 5, pp. 2437–2446, May 2000, doi: 10.1121/1.428630.

[172] T. L. Szabo, 'Time domain wave equations for lossy media obeying a frequency power law', *J. Acoust. Soc. Am.*, vol. 96, no. 1, pp. 491–500, Jul. 1994, doi: 10.1121/1.410434.

[173] W. Chen and S. Holm, 'Modified Szabo's wave equation models for lossy media obeying frequency power law', *J. Acoust. Soc. Am.*, vol. 114, no. 5, p. 2570, 2003, doi: 10.1121/1.1621392.

[174] J. M. Carcione, F. Cavallini, F. Mainardi, and A. Hanyga, 'Time-domain Modeling of Constant- Q Seismic Waves Using Fractional Derivatives', *Pure Appl. Geophys.*, vol. 159, no. 7–8, pp. 1719–1736, Jul. 2002, doi: 10.1007/s00024-002-8705-z.

[175] W. Chen and S. Holm, 'Fractional Laplacian time-space models for linear and nonlinear lossy media exhibiting arbitrary frequency power-law dependency', *J. Acoust. Soc. Am.*, vol. 115, no. 4, pp. 1424–1430, Apr. 2004, doi: 10.1121/1.1646399.

[176] V. Kouznetsova, 'Computational homogenization for the multi-scale analysis of multi-phase materials', Doctor of Philosophy, Technische Universiteit Eindhoven, Eindhoven, 2002.

[177] R. Younes, A. Hallal, F. Fardoun, and F. Hajj, 'Comparative Review Study on Elastic Properties Modeling for Unidirectional Composite Materials', in *Composites and Their Properties*, N. Hu, Ed. InTech, 2012.

[178] F. Pavia, 'How to Simulate and Design the Microstructures of Composites and Other Complex Materials'. https://www.ansys.com/blog/how-to-simulate-microstructures-composites#:~:text=Ansys%20Material%20Designer%2C%20available%20in,of%20complex%20materials%20and%20composites. (accessed Jul. 16, 2020).

[179] M. G. D. Geers, V. G. Kouznetsova, and W. A. M. Brekelmans, 'Multi-scale computational homogenization: Trends and challenges', *J. Comput. Appl. Math.*, vol. 234, no. 7, pp. 2175–2182, Aug. 2010, doi: 10.1016/j.cam.2009.08.077.

[180] R. Hill, 'Elastic properties of reinforced solids: Some theoretical principles', *J. Mech. Phys. Solids*, vol. 11, no. 5, pp. 357–372, Sep. 1963, doi: 10.1016/0022-5096(63)90036-X.

[181] S. L. Omairey, P. D. Dunning, and S. Sriramula, 'Development of an ABAQUS plugin tool for periodic RVE homogenisation', *Eng. Comput.*, vol. 35, no. 2, pp. 567–577, Apr. 2019, doi: 10.1007/s00366-018-0616-4.

[182] S. Li, L. F. C. Jeanmeure, and Q. Pan, 'A composite material characterisation tool: UnitCells', *J. Eng. Math.*, vol. 95, no. 1, pp. 279–293, Dec. 2015, doi: 10.1007/s10665-014-9776-4.

[183] A. Bertarelli *et al.*, 'Updated Robustness Limits for Collimator Materials (HRMT09 & HRMT14)', Annecy, France, 2013, p. 6.

[184] H. Kolsky, *Stress waves in solids*, New, 2. ed., Corrected by the author, Suppl. bibliogr. New York: Dover Publications, 1963.

[185] M. Portelli *et al.*, 'Thermomechanical Characterisation of Copper Diamond and Benchmarking with the MultiMat experiment', *Shock Vib.*, no. Special Issue: Structural and Wave Propagation Effects in High-Energy Particle Impacts, Accepted for publication 2020, doi: 10.1155/2020/8879400.

[186] P. W. Bridgman, 'Recent Work in the Field of High Pressures', *Rev. Mod. Phys.*, vol.

18, no. 1, pp. 1–93, 1946, doi: doi.org/10.1103/RevModPhys.18.1.

[187] J. M. Walsh and R. H. Christian, 'Equation of State of Metals from Shock Wave Measurements', *Phys. Rev.*, vol. 97, no. 6, pp. 1544–1556, 1955, doi: doi.org/10.1103/PhysRev.97.1544.

[188] R. W. Goranson *et al.*, 'Dynamic Determination of the Compressibility of Metals', *J. Appl. Phys.*, vol. 26, no. 12, pp. 1472–1479, Dec. 1955, doi: 10.1063/1.1721933.

[189] R. G. McQueen and S. P. Marsh, 'Hugoniots of Graphites of Various Initial Densities and the Equation of State of Carbon', in *Behavior of Dense Media under High Dynamic Pressures*, Paris, 1967, pp. 207–216.

[190] M. Van Thiel, A. S. Kusubov, and A. C. Mitchell, 'Compendium of Shock Wave Data', Lawrence Radiation Laboratory, Livermore, UCRL-50108, 1967.

[191] R. G. McQueen, 'Laboratory techniques for very high pressures and the behaviour of metals under dynamic loading', LADC-5561, CONF-331-4, 4013771, Jan. 1962. doi: 10.2172/4013771.

[192] R. G. McQueen and S. P. Marsh, 'Equation of State for Nineteen Metallic Elements from Shock-Wave Measurements to Two Megabars', *J. Appl. Phys.*, vol. 31, no. 7, pp. 1253–1269, Jul. 1960, doi: 10.1063/1.1735815.

[193] J. M. Walsh, M. H. Rice, R. G. McQueen, and F. L. Yarger, 'Shock-Wave Compressions of Twenty-Seven Metals. Equations of State of Metals', *Phys. Rev.*, vol. 108, no. 2, pp. 196–216, Oct. 1957, doi: 10.1103/PhysRev.108.196.

[194] M. H. Rice, R. G. McQueen, and J. M. Walsh, 'Compression of Solids by Strong Shock Waves', in *Solid State Physics*, vol. 6, Elsevier, 1958, pp. 1–63.

[195] R. G. McQueen, S. P. Marsh, J. W. Taylor, J. N. Fritz, and W. J. Carter, 'The Equation of State of Solids from Shock Wave Studies', in *High-Velocity Impact Phenomena*, Elsevier, 1970, pp. 293–417.

[196] R. G. McQueen and S. P. Marsh, 'The Determination of New Standards for Shock Wave Equation-of-State Work', in *Behavior of Dense Media under High Dynamic Pressures*, Paris, 1967, pp. 67–83.

[197] B. I. Bennett, 'Equations of State—Theoretical Formalism', *Los Alamos Sci.*, vol. 1, 2000, Accessed: Aug. 13, 2020. [Online]. Available: https://fas.org/sgp/othergov/doe/lanl/pubs/00818023.pdf.

[198] F. H. Crawford, *Heat, Thermodynamics, and Statistical Physics*. London: Harcourt, Brace & World, Inc., 1963.

[199] R. Haase, 'Chapter 1: Survey of Fundamental Laws', in *Physical Chemistry: An Advanced Treatise*, vol. Volume I: Thermodynamics, 1971, pp. 1–97.

[200] H. von Helmholtz, J. W. Hittorf, and J. D. Waals, *Physical Memoirs Selected and Translated from Foreign Sources*. Taylor & Francis, 1888.

[201] P. Perrot, *A to Z of thermodynamics*, Reprinted. Oxford: Oxford Univ. Press, 2008.

[202] M. Portelli, A. Bertarelli, F. Carra, M. Pasquali, N. Sammut, and P. Mollicone, 'Numerical and experimental benchmarking of the dynamic response of SiC and TZM specimens in the MultiMat experiment', *Mech. Mater.*, vol. 138, p. 103169, Nov. 2019, doi: 10.1016/j.mechmat.2019.103169.

Bibliography

A. Bertarelli, *'Beam-Induced Damage Mechanisms and their Calculation'*, CERN, Geneva, Switzerland, 2016

M. Meyers, '*Dynamic Behavior of Materials'*, New York, 1994

K. F. Graff, '*Wave Motion in Elastic Solids*', San Diego, 1991

O. Brüning, P. Collier, P. Lebrun, S. Myers, R. Ostojic, J. Poole, P. Proudlock, *'LHC Design Report'*, CERN, Geneva, Switzerland, 2004

G. Apollinari, I. Béjar Alonso, O. Brüning, M. Lamont, L. Rossi, *'High-Luminosity Large Hadron Collider (HL-LHC) Preliminary Design Report'*, CERN, Geneva, Switzerland, 2015